

MODEL ATMOSPHERES FOR ACCRETING SYSTEMS

A THESIS SUBMITTED FOR THE DEGREE
OF DOCTOR OF PHILOSOPHY

by

J.R.E. Brooker

DEPARTMENT OF ASTRONOMY
UNIVERSITY OF LEICESTER

1987

UMI Number: U004228

All rights reserved

INFORMATION TO ALL USERS

The quality of this reproduction is dependent upon the quality of the copy submitted.

In the unlikely event that the author did not send a complete manuscript and there are missing pages, these will be noted. Also, if material had to be removed, a note will indicate the deletion.



UMI U004228

Published by ProQuest LLC 2015. Copyright in the Dissertation held by the Author.
Microform Edition © ProQuest LLC.

All rights reserved. This work is protected against
unauthorized copying under Title 17, United States Code.



ProQuest LLC
789 East Eisenhower Parkway
P.O. Box 1346
Ann Arbor, MI 48106-1346

ACKNOWLEDGEMENTS

I am indebted to many people for their help and encouragement during the last three years. Foremost, I thank Dr. A.R. King for his excellent supervision of this work and for not noticing when I wasn't there. Many thanks must go to Dr. G.A. Williams for providing the original version of ATMOS and for his help in applying it to accreting systems. Thanks are also due to Dr. M.G. Watson for many fruitful discussions concerning this work.

Many thanks go to the members of the Astronomy Department, especially Norma for offering her help when the word-processor went haywire. Special thanks to the occupants of the Bennett Underpass; Charon Birkett, Alan Fitzsimmons, Randall Brooks and Mark O'Reilly, for putting up with my abuse of the University mainframe (and word-processor !) and for providing the lighter moments during my stay.

I am grateful to my family, especially my mother, for their encouragement throughout my years here at Leicester and for believing, even when I didn't. Thanks must also go to all my friends (who are too numerous to mention) for their kindness and support.

Finally, none of this would have been possible without the help of the University mainframe and Starlink computers; I certainly learnt a great deal from using them !!

CONTENTS

CHAPTER 1	INTRODUCTION	1.1
1.1	Interacting binary systems	1.3
1.2	Accretion disc formation	1.6
1.3	Column accretion	1.9
1.4	Model atmospheres .v. black bodies	1.14
1.5	Model polecap atmospheres - other uses	1.16 1.17
CHAPTER 2	THE CALCULATION OF A STELLAR ATMOSPHERE MODEL	2.1
2.1	Introduction	2.2
2.2	The initial model	2.2
2.2.1	An approximate solution - the grey atmosphere	2.4
2.2.2	Mean opacities and the grey solution	2.8
2.3	The solution of the transfer equation	2.11
2.3.1	The transfer equation as a two-point boundary value problem	2.11
2.4	Correcting the temperature structure	2.21
2.5	Hydrostatic equilibrium	2.24 2.25
CHAPTER 3	DESCRIPTION OF POLECAP ATMOSPHERE CODE	3.1
3.1	Introduction	3.2
3.2	Calculating a model polecap atmosphere	3.2 3.9
CHAPTER 4	MODEL ATMOSPHERE SPECTRA	4.1
4.1	Introduction	4.2
4.2	The outward surface spectrum	4.2
4.3	Spectral shape .v. input parameters	4.4
4.3.1	Spectral shape .v. effective temperature	4.5
4.3.2	Spectral shape .v. white dwarf gravity	4.7
4.3.3	Spectral shape .v. strength of illumination	4.9
4.3.4	Summary	4.12
4.4	Limb effects in a model atmosphere spectrum	4.13
4.5	The temperature structure of the atmosphere	4.15
4.6	Discussion of the calculated spectra	4.20
4.7	Model atmospheres and the Eddington limit	4.21 4.25

CHAPTER 5	BLACK BODY FITS TO MODEL ATMOSPHERE SPECTRA	5.1
5.1	Introduction	5.2
5.2	Black body fitting - the method	5.3
5.3	Black body fitting - the results	5.5
5.4	Conclusions	5.19
		5.20
CHAPTER 6	SIMULATION OF LIGHTCURVES	6.1
6.1	Introduction	6.2
6.2	X-ray lightcurves from magnetic polars	6.2
6.2.1	Hard X-ray lightcurves	6.3
6.2.2	Soft X-ray lightcurves	6.5
6.2.3	Two pole effects	6.6
6.2.4	Observed lightcurve shapes	6.6
6.3	Why use model atmospheres ?	6.11
6.4	Calculating a simulated lightcurve	6.14
6.4.1	Calculating the angle to the line of sight	6.18
6.4.2	Calculating the observed flux from the polecap	6.20
6.4.3	The EXOSAT detectors	6.21
6.4.4	The 'observed' lightcurve	6.26
6.4.5	The random polecap	6.27
6.5	Sample lightcurves	6.28
6.6	A full parameter fit to AM Herculis	6.54
6.6.1	The X-ray lightcurves of AM Herculis	6.55
6.6.2	Fitting the ME lightcurve from the first observation	6.60
6.6.3	Fitting the soft X-ray lightcurve	6.68
6.6.4	Conclusions from the fitting of the first observation lightcurve	6.77
6.6.5	Fitting the second observation lightcurves	6.80
6.6.6	Comparison of the two fits to AM Herculis	6.89
6.6.7	Conclusions from this lightcurve fitting	6.93
6.7	Conclusions and further work possible	6.97
		6.103
CHAPTER 7	MODELLING OF ACCRETION DISCS IN ACTIVE GALACTIC NUCLEI	7.1
7.1	Introduction	7.2
7.1.1	Accretion into a supermassive black hole	7.4
7.1.2	Structure of a thin accretion disc	7.5
7.1.3	The emitted spectrum	7.7
7.2	Stellar atmosphere disc models	7.8
7.2.1	Accretion disc .v. magnetic polecap	7.9
7.2.2	A model atmosphere grid	7.10

7.2.3	Calculating the emergent spectrum	7.14
7.3	The results of an AGN disc calculation	7.18
7.3.1	The AGN disc structure	7.18
7.3.2	Calculated AGN spectra	7.21
7.4	Discussion of results and possible improvements	7.23 7.27
CHAPTER 8	CONCLUSIONS	8.1 8.4
REFERENCES		R.1 R.5
APPENDIX	ASTROPHYSICAL TERMS	A.1 A.2

CHAPTER 1

INTRODUCTION

Imagine two stars orbiting around each other, a binary star system. As time passes and each star gradually uses all its available fuel changes will occur. If one star is more massive than the other it will use up its fuel more quickly and evolve quicker than its companion. At the end of its life it will become, depending on its mass, either a white dwarf, a neutron star or a black hole. We assume that the system as a whole survives this change, i.e., the stars continue to orbit each other but with different orbital parameters due to the change in mass of the evolved star. In due course the other star may evolve and increase in radius, or the binary separation may shrink, to a point where the gravitational pull of the companion will remove the outer layers of its envelope. This is called Roche lobe overflow. The material lost from one star falls toward the surface of the other. Its motion toward the second, compact, star depends primarily on the strength of the magnetic field around that star. The end result is always that the material lands on the surface releasing energy in the forms of X-radiation and heat. This is one example of an accreting system.

The rest of this chapter is devoted to a critical review of the accretion processes we are concerned with, e.g., accretion discs and column accretion, and why we have calculated model atmospheres for these systems. Chapters 2 and 3 describe the method by which we calculate a model atmosphere. Chapters 4-8 describe the uses we have put our atmospheres to and the results we have obtained. References are listed after Chapter 8. The background theory for model atmosphere work is contained in an

Appendix. Footnotes will found at the end of the chapter.

1.1 Interacting Binary Systems

Returning to the system I briefly described before, it is important to realise that the actual process by which the stars reached the point of accretion is unimportant in the discussion of the accretion process itself. The accretion process has a close parallel in another branch of astronomy, namely the destruction of planetary satellites that come too close to their parent. It was this problem that was first studied by the French mathematician Edouard Roche in the 19th Century. The essence of the Roche problem is to consider the motion of a test particle under the gravitational influence of two massive bodies orbiting each other under the influence of their mutual gravitational attractions. The test particle is assumed to be massless compared to its companions. This means the two bodies (stars) orbit each other in circular Keplerian orbits. The circular approximation is a good approximation for binary systems since tidal effects will tend to circularize originally eccentric orbits on timescales short compared to the time over which mass transfer will occur. A further restriction on the Roche problem is the assumption that the two stars are 'centrally condensed' so that they can be regarded as point masses; this is also a fair assumption for most types of star.

In a frame of reference rotating with the binary system at an angular velocity w the two stars are fixed. The

Roche potential is given by

$$\phi_R(\underline{r}) = -\frac{GM_1 M_x}{|\underline{r}-\underline{r}_1|} - \frac{GM_2 M_x}{|\underline{r}-\underline{r}_2|} - \frac{1}{2}(\underline{\omega} \cdot \underline{r})^2 \quad (1.1)$$

where ; M_1 and M_2 are the masses of the components in solar masses ($M_x =$ solar mass)

\underline{r}_1 and \underline{r}_2 are the position vectors of the centres of the two stars.

ϕ_R does not describe all the forces acting on the test particle, for example, the Coriolis forces. Figure 1.1 shows the Roche equipotentials for a binary system with mass ratio $q=M_2/M_1=0.2$. Matter orbiting at a great distance from the system ($r \gg a$, the separation between the two stars) sees it as a point mass concentrated at the

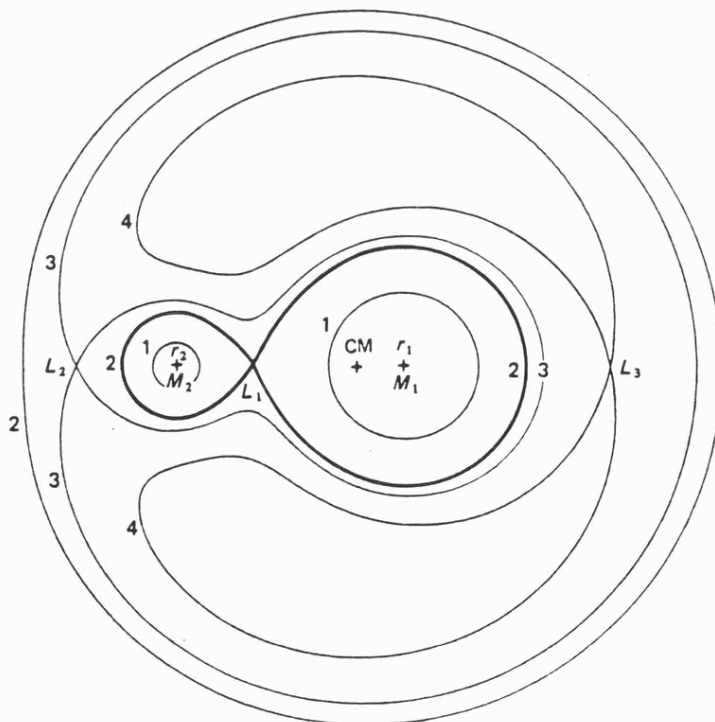


Figure 1.1 Sections in the orbital plane of Roche equipotentials, lines of constant ϕ_R , for a binary system with $q=M_2/M_1=0.2$. The centre of mass (CM) and the L_1, L_2 and L_3 Lagrange points are shown. The equipotentials are labelled 1-4 in order of increasing ϕ_R .

centre of mass, so the Roche equipotentials are circular at large distances. Similarly there are circular equipotentials around the centres of the two stars themselves; the motion of the particle here is dominated by the gravitational pull of the nearer star. Hence the potential ϕ_R has two deep valleys centred on \underline{r}_1 and \underline{r}_2 . The figure-of-eight equipotential (shown as a heavy line in the figure) shows how these two valleys are connected. In three dimensions this 'critical surface' has a dumbbell shape, the part surrounding each star is called its Roche lobe. The lobes join at the inner Lagrangian point L_1 . To continue the analogy, L_1 is like a high mountain pass between two valleys. Material near to L_1 finds it much easier to pass through L_1 to the other side than to escape the critical surface altogether.

Now, returning to our original system, we have reached a point where one star has filled its Roche lobe. From now on I will refer to the star that has filled its Roche lobe as the secondary and to its compact companion as the primary. A system like this is called a semi-detached system. Of course the process of mass transfer will change the mass ratio q and affect the rate of mass transfer so as to slow it down and, eventually, to stop it entirely. On the other hand, other processes, gravitational radiation for example, will tend to shrink the orbits and therefore increase the mass transfer. How these two effects trade off and the resultant evolution of the system does not concern us. For our purposes the fact that accretion is taking place is all that is important. The next question is, what happens to the matter that passes through the L_1

point ?

1.2 Accretion Disc Formation

From the viewpoint of the primary the matter passing through the L_1 point appears as though it is being ejected from a nozzle rotating around the primary. Unless the rotation period is quite long the material will not accrete directly onto the primary as it will have too much angular momentum. Assuming that the matter does not lose a lot of angular momentum by dissipation in the stream then the orbit will circularise at a radius R_{circ} where R_{circ} is the Kepler orbit that has the same specific angular momentum as the transferring gas had on passing through L_1 . Usually R_{circ} is greater than R_* , the stellar radius, and the matter does not accrete directly onto the primary. Clearly, within this gaseous ring there will be dissipative processes (e.g. collisions of gas elements, viscous dissipation, etc.) that will convert some of the energy of the orbital motion into internal (i.e., heat) energy. Eventually this energy will be radiated and lost to the gas. To meet this drain of energy the gas must sink deeper into the gravitational potential well of the primary, that is, to orbit at a reduced radius, this in turn requires it to lose angular momentum. The timescale for an orbiting gas to redistribute its angular momentum is normally much longer than the timescale over which it loses energy by radiative cooling and the dynamical (or orbital) timescale. Therefore the gas will lose as much energy as possible for a given angular momentum, which itself decreases more

slowly. Since a circular orbit has the least energy for a given angular momentum the gas will slowly spiral towards the primary through a series of approximately circular orbits, in the binary orbital plane. This is an accretion disc. The spiralling-in process implies the loss of angular momentum, in the absence of external forces this can only occur by transfer of angular momentum outwards through the disc by internal torques. Thus the outer parts of the disc will gain angular momentum and spiral outwards. The original ring of matter will therefore spread to both smaller and larger radii by this process. At the outer edge of the disc some other process must remove the angular momentum, for example the angular momentum is fed back into the binary orbit by tides exerted on the outer edge by the secondary. Figure 1.2 shows the situation we now have.

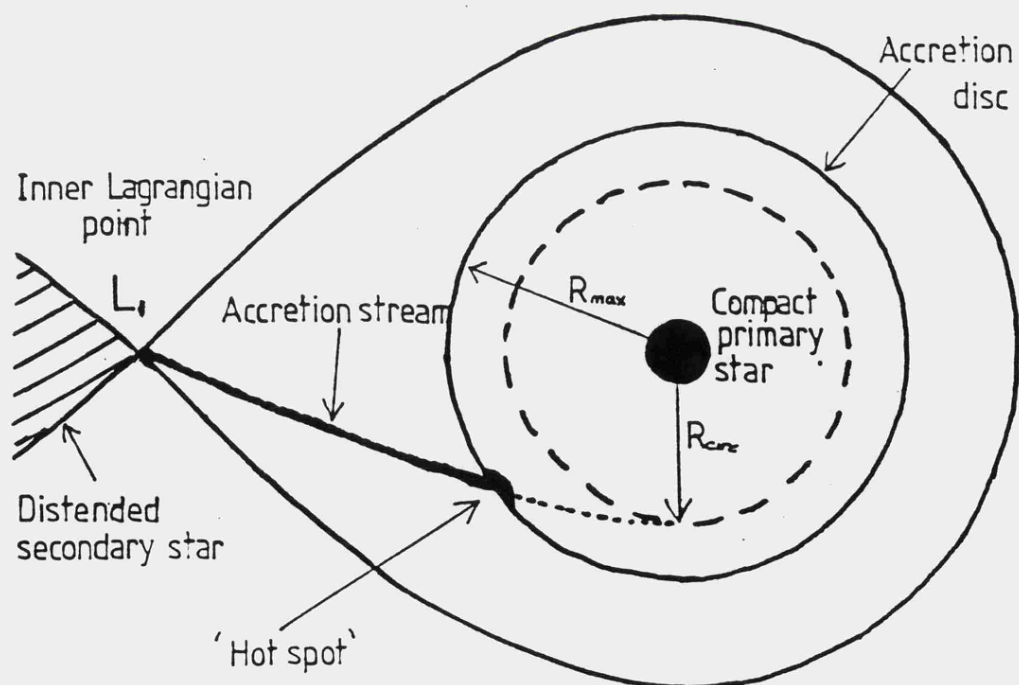


Figure 1.2 The structure of the accretion disc around the primary star of an interacting binary system. R_{max} is the maximum radius of the disc, R_{circ} is the stream circularisation radius.

A disc has been formed around the primary with material constantly flowing through the L_1 point and spiralling via the disc onto the surface of the primary. Where the accretion stream meets the outer edge of the disc a 'hot spot' is formed due to the collision of the stream with the outer edge of the disc. If the primary is a white dwarf star and the secondary is a red dwarf, or sometimes a red giant then this system is known as a cataclysmic variable. It is these systems that we are mostly concerned with.

In cataclysmic variables an accretion disc is not the only way the matter can reach the surface of the primary. its path to the primary depends on the strength of the primary's magnetic field. To distinguish the different types of CV they are sub-divided into classes depending on the accretion process. If the magnetic field is weak then an accretion disc is formed and the matter will spiral in and impact on the primary in a ring around its surface. Those systems that accrete by an accretion disc only include the Dwarf Novae, which undergo repeated nova-like outbursts in brightness. As the primary spectral component of the system is the accretion disc (due to the vast amount of energy radiated away in spiralling toward and striking the primary) these outbursts are thought to be due to either instabilities in the disc or a sudden increase in the mass transfer rate. If, however, the magnetic field is very strong (greater than a few $\times 10^7$ G) an accretion disc will be prevented from forming by this field and instead the matter will accrete directly along the field lines to the magnetic poles. If the binary period is short enough, the white dwarf spins synchronously with the binary and

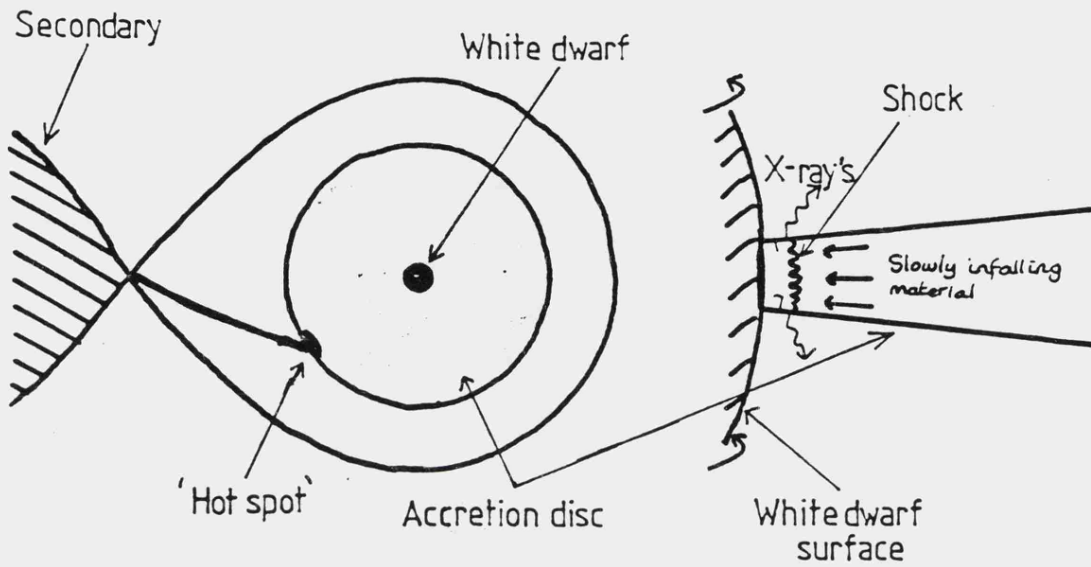
these systems are known as Polars, or AM Herculis stars after their prototype. For Polars the matter impacts over a very small area of the white dwarfs surface and we talk of an accretion column to describe the motion of the accreting matter near to the white dwarf. A related sub-division of CV's are the Intermediate Polars. Here the magnetic field is strong but the white dwarf spins faster than the orbital rotation. This sub-division is also called DQ Herculis stars after a possible prototype object. Figure 1.3 shows two of the cases described above, Dwarf Novae and Polars.

In our work we concentrated our efforts on the second and third cases described above (case (ii) in Figure 1.3), polars and intermediate polars. However an atmosphere code for a magnetic CV can easily be used/adapted to describe the inner edge of an accretion disc or, as indeed was the case with our code, to calculate the emergent spectrum from an accretion disc as a whole. As I described above, in a magnetic CV the matter accretes directly onto the surface of the white dwarf at the magnetic poles, this process is called column accretion.

1.3 Column Accretion

We have seen that for AM Her systems where the white dwarf primary has a strong magnetic field, the matter flowing through the L_1 point is accreted directly onto the polecaps of the white dwarf, travelling down the magnetic field lines. Since no accretion disc is formed the angular momentum possessed by the accreting matter must go

(i) Disc accretion - $B < 10^4$ G



(ii) Column accretion - $B > 10^7$ G

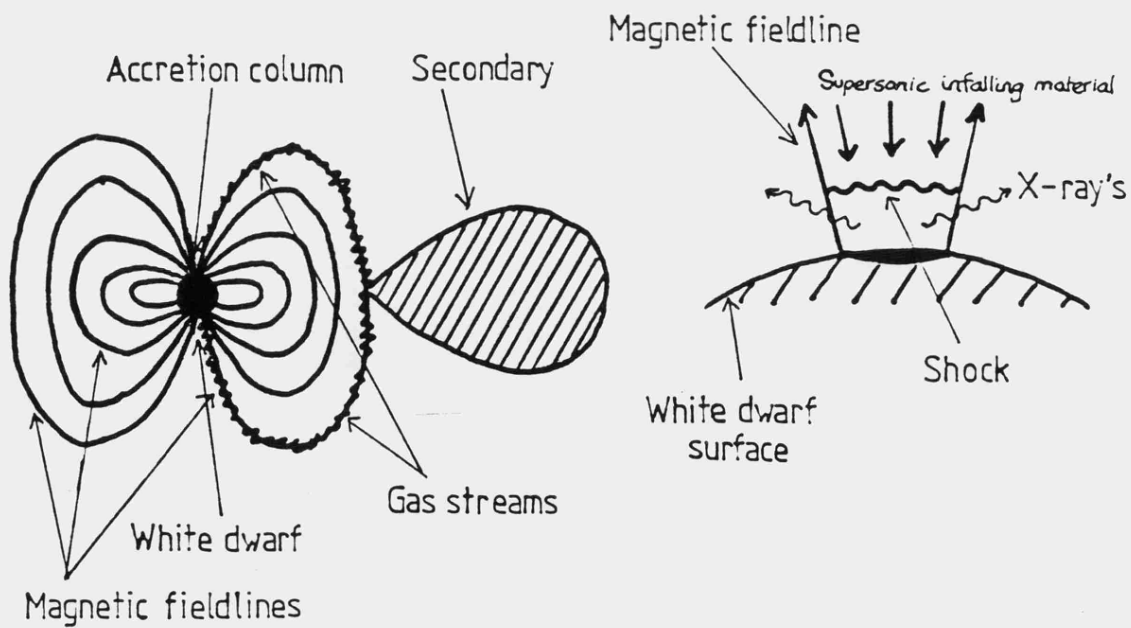


Figure 1.3 Accretion in cataclysmic variables. The two main possibilities (not to scale).

somewhere. As a result, complicated torques are exerted on the magnetic field and ultimately the white dwarf. However the interaction of the white dwarf's magnetic field with the secondary stars envelope produces an opposing torque. The end result of this is thought to be a 'phase-locked' binary configuration. That is, the white dwarf and the secondary star spin synchronously with each other and with the orbital motion, so that the configuration shown in Figure 1.3 rotates rigidly in space. Direct observational evidence of this is hard to detect as the region near the white dwarf dominates, generally, at all frequencies and the radial velocity curves are dominated by the gas stream. Nonetheless the phase-locked model is generally accepted.

We can treat the accretion column as essentially a one-dimensional region, Figure 1.4 shows its essential features. Since the infalling matter is in free-fall and highly supersonic it can be shown that it must be decelerated to subsonic velocities in order for it to accrete onto the white dwarf's surface (see Frank, King and Raine, 1985, Chapter 4). Hence a standing shock must occur over the polecap. Below the shock the matter must cool and settle onto the stellar surface. If we assume that the cooling is purely radiative (note that this assumption is questionable - see below) then the matter is characterised by the adiabatic shock temperature

$$T_s = 3.7 \times 10^8 M_1 R_9^{-1} \quad (1.2)$$

where ; M_1 is the mass of the white dwarf in solar masses and R_9 is the radius in units of 10^9 cm.

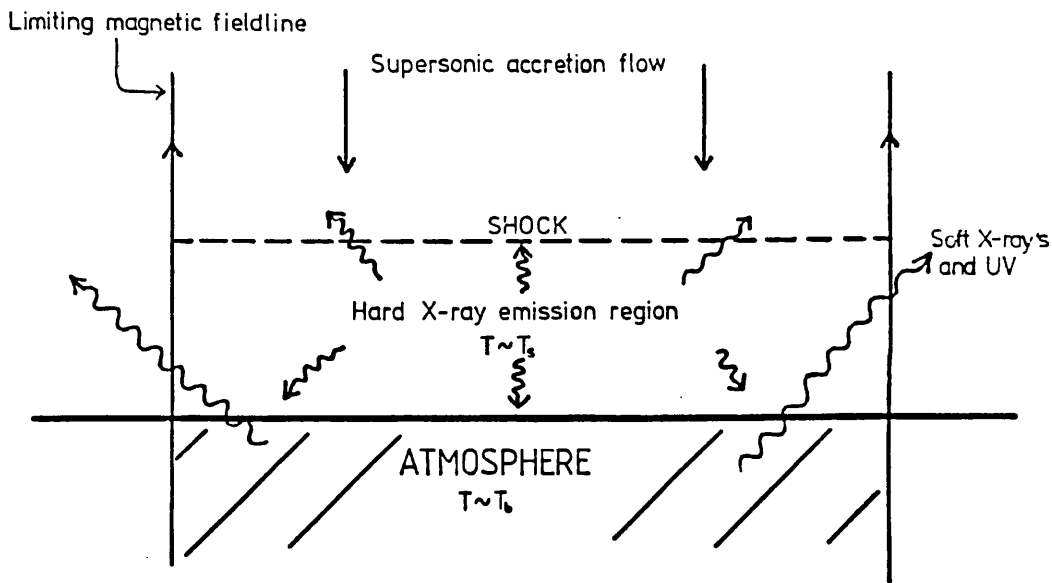


Figure 1.4 Accretion column geometry for a magnetized white dwarf.

Hence most of the accretion luminosity will be released as hard X-rays since the column is very optically thin. One half of this radiation is emitted toward the white dwarf surface where it is partly reflected and partly re-radiated from the white dwarf photosphere with a characteristic temperature

$$T_b = 1.2 \times 10^5 M_{16}^{1/4} f_{-2}^{1/4} M_1^{1/4} R_9^{-3/4} f_{\text{soft}}^{1/4} \quad (1.3)$$

where ; f_{soft} is the fraction of the accretion luminosity re-radiated in this way

M_{16} is the accretion rate in units of 10^{16} g s^{-1}

f_{-2} is the accreting area in units of 10^{-2} of the total white dwarf surface area.

The spectral form for this radiation is usually assumed to be black body-like but, as we shall see later, this is not necessarily correct.

The accretion flow will be brought to a halt in a region of the white dwarf photosphere where the gas pressure is of the same order as the ram pressure of the infalling matter.

If we assume that all of the accretion luminosity L_{acc} is radiated as hard X-rays then $1/2L_{acc}$ is directed toward the white dwarf photosphere. If a fraction a_x is reflected directly then

$$f_{soft} \sim 1/2(1-a_x) \quad (1.4)$$

$$\text{and } \frac{L_x}{L_{soft}} \sim \frac{1/2(1+a_x)}{1/2(1-a_x)} \quad (1.5)$$

For a typical value of a_x (~ 0.3) we get $f_{soft} \sim 0.35$ and $(L_x/L_{soft}) \sim 2$. This means for radiative column the hard X-ray luminosity is approximately twice the soft X-ray luminosity. However, from observations of AM Herculis, we have $(L_x/L_{soft}) \sim 0.1$. This discrepancy is called the 'soft X-ray excess' or 'soft X-ray problem'. It is made more acute by the fact that interstellar absorption effectively makes most of the soft X-ray region unobservable. The values for L_{soft} have to be derived by fitting a UV continuum at energies less than 13 eV and a sharply falling continuum in the soft X-ray range $\sim 0.1-0.3$ keV. For high absorptions or low temperatures these can disappear

altogether. The fitting is usually done using black bodies but what is really needed is a better estimate for the continuum spectrum of the soft component.

1.4 Model Atmospheres .v. Black Bodies

We have seen that the value for L_{soft} for a radiative column has to be derived by spectral fitting since interstellar absorption effectively removes most of the soft X-ray spectral component. Until recently black bodies have been used to fit the missing component. This is highly unsatisfactory as a black body at best only provides a crude approximation to the overall spectral shape of the soft component. In restricted spectral regions a black body continuum is a poor approximation as was pointed out by Heise (1982) in a pioneering investigation using white dwarf atmospheres to fit the soft X-ray spectrum. The high frequency continua of such spectra usually imply colour temperatures which are not only higher than T_b but also almost independent of its precise value, the reason being that at these frequencies the low continuum opacity means that one sees into deeper, hotter layers of the photosphere.

To improve the fitting of the soft X-ray component we need a model atmosphere spectrum. By solving the equations that govern the structure of an atmosphere we can calculate, for the polecap region of the white dwarf, the emergent spectrum from this region. If the assumptions used to calculate this 'self-consistent' atmosphere model are reasonable then it is clear that it would be a better

estimate for the soft X-ray spectral component than a black body. There are two other reasons why model atmospheres are desirable. Firstly, the soft X-ray polecap is irradiated by the hard X-ray component. A fraction of these incident X-rays will be reflected without a change of frequency, the 'albedo' component. Since the ratio of reflectance to absorption is a function of photon energy this component will have a distinct spectral shape, which will have to be taken into account in order to interpret the hard X-ray spectrum. An atmosphere calculation is essential for this purpose. Secondly, unlike a black body which emits isotropically outwards, an atmosphere will exhibit limb-darkening (or brightening if there is appreciable illumination from above). These effects will greatly influence the shape of the soft X-ray lightcurves generated by the rotation of the white dwarf. A proper treatment of these effects is essential in order to fit observed lightcurves theoretically.

The realisation that a model atmosphere would prove to be a better 'tool' in this situation than a black body motivated us to construct a suitable code for the polecap region of a magnetic CV, sufficiently general that it could be used for any accreting white dwarf. In Chapter 2 I describe the procedure for calculating a model atmosphere in general. In Chapter 3 I explain the specific requirements of our code that make it different from other atmosphere calculations (for example Kurucz (1979) and Heise (1982)).

Returning to the problem of the soft X-ray excess, while it is sometimes hoped that the soft X-ray "problem"

will disappear altogether with a better estimate for the soft X-ray spectral shape in reality this is unlikely to happen. A self-consistent atmosphere does give a more realistic shape for the soft X-ray spectral region but the complete removal of the problem requires that another process within the column or on the white dwarf surface is producing large amounts of soft X-rays. Three possibilities have so far been considered; (i) steady nuclear burning on the surface of the white dwarf; (ii) inhomogeneous accretion flow down the column and (iii) non-radiative energy transport into the white dwarf photosphere by energetic electrons. The pro's and con's of each possibility will not be discussed herein but suffice it to say that (iii) looks like providing us with more realistic values for (L_x/L_{soft}) . For discussion of (i) and (ii) above see King (1987) and for a complete discussion of (iii) see Frank, King and Lasota (1983) and Frank and King (1984).

1.5 Model polecap atmospheres - other uses

While the original motivation for constructing the model atmosphere code was to provide an accurate representation of the 'hidden' soft X-ray continuum its uses go far beyond this. Fitting observed hard and soft X-ray spectra is obviously the first use for such a code. Secondly, by fitting black body spectra to the soft X-ray region of our atmosphere spectra we can effectively model the approach usually taken to derive values for the luminosity and effective temperature of an observed source.

This provides us with estimates of the errors produced when black bodies are used as fitting tools. In Chapter 5 I describe the results produced by such a method. A third use for the atmosphere spectra is in the calculation of lightcurves. Our spectra are of importance here because they exhibit limb darkening effects. The method used to calculate lightcurves and the results obtained can be found in Chapter 6. The last use to which we put our atmosphere spectra was to calculate the emergent spectrum from the accretion disc of an active galactic nucleus (AGN). At the centre of an AGN is a supermassive black hole ($\sim 10^8$ solar masses). Matter accreting onto this black hole may form an accretion disc analogous to those in Dwarf Novae. The calculation of such an emergent spectrum and the results obtained are described in detail in Chapter 7. Chapter 8 discusses the results of our work and suggests future work that could be undertaken in this field using our atmosphere code.

In this chapter I have described the reasons for calculating an atmosphere code and the region it must describe; in the next chapter I will describe the procedure for calculating a model atmosphere in general.

CHAPTER 2

THE CALCULATION OF A STELLAR ATMOSPHERE MODEL

2.1 Introduction

The calculation of a model stellar atmosphere follows an iterative path. Given some initial conditions a new guess at those conditions is made which depends upon the original ones. The principal variable that is corrected is the temperature at each depth in the atmosphere which, as we shall see, has the most effect. Repeating the correcting process causes the model to converge to the correct structure. Convergence to a few tenths of a percent is enough, any further convergence lengthens the run-time on the computer without giving appreciable returns in terms of accuracy.

In order that the reader can understand each step in the calculation I will break this chapter into sections, each section describing one particular step in the calculation. The order of the sections will follow the flow of the calculation itself. Figure 2.1 shows the flow diagram for a typical stellar atmosphere calculation.

The derivation of the equations associated with atmosphere calculations and a description of the terms contained within them can be found in the Appendix. Readers not familiar with astrophysical terms are advised to read through this before continuing with this chapter.

2.2 The Initial Model

The standard planar transfer equation, from equation (A.26), is

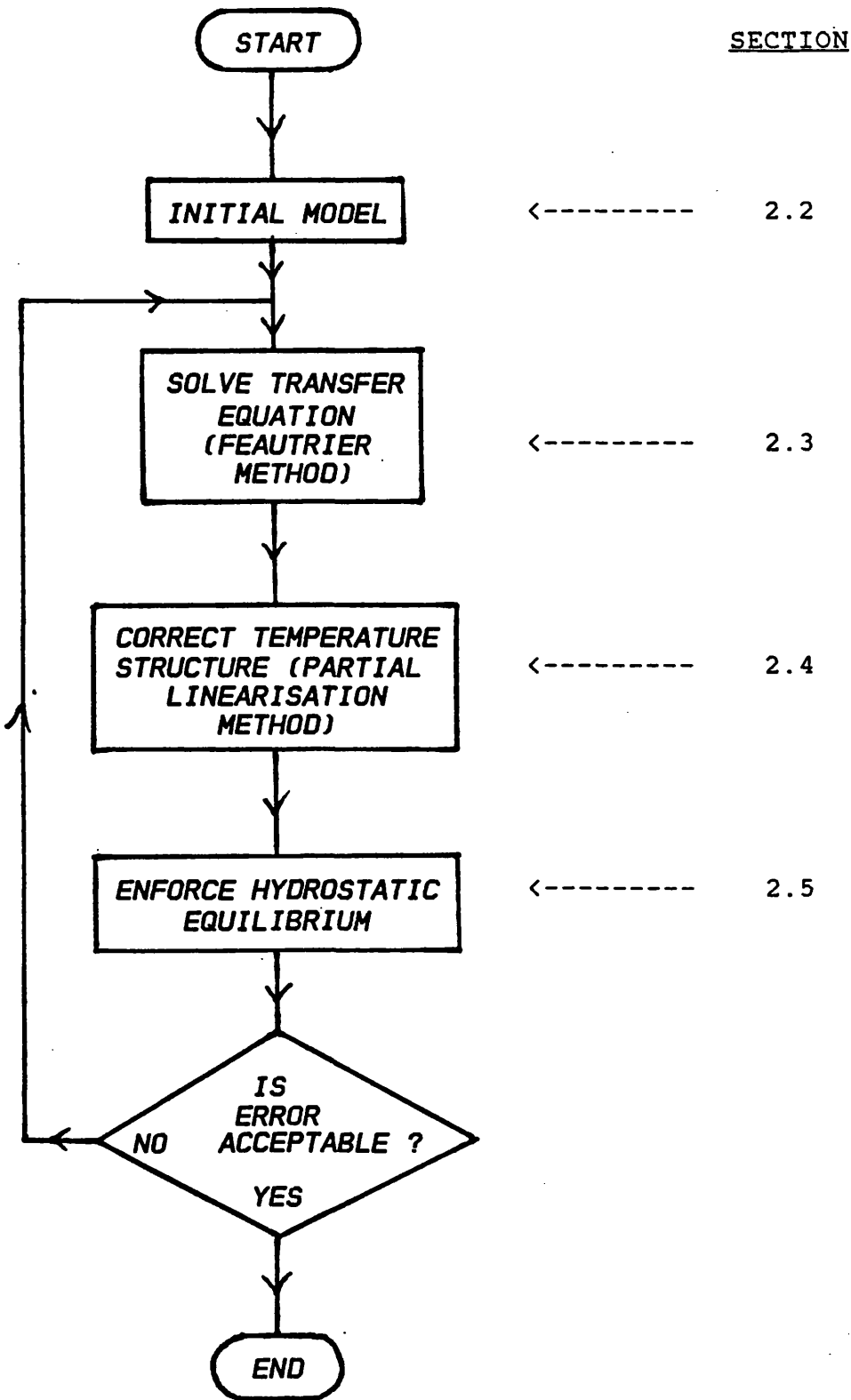


Figure 2.1 Flow chart for the standard calculation of a stellar atmosphere model.

$$\mu(\partial I_{\nu}/\partial \tau_{\nu}) = I_{\nu} - S_{\nu} \quad (2.1)$$

where $\tau(z, \nu)$ is given by equation (A.24),

$$\tau(z, \nu) = \int_z^{z^{\max}} \chi(z', \nu) dz' \quad (2.2)$$

In order to solve this equation by iteration we need an initial model. This initial model takes the form of an approximate solution to the transfer equation.

2.2.1 An approximate solution - the grey atmosphere

We can simplify the transfer equation by assuming that the opacity of the stellar material is independent of frequency; i.e., $\chi_{\nu} \equiv \chi$. This is called the Grey Atmosphere Approximation, grey signifying that the opacity has no dependence on frequency (colour). Therefore equation (2.1) becomes

$$\mu(\partial I_{\nu}/\partial \tau) = I_{\nu} - S_{\nu} \quad (2.3)$$

By integrating over frequency and writing

$$I = \int_0^{\infty} I_{\nu} d\nu \quad (2.4) \quad S = \int_0^{\infty} S_{\nu} d\nu \quad (2.6)$$

$$J = \int_0^{\infty} J_{\nu} d\nu \quad (2.5) \quad B = \int_0^{\infty} B_{\nu} d\nu \quad (2.7)$$

we get,

$$\mu(\partial I/\partial \tau) = I - S \quad (2.8)$$

The condition of radiative equilibrium, from equation (A.39), requires

$$\int_0^{\infty} \chi_{\nu} J_{\nu} d\nu = \int_0^{\infty} \chi_{\nu} S_{\nu} d\nu \quad (2.9)$$

For grey material this reduces to

$$J = S \quad (2.10)$$

Therefore equation (2.8) becomes

$$\mu(\partial I / \partial \tau) = I - J \quad (2.11)$$

If we assume Local Thermodynamic Equilibrium (LTE) then

$$J(\tau) = S(\tau) = B[T(\tau)] = \sigma T^4 / \pi \quad (2.12)$$

i.e., we can associate a temperature with the equilibrium radiation field using equation (2.12).

By taking the moments of equation (2.11) we find several important results. For example, take the zero-order moment and impose radiative equilibrium. Then equation (A.33);

$$(\partial H_{\nu} / \partial \tau_{\nu}) = J_{\nu} - S_{\nu} \quad (2.13)$$

becomes

$$(dH/d\tau) = J - S = J - J = 0 \quad (2.14)$$

which implies that the flux through the atmosphere is constant. The first moment gives

$$(dK/d\tau) = H \quad (2.15)$$

which, because H is constant, gives

$$K(\tau) = H\tau + c = 1/4F\tau + c \quad (2.16)$$

Now, the diffusion approximation (equations A.52b and d) implies

$$K(\tau) = 1/3J(\tau) \quad (\text{for } \tau \gg 1) \quad (2.17)$$

so given that $K(\tau) \approx 1/4F\tau$ for $\tau \gg 1$ this implies that at great depth

$$J(\tau) \approx 3/4F\tau \quad (\tau \gg 1) \quad (2.18)$$

For $\tau \ll 1$ we expect that $J(\tau)$ does not follow a linear function of optical depth, so a reasonable general expression for $J(\tau)$ might be

$$J(\tau) = 3/4F[\tau + q(\tau)] = (3\sigma/4\pi)T_{\text{eff}}^4 [\tau + q(\tau)] \quad (2.19)$$

where $q(\tau)$ is known as the Hopf function. If we take the limit,

$$\lim_{\tau \rightarrow \infty} \left[\frac{1}{3}J(\tau) - K(\tau) \right] = \frac{1}{4}F \lim_{\tau \rightarrow \infty} [\tau + q(\tau) - \tau - c] = 0 \quad (2.20)$$

we find that

$$c = q(\infty) \quad (2.21)$$

So,

$$K(\tau) = 1/4F[\tau + q(\infty)] \quad (2.22)$$

The solution of the grey atmosphere problem requires that we know $q(\tau)$. Given $q(\tau)$ we can combine equations (2.12) and (2.19) into the relation

$$T^4 = 3/4T_{eff}^4 [\tau + q(\tau)] \quad (2.23)$$

A closed form expression can be written for $q(\tau)$ (Mark, 1947) which has the form

$$q(\tau) = q(\infty) - \frac{1}{2\sqrt{3}} \int_0^1 \frac{e^{-\tau/u}}{H(u)Z(u)} du \quad (2.24)$$

where;

$$H(u) = (u+1)^{-1/2} \exp\left[\frac{1}{\pi} \int_0^{\pi/2} \frac{\theta \tan^{-1}(u \tan \theta)}{1 - \theta \cot \theta} d\theta\right] \quad (2.25)$$

$$\text{and } Z(u) = \left[1 - \frac{1}{2}u \ln\left(\frac{1+u}{1-u}\right)\right]^2 + \frac{1}{4} \pi^2 u^2 \quad (2.26)$$

Results obtained by numerically evaluating equation (2.24) are given in Table 2.1.

So, the grey atmosphere approximation gives us an exact solution to the transfer equation; i.e., we have a form for the temperature structure. One question remains, can we relate the non-grey problem to the grey problem and thus set an initial model for the temperature structure in the atmosphere ?

Table 2.1 The exact solution for $q(\tau)$.

τ	$q(\tau)$	τ	$q(\tau)$
0.00	0.577351	0.8	0.693534
0.01	0.588236	1.0	0.698540
0.03	0.601242	1.5	0.705130
0.05	0.610758	2.0	0.707916
0.10	0.627919	2.5	0.709191
0.20	0.649550	3.0	0.709806
0.30	0.663365	3.5	0.710120
0.40	0.673090	4.0	0.710270
0.50	0.680240	5.0	0.710398
0.60	0.685801	∞	0.710446

2.2.2 Mean opacities and the grey solution

The opacity in real stellar atmospheres is certainly not independent of frequency, indeed it exhibits strong variations when spectral lines are present. If we compare the grey and non-grey transfer equations and their moments we have

$$\mu(\partial I_{\nu}/\partial z) = \chi_{\nu}(I_{\nu} - S_{\nu}) \quad (2.27a)$$

$$\mu(\partial I/\partial z) = \chi(J - I) \quad (2.27b)$$

$$(\partial H_{\nu}/\partial z) = \chi_{\nu}(S_{\nu} - J_{\nu}) \quad (2.28a) \quad dH/dz = 0 \quad (2.28b)$$

$$(\partial K_{\nu}/\partial z) = -\chi_{\nu}H_{\nu} \quad (2.29a) \quad dK/dz = -\chi H \quad (2.29b)$$

where the variables without subscripts represent integrated quantities. In order to reduce the non-grey problem to a grey problem, can we define a mean opacity $\bar{\chi}$ formed as a weighted average of the monochromatic opacities in such a way that the monochromatic transfer equation, or one of its

moments, has exactly the same form as the grey equation, when integrated over frequency. Several solutions can be defined, I will only describe the one used for our models, the Rosseland Mean Opacity.

If we wish to obtain the correct value for the integrated energy flux, from equation (2.29a) we chose $\bar{\chi}$ such that

$$\begin{aligned} - \int_0^\infty \chi_\nu^{-1} (\partial K_\nu / \partial z) d\nu &= \int_0^\infty H_\nu d\nu = H \\ &= - \bar{\chi}^{-1} (dK/dz) \end{aligned} \quad (2.30)$$

or, rearranging,

$$\bar{\chi}^{-1} = \int_0^\infty \chi_\nu^{-1} (\partial K_\nu / \partial z) d\nu / \int_0^\infty (\partial K_\nu / \partial z) d\nu \quad (2.31)$$

We are faced with the problem that we do not know K_ν until the transfer equation has been solved but, equation (2.31) can be approximated in the following way. At great depth in the atmosphere, $K_\nu \rightarrow 1/3 J_\nu$ while $J_\nu \rightarrow B_\nu$. Therefore we can write,

$$(\partial K_\nu / \partial z) \approx 1/3 (\partial B_\nu / \partial T) (dT/dz) \quad (2.32)$$

We can then define the mean opacity χ_R ($\equiv \bar{\chi}$) as

$$\frac{1}{\chi_R} = \frac{\int_0^\infty \left(\frac{1}{\chi_\nu} \right) \left(\frac{\partial B_\nu}{\partial T} \right) d\nu}{\int_0^\infty \left(\frac{\partial B_\nu}{\partial T} \right) d\nu} = \left(\frac{\pi}{4\sigma T^3} \right) \int_0^\infty \left(\frac{1}{\chi_\nu} \right) \left(\frac{\partial B_\nu}{\partial T} \right) d\nu \quad (2.33)$$

χ_R is called the Rosseland Mean Opacity, in honour of its originator. Note that this average opacity gives highest weighting to those regions where the opacity is lowest, where, as a result, most of the energy is transported. However the use of χ_R as the mean opacity does not reduce equation (2.28a) to equation (2.28b) so that the non-grey problem can be replaced by a grey problem. On the other hand, the approximations made to obtain equation (2.33) are precisely those introduced in the derivation of the diffusion approximation to the transfer equation (equation (A.53)); i.e.,

$$H_V = -1/3(1/\chi_V)(\partial B_V/\partial T)(dT/dz) \quad (2.34)$$

Therefore, using the Rosseland Mean optical depth scale τ_R recovers the correct solution of the transfer equation at great depth. This implies that for $\tau_R \gg 1$ the temperature structure is exactly given by the relation

$$T^4 = 3/4T_{eff}^4 [\tau_R + q(\tau_R)] \quad (2.35)$$

Note that this is only true at great depth, exact flux conservation is not guaranteed by use of the Rosseland Mean in the upper layers of a stellar atmosphere. For the purposes of setting the initial model the Rosseland Mean optical depth scale provides us with an easy form for the temperature structure. Using this, the initial values for gas pressure, electron density, etc., at each depth can be calculated, ready for the solution of the transfer equation. The inaccuracy at low optical depth will be

corrected as the model converges.

2.3 The solution of the Transfer Equation

In order to calculate the intensity of radiation at each depth in the atmosphere, at each frequency and at each angle μ we need to solve the transfer equation. In this section I will describe the solution of the transfer equation by differential equations, the solution by integral equations will not be described but if interested the reader should consult Athay (1972, Chapter 8) for a description.

2.3.1 The Transfer Equation as a two-point boundary value problem

The basic ideas for this method were presented in a paper by Feautrier (1964). It requires that the transfer equation is written as a second-order differential equation subject to two-point boundary conditions.

If we assume that the atmosphere is plane-parallel then we can write two equations for the inward and outward radiation field at angle $\pm\mu$,

$$\pm\mu[\partial I(z, \pm\mu, \nu)/\partial z] = \chi(z, \nu)[S(z, \nu) - I(z, \pm\mu, \nu)] \quad (2.36)$$

here μ is restricted to the range $0 \leq \mu \leq 1$. Defining symmetric and anti-symmetric averages we get

$$u(z, \mu, \nu) = 1/2[I(z, \mu, \nu) + I(z, -\mu, \nu)] \quad (2.37)$$

$$v(z, \mu, \nu) = 1/2[I(z, \mu, \nu) - I(z, -\mu, \nu)] \quad (2.38)$$

If we add and subtract the two equations (2.36) we get

$$\begin{aligned} & \mu(\partial/\partial z[I(z, \mu, \nu) - I(z, -\mu, \nu)]) \\ &= \chi(z, \nu)\{2S(z, \nu) - [I(z, \mu, \nu) + I(z, -\mu, \nu)]\} \end{aligned} \quad (2.39)$$

and, assuming $S(z, \nu)$ is symmetric in μ ,

$$\begin{aligned} & \mu(\partial/\partial z[I(z, \mu, \nu) + I(z, -\mu, \nu)]) \\ &= -\chi(z, \nu)[I(z, \mu, \nu) - I(z, -\mu, \nu)] \end{aligned} \quad (2.40)$$

Substituting u and v into the above we get

$$\mu[\partial v(z, \mu, \nu)/\partial z] = \chi(z, \nu)[S(z, \nu) - u(z, \mu, \nu)] \quad (2.41)$$

$$\text{and } \mu[\partial u(z, \mu, \nu)/\partial z] = -\chi(z, \nu)v(z, \mu, \nu) \quad (2.42)$$

By eliminating v between equations (2.41) and (2.42) we get

$$\begin{aligned} & \mu^2 \{ \partial/\partial z [(-1/\chi(z, \nu)) (\partial u(z, \mu, \nu)/\partial z)] \} \\ &= \chi(z, \nu)[S(z, \nu) - u(z, \mu, \nu)] \end{aligned} \quad (2.43)$$

By abbreviating the notation and letting

$$d\tau_\nu = d\tau(z, \nu) = -\chi(z, \nu)dz \quad (2.44)$$

equation (2.43) becomes

$$\mu^2 (\partial^2 u_{\mu\nu} / \partial \tau_\nu^2) = u_{\mu\nu} - S_\nu \quad (2.45)$$

This is the second-order equation that we must solve. What are the boundary conditions ?

Boundary conditions

Equation (2.45) must be solved subject to boundary conditions at $\tau=0$ and $\tau=\tau_{\max}$ such that the diffusion approximation applies at τ_{\max} .

At $\tau=0$: for no incoming radiation

$$I(0, -\mu, \nu) = 0 \quad (2.46)$$

which means that $v_{\mu\nu}(0) = u_{\mu\nu}(0)$. Therefore equation (2.42) becomes

$$\mu (\partial u_{\mu\nu} / \partial \tau_\nu)_0 = u_{\mu\nu}(0) \quad (2.47)$$

If however there IS incoming radiation then $I(0, -\mu, \nu) \neq 0$, the upper boundary condition, from equation (2.42), becomes

$$\mu (\partial u_{\mu\nu} / \partial \tau_\nu)_0 = v_{\mu\nu}(0) = 1/2 [I_\nu(+\mu) - I_\nu(-\mu)] \quad (2.48)$$

which, substituting for $I_\nu(+\mu)$ from equations (2.37) and (2.38), becomes

$$\mu(\partial u_{\mu\nu}/\partial\tau_{\nu})_0 = 1/2[2u_{\mu\nu}(0) - 2I_{\nu}(-\mu)] \quad (2.49)$$

i.e.,

$$\mu(\partial u_{\mu\nu}/\partial\tau_{\nu})_0 = u_{\mu\nu}(0) - I(0, -\mu, \nu) \quad (2.50)$$

This is the upper boundary condition for an atmosphere with incoming radiation.

At $\tau=\tau_{\max}$:

From equations (2.37) and (2.38) we have

$$v(z, \mu, \nu) = 1/2[I(z, \mu, \nu)+I(z, \mu, \nu)-2u(z, \mu, \nu)] \quad (2.51)$$

$$= I(z, \mu, \nu) - u(z, \mu, \nu) \quad (2.52)$$

Which at $\tau=\tau_{\max}$ gives, from equation (2.42),

$$\mu(\partial u_{\mu\nu}/\partial\tau_{\nu})_{\tau_{\max}} = I(\tau_{\max}, \mu, \nu) - u_{\mu\nu}(\tau_{\max}) \quad (2.53)$$

If the diffusion approximation is valid at $\tau=\tau_{\max}$ then

$$I(\tau_{\max}, \mu, \nu) = B_{\nu}(\tau_{\max}) + \mu(1/\chi_{\nu} |\partial B_{\nu}/\partial z|)_{\tau_{\max}} \quad (2.54)$$

so that, from equation (2.52), $u_{\mu\nu}(\tau_{\max})=B_{\nu}(\tau_{\max})$ and

$v_{\mu\nu}(\tau_{\max})=\mu(\chi_{\nu}^{-1} |\partial B_{\nu}/\partial z|)_{\tau_{\max}}$, which gives

$$(\partial u_{\mu\nu}/\partial\tau_{\nu})_{\tau_{\max}} = (\chi_{\nu}^{-1} |\partial B_{\nu}/\partial z|)_{\tau_{\max}} \quad (2.55)$$

as the lower boundary condition.

The next step in the solution is to rewrite equation (2.45) into a set of difference equations by making the variables discrete. Therefore we choose a set of depth points τ_d , $d=1,2,\dots,D$, where $\tau_1 < \tau_2 < \dots < \tau_D$; a set of angle points μ_m , $m=1,2,\dots,M$; and a set of frequency points ν_n , $n=1,2,\dots,N$. $I(z,\mu,\nu)$ becomes I_{dmn} and integrals are replaced by quadrature sums. To reduce the subscripts still further we group the angles and frequencies into one subscript i such that $(\mu_i, \nu_i) = (\mu_m, \nu_n)$ at $i=m+(n-1)M$. Further, derivatives are replaced by difference formulae, e.g.,

$$\begin{aligned} (dX/d\tau)_{d+1/2} &\approx (\Delta X_{d+1/2} / \Delta \tau_{d+1/2}) \\ &\approx (X_{d+1} - X_d) / (\tau_{d+1} - \tau_d) \end{aligned} \quad (2.56)$$

and

$$\left(\frac{d^2 X}{d\tau^2}\right)_d \approx \frac{\left[\left(\frac{dX}{d\tau}\right)_{d+1/2} - \left(\frac{dX}{d\tau}\right)_{d-1/2}\right]}{\left[\frac{1}{2}(\Delta \tau_{d+1/2} + \Delta \tau_{d-1/2})\right]} \quad (2.57)$$

which, from equation (2.44), defines

$$\Delta \tau_{d\pm 1/2, i} = 1/2(X_{d\pm 1, i} + X_{d, i}) |z_{d\pm 1} - z_d| \quad (2.58)$$

$$\text{and } \Delta \tau_{d, i} = 1/2(\Delta \tau_{d-1/2, i} + \Delta \tau_{d+1/2, i}) \quad (2.59)$$

So the LHS of equation (2.45) becomes

$$\begin{aligned}
& \mu_i^2 \frac{\left[\left(\frac{du}{d\tau} \right)_{d+1/2} - \left(\frac{du}{d\tau} \right)_{d-1/2} \right]}{\left[\frac{1}{2} (\Delta\tau_{d+1/2} + \Delta\tau_{d-1/2}) \right]} \\
&= \frac{\mu_i^2}{\Delta\tau_{d,i}} \left[\frac{u_{d+1,i} - u_{d,i}}{\Delta\tau_{d+1/2,i}} - \frac{u_{d,i} - u_{d-1,i}}{\Delta\tau_{d-1/2,i}} \right] \\
&= \frac{\mu_i^2 u_{d+1,i}}{\Delta\tau_{d,i} \Delta\tau_{d+1/2,i}} - \frac{\mu_i^2 u_{d,i}}{\Delta\tau_{d,i} \Delta\tau_{d+1/2,i}} \\
&\quad - \frac{\mu_i^2 u_{d,i}}{\Delta\tau_{d,i} \Delta\tau_{d-1/2,i}} + \frac{\mu_i^2 u_{d-1,i}}{\Delta\tau_{d,i} \Delta\tau_{d-1/2,i}} \tag{2.60}
\end{aligned}$$

So, equating both sides, we have

$$\begin{aligned}
& \left(\frac{\mu_i^2}{\Delta\tau_{d-1/2,i} \Delta\tau_{d,i}} \right) u_{d-1,i} + \left(\frac{\mu_i^2}{\Delta\tau_{d,i} \Delta\tau_{d+1/2,i}} \right) u_{d+1,i} \\
&\quad - \frac{\mu_i^2}{\Delta\tau_{d,i}} \left(\frac{1}{\Delta\tau_{d-1/2,i}} + \frac{1}{\Delta\tau_{d+1/2,i}} \right) u_{d,i} \\
&= u_{d,i} - S_{d,i} \tag{2.61}
\end{aligned}$$

Which reduces to

$$\begin{aligned}
& - \left(\frac{\mu_i^2}{\Delta\tau_{d-1/2,i} \Delta\tau_{d,i}} \right) u_{d-1,i} - \left(\frac{\mu_i^2}{\Delta\tau_{d,i} \Delta\tau_{d+1/2,i}} \right) u_{d+1,i} \\
&\quad + \frac{\mu_i^2}{\Delta\tau_{d,i}} \left(\frac{1}{\Delta\tau_{d-1/2,i}} + \frac{1}{\Delta\tau_{d+1/2,i}} + 1 \right) u_{d,i} = S_{d,i} \tag{2.62}
\end{aligned}$$

where ; $i=1,2,3,\dots,I$ and $d=2,3,\dots,D-1$.

If we define a vector, u_d , which contains the angle-frequency components at depth point d then equation (2.62) can be written as a matrix equation, as follows

$$-A_d u_{d-1} + B_d u_d - C_d u_{d+1} = L_d \quad (2.63)$$

The last step before solution is to convert the boundary conditions to difference formulae. So,

at $\tau=0$: (with incoming radiation as I_{inc})

$$\mu_i (u_{2i} - u_{1i}) / \Delta\tau_{3/2,i} = u_{1i} - I_{inc} \quad (2.64)$$

Second order accuracy is obtained by expanding u_{2i} as a Taylor series, i.e.,

$$u_{2i} = u_{1i} + \Delta\tau_{3/2} (du/d\tau) + 1/2 \Delta\tau_{3/2}^2 (d^2u/d\tau^2) \quad (2.65)$$

which, by substituting into equation (2.65) from equations (2.45) and (2.50), gives

$$u_{2i} = u_{1i} + \mu_i^{-1} \Delta\tau_{3/2} (u_{1i} - I_{inc}) + \mu_i^{-2} \Delta\tau_{3/2}^2 (u_{1i} - S_{1i}) \quad (2.66)$$

Expanding and collecting together like terms we get

$$\begin{aligned}
& - \left(\frac{2\mu_i^2}{\Delta\tau_{3/2}^2} \right) u_{2i} + \left(\frac{2\mu_i^2}{\Delta\tau_{3/2}^2} + \frac{2\mu_i}{\Delta\tau_{3/2}} + 1 \right) u_{1i} \\
& = S_{1i} + \frac{2\mu_i^2 I_{inc}}{\Delta\tau_{3/2}} \quad (2.67)
\end{aligned}$$

Which is the same, in matrix form, as equation (2.63) but with $A_1=0$. So the upper boundary condition is

$$B_1 u_1 - C_1 u_2 = L_1 \quad (2.68)$$

Similarly for the lower boundary condition, expanding u_{0-1} as a Taylor series and substituting from equations (2.45) and (2.55) we find,

$$\begin{aligned}
& - \left(\frac{2\mu_i^2}{\Delta\tau_{0-1/2}^2} \right) u_{0-1} + \left(\frac{2\mu_i^2}{\Delta\tau_{0-1/2}^2} \right) u_0 = S_0 + \frac{2\mu_i^2}{\Delta\tau_{0-1/2}} \frac{\partial B_v}{\partial \tau_v} \Big|_0 \\
& \quad (2.69)
\end{aligned}$$

which is the same, in matrix form, as equation (2.63) but with $C_0=0$. So the lower boundary condition is,

$$- A_{0-1} u_{0-1} + B_0 u_0 = L_0 \quad (2.70)$$

The matrix equations are now complete, the solution of these follows that described by Feautrier (1964) and is known as the Feautrier Solution.

$$S_{\nu} = e_{\nu} J_{\nu} + (1 - e_{\nu}) B_{\nu} \quad (2.75)$$

where,

$$e_{\nu} = \sigma_{\nu} / \chi_{\nu} = \sigma_{\nu} / (\sigma_{\nu} + \kappa_{\nu}) \quad (2.76)$$

So, to recap, the solution of the transfer equation proceeds as follows :-

(i) From a guess at S_{ν} ($=B_{\nu}$ usually) equation (2.45) is solved for u_{di} for all d , one angle and frequency at a time, using the Feautrier method.

(ii) Variable Eddington factors are calculated from the values for u_{dmn} such that

$$f_{dn} = \frac{\sum_m b_m \mu_m^2 u_{dmn}}{\sum_m b_m u_{dmn}} \quad (2.77)$$

where, b_m are the angle weights. And, also,

$$h_n = \frac{\sum_m b_m \mu_m u_{1mn}}{\sum_m b_m u_{1mn}} \quad (2.78)$$

(iii) Equations (2.72) - (2.74) are solved for J_{ν} , at all depths, one frequency at a time, using explicit expressions for S_{ν} in terms of J_{ν} (from equation (2.75)).

(iv) Re-evaluate S_{ν} using the values for J_{ν} .

(v) Since S_{ν} will differ from that originally used, steps (i) - (iv) are repeated until S_{ν} converges to the correct value (an error of 1.0×10^{-6} is acceptable).

Once the radiation field throughout the atmosphere has been calculated it must be tested to see if it satisfies

the constraint of Radiative Equilibrium. Since it is highly unlikely that the initial model is correct we must have a means of correcting the temperature structure so that the radiation field does satisfy the requirement of energy balance. In the next section I will describe the modified correction method we used to do this.

In this section I have described the solution of the transfer equation using difference equations and the Feautrier method. If the reader is interested, Mihalas (1978, pp158-161) describes an alternative method, the Rybicki Solution, of solving the difference equations when the frequency dependent information is redundant due to complete redistribution (see also, Rybicki, 1971).

2.4 Correcting the temperature structure

In order to correct the temperature structure we need to linearise the transfer equation. From equations (2.72) and (2.75) we have, ν subscript dropped for convenience,

$$d^2 fJ/d\tau^2 = J - S = (1 - \rho)(J - B) \quad (2.79)$$

With boundary conditions included this can be written in matrix form as

$$A \begin{pmatrix} J_1 \\ J_2 \\ \dots \\ J_0 \end{pmatrix} = \begin{pmatrix} (1-\rho_1)B_1 + 2\int\mu I_{inc} d\mu/\Delta\tau_1 \\ (1-\rho_2)B_2 \\ \dots \\ (1-\rho_0)B_0 + 2/3(dB/d\tau)_0/\Delta\tau_{0-1} \end{pmatrix} \quad (2.80)$$

where I_{inc} is the incident optical/UV radiation. We can expand $J \rightarrow J + \delta J$ and $B \rightarrow B + \delta B$ and subtract the transfer equation to give,

$$A \begin{pmatrix} \delta J_1 \\ \delta J_0 \end{pmatrix} = \begin{pmatrix} (1-e_1) \dot{B}_1 \delta T_1 \\ (1-e_0) \dot{B}_0 \delta T_0 + \Delta(2/3(\partial B/\partial \tau))_0 / \Delta \tau_{0-1} \end{pmatrix} \quad (2.81)$$

Inverting, we get

$$\begin{pmatrix} \delta J_1 \\ \delta J_0 \end{pmatrix} = A^{-1} \begin{pmatrix} (1-e_1) \dot{B}_1 \delta T_1 \\ (1-e_0) \dot{B}_0 \delta T_0 + \Delta(2/3(\partial B/\partial \tau))_0 / \Delta \tau_{0-1} \end{pmatrix} \quad (2.82)$$

At each depth we can write $dH_V/d\tau_V$ in two ways. From equation (A.33) we have

$$dH_V/d\tau_V = J_V - S_V = (1 - e_V)(J_V - B_V) \quad (2.83)$$

or, from the non-integrated form of equation (2.72),

$$dH_V/d\tau_V = d^2 f_V J_V / d\tau_V^2 \quad (2.84)$$

Equation (2.83) is not accurate for $\tau_V \gg 1$ as, from equation (A.52b) $J_V \approx B_V$. Similarly equation (2.84) is not accurate for $\tau_V \ll 1$ as $1/\Delta \tau_V^2$ is large. Expanding equation (2.83) we get

$$\begin{aligned} \delta(dH_V/d\tau_V)_d &= (1 - e_V)_d (\delta J_{Vd} - \delta B_{Vd}) \\ &= (1 - e_V)_d (\delta J_{Vd} - \dot{B}_{Vd} \delta T_d) \end{aligned} \quad (2.85)$$

Substituting for δJ_{vd} from equation (2.82) we have

$$\delta(dH_v/d\tau_v)_d = (1-e_v)_d [(\sum_{j=1}^D A_{d,j}^{-1} (1-e_v)_j \dot{B}_j \delta T_j) - \dot{B}_d \delta T_d] \quad (2.86)$$

For the second equation we get,

$$\delta(dH_v/d\tau_v)_d = A \begin{pmatrix} \delta J_1 \\ \vdots \\ \delta J_D \end{pmatrix}_v \equiv \delta^2 fJ_v/d\tau_v^2 \quad (2.87)$$

The matrix A is tri-diagonal so,

$$\delta(dH_v/d\tau_v)_d = A_{d,d-1} \delta J_{d-1} + A_{d,d} \delta J_d + A_{d,d+1} \delta J_{d+1} \quad (2.88)$$

Again substituting from equation (2.82) for the δJ 's we have,

$$\begin{aligned} \delta(dH_v/d\tau_v)_d &= A_{d,d-1} [\sum_{j=1}^D A_{d-1,j}^{-1} (1-e_v)_j \dot{B}_j \delta T_j] \\ &+ A_{d,d} [\sum_{j=1}^D A_{d,j}^{-1} (1-e_v)_j \dot{B}_j \delta T_j] \\ &+ A_{d,d+1} [\sum_{j=1}^D A_{d+1,j}^{-1} (1-e_v)_j \dot{B}_j \delta T_j] \end{aligned} \quad (2.89)$$

Converting $(dH_v/d\tau_v)$ to $(dH_v/d\tau_R)$, using

$$dH_v/d\tau_R = (d\tau_v/d\tau_R)(dH_v/d\tau_v) \quad (2.90)$$

we will then have $D \times D$ simultaneous equations for the D δT 's, with the boundary conditions included. The values

for $dH_{\nu}/d\tau_R$ can be computed from the model (as are the terms in the matrix A). In Chapter 3, however, we will see that for incoming X-ray radiation, $dH_{\nu}/d\tau_R$ can be written in terms of the sum of the optical and X-ray derivatives of the flux.

This linearisation method is known as Partial Linearisation. It differs from Complete Linearisation (see Mihalas, 1978, pp180-185) in that the conditions of radiative and hydrostatic equilibrium are not included, explicitly, in the matrices.

2.5 Hydrostatic Equilibrium

In a static stellar atmosphere the weight of any layer is supported by the total pressure (gas pressure + radiation pressure) beneath it. The density structure of the atmosphere is effectively determined by this balance. We have seen, from equation (A.59),

$$(dP_g/dm) = g - (4\pi/c) \int_0^{\infty} (\chi_{\nu}/\rho) H_{\nu} d\nu \quad (2.91)$$

where the last term is that associated with radiation pressure. Since H_{ν} is known from the solution of the transfer equation we can solve equation (2.91), one depth at a time, to find the correct value for $P_{g,d}$ and then use this to find $N_{e,d}$; by solving the Saha equation for all states and imposing charge neutrality (see Mihalas, 1978, pp112-114). Since T_d and $N_{e,d}$ determine the opacity χ_{ν} at each depth we can loop back to solve the transfer equation again with the new values for T_d , $N_{e,d}$ and χ_{ν} . This process

can be repeated until the model converges to the correct structure, within acceptable error.

In this chapter we have seen how a simple stellar atmosphere model is calculated. In the next chapter I will go on to describe how we adapt this to model the conditions that apply at the magnetic pole of an AM Her white dwarf.

CHAPTER 3

DESCRIPTION OF POLECAP ATMOSPHERE CODE

3.1 Introduction

In the previous chapter I described, step by step, the procedure for calculating any stellar atmosphere model. Whether the star to be modelled is a red giant or a white dwarf the basic iterative method is always the same. The essential assumptions associated with that calculation were :-

(i) the atmosphere is made up of plane-parallel layers where the thickness of each layer is small compared to the radius of the star

(ii) the atmosphere is in a steady state

(iii) the atmosphere is in hydrostatic equilibrium

(iv) the atmosphere is in radiative equilibrium.

Of course, to model certain types of star, it may be required to relax some of these restrictions, for example, to include convection for late-type stars such as red giants, but this has the disadvantage of making the calculation more complicated. For the case of modelling the polecap region of a magnetic white dwarf all of the above apply.

3.2 Calculating a model polecap atmosphere

In Chapter 1 I described the structure of the polecap of a magnetic cataclysmic variable. We must mathematically model these conditions as accurately as possible. We defined the top of our atmosphere to be just below the hard

X-ray emitting region where $T \sim T_{\text{eff}}$. At this region the atmosphere is hydrostatic since the inflow velocity has fallen to $< 10^{-3}$ of the free-fall velocity due to deceleration over the shock (Frank, King and Lasota, 1983). The infalling material subjects the top of the atmosphere (optical depth $\tau \sim 0$) to a pressure $P_0 \sim P_{\text{ram}}$ where

$$P_{\text{ram}} = (\dot{M}/4\pi R_x^2 f)(2GM/R_x)^{1/2} \quad (3.1)$$

is the ram pressure of the accretion flow. The extra pressure due to the weight of the X-ray emitting material below the shock is negligible by comparison with P_{ram} (Frank, King and Lasota, 1983). The atmosphere is irradiated by hard X-rays from this region with intensity I_{ν}^x . The spectral form of I_{ν}^x was taken to be thermal bremsstrahlung at a temperature of T_s (given by equation 1.2) and was considered to be isotropic, which is reasonable for irradiation by a large, plane-symmetric, optically thin accretion column. The strong magnetic field of the polecap ($\sim 10^7$ G) guarantees radiative equilibrium and convection is strongly suppressed due to magnetic stresses, $4B^2/8\pi \sim 10^{13}$ dynes cm^{-2} , outweighing material stresses, $\sim 10^{11}$ dynes cm^{-2} at their maximum point at the base of the polecap. Local thermodynamic equilibrium is assumed throughout the atmosphere¹. In the simplest radiative-loss column structures the irradiation by hard X-rays is the only source of energy, apart from the small intrinsic stellar flux. However we also considered the situation where additional accretion energy is deposited non-radiatively at large optical depths, this was achieved

by increasing the intrinsic stellar flux such that,

$$F = \sigma T_{\text{eff}}^4 = Q_{\text{x}} + \int I_{\text{v}}^{\text{x}} d\nu \quad (3.2)$$

where $Q_{\text{x}} = \sigma T_{\text{x}}^4$, the intrinsic stellar flux. The ratio

$$R^{\text{x}} = \int I_{\text{v}}^{\text{x}} d\nu / \sigma T_{\text{eff}}^4 \quad (3.3)$$

defines the amount of energy derived from the X-ray irradiation and is an important variable in our calculations. With this variable we were able to model atmospheres that were unilluminated as well as those which derived all their energy from the X-ray illumination. It should be noted, though, that the main limitation imposed on our atmosphere model is in treating the very thin transition layer at the base of the hard X-ray region since here the electron temperature must drop sharply from $\sim T_{\text{s}}$ to $\sim T_{\text{eff}}$ (Frank, King and Lasota, 1983) and non-LTE effects can produce fluorescent line emission and photoionisation. This region is not described by our calculation.

With the above quantities specified the calculation follows the procedure described in Chapter 2. Figure 3.1 shows a flow diagram which outlines the general flow of the program between the more important steps involved. With reference to Figure 3.1 the calculation proceeds as follows :-

1) The calculation of the atmosphere model requires only three parameters; effective temperature T_{eff} ; gravity g and fraction of total flux derived from the X-ray illumination R^{x} . These three parameters characterise any

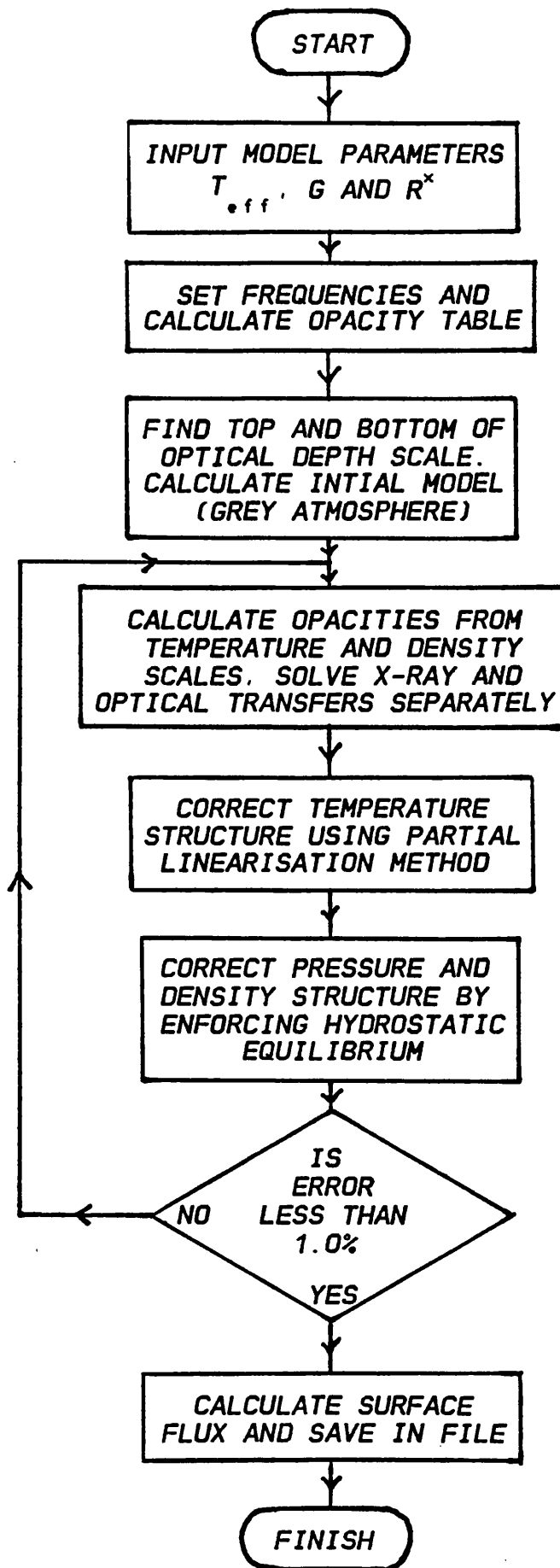


Figure 3.1 Flow diagram for polecap atmosphere calculation

polecap model, hence it is possible to calculate a three-dimensional 'grid' of models to be used in any application where a polecap atmosphere is the best approximation.

2) The optical/UV frequencies used in the calculation are chosen such that a black body at the same effective temperature has 99.9% of its total flux contained between the upper and lower frequency limits. This range is then split into 100 bins, spaced logarithmically, with at least two frequency points between any opacity jumps. 30 X-ray frequency bins are used, spaced in the same way between the upper optical/UV point and an energy of 30keV. Opacities included in the model are, assuming stellar abundances;

- i) HI, HeI and HeII continuum opacities
- ii) K-shell photoelectric absorptions of carbon, nitrogen, oxygen, neon, sodium, magnesium, silicon and sulphur
- iii) inelastic Compton scattering treated as a fictitious absorption process for photons with $h\nu > 4kT$, where T is the local atmospheric temperature (e.g. Milgrom and Salpeter, 1975). Bound-bound transitions are neglected as they are unimportant for both the gross atmospheric structure and the continuum spectrum.

The opacity per absorber over the optical/UV frequency range is calculated over the range of temperatures and electron densities used in calculating the partition functions for HI, HeI and HeII. The calculation of the partition functions is performed in a separate program and the data stored in three arrays of forty temperatures by forty densities. The true opacity at a given temperature and electron density is calculated from this data by

interpolating a value from the opacity data and multiplying this by the number density of absorbers.

3) The Rosseland Mean optical depth scale is used throughout the calculation of the initial model. Working down through the atmosphere using a constant optical depth step the Hydrostatic Equilibrium equation is solved to find the density and pressure at that depth. The temperature at each depth is given by equation (2.36) with $q(\tau_R)$ being derived from Table 2.1. The bottom of the atmosphere is defined such that at $(\tau_R)_{\max}$ the monochromatic optical depth τ_ν at each frequency (optical/UV and X-ray) has a value of at least 50. This ensures that the diffusion approximation holds for the lower boundary limit of the transfer equation at all frequencies. The region between the top and bottom of the Rosseland Mean optical depth scale is then divided into fifty points, evenly spaced in the logarithm. The range for most models is $10^{-6} < \tau_R < 10^3$.

4) For each frequency the true opacity at each depth is calculated and the transfer equation solved, using six inward and six outward rays for the Feautrier method. The optical and X-ray transfers are treated separately since at X-ray frequencies $B_\nu = 0$, and this means that $S_\nu = B_\nu$ cannot be used as a first guess for the solution of the transfer equation at X-ray frequencies. The problem was solved by using the method of discrete ordinates to find the eigenvalues of the characteristic equation for an atmosphere with no thermal source term, only scattering (Mihalas, pp64-68, 1978) and hence an initial guess for S_ν .

5) The temperature structure of the atmosphere was corrected using the partial linearisation method described

in Chapter 2. The largest fractional change in the temperature at any depth was taken to be the error in the model. With incoming X-ray radiation being absorbed at each depth the condition of radiative equilibrium requires

$$\int_0^{\infty} H_{\nu} d\nu = \sigma T_{*}^4 \quad (3.4)$$

at each depth. Since the total flux at each depth is equal to the sum of the optical and X-ray fluxes we can say

$$\int_0^{\infty} H_{\nu} d\nu = \int_0^{\infty} H_{opt}(\nu) d\nu + \int_0^{\infty} H_x(\nu) d\nu \quad (3.5)$$

Differentiating with respect to the Rosseland Mean optical depth and substituting equation (3.5) into equation (3.4) we get the condition of radiative equilibrium used in correcting the temperature structure

$$\int_0^{\infty} \left[\frac{dH_{opt}}{d\tau_R}(\nu) \right] d\nu = - \int_0^{\infty} \left[\frac{dH_x}{d\tau_R}(\nu) \right] d\nu \quad (3.6)$$

6) Hydrostatic equilibrium is enforced at each depth in the atmosphere to correct the pressure and density structure.

7) If the error in the model (from step 5) is greater than 1.0% the calculation loops back to step 4 and repeats until the error is less than 1.0%. Once the model has converged the optical and X-ray surface fluxes are calculated from

$$F_{\nu} = 2\pi \int_0^1 I_{\mu\nu}(0) \mu d\mu \quad (3.7)$$

and stored, along with the surface intensities $I_{\mu\nu}(0)$, in a file, for future use. Convergence to less than 1.0% is usually achieved by the fourth iteration.

In the last two chapters I have described the procedure for calculating a model stellar atmosphere subjected to the conditions that prevail at the base of the accretion column in AM Her white dwarfs. In the following chapters I will show the results that are obtained from these calculations and the uses that these model atmospheres can be put to.

¹ LTE can be assumed as we are modelling the region below the shock such that the electron density is high throughout the atmosphere. The non-LTE region just below the shock is not described by our model.

CHAPTER 4

MODEL ATMOSPHERE SPECTRA

4.1 Introduction

In the previous chapters I have described the calculation of a stellar atmosphere model for the polecap of a magnetic white dwarf. In this chapter I will show the general results of this calculation; in later chapters I will describe the uses that these models have been put to and the results of any fitting to observed systems.

We have seen that a model polecap atmosphere can be described by three parameters; the effective temperature, T_{eff} ; the white dwarf gravity, g (related to its mass, see later) and the percentage of its flux derived from the hard X-ray irradiation, P_{111} . The parameter range associated with each is; $5.0 \times 10^4 < T_{eff} < 3.0 \times 10^5$ K, $1.0 \times 10^5 < g < 1.0 \times 10^9$ cm s⁻¹ and $0.01 < P_{111} < 99.9\%$ (not 100% as there must be some intrinsic stellar flux from the white dwarf itself). After the model has converged to within an acceptable error (<1.0%) the optical/UV and X-ray surface fluxes and intensities along the six outward rays are stored. The shock intensity is also stored to allow the total outward flux to be calculated. How these are affected by changes in the initial parameters of the model is the subject of this chapter.

4.2 The outward surface spectrum

Figure 4.1 shows the outward surface flux from the atmosphere as a function of frequency. The optical/UV and X-ray components are shown, together with a black body of the same effective temperature and the hard X-ray flux from

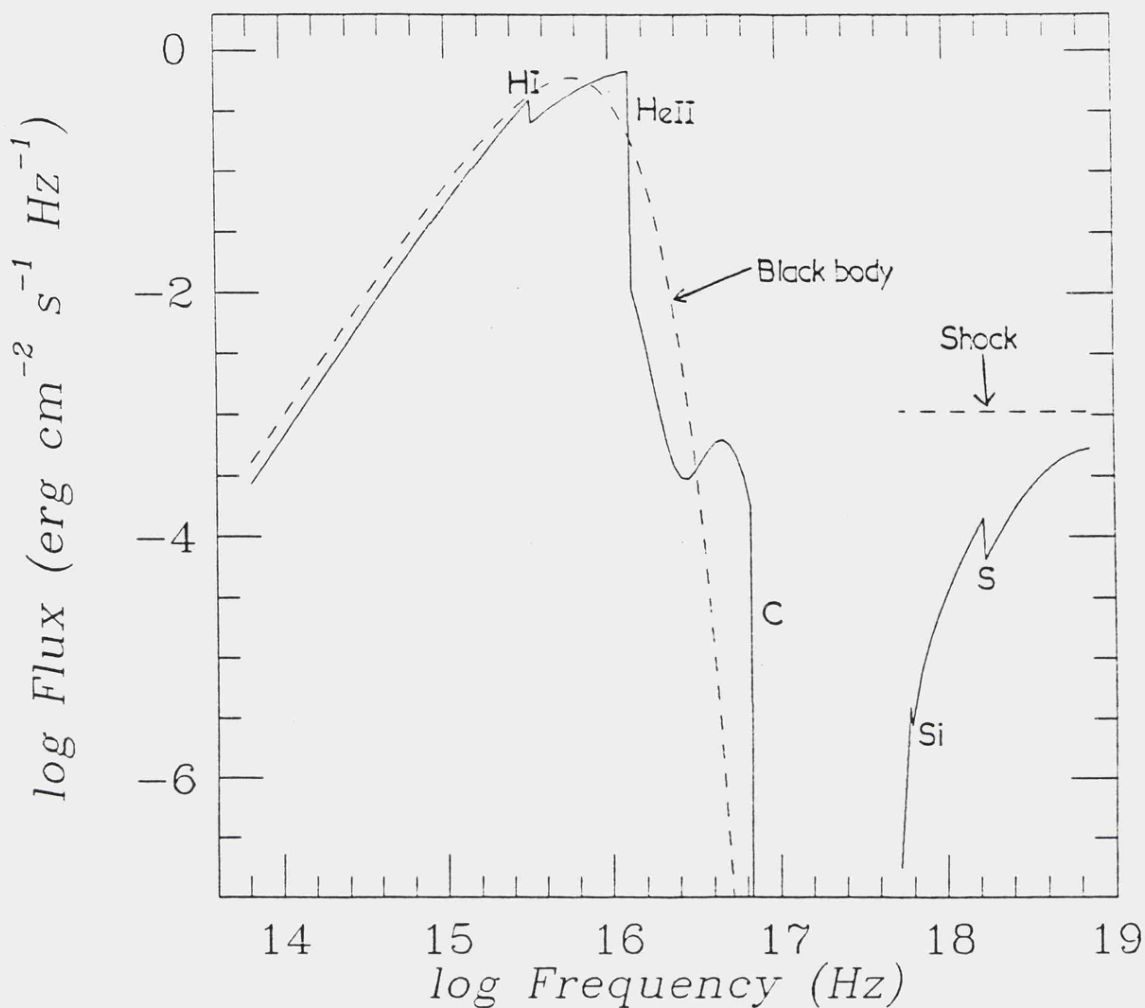


Figure 4.1 Outward surface flux from the atmosphere plotted as a function of frequency ($T_{\text{eff}}=1.0 \times 10^5$ K, $P_{\text{ill}}=99.9\%$ and $M=1$ solar mass). Absorption features are labelled with the elemental ionisation state responsible.

the shock. The model has $T_{\text{eff}}=1.0 \times 10^5$ K, $g=4.451 \times 10^8$ cm s $^{-1}$ (≈ 1 solar mass) and $P_{\text{ill}}=99.9\%$. The absorption features are labelled with the elemental ionisation state responsible (e.g., HI - absorption is neutral hydrogen, C - absorption is K-shell carbon, etc.).

At this effective temperature the optical/UV continuum is dominated by the HeII and K-shell carbon absorption edges ($\log v=16.1$ and 16.83 respectively). The spectrum is

slightly harder in the soft X-ray region than a black body of the same effective temperature. The 'hump' at frequencies above the HeII edge is due to the low opacity allowing us to see a deeper and hotter region of the atmosphere, where the local Planck function $B_{\nu}(T)$ is still rising. Note that the HeI absorption feature at $\log v = 15.77$ is not seen, as nearly all the helium is at least singly-ionised at this temperature.

The hard X-ray spectrum comes from the absorption and re-radiation of the incident hard X-rays. Over the whole parameter space the fraction, a_x , of the incident X-rays reflected in this component only varies from 0.27-0.29. This albedo component has a strong dependence on frequency. The two absorption features seen are due to K-shell silicon ($\log v = 17.78$) and K-shell sulphur ($\log v = 18.23$).

4.3 Spectral shape .v. input parameters

Three parameters characterise these model atmospheres; the effective temperature, the white dwarf gravity and the strength of the X-ray irradiation. The gravity of a white dwarf can be related to its mass using the mass-radius relationship derived by Nauenberg (1972),

$$R/R_s = 1.12 \times 10^{-2} [(M/M_*)^{-2/3} - (M/M_*)^{2/3}]^{1/2} \quad (4.1)$$

where M is the mass of the white dwarf in solar masses, R_s is the solar radius and M_* is the Chandrasekhar mass (1.44 solar masses). Since $g = GM_s/R^2$ we get

$$g = GMM_s / (1.2544 \times 10^{-4} R_s^2 [(M/M_\star)^{-2/3} - (M/M_\star)^{2/3}])$$

(4.2)

where M_s is the solar mass.

The changes in the spectral shape for the optical/UV and X-ray components will be considered separately for each input parameter.

4.3.1 Spectral shape .v. effective temperature

The variation of the spectrum with effective temperature is shown in Figure 4.2 for the optical/UV component and Figure 4.3 for the hard X-ray albedo component. All the models are for one solar mass white dwarfs with $P_{111} = 99.9\%$. The effective temperatures range from 5.0×10^4 K to 3.0×10^5 K in steps of 5.0×10^4 K.

The strengths of the main absorption features (HI, HeII and K-shell carbon) vary quite strongly with temperature. The HeI feature is only seen for the lowest temperature and the K-shell edges of nitrogen and oxygen are only seen in the highest temperatures. The relationship between these models and black bodies at the same effective temperatures will be seen in the next chapter.

In Figure 4.3 the hard X-ray albedo component varies as T_{eff}^4 , as we would expect for constant illumination. Since this is a reflected component the strengths of the absorption features stay approximately constant with temperature.

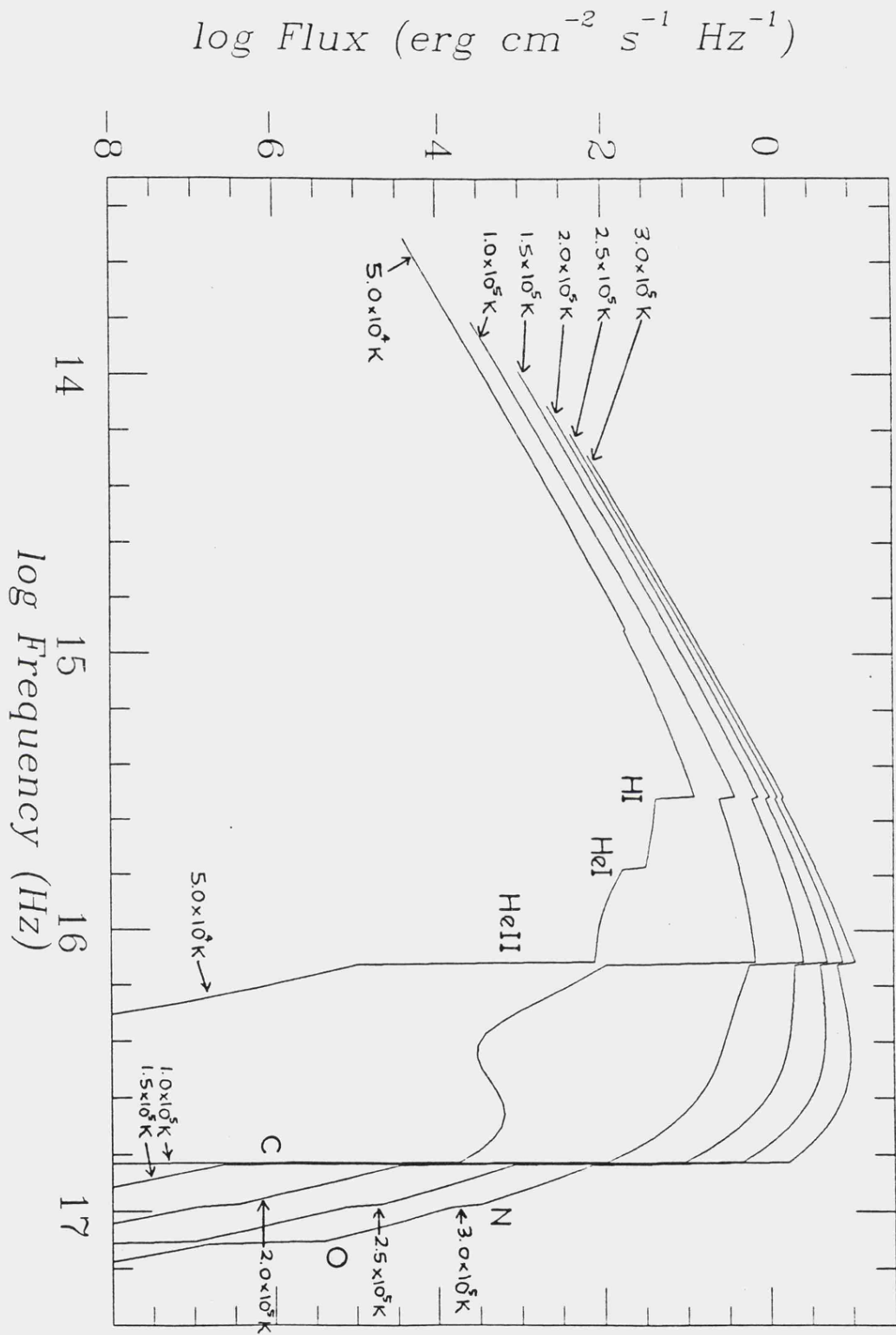


Figure 4.2 Variation of the optical/UV continuum with effective temperature (all models are for one solar mass white dwarfs with $P_{111} = 99.9\%$). Absorption features are labelled with the elemental ionisation state responsible.

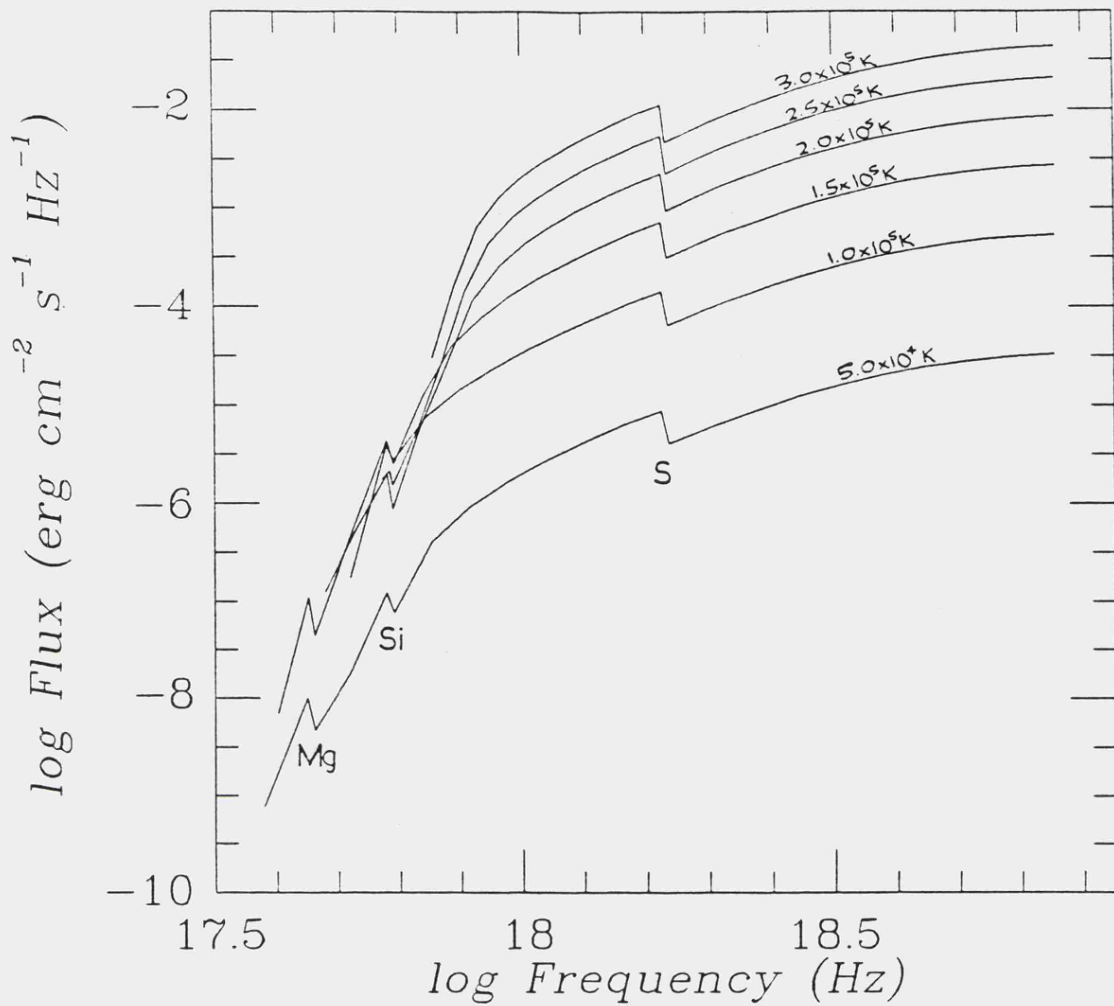


Figure 4.3 Variation of the hard X-ray albedo component with effective temperature (parameters the same as in Figure 4.2). Absorption features are labelled with element responsible (K-shell only).

4.3.2 Spectral shape .v. white dwarf gravity

The variation of the spectrum with white dwarf gravity is shown in Figure 4.4, for the optical/UV component and, for the hard X-ray component, Figure 4.5. All the models are for $T_{\text{eff}} = 1.0 \times 10^5 \text{ K}$ and $P_{\text{ill}} = 99.9\%$. The gravities range from $10^5 - 10^9 \text{ cm s}^{-1}$.

Somewhat surprisingly the white dwarf gravity has little effect on the strengths of the main absorption

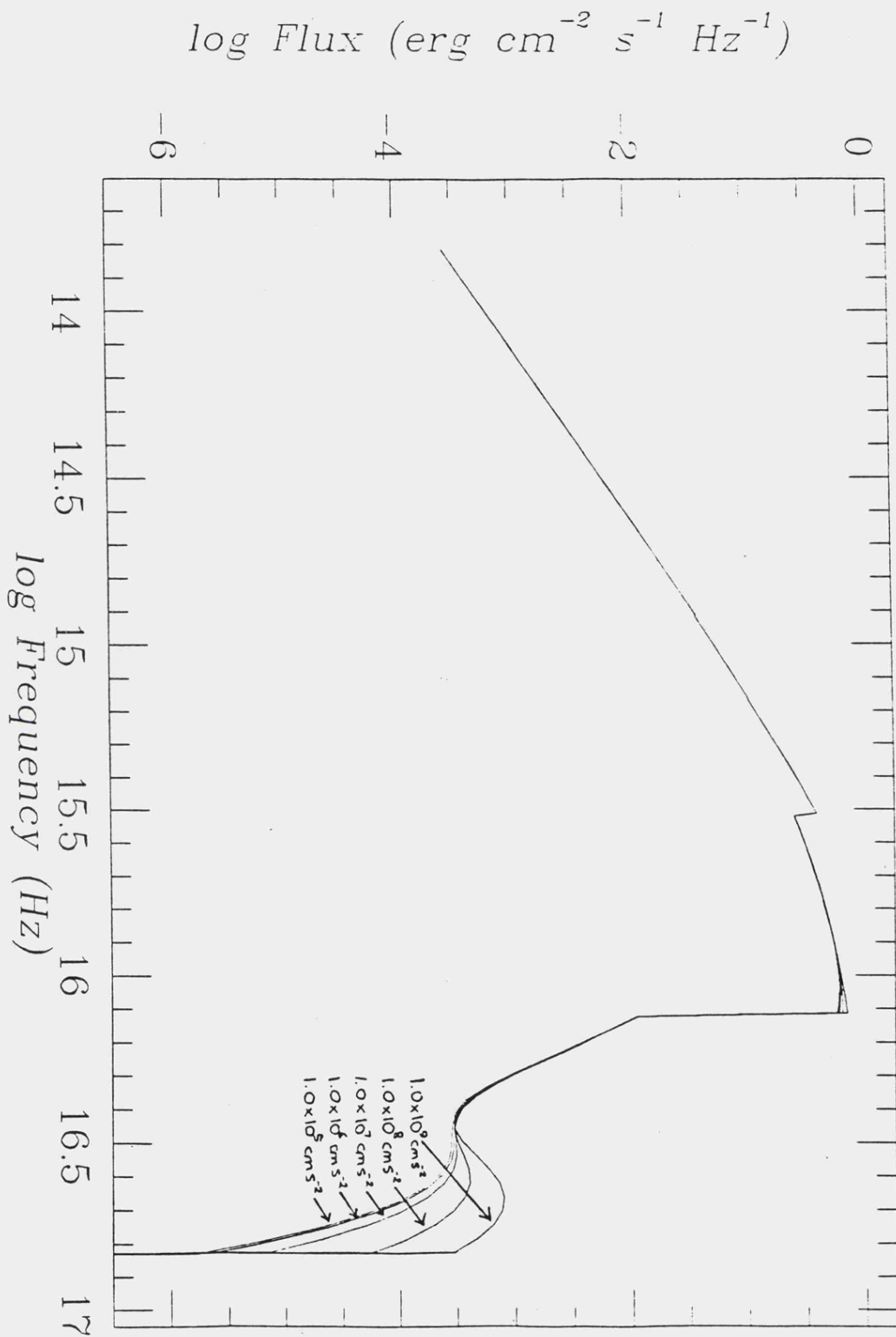


Figure 4.4 Variation of the optical/UV continuum with white dwarf gravity (all models have $P_{111} = 99.9\%$ and $T_{\text{eff}} = 1.0 \times 10^5 \text{ K}$).

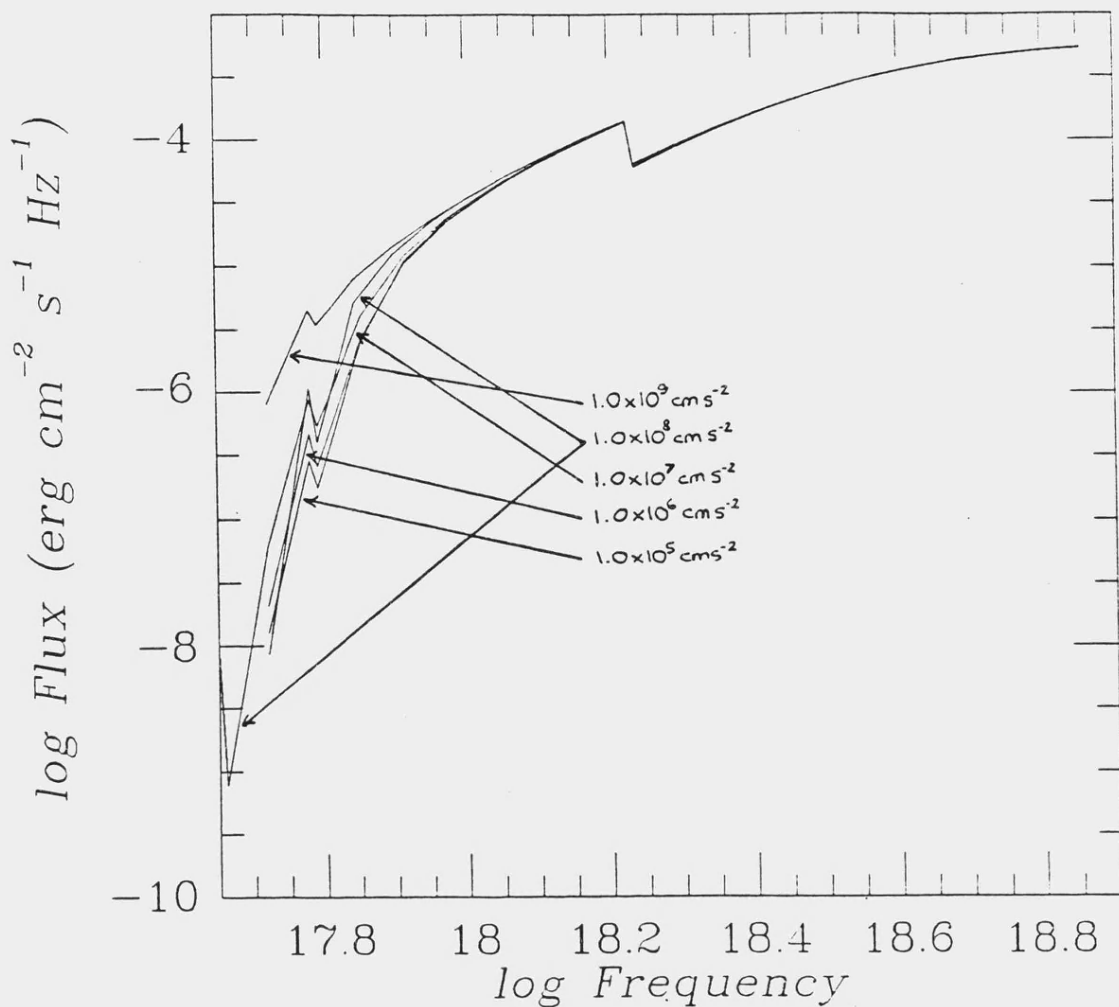


Figure 4.5 Variation of the hard X-ray albedo component with white dwarf gravity (model parameters the same as in Figure 4.4).¹

features. The 'hump' in the spectrum is reduced with gravity due to the expansion of the atmosphere reducing the temperature seen here. There is little overall change in the albedo component with gravity.

4.3.3 Spectral shape .v. strength of illumination

The variation of the spectrum with the percentage of the flux derived from the X-ray illumination is shown in

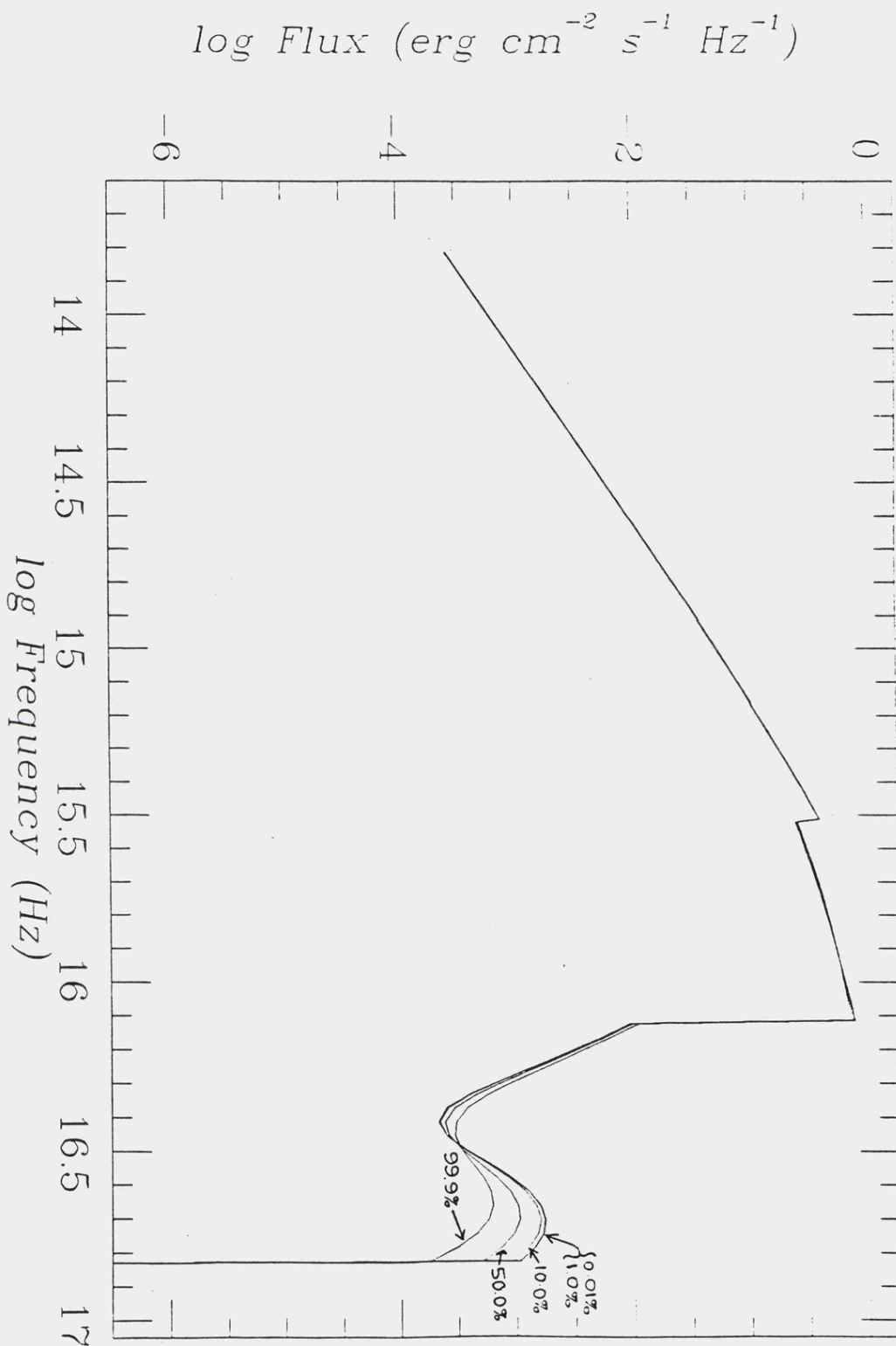


Figure 4.6 Variation of the optical/UV continuum with percentage of X-ray illumination (models are for one solar mass white dwarfs with $T_{\text{eff}} = 1.0 \times 10^5 \text{ K}$).

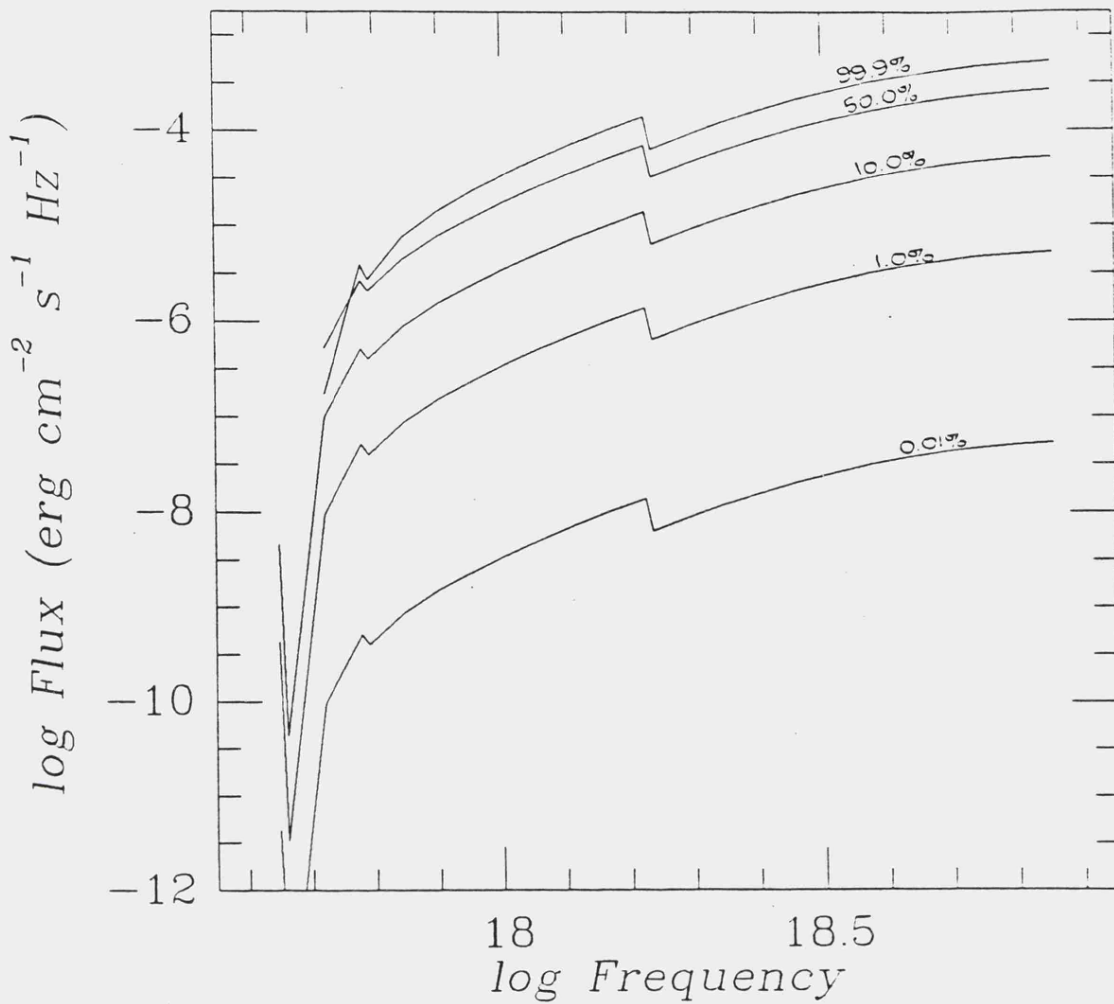


Figure 4.7 Variation of the hard X-ray albedo component with percentage of X-ray illumination (model parameters the same as for Figure 4.6).

Figures 4.6 and 4.7, for the optical/UV and hard X-ray components respectively. All the models are for one solar mass white dwarfs with $T_{\text{eff}} = 1.0 \times 10^5$ K. The illuminations range from 0.01-99.9%.

In the optical/UV region, decreasing the strength of the illumination results in a hardening of the spectrum in the soft X-ray region. For $P_{\text{ill}} < 10.0\%$ there is little change in the shape of the spectrum so the model has become essentially unilluminated at this point.

In the hard X-ray region the albedo component decreases linearly with P_{111} , as would be expected; there is little change in the overall spectral shape.

4.3.4 Summary

In the optical/UV spectral region the overall model atmosphere spectrum is a strong function of the effective temperature as are the strengths of the individual absorption features. Reducing the mass of the white dwarf results in a softening of the soft X-ray continuum but has little effect elsewhere. Reducing the strength of the hard X-ray illumination has the opposite effect. The reasons for this will be discussed in a later section.

The hard X-ray albedo component is a strong function of the effective temperature and the strength of the illumination, but only in overall shape. The absorption strengths are largely unaffected by changes in the model parameters. Changing the mass of the white dwarf has little effect on the albedo component.

We have seen that the calculated spectrum from a model atmosphere is very different from its corresponding black body spectrum. The fact that the atmosphere has absorption features is not the only difference between the two; there is another difference that is not seen in the figures shown so far. Whereas a black body emits with equal intensity in all directions a model atmosphere does not.

4.4 Limb effects in a model atmosphere spectrum

In the calculation of these model atmospheres six outward rays were used, equally spaced from close to the perpendicular to the atmosphere (ray number 1) to close to parallel with it (ray number 6). In a black body the specific intensity along each ray is the same. In a model atmosphere the intensity along each ray is a function of many things and is unlikely to be constant. The variation of the intensity with emitted angle is known as limb darkening or limb brightening, depending on whether the intensity decreases or increases as we move away from the normal. The 'limb' reference comes from early telescopic observations of the sun that showed that it was not uniformly bright over its whole disc but that its brightness decreased towards the limb. The physical reason for this is that at the centre we see into deeper, hotter layers whereas at the limb we see only the cooler outer layers; the specific intensities along each ray reflect this.

The intensities along each outward ray from the atmosphere as a function of frequency are shown in Figures 4.8 and 4.9 for the optical/UV and hard X-ray components respectively; the model parameters are the same as those in Figure 4.1. We see that for the optical/UV component there is a strong decrease in the intensity at higher frequencies, as we go away from the normal to the atmosphere. However the hard X-ray irradiation causes limb brightening in the albedo component², although, unlike in the optical/UV region, there is little change in the

$\log \text{ Intensity (erg cm}^{-2} \text{ s}^{-1} \text{ Hz}^{-1} \text{ ster}^{-1})$

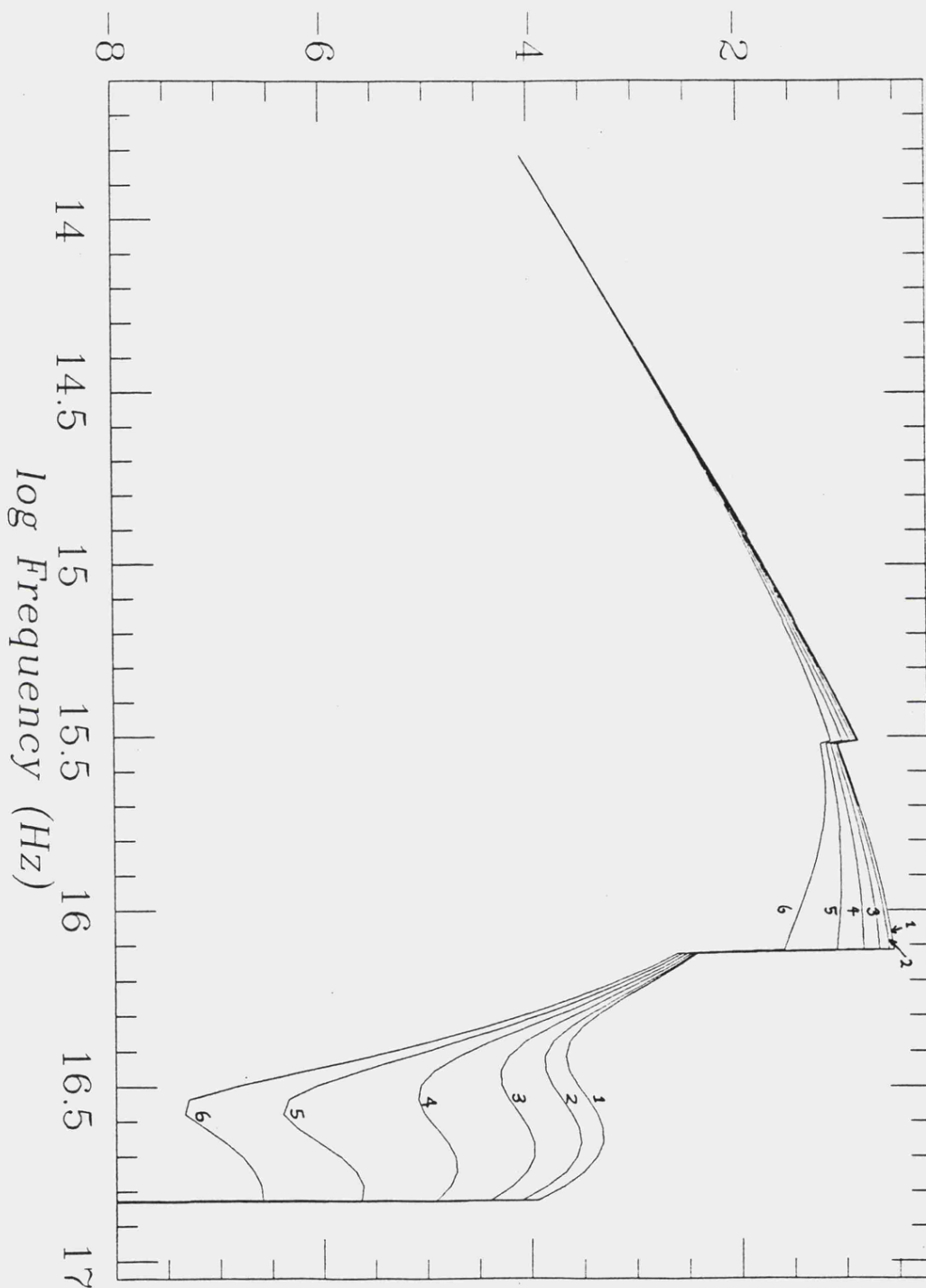


Figure 4.8 The intensity along each outward ray plotted as a function of frequency (model parameters the same as in Figure 4.1). Spectra are numbered 1-6, spectra 1 is for the ray normal to the atmosphere, spectra 6 is for the ray almost parallel to the atmosphere.

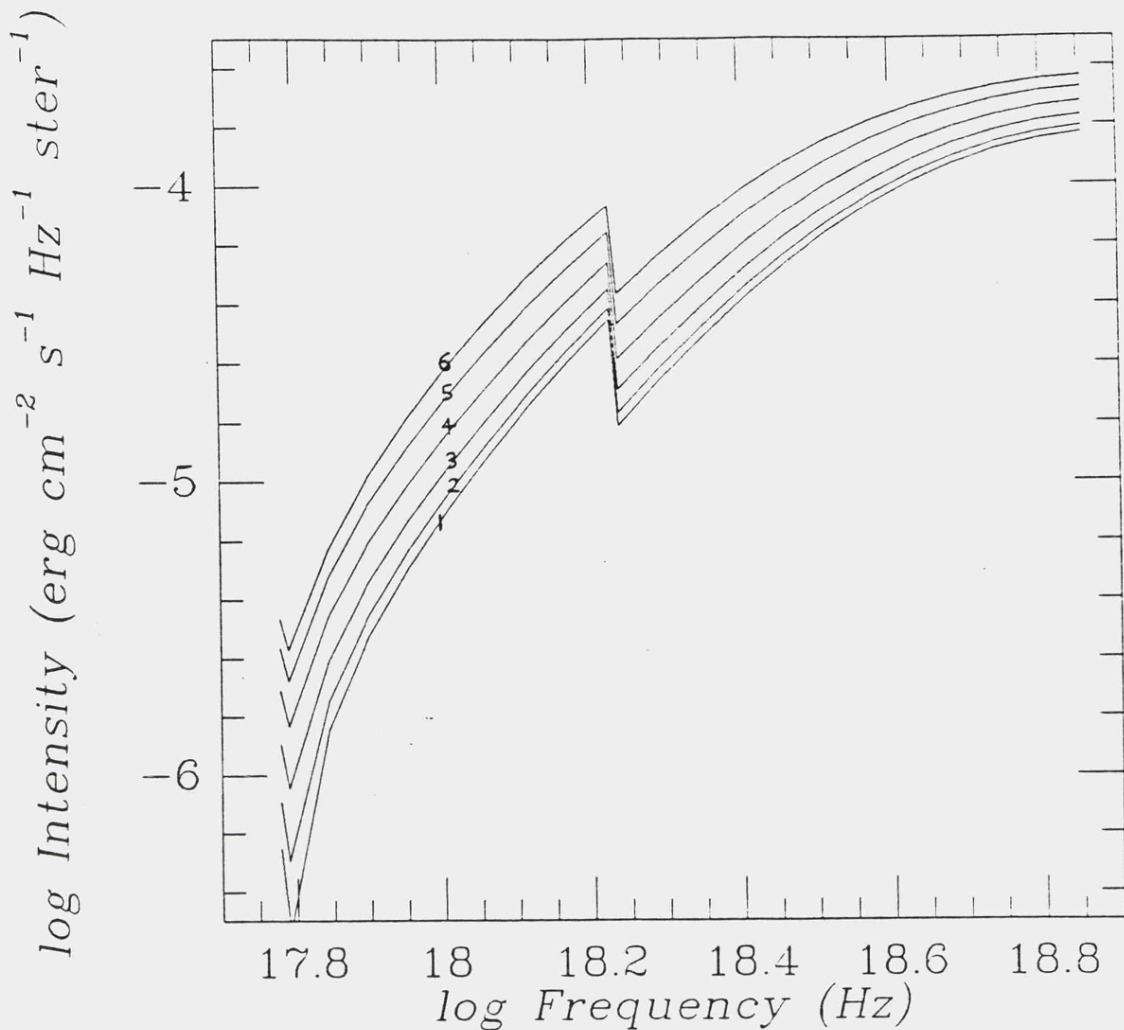


Figure 4.9 Intensity along each ray for the hard X-ray albedo component (model parameters and ray numbers the same as for Figure 4.8).

overall spectral shape with emitted angle. These limb variations will become important in the calculation of lightcurves, as we shall see in Chapter 6.

4.5 The temperature structure of the atmosphere

We have seen in Figure 4.6 that reducing the amount of X-ray irradiation of the model atmosphere increases the hardness of the soft X-ray continuum. In Figure 4.4 we saw

that the opposite occurred, when the white dwarf gravity was reduced. We can understand the reasons for the above if we consider the temperature structure of the atmosphere for illuminated and unilluminated models.

Figure 4.10 shows the temperature of the atmosphere plotted against the Rosseland mean optical depth into the atmosphere. The models have $T_{\text{eff}} = 1.0 \times 10^5$ K and are for one solar mass white dwarfs. We see that irradiating a model atmosphere softens the temperature structure until all the incident radiation is absorbed (at $\log \tau_R \approx 4$); the temperature then rises normally. Both models do not depart from their initial structures to any great extent indicating the accuracy of the initial models used in the calculations.

From previous discussions we know that the soft X-ray continuum at frequencies above the HeII feature is due to deeper regions of the atmosphere. In an unilluminated atmosphere these deeper regions are much hotter than those in an illuminated atmosphere, so we see a harder soft X-ray continuum. Similarly, in a model with reduced gravity, the atmosphere will be expanded and therefore cooler, so we see a softer soft X-ray continuum. To better illustrate the differences between illuminated and unilluminated model atmospheres the flux at each frequency, at each depth in the atmosphere, is shown in Figures 4.11 and 4.12, for illuminated and unilluminated models respectively. The region over which the hard X-rays are absorbed is clearly seen in Figure 4.11.

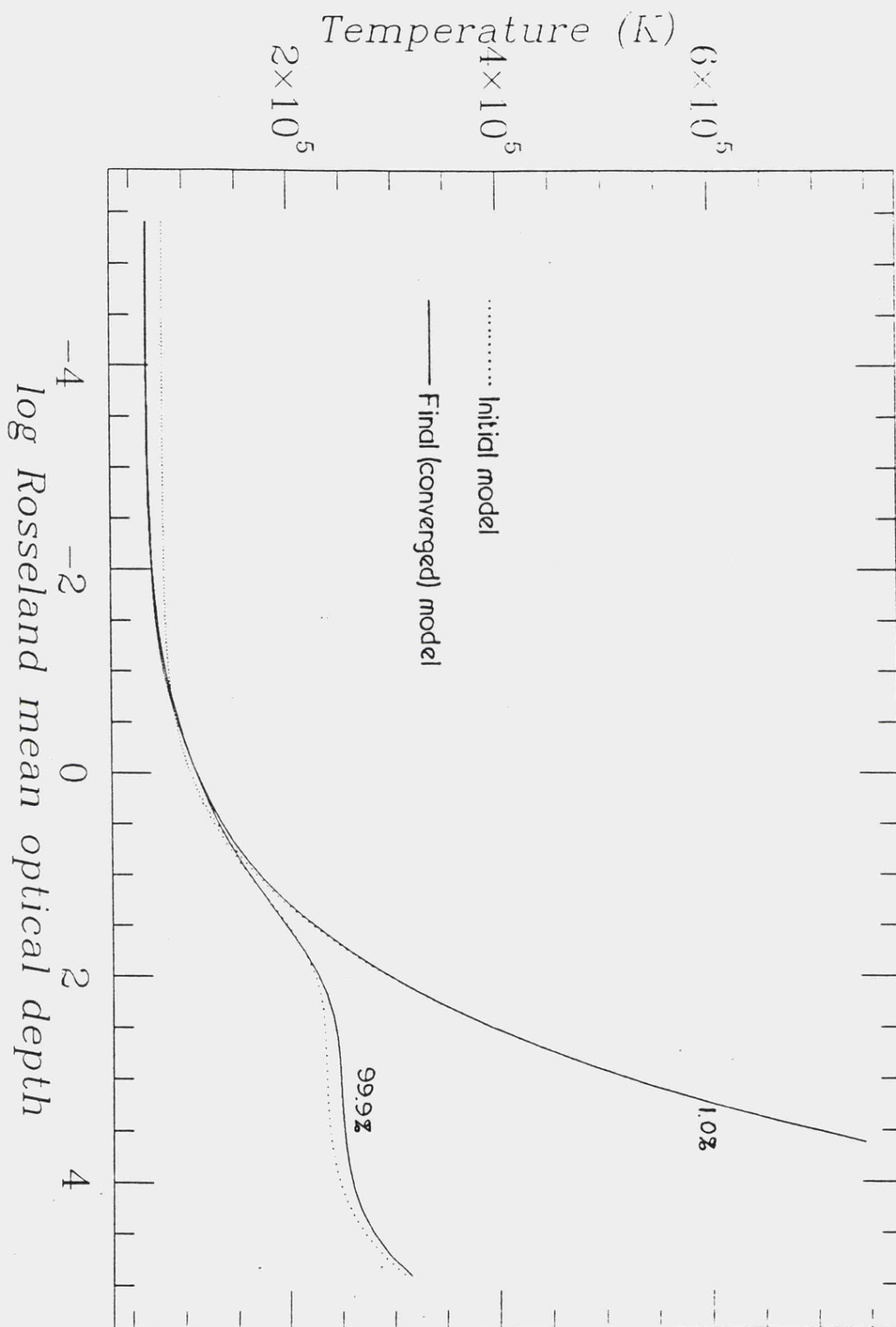


Figure 4.10 Temperature within the model atmosphere as a function of the Rosseland mean optical depth for illuminated and unilluminated models ($T_{\text{eff}} = 1.0 \times 10^5$ K and $M = 1$ solar mass). The initial models and final models are shown.

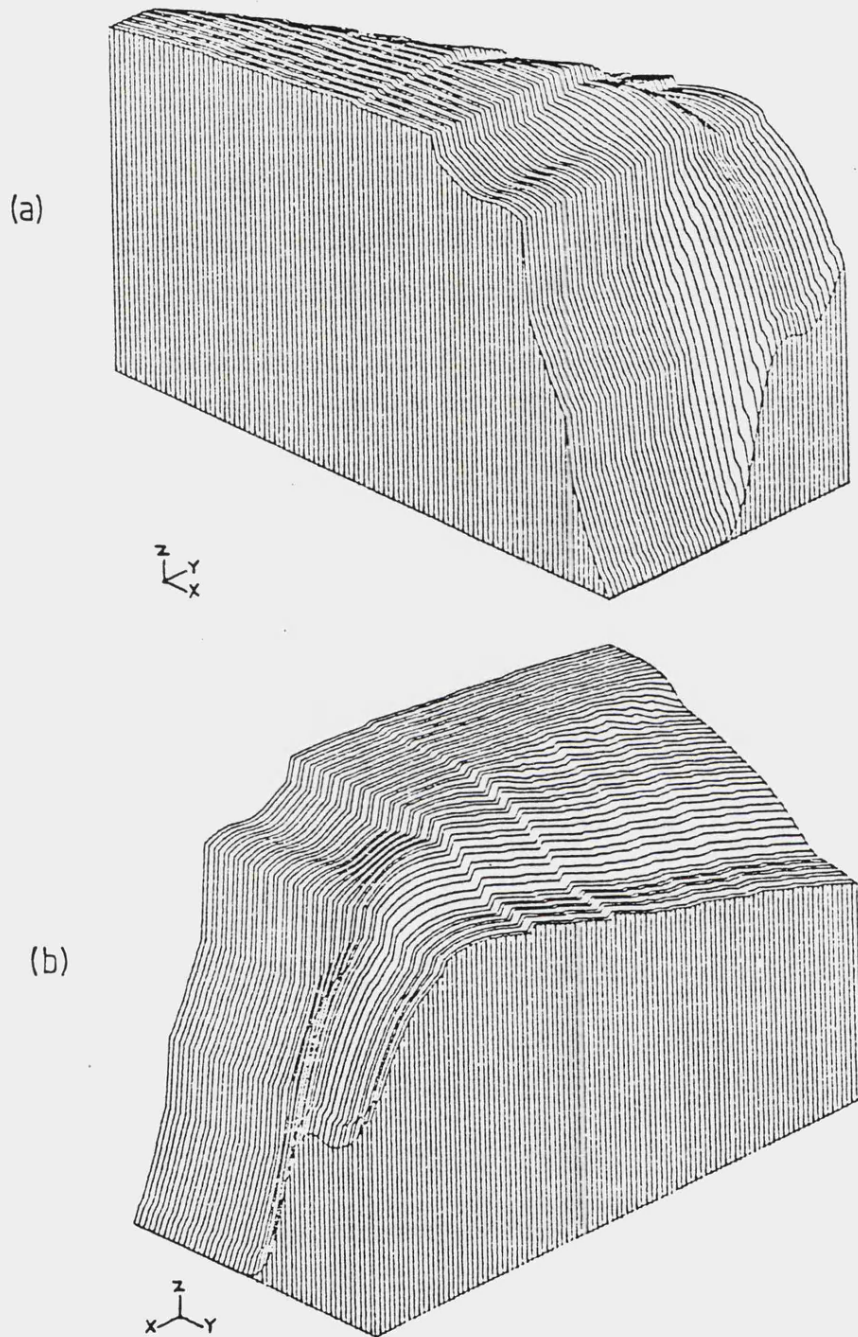


Figure 4.11 The flux at each depth in the atmosphere plotted as a function of frequency; viewed (a) 'from the top' and (b) 'from the bottom', for an illuminated atmosphere with $M=1$ solar mass and $T_{eff} = 1.0 \times 10^5$ K (x =frequency, y =depth and z =flux).

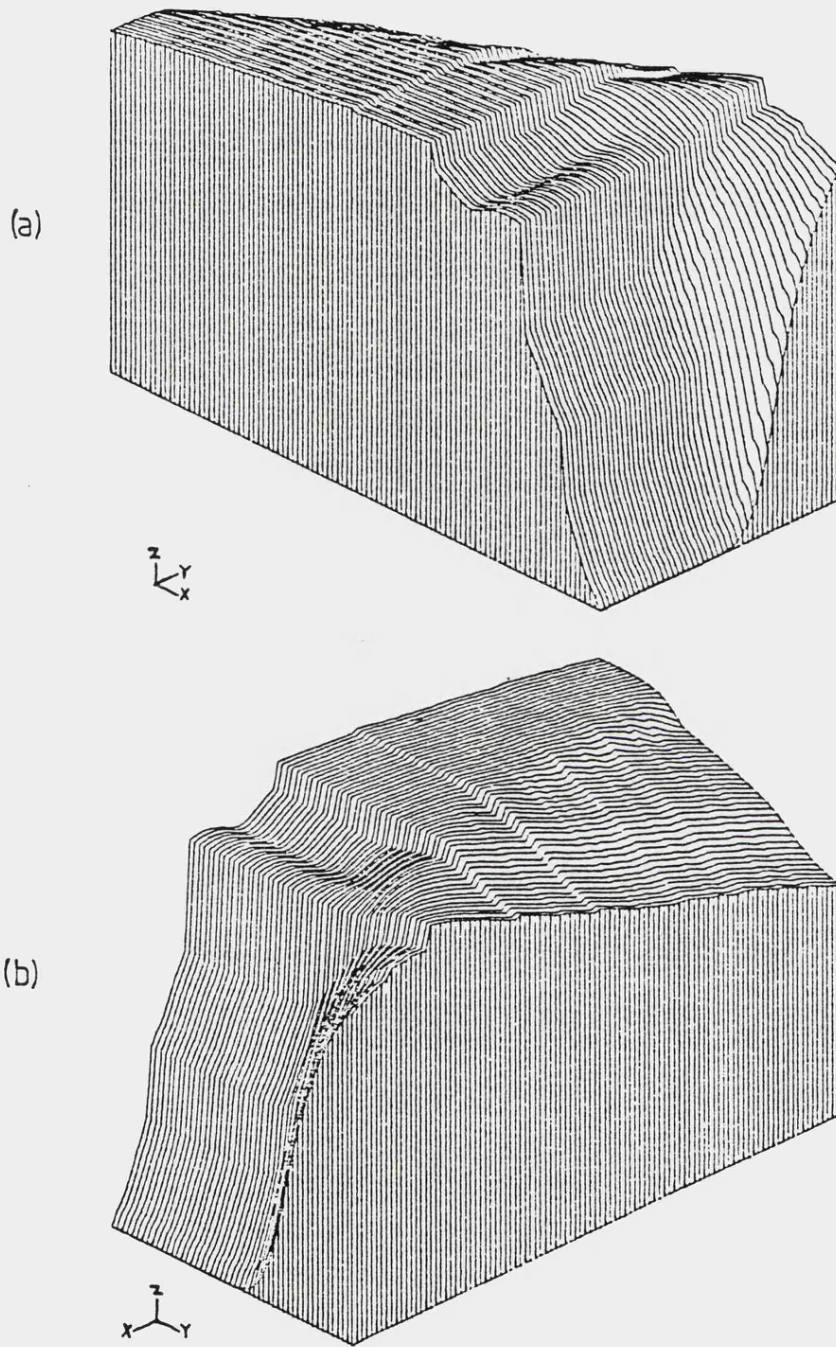


Figure 4.12 The flux at each depth in the atmosphere plotted as a function of frequency; viewed (a) 'from the top' and (b) 'from the bottom', for an unilluminated atmosphere with $M=1$ solar mass and $T_{\text{eff}} = 1.0 \times 10^5$ K (x =frequency, y =depth and z =flux).

4.6 Discussion of the calculated spectra

We have seen the results of calculating model atmosphere spectra for the polecap of an accreting magnetic white dwarf. One of the original reasons for making these calculations was the suggestion that the model spectra would remove the soft X-ray excess inferred for observed sources from black body fits to the soft X-ray continua. From black body fitting of these fully-illuminated model atmosphere spectra (described in the next chapter) it was found that this was not the case. This made it important to model atmospheres where only a fraction of the flux in the atmosphere is derived from the hard X-ray irradiation, the rest being derived from some mechanism whereby large quantities of energy are deposited at depth in the atmosphere (possible mechanisms where discussed in Chapter 1).

By altering the model parameters it was found that as the effective temperature was increased the optical/UV continuum became more black body-like as the absorption features decreased in strength. Reducing the white dwarf gravity softened the soft X-ray continuum as did increasing the strength of the illumination. These changes are due to changes in the temperature structure of the atmosphere; irradiating the model causes a softening of the temperature gradient and a reduction of the soft X-ray flux. Reducing the gravity cools the atmosphere and causes a similar reduction.

In the next few chapters I will describe the uses for these model spectra and the results of actual observational

fitting but before that there is one more important result that can be found from atmosphere calculations.

4.7 Model atmospheres and the Eddington limit

The Eddington temperature limit, given by,

$$T_{edd} = (gc/\sigma_s \kappa_{es})^{1/4} \quad (4.3)$$

where κ_{es} is the electron scattering opacity and σ_s is the Stefan-Boltzmann constant, is the limit beyond which a fully ionized atmosphere will be hydrostatically unstable. At $T_{eff} > T_{edd}$ the radiation pressure exceeds the downward pressure due to the material above and the higher layers of the atmosphere are blown away. This type of event is seen in supernovae as well as in some types of variable star. The Eddington limit assumes that the opacity is constant at κ_{es} . We have seen from previous results that the opacity in a model atmosphere is far from constant and is always greater than κ_{es} . Thus in these atmospheres the limiting effective temperature T_{crit} is always less than T_{edd} .

In order to find T_{crit} , the critical temperature as a function of white dwarf mass, it was necessary to adopt a trial-and-error approach to the problem. The white dwarf's mass (gravity) was fixed and the effective temperature increased in uniform steps, each time running a model to convergence, until at some point the model failed with a negative gas pressure (indicating that the outer layers would be blown away); T_{crit} was then chosen to be the last stable model temperature. Since this was a rather

Table 4.1 Calculated values for T_{crit} .

*WD mass, M	gravity, g (cm s^{-1})	T_{crit} ($\times 10^5$ K)	T_{edd} ($\times 10^5$ K)
0.10	3.8×10^6	2.25	2.77
0.15	7.6×10^6	2.45	3.30
0.22	1.5×10^7	2.70	3.91
0.32	3.0×10^7	3.05	4.65
0.46	6.0×10^7	3.40	5.53
0.63	1.2×10^8	3.65	6.57
0.83	2.4×10^8	4.05	7.82
1.02	4.8×10^8	4.50	9.30
1.10	6.7×10^8	4.80	10.10

* M was calculated using a Newton iterative procedure to solve equation (4.2) for a given g.

laborious procedure the resultant graph, shown in Figure 4.13, has been interpolated from the known values given in Table 4.1. However the results indicate that the variation of T_{crit} with white dwarf mass is a smooth one, so the interpolated values can be assumed to be correct to within $\pm 10^4$ K.

It is important to note that the values for T_{crit} are conservative in the sense that they represent the highest values for T_{eff} that allow a model atmosphere to converge. While it is clear that the radiation pressure term (see equation A.58) would prevent convergence for larger T_{eff} it might be that an inefficient iteration procedure overestimates this term somewhat. Nonetheless, examination of the structure of the atmosphere with $T_{eff} = T_{crit}$ suggest that T_{crit} exceeds our estimates by less than 10%. It can be seen from the graph that, at the highest masses, T_{crit} is down to half of the Eddington limiting temperature and hence that L_{crit} is $1/16 L_{edd}$ for a given emitting area.

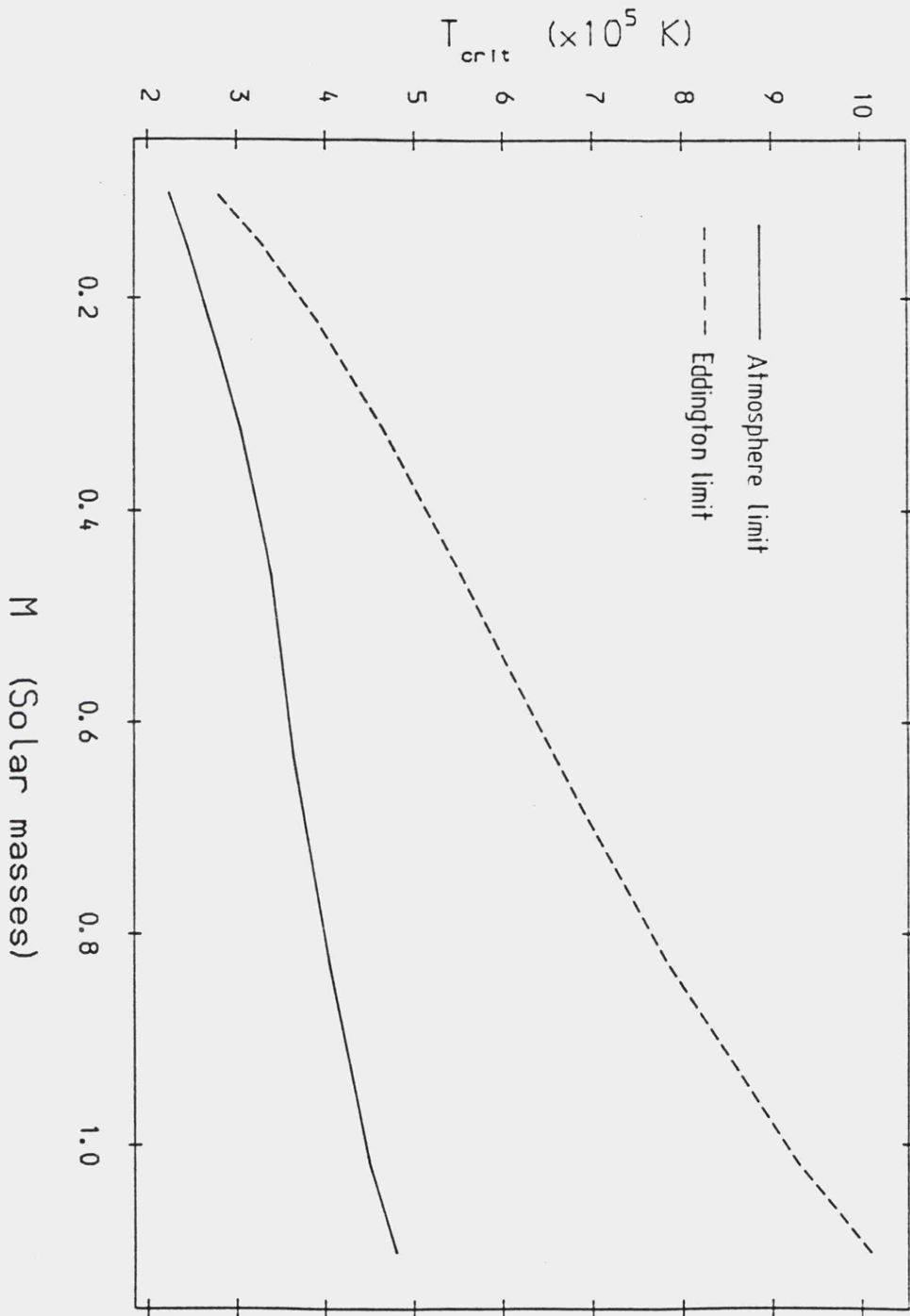


Figure 4.13 Variation of the critical temperature, T_{crit} , with white dwarf mass, M . The Eddington limit for a stable atmosphere is shown by the dashed line.

It is not uncommon to see values for T_{eff} quoted in literature which exceed T_{crit} for the assumed white dwarf mass by appreciable amounts and are therefore physically unreasonable. These generally result from black body fits for which no self-consistent treatment of the hydrostatic equilibrium of the polecap is required. Sometimes this procedure is claimed to be justified, on the grounds that for the inferred T_{eff} , the photospheric pressure implies a Kramers' opacity below the electron scattering value, and hence that bound-free and free-free processes are negligible. This is clearly questionable as Figure 4.13 shows that, for accreting white dwarfs, neglect of bound-free and free-free processes is never justified when considering radiation pressure. We will encounter these limiting temperatures again in Chapter 7, when calculating accretion disc spectra for active galactic nuclei (AGN's).

In the discussion above I mentioned that most observational fitting is done using black bodies. We have seen how different model atmosphere spectra are from a black body spectra and therefore it must be assumed that observational spectra are different in the same way. Fitting these spectra with black bodies is clearly wrong, but how wrong? By using model atmosphere spectra as 'observed' spectra and fitting black bodies to them, in a similar way as with observed spectra, it is possible to find how large the errors are in the inferred values for the effective temperature and luminosity of a particular object. This is the subject of the next chapter.

¹ The curve for $g=1.0 \times 10^8 \text{ cm s}^{-1}$ was calculated with a different lower frequency limit. The upper optical/UV frequency limit is not constant with gravity and so the lower X-ray frequency limit can vary with g . In any case the variations at low X-ray frequencies may only be due to 'rounding' errors introduced by the computer in solving the transfer equation with these low (compared to the optical/UV region) fluxes.

² The limb brightening of the scattered hard X-ray albedo component is due to the increase in the scattering depth along the direction of a ray seen at the limb. The scattering is proportional to this depth and so the albedo component is limb brightened.

CHAPTER 5

BLACK BODY FITS TO MODEL ATMOSPHERE SPECTRA

5.1 Introduction

In Chapter 1 I discussed the general problem associated with black bodies and the spectral fitting of the soft X-ray continuum from a radiative column, namely the loss of information due to interstellar absorption. The use of model atmosphere spectra in the fitting of this component will not resolve this general problem but it should provide a more accurate method of spectral fitting. The differences between black body spectra and model atmosphere spectra were clearly shown in the previous chapter. Despite these obvious differences black bodies have nearly always been used in the fitting of observed spectra. Since we expect a model atmosphere to give a better overall estimate of the spectral shape the continued use of black bodies as fitting 'tools' is clearly erroneous. Of course, black bodies have one great advantage over model atmospheres, for a given effective temperature they are quick and easy to calculate and therefore make repeated spectral fitting a much faster process. What is needed is a method of 'correcting' the fitted black body parameters to the values that would have been found had model atmosphere spectra been used. This correction function could take the form of a calibration graph so that the 'true' values for the effective temperature and emitting area of the polecap can be found from the black body ones. This calibration graph can be found by fitting black body spectra, as a simulation of observational fitting, to model atmosphere spectra. The derivation of such a graph is the subject of this chapter. It should be noted that black

body fitting to model atmosphere spectra is not a new idea; Heise (1982) carried out extensive work in this area and found that the implied black body temperature nearly always exceeded the model atmosphere value. We expected that a similar result would be found in this work.

5.2 Black body fitting - the method

Black body spectra were fitted to the model atmosphere data in the soft X-ray range. The fits were restricted to an energy range $E_1 \leq E \leq E_2$, where E_2 was chosen to be the last frequency point in the optical/UV region of the atmosphere model (always less than 2.5 keV). E_1 was chosen so as to represent the effects of instrumental and/or interstellar cutoffs (interstellar absorption of soft X-rays will be discussed in more detail in the next chapter). The values chosen were; $E_1 = 0.03, 0.06$ and 0.10 keV. The cutoff at 0.03 keV represents the low energy limit on the EXOSAT (European X-ray Observatory Satellite) Low Energy Detector (also to be discussed in more detail in the next chapter); the other two values represent the same but with varying degrees of interstellar absorption present. Figure 5.1 shows how these cutoffs relate to two different model atmosphere spectra, $T_{eff} = 1.0 \times 10^5$ and 3.0×10^5 K. Note that the 0.03 keV cutoff lies the other side of the HeII absorption feature from the other two, the effect of this on the fitting will become apparent later.

To simulate the finite dynamic range of an X-ray detector, fluxes less than 1.0% of the peak value in the range $E_1 \leq E \leq E_2$ were removed from the fit. Constant errors

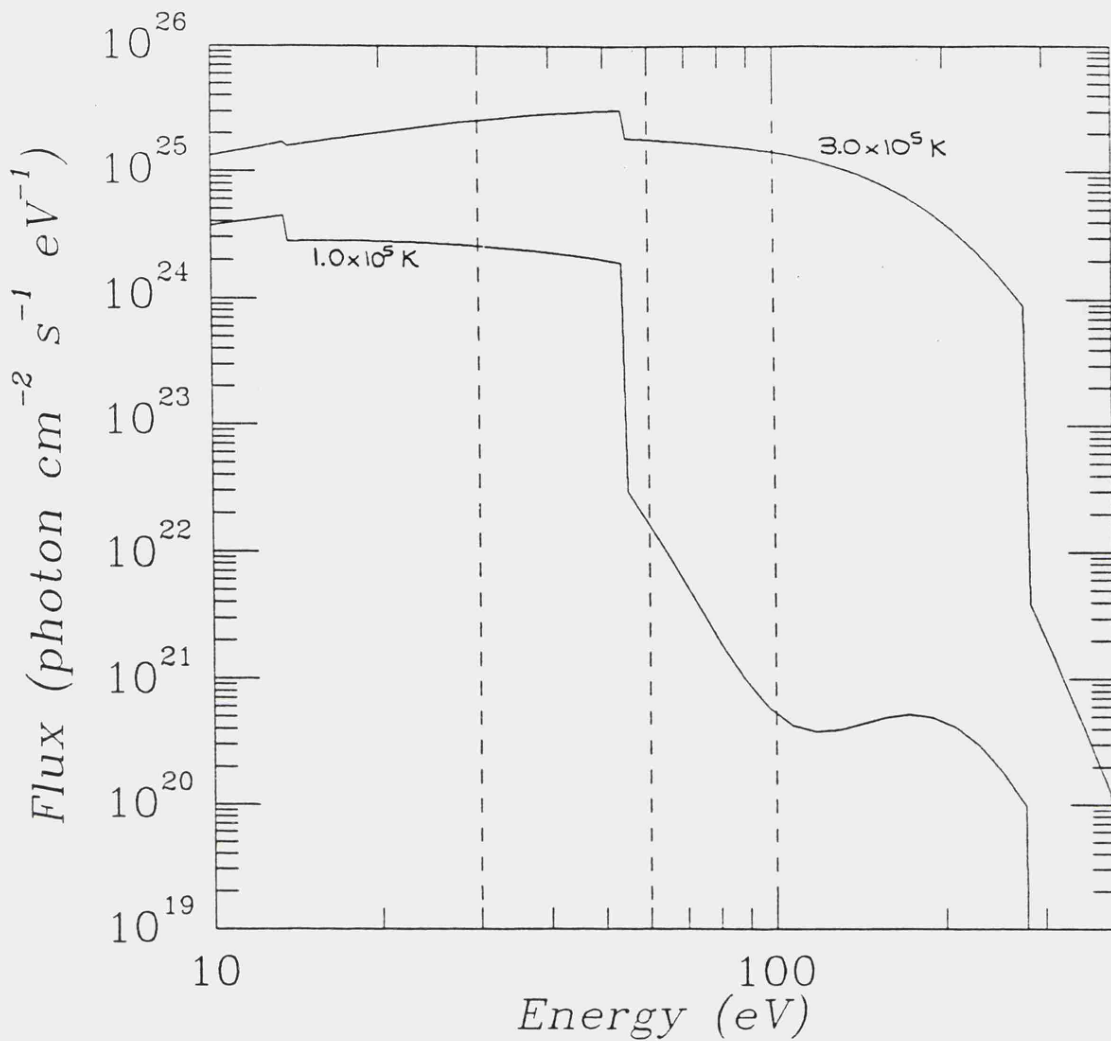


Figure 5.1 Position of the three cutoffs used in the black body fitting shown in relation to two model atmosphere spectra ($T_{\text{eff}} = 1.0 \times 10^5$ K and 3.0×10^5 K). The cutoffs at 0.03, 0.06 and 0.10 keV are shown by the dashed lines.

of 1.0% of the peak flux were then assigned to the remaining points in the energy range. The distance to the 'source' was kept fixed so that the normalisation of the black body used in the fit, C_{norm} , could be related to the fractional emitting area, f_{bb} by,

$$(f_{\text{bb}}/f) = C_{\text{norm}} \quad (5.1)$$

where f is the fractional emitting area assumed for the model atmosphere.

The black body fitting was therefore a two parameter fit of $C_{norm} T_{bb}$ versus T_{eff} . The position of the minimum chi-squared was found in a grid of 20x20 effective temperatures and normalisation constants. The region around this fit was then expanded and the minimum found again; thus allowing the fitted parameters to be found to an accuracy of better than 1.0%. One solar mass models were used throughout, the full parameter range of effective temperature and percentage of illumination being fitted. The results of this are presented in the next section.

5.3 Black body fitting - the results

Tables 5.1 to 5.6 show the results of fitting black bodies to each effective temperature for five different illumination strengths using the three cutoffs. All the fitted values have uncertainties of less than 1.0%. In some cases, i.e., low effective temperatures and high cutoffs, the fit was only done over three points so the corresponding values of chi-squared are low for these (it was felt that the calculation of reduced chi-squares was unnecessary since, for a given effective temperature, illumination and cutoff, the number of degrees of freedom in the fit is constant). The fitted luminosity ratio was calculated from,

$$(L_{bb}/L_{atmos}) = (f_{bb}/f) T_{bb}^4 / T_{eff}^4 \quad (5.2)$$

Table 5.1 Results of black body fitting for $T_{eff} = 5.0 \times 10^4$ K

Cutoff (keV)	P_{ill} (%)	T_{bb} ($\times 10^4$ K)	(f_{bb}/f)	(L_{bb}/L_{atmos})	χ^2
0.03	99.9	7.917	0.0687	0.4320	4.298×10^3
0.03	50.0	7.778	0.0774	0.4532	5.927×10^3
0.03	10.0	8.278	0.0600	0.4508	5.876×10^3
0.03	1.00	8.056	0.0687	0.4630	6.713×10^3
0.03	0.01	8.056	0.0687	0.4630	6.740×10^3
0.06	99.9	4.000	0.8222	0.3368	6.013×10^{-2}
0.06	50.0	4.000	0.8056	0.3300	4.187×10^{-2}
0.06	10.0	4.000	0.8222	0.3368	6.065×10^{-2}
0.06	1.00	4.000	0.8278	0.3391	1.587×10^{-2}
0.06	0.01	4.000	0.8278	0.3391	2.466×10^{-2}
0.10	99.9	4.000	1.0111	0.4141	1.046
0.10	50.0	4.000	0.9778	0.4005	9.980×10^{-1}
0.10	10.0	4.000	1.0056	0.4119	1.003
0.10	1.00	4.000	1.0111	0.4141	1.006
0.10	0.01	4.000	1.0111	0.4141	1.024

Table 5.2 Results of black body fitting for $T_{eff} = 1.0 \times 10^5$ K

Cutoff (keV)	P_{ill} (%)	T_{bb} ($\times 10^5$ K)	(f_{bb}/f)	(L_{bb}/L_{atmos})	χ^2
0.03	99.9	1.444	0.3278	1.4252	5.952×10^3
0.03	50.0	1.501	0.2953	1.4989	5.959×10^3
0.03	10.0	1.530	0.2778	1.5223	5.966×10^3
0.03	1.00	1.558	0.2691	1.5856	5.973×10^3
0.03	0.01	1.558	0.2691	1.5856	5.972×10^3
0.06	99.9	0.706	0.9389	0.2327	724.2
0.06	50.0	0.706	0.8278	0.2052	1.888×10^3
0.06	10.0	0.706	0.7778	0.1923	4.372×10^3
0.06	1.00	0.700	0.8333	0.2001	5.238×10^3
0.06	0.01	0.700	0.8333	0.2001	5.340×10^3
0.10	99.9	1.161	0.0222	0.0403	4.924×10^4
0.10	50.0	1.161	0.0222	0.0403	4.863×10^4
0.10	10.0	1.161	0.0222	0.0403	4.740×10^4
0.10	1.00	1.161	0.0222	0.0403	4.738×10^4
0.10	0.01	1.161	0.0222	0.0403	4.738×10^4

Table 5.3 Results of black body fitting for $T_{eff} = 1.5 \times 10^5$ K

Cutoff (keV)	P_{ill} (%)	T_{bb} ($\times 10^5$ K)	(f_{bb}/f)	(L_{bb}/L_{atmos})	χ^2
0.03	99.9	1.358	1.4444	0.9703	5.915×10^3
0.03	50.0	1.358	1.4222	0.9554	6.218×10^3
0.03	10.0	1.358	1.4111	0.9480	6.452×10^3
0.03	1.00	1.358	1.4056	0.9443	6.505×10^3
0.03	0.01	1.358	1.4056	0.9443	6.511×10^3
0.06	99.9	2.100	0.1036	0.3980	2.466×10^3
0.06	50.0	2.982	0.0247	0.3858	1.374×10^3
0.06	10.0	3.283	0.0174	0.3993	2.030×10^3
0.06	1.00	3.369	0.0156	0.3970	2.197×10^3
0.06	0.01	3.412	0.0150	0.4016	2.214×10^3
0.10	99.9	2.508	0.0556	0.4345	1.727×10^3
0.10	50.0	2.642	0.0444	0.4273	3.744×10^3
0.10	10.0	2.508	0.0600	0.4689	8.862×10^3
0.10	1.00	2.592	0.0513	0.4574	9.103×10^3
0.10	0.01	2.600	0.0513	0.4631	9.229×10^3

Table 5.4 Results of black body fitting for $T_{eff} = 2.0 \times 10^5$ K

Cutoff (keV)	P_{ill} (%)	T_{bb} ($\times 10^5$ K)	(f_{bb}/f)	(L_{bb}/L_{atmos})	χ^2
0.03	99.9	1.922	0.8611	0.7344	5.617×10^3
0.03	50.0	1.900	0.8667	0.7059	6.533×10^3
0.03	10.0	1.889	0.8611	0.6853	7.426×10^3
0.03	1.00	1.889	0.8556	0.6809	7.650×10^3
0.03	0.01	1.889	0.8556	0.6809	7.676×10^3
0.06	99.9	3.289	0.0938	0.6860	282.9
0.06	50.0	3.287	0.0949	0.6924	1.533×10^3
0.06	10.0	3.356	0.0861	0.6826	3.395×10^3
0.06	1.00	3.356	0.0861	0.6826	4.150×10^3
0.06	0.01	3.356	0.0861	0.6826	4.240×10^3
0.10	99.9	3.461	0.0764	0.6851	16.59
0.10	50.0	4.034	0.0410	0.6786	6.946
0.10	10.0	4.492	0.0280	0.7125	21.76
0.10	1.00	4.607	0.0259	0.7292	22.15
0.10	0.01	4.607	0.0259	0.7292	21.05

Table 5.5 Results of black body fitting for $T_{eff} = 2.5 \times 10^5$ K

Cutoff (keV)	P_{ill} (%)	T_{bb} ($\times 10^5$ K)	(f_{bb}/f)	(L_{bb}/L_{atmos})	χ^2
0.03	99.9	2.972	0.3998	0.7985	5.897×10^3
0.03	50.0	3.153	0.3214	0.8132	7.729×10^3
0.03	10.0	3.319	0.2691	0.8356	9.632×10^3
0.03	1.00	3.389	0.2517	0.8500	1.011×10^4
0.03	0.01	3.389	0.2517	0.8500	1.017×10^4
0.06	99.9	3.681	0.1733	0.8145	324.7
0.06	50.0	4.254	0.1036	0.8685	359.2
0.06	10.0	4.684	0.0774	0.9538	795.4
0.06	1.00	4.684	0.0774	0.9538	880.9
0.06	0.01	4.684	0.0774	0.9538	895.5
0.10	99.9	3.667	0.1820	0.8425	166.4
0.10	50.0	4.028	0.1297	0.8741	471.1
0.10	10.0	4.222	0.1123	0.9135	1.359×10^3
0.10	1.00	4.431	0.0949	0.9365	1.067×10^3
0.10	0.01	4.431	0.0949	0.9365	1.104×10^3

Table 5.6 Results of black body fitting for $T_{eff} = 3.0 \times 10^5$ K

Cutoff (keV)	P_{ill} (%)	T_{bb} ($\times 10^5$ K)	(f_{bb}/f)	(L_{bb}/L_{atmos})	χ^2
0.03	99.9	3.950	0.2953	0.8875	4.959×10^3
0.03	50.0	4.283	0.2256	0.9372	6.952×10^3
0.03	10.0	4.517	0.1907	0.9801	9.141×10^3
0.03	1.00	4.600	0.1820	1.0060	9.691×10^3
0.03	0.01	4.600	0.1820	1.0060	9.765×10^3
0.06	99.9	4.367	0.1994	0.8953	125.5
0.06	50.0	4.717	0.1558	0.9522	437.7
0.06	10.0	5.017	0.1297	1.0145	1.162×10^3
0.06	1.00	5.017	0.1297	1.0145	1.642×10^3
0.06	0.01	5.133	0.1210	1.0370	1.255×10^3
0.10	99.9	4.400	0.1944	0.8995	32.34
0.10	50.0	4.733	0.1558	0.9652	291.6
0.10	10.0	5.033	0.1297	1.0275	918.4
0.10	1.00	5.150	0.1210	1.0508	980.5
0.10	0.01	5.150	0.1210	1.0508	1.020×10^3

As can be seen from the tables the results for the illuminations of 1.0% and 0.01% are exactly the same in almost all cases. This was to be expected as we saw in the previous chapter the similarity of these two spectra. The data presented in the table is shown graphically in Figures 5.2 to 5.5 for $P_{ill} = 99.9, 50.0, 10.0, 1.0\%$ respectively. The fitted curves have been interpolated as best as possible from the limited fitting data but the general trends are clear. It is possible to draw two conclusions from the figures :

- (i) the fitted variations are much smoother for illuminated atmospheres compared to non-illuminated ones;
- (ii) except for very low cutoffs, black bodies systematically overestimate the effective temperature (up to a factor of two) and underestimate the emitting area (up to a factor of fifty), compared with the true values. The relative luminosities are however somewhat better estimated for $T_{eff} > 1.5 \times 10^5$ K (less than a factor of two, depending on the illumination strength). As T_{eff} increases the fitted luminosity approaches the correct value for all cutoffs and illuminations. Below $T_{eff} < 1.5 \times 10^5$ K the fitted luminosity varies quite strongly with the cutoff used and can be underestimated by as much as a factor of 25 or more.

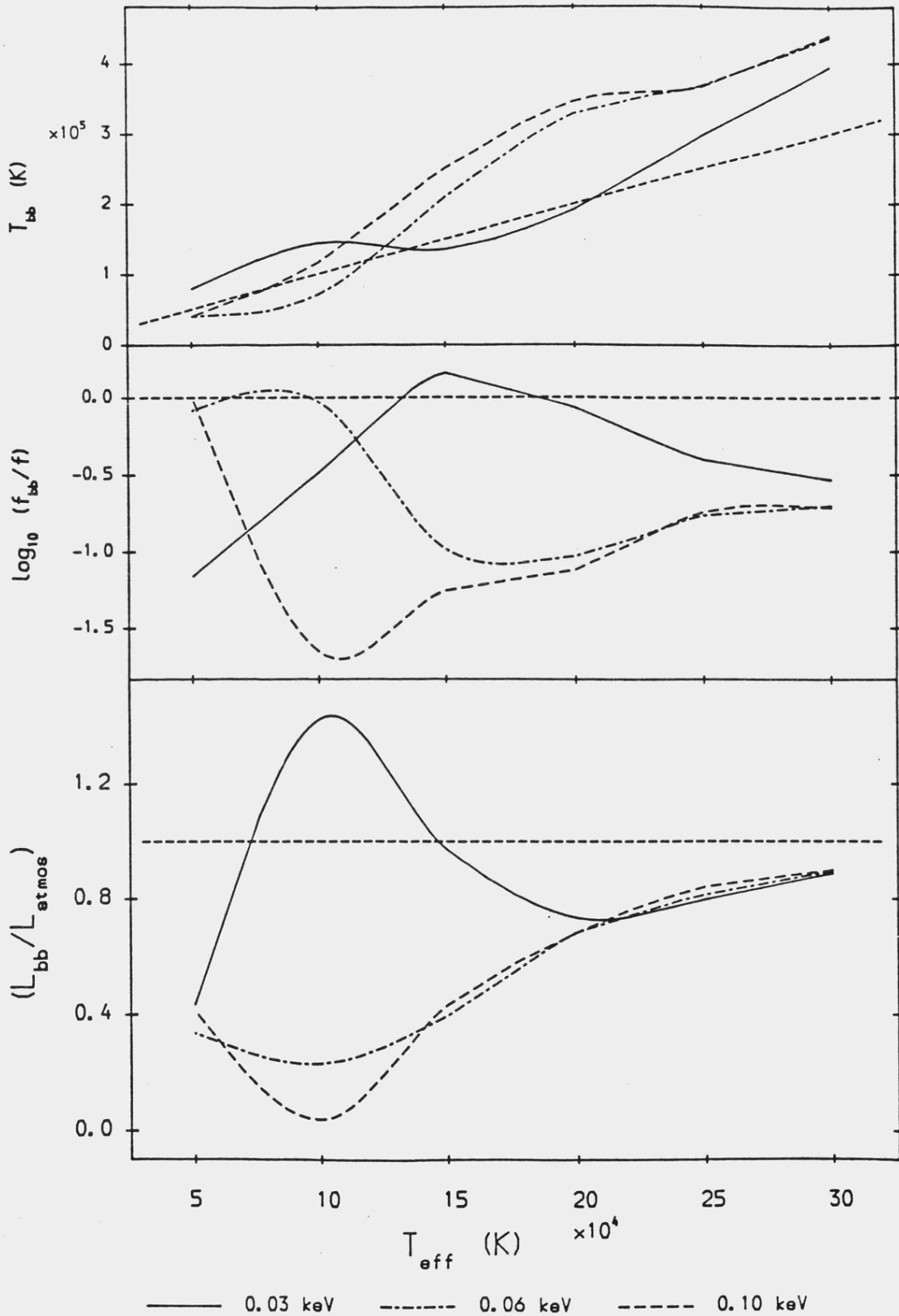


Figure 5.2 Fitted black body parameters plotted as a function of T_{eff} for model atmospheres with $P_{\text{ill}} = 99.9\%$.

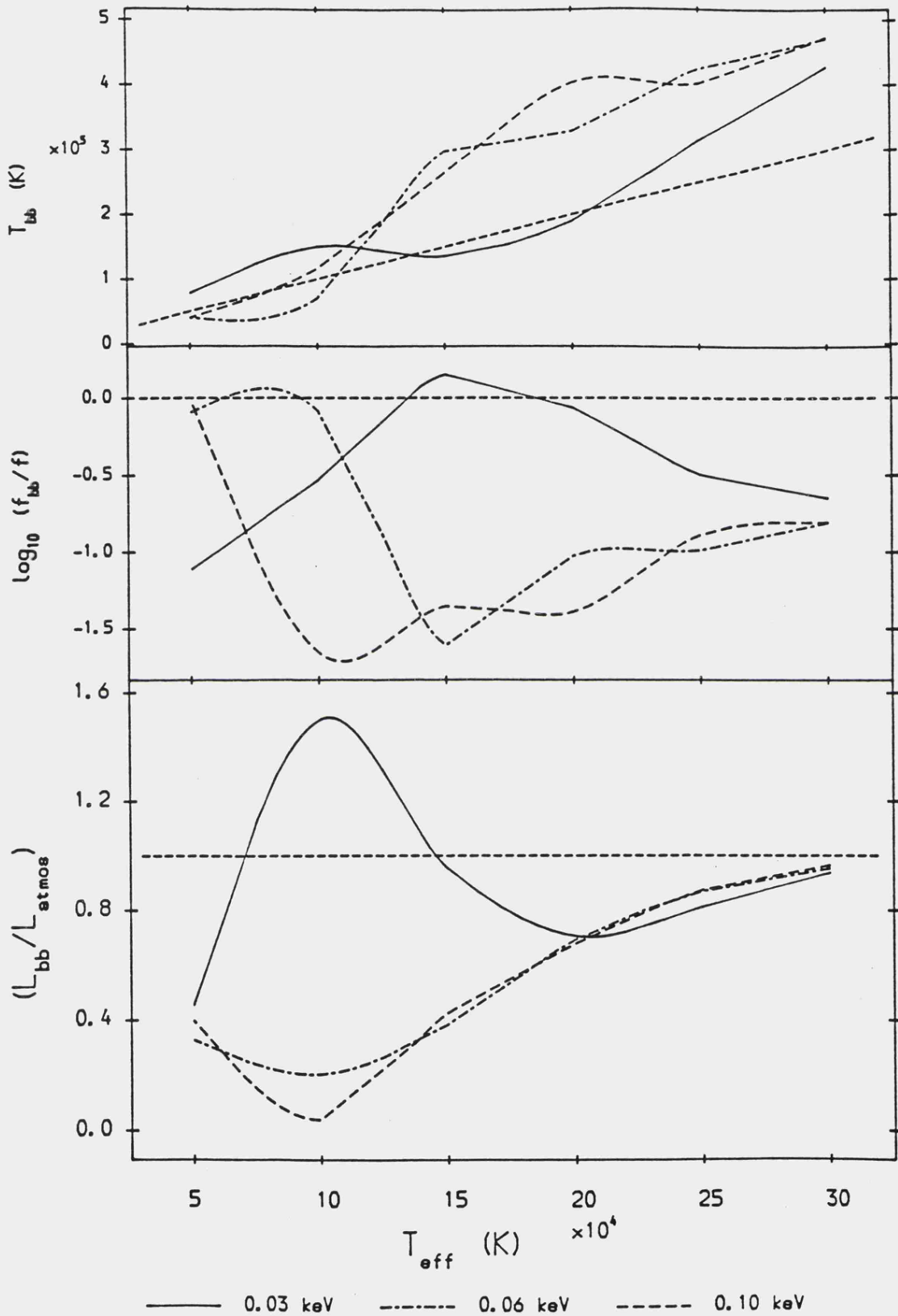


Figure 5.3 Fitted black body parameters plotted as a function of T_{eff} for model atmospheres with $P_{\text{ill}} = 50.0\%$.

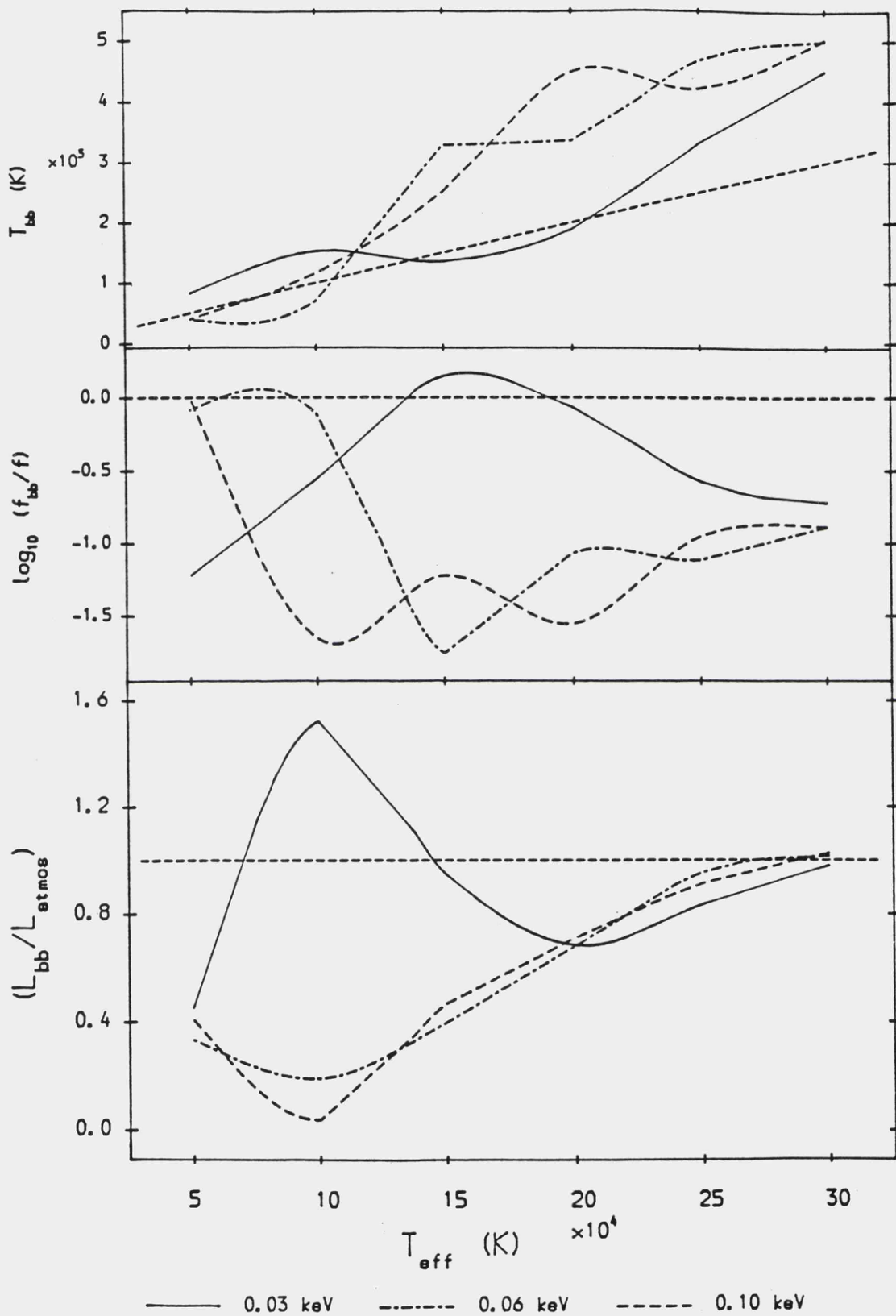


Figure 5.4 Fitted black body parameters plotted as a function of T_{eff} for model atmospheres with $P_{\text{ill}} = 10.0\%$.

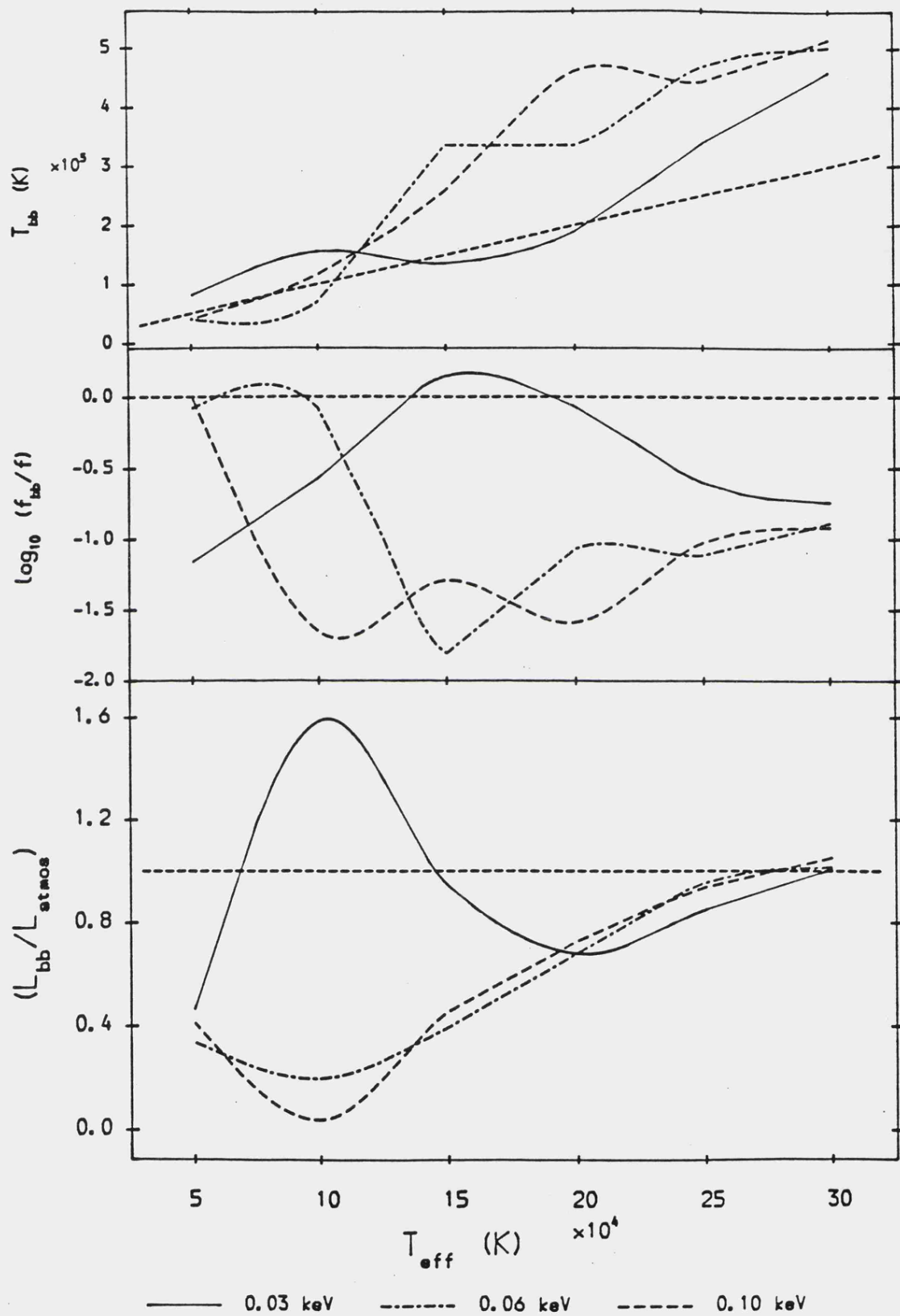


Figure 5.5 Fitted black body parameters plotted as a function of T_{eff} for model atmospheres with $P_{\text{ill}} = 1.0\%$.

These results are easy to understand. First, the result (i) is expected due to the flatter temperature gradient of the atmosphere producing a softer, more black body like soft X-ray continuum. Secondly, result (ii) is expected as in this region of the spectrum an atmosphere is slightly harder than a black body (the 'hump' seen in some figures in the previous chapter occurs in precisely this fitting region and may go some way to explain the strong variations in the fitted parameters for $T_{eff} = 1.0 \times 10^5$ K). This forces the fitted temperature T_{bb} above T_{eff} . To compensate for the now higher absolute flux at a fixed distance, f_{bb} is forced down below f . This tends to compensate for the rise in T_{bb} so as to bring the luminosity close to the true value. The different behaviour with the 0.03 keV cutoff is due to the presence of the HeII absorption feature at ~ 54 keV. For low effective temperatures this dominates the spectrum and forces T_{bb} to be low. The reverse of the above argument forces f_{bb} above f , again tending to compensate the luminosity estimates. It should be noted that this cutoff could only occur for unusually low interstellar column densities and therefore the more realistic fits are for the two higher cutoffs above the HeII edge. Some examples of the black body fits are shown in Figures 5.6 to 5.9; for $T_{eff} = 1.0 \times 10^5$ and 3.0×10^5 K, $P_{ill} = 99.9$ and 1.0% and for cutoffs at 0.03 and 0.06 keV. These show quite clearly that the best fitting black bodies do not really give a good approximation to the true spectrum in this restricted spectral region.

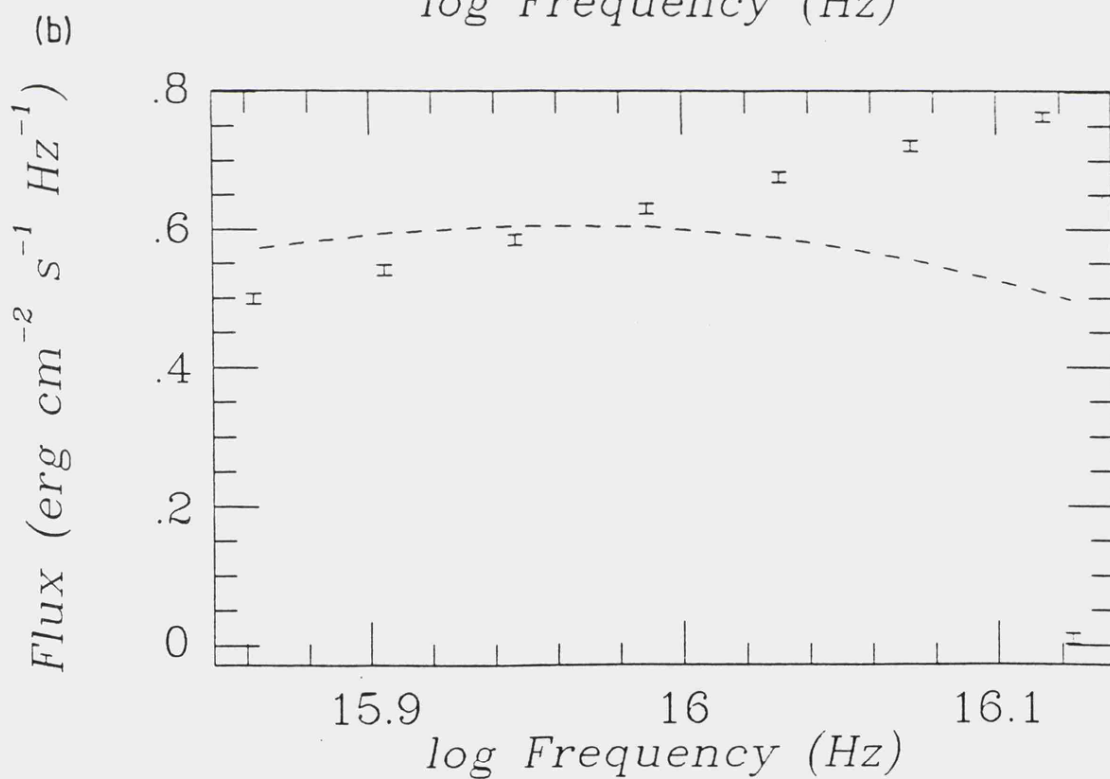
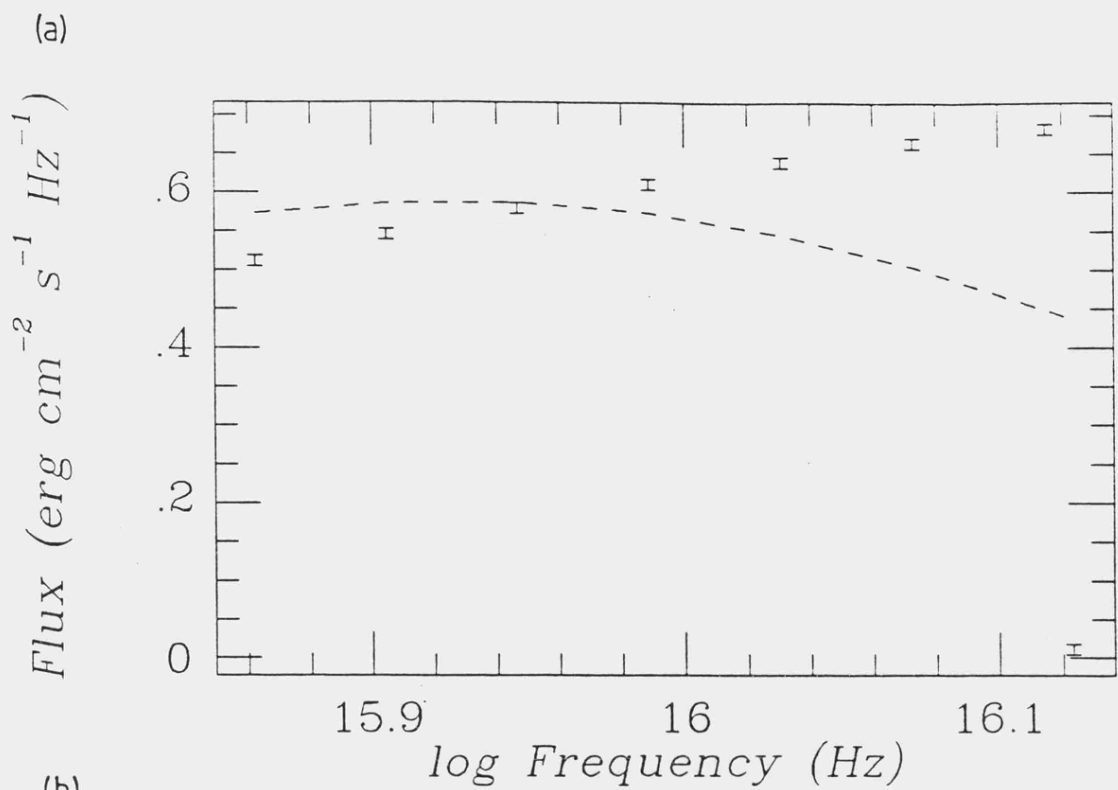


Figure 5.6 Representative black body fits for a cutoff at 0.03 keV; (a) $T_{\text{eff}} = 1.0 \times 10^5$ K, $P_{\text{ill}} = 99.9\%$ and (b) $T_{\text{eff}} = 1.0 \times 10^5$ K, $P_{\text{ill}} = 1.0\%$. The 1.0% error bars are shown on the atmosphere data points, the best fitting black body is shown by the dashed line.

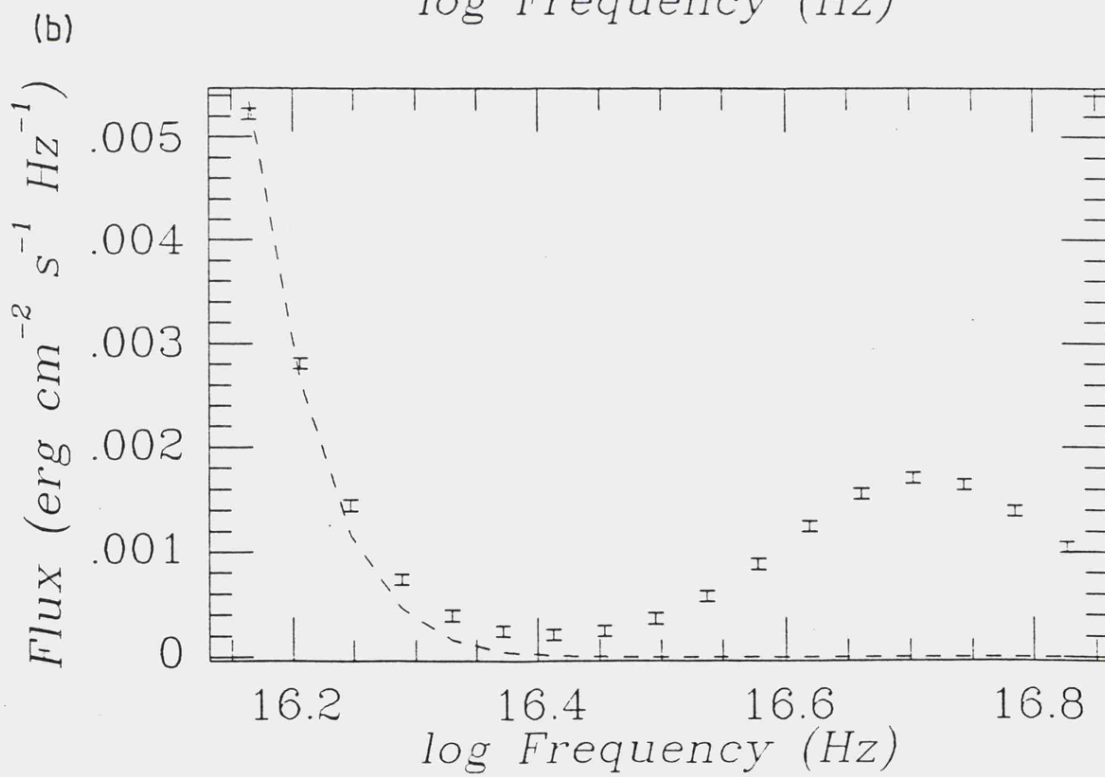
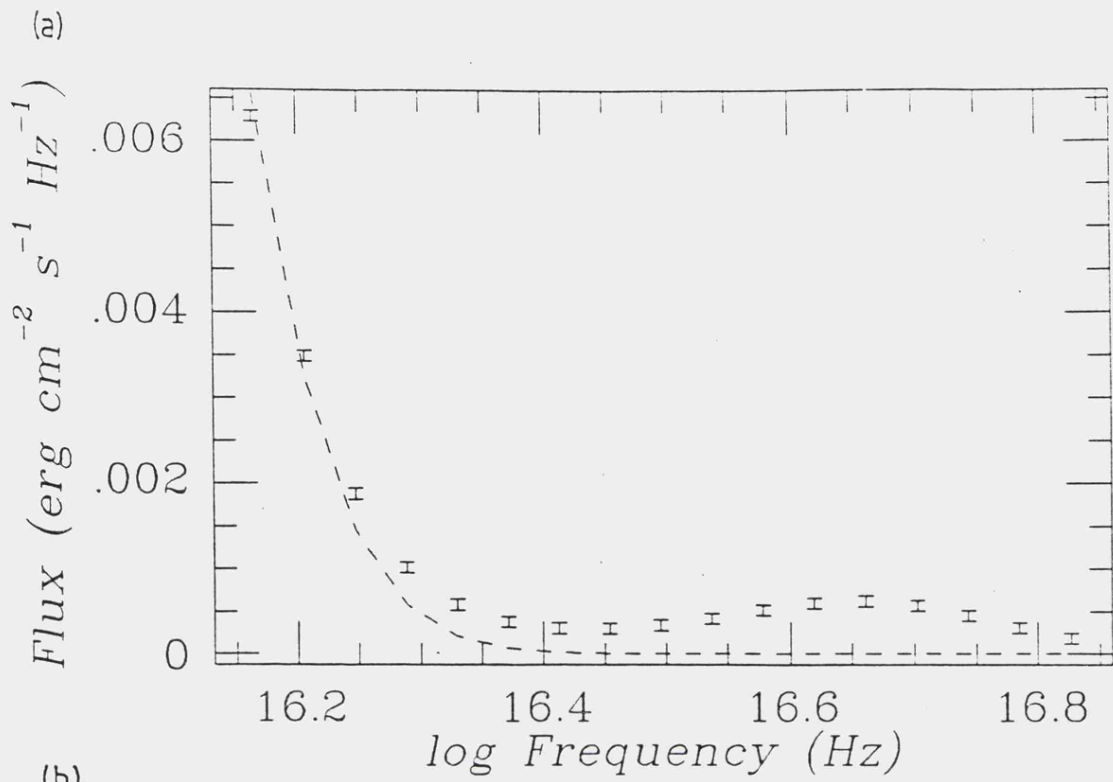


Figure 5.7 As for Figure 5.6 but for a cutoff at 0.06 keV.

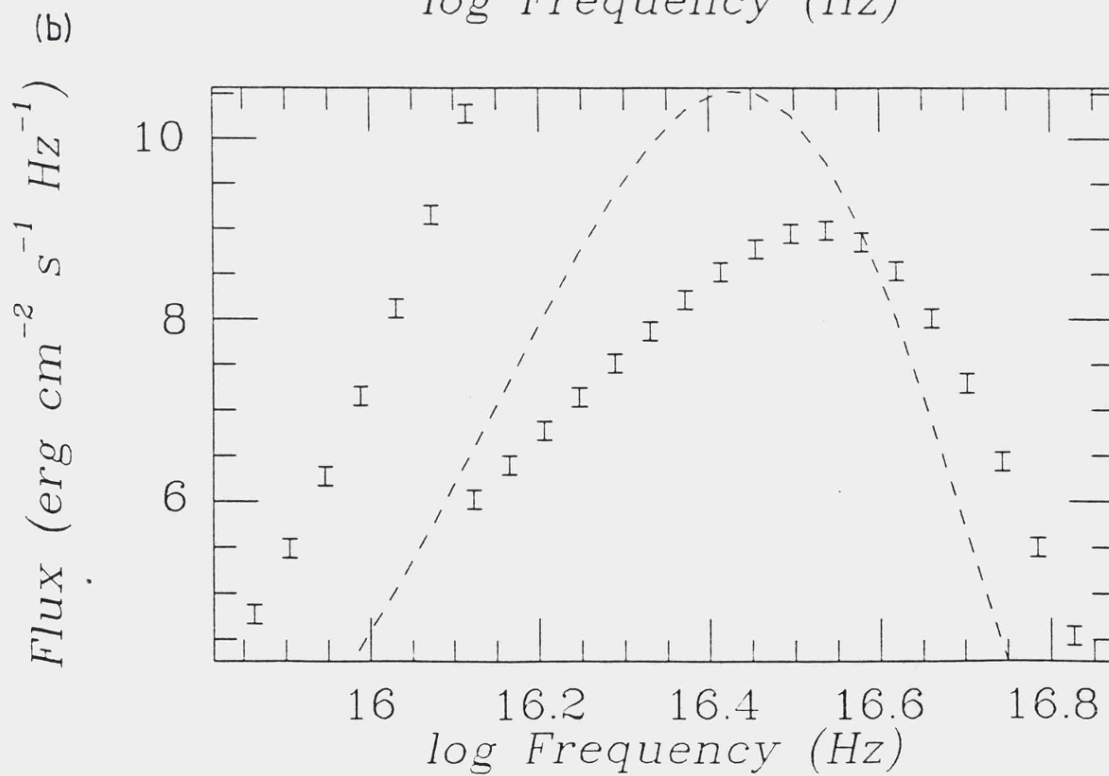
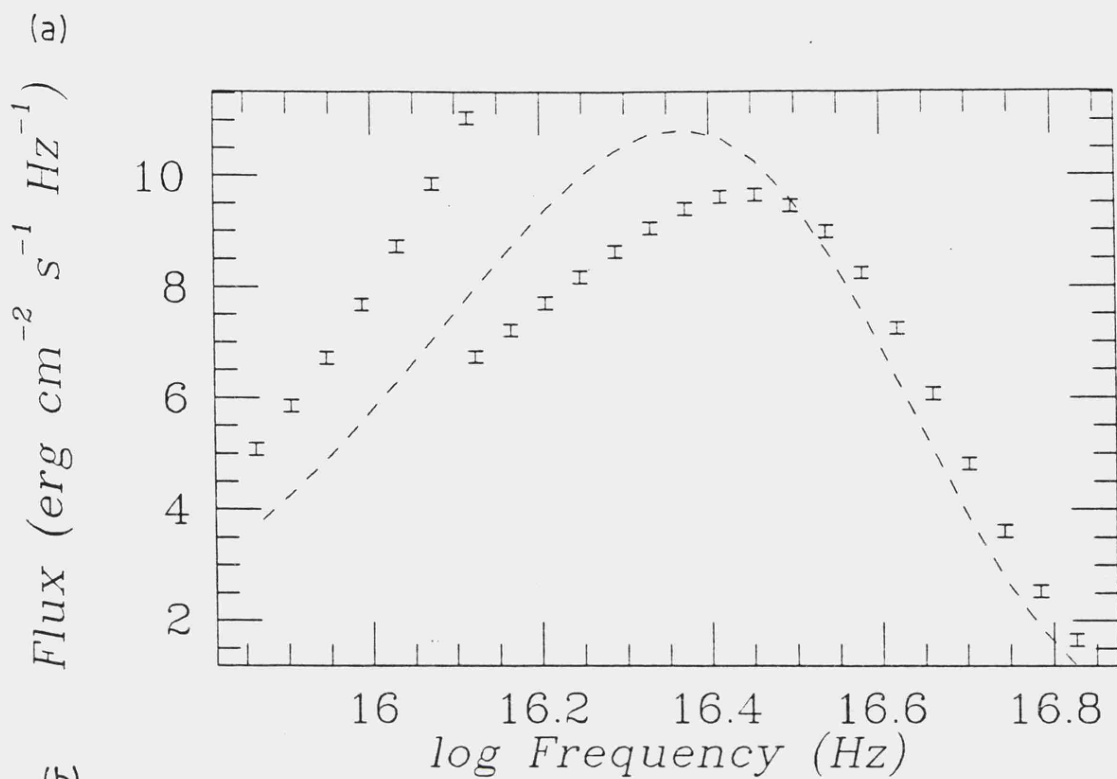


Figure 5.8 Representative black body fits for a cutoff at 0.03 keV; (a) $T_{\text{eff}} = 3.0 \times 10^5$ K, $P_{\text{ill}} = 99.9\%$ and (b) $T_{\text{eff}} = 3.0 \times 10^5$ K, $P_{\text{ill}} = 1.0\%$.

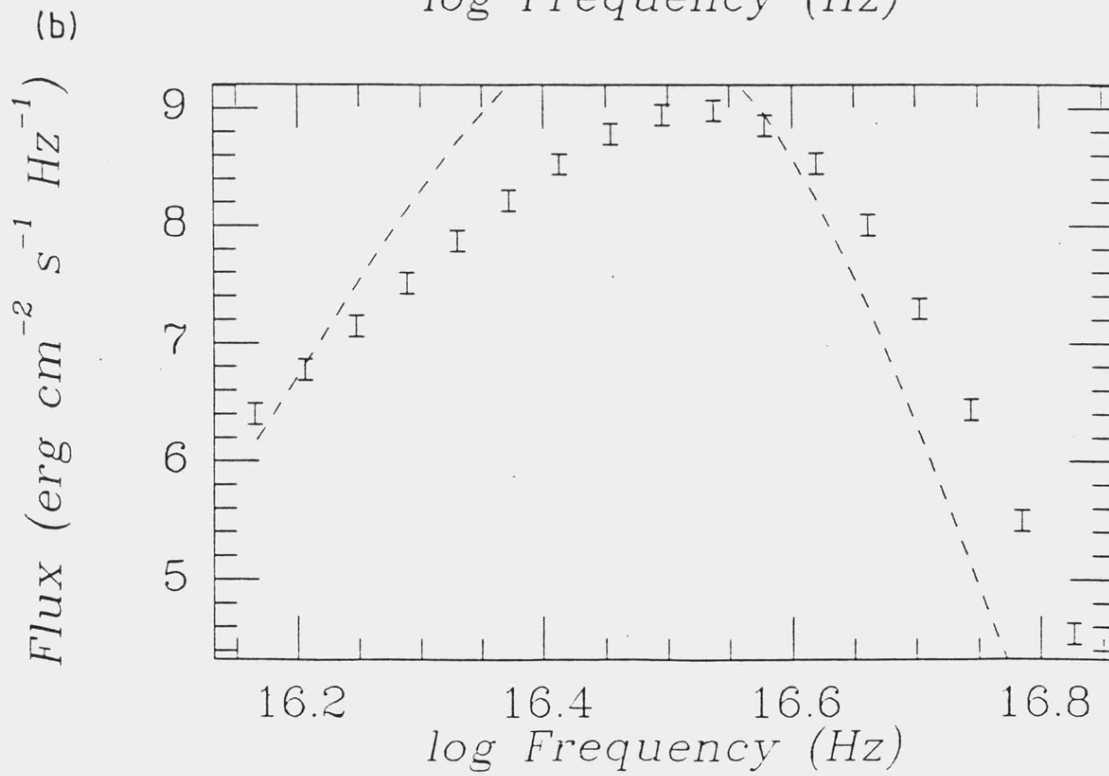
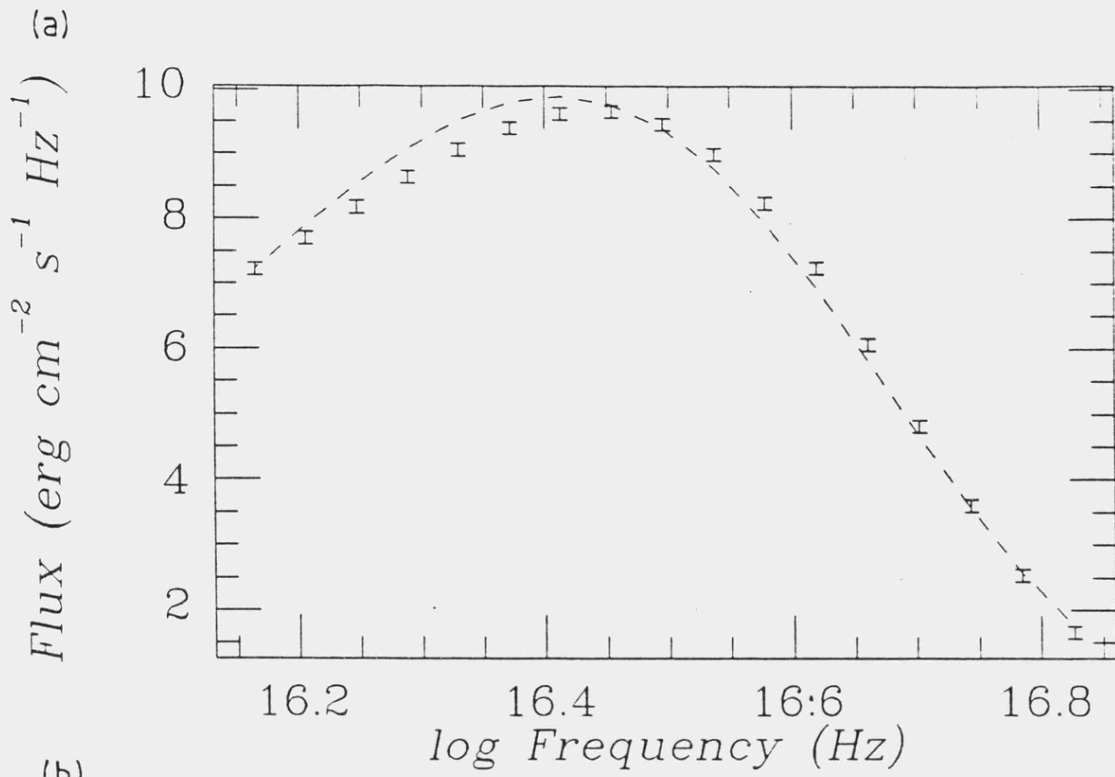


Figure 5.9 As for Figure 5.8 but for a cutoff at 0.06 keV.

5.4 Conclusions

The results of this black body fitting have shown that while a black body tends to overestimate the effective temperature of a source it compensates by underestimating the emitting area. The result of this is that the luminosity, over most of the effective temperature range, tends to be within a factor of two of the correct value. As was hoped, the results of Heise's black body fitting to model atmospheres were reproduced correctly here, namely the overestimation of the effective temperature.

The accuracy of the fitted luminosity increased with effective temperature, this is due to the spectrum becoming more black body like at higher temperatures. The error in the fitted effective temperature was up to factor of two at the highest temperatures, this error could become important in the fitting of lightcurves as the emitting area is fixed by geometry and therefore any error in the fitted temperature can wildly affect the fitted luminosity. The fact that the fitted black body luminosities are surprisingly close to the correct values (for reasonable cutoffs and effective temperatures) for the soft X-ray components strongly suggests that the soft X-ray excess is unlikely to disappear as a result of more accurate spectral fitting. Indeed, since L_{bb} is usually below L_{atmos} in these fits we can expect even larger excesses from these systems when model atmospheres are used for fitting.

The initial aim of this black body fitting was to find a means of 'calibrating' fitted black body values to atmospheric values. Calibration graphs have been found in

the course of this fitting but in some cases a particular black body temperature corresponds to up to three different atmosphere temperatures ! This, plus the fact that the cutoffs used in the fitting do not accurately model the effects of interstellar absorption (we will see in the next chapter that the absorption cutoff is not sharp), means that these graphs cannot really be used for their original purpose; however, the fitting of black bodies to model atmosphere spectra has given us an insight into the errors associated with observational fitting and therefore these results should not be ignored. Definite improvements in accuracy, especially concerning the fitted effective temperature, could be made by using model atmospheres to fit observational data. It is hoped that in the future grids of these model atmospheres could become available for use by anyone needing to carry out spectral fitting of AM Herculis systems. The results of convolved spectral fitting of AM Herculis will be seen in the next chapter when I discuss the calculation and use of lightcurves.

CHAPTER 6

SIMULATION OF LIGHTCURVES

6.1 Introduction

In a magnetic polar system the white dwarf primary revolves, synchronously with its rotation, around the late-type secondary star. As it rotates we will see varying amounts of the polecap's surface, in some cases the polecap will be eclipsed by the companion completely; at the other extreme it may always be visible.

In this chapter I will describe the calculation of a simulated lightcurve and the general features produced. Using these model lightcurves I carried out a full parameter fit to the EXOSAT soft and hard X-ray lightcurves of AM Herculis; the results of this are contained within.

6.2 X-ray lightcurves from magnetic polars

In Chapter 1 we saw that the X-ray emission from a magnetic polar has two components. The hard X-ray (2-10 keV) component comes from the shock region above the polecap, with a small reflected component from the photosphere below, and is of thermal bremsstrahlung form with a characteristic temperature of approximately 10^8 K. The soft X-ray component (<2 keV) comes from the optically thick photosphere itself and was previously assumed to be of black body form, at a temperature of a few 10^5 K.

Throughout this chapter I will consider a system where the primary is not occulted by the secondary. If we consider the types of emission seen from the white dwarf polecap we have that the hard X-ray emission is an optically thin, isotropic, thermal bremsstrahlung so the

observed intensity at any moment is directly proportional to the volume of the emission region visible to the observer. It follows that any modulation of the hard X-rays at the white dwarf spin period can only be the result of the white dwarf body obscuring parts of the emission region. The soft X-rays, however, come from an optically thick region and are automatically modulated at the white dwarf spin rate by the projection effect of the emitting area being at different angles to the observer. If there were occultations by the secondary star they would be characterised by virtually total and very short eclipses in all wavebands, since the emission from the system as a whole is dominated by the primary. Considering each spectral component in turn I will describe the expected shape of these lightcurves.

6.2.1 Hard X-ray lightcurves

Figure 6.1 shows the accretion geometry used throughout this chapter. The magnetic polecap is assumed to subtend an angle β at the centre of the white dwarf and is at an angle m to the rotational axis. The rotational axis is assumed to be perpendicular to the plane of the orbit and is at an angle i to the line of sight. In a one-pole system these angles have the range $0^\circ < m < 180^\circ$ and $0^\circ < i < 90^\circ$. It is assumed that the shock height is very much less than the white dwarf radius so the hard X-ray intensity is proportional to the visible area of the polecap (not the 'projected' visible area). If we neglect the albedo component for the moment then, since photo-

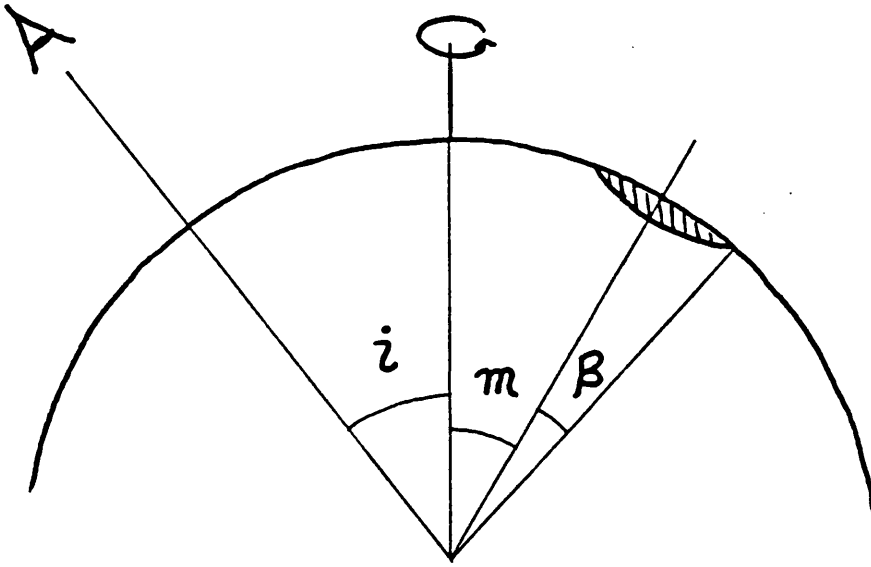


Figure 6.1 The accretion geometry.

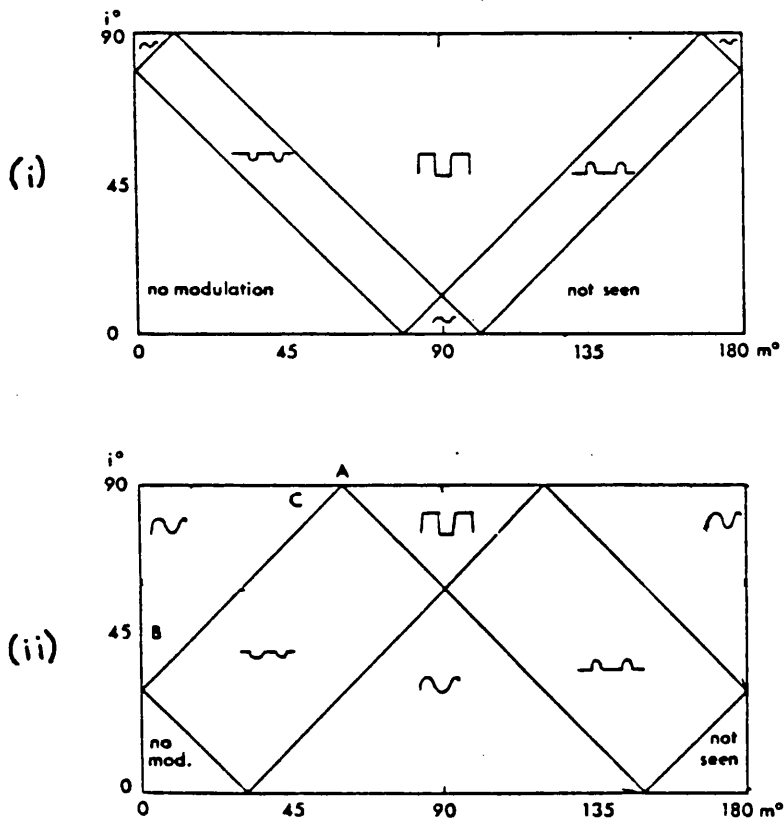


Figure 6.2 Hard X-ray lightcurve shapes as a function of the angles i and m for, (i) $\beta=11.5^\circ$ ($f=10^{-2}$) and (ii) $\beta=60^\circ$ ($f=0.25$). (From King and Shaviv, 1984)

electric absorption is not important at these energies it is easy to calculate the conditions for partial or total occultations, for example, if $i+m-\beta > 90^\circ$ the emitting region will be totally obscured. King and Shaviv (1984) calculated the possible regions in i and m for given lightcurve shapes. Figure 6.2 shows two diagrams (reproduced from their paper) that show the hard X-ray lightcurve shape as a function of i and m for $\beta=11.5^\circ$ ($f=10^{-2}$) and $\beta=60^\circ$ ($f=0.25$). Estimates of the fractional emitting area of the polecap, f , based on assuming the accretion is channelled along field lines from the 'Alfvén point' inwards suggest that f lies in the range $10^{-2} - 10^{-3}$ indicating that 'square wave' (flat top + total eclipse) lightcurves are most likely for these systems. The observational evidence for this will be discussed later.

6.2.2 Soft X-ray lightcurves

In this case the emission is from an optically thick region just below the shock so the observed intensity depends on the projected area visible (limb darkening effects have to be considered as well). For the range of f described above the resultant lightcurves will commonly be sinusoidal in shape but with flat minima. Since at these energies photoelectric absorption is important occultation of the polecap by the accretion stream can cause dips in the observed lightcurve due to the increased column density. King and Williams (1985) discussed this possibility and concluded that short dips in the lightcurve can occur if the polecap is eclipsed by parts of the

accretion stream distant from it. However these dips can only occur for systems with $i > m$. Observational evidence for this is discussed later.

6.2.3 Two pole effects

If the emission from the white dwarf comes from two regions on its surface the hard and soft lightcurves no longer have simple shapes. Depending on the relative strengths of the poles and their separation angle (the magnetic axis may be off-centred) the resultant X-ray lightcurves may have two minima and two maxima; one minimum and one maximum; or show a constant flux. Double poled hard X-ray lightcurves are discussed in more detail in the section dealing with the AM Herculis lightcurve fitting.

6.2.4 Observed lightcurve shapes

There are thirteen known magnetic polars, ten of which have been observed by the European X-ray Observatory Satellite (EXOSAT). Eight of these have had lightcurves published to date; of which only five have observable hard X-ray lightcurves, they are, EF Eridani, V834 Cen (E1405-451), ST LMi (CW1103+254), AM Herculis and QQ Vul (E2003+225). The three polars that have no observable hard X-ray lightcurves are VV Puppis, BL Hyi (HO139-68) and AN Ursae Majoris. The lightcurve shapes for the eight systems are described briefly below. Watson (1986) and Mason (1985) describe these systems in more detail (see also references herein). The actual lightcurves themselves will

not be reproduced here, the reader should consult the above for them.

EF Eridani

The second brightest known source next to AM Herculis. The hard X-ray lightcurve shows a smooth quasi-sinusoidal variation while the soft X-ray lightcurve, although having a similar overall shape, shows large amplitude fluctuations with a prominent absorption dip at phase 0.45 (Watson, et al., 1985). From our previous geometrical arguments we have seen that, for a smooth hard X-ray lightcurve and an assumed polecap area of 10^{-2} of the white dwarf surface, $i+m \approx 90^\circ$ with i close to 90° or 0° . The dip in the soft X-ray lightcurve could be due to occultation by the accretion stream.

VV Puppis

No observable hard X-ray lightcurve. The soft X-ray lightcurve is unusual in that the source is 'off' for over half the binary cycle. It turns 'on' at phase 0.6 and has a gradual rise followed by a sharp fall (Mason, 1985). The short duty cycle can be explained if the active pole is in the hemisphere of the white dwarf that is inclined away from us, for most of the cycle the pole is blocked from view by the body of the white dwarf.

V834 Cen (E1405-451)

The hard X-ray lightcurve shows a quasi-sinusoidal variation similar to that in EF Eri. Like EF Eri the soft X-ray lightcurve shows a prominent dip, at linear polarisation phase 0.27 (Mason, 1985). Interestingly the hard X-ray lightcurve shows a 30% rise at this point (Bonnet-Bidaud et al., 1985). If this dip is due to the

pole going into eclipse then this conflicts with the required geometry for a quasi-sinusoidal hard X-ray lightcurve (King and Shaviv (1984)). Bonnet-Bidaud et al. suggest that this can be explained by assuming that V834 Cen is a two pole system with a 'hard' and 'soft' pole approximately 180° apart. The 'hard' pole comes out of eclipse (hard maximum) at the same time as the 'soft' pole goes into eclipse (soft minimum). They report that this is consistent with the linear polarisation at this phase and that such a geometry could explain the phase changes that have been observed in this system.

BL Hvi (HO139-68)

This source has been seen to have high and low states. There is no observable hard X-ray lightcurve. The soft X-ray lightcurve shows a quasi-sinusoidal shape with no strong absorption dips (Schwope and Beuermann (1985)). Some residual soft X-ray flux is seen at the minimum. If this is due to the pole being almost totally eclipsed then from the values for i and m deduced from the polarisation measurements, i.e., $i=25^\circ \pm 15^\circ$, $m=98^\circ \pm 5^\circ$ (Schwope and Beuermann (1985)), β must lie in the range $13^\circ < \beta < 53^\circ$, in order that the pole is only partially eclipsed. This indicates that the polecap is larger than that usually assumed for polars.

ST LMi (CW1103+254)

Similar to VV Puppis in that the source is 'on' for less than half the cycle indicating that the source is in the lower half of the rotational hemisphere. Both lightcurves have a similar shape with no special features.

AN Ursae Majoris

There is no observable hard X-ray lightcurve. The soft X-ray lightcurve shows complex modulation including absorption dips. Dips may be due to occultations by the accretion stream and the white dwarf body.

AM Herculis

The prototype magnetic polar, being the brightest of the known polars and the most studied. When recently observed using EXOSAT, Heise et al. (1985) found that the relative phasing of the hard and soft X-ray lightcurves had changed by 180°. This is known as its anomalous state and it is characterised by the soft X-rays being eclipsed at a phase corresponding to a maximum of the hard X-ray lightcurve. The soft X-ray minimum lasts longer than that seen in its normal mode (Tuohy et al., 1978) and is non-zero. The hard X-ray eclipses last for approximately 20% of the cycle and are also non-zero. This change in the observed lightcurves almost certainly indicates a drastic change in the geometry of the system; AM Her seems to have changed from a single to a double pole source.

QQ Vul (E2003+225)

Observations by Osborne et al. (1985) show that the source is only just visible in the hard X-ray region. The soft X-ray lightcurve shows two clear minima. One minimum coincides with a minimum of the hard X-ray lightcurve and could possibly be due to occultation by the accretion stream (Osborne et al., 1986a). The second wide minimum seems to coincide with a minimum in the hard X-ray lightcurve and is probably due to the white dwarf body eclipsing the polecap. Osborne et al. (1986a) point out

that this is open to interpretation and indeed a two pole system could reproduce some, if not all, of these effects. Later observations (Osborne et al., 1986b) show dramatic changes to the soft X-ray lightcurve (see also Watson (1986)) which seem to reinforce the possibility that QQ Vul is a two pole system like AM Her.

Conclusions

Four of the eight systems described show strong absorption dips in the soft X-ray lightcurve, possibly due to the accretion stream or, less likely, obscuration by the accretion column itself, although the former is preferred for EF Eri and AN Uma. Of the five sources visible in the hard X-ray region EF Eri, V834 Cen and possibly QQ Vul show quasi-sinusoidal lightcurve variations. Magnetic polars are commonly assumed to have fractional polecap areas in the range 10^{-2} to 10^{-3} . However, for BL Hyi the fractional polecap area needed to give the required lightcurve shape is much larger than this which means that further quasi-sinusoidal source lightcurves may be found with f 's that are much larger, in general, than normally expected. Three of the systems, QQ Vul, V834 Cen and AM Her, show lightcurves that indicate two pole emission, although the cases for the first two are not as strong as that for AM Her. Only two of the eight systems have polecaps in the rotational hemisphere that points away from us, namely VV Puppis and ST Lmi which may point to some selection effect being present in the observable geometries.

In general it is clear that magnetic polar systems can undergo quite drastic changes in their geometries causing large variations in their lightcurve shapes. However,

there is a lot to be gained in trying to deduce the geometry of the system from the shape of its lightcurve and therefore a method of simulating the real process is required. Obviously, a black body could be used as the source spectrum but this neglects some important physical effects.

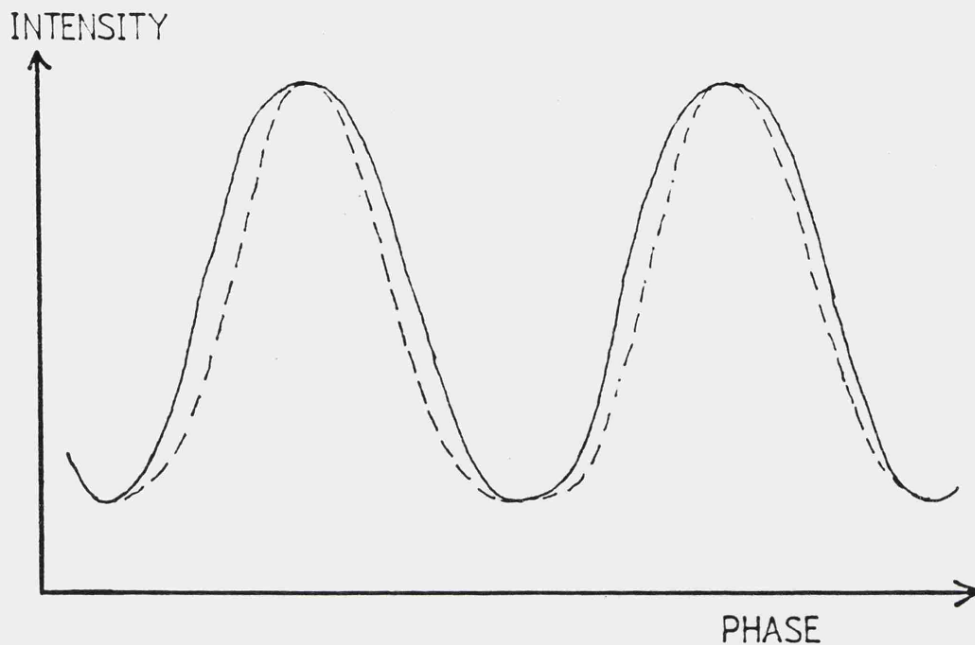
6.3 Why use model atmospheres ?

For a single polecap, the calculation of the observed flux at any orientation to the observer is essentially a trivial task. The choice of outward spectrum to be used is the most important thing. A black body could be used to model the soft X-ray component and a thermal bremsstrahlung could be used to model the hard X-ray component. An atmosphere, however, has two main advantages over these; it contains limb darkening information and has an albedo component in the hard X-ray region. I will consider each of these in turn and discuss the differences we might expect to see in the lightcurve shapes.

In the soft X-ray region limb darkening will enhance the projection effect caused by the changing aspect angle of the polecap relative to the line of sight. This will cause the rise and fall of the lightcurve to be steeper, causing 'peaky' maxima. Figure 6.3(i) shows the difference in the lightcurve that we might expect when a model atmosphere is used as the source instead of a black body.

In the hard X-ray region, the changes will not be so pronounced since the albedo component does not dominate the shock component. However, there will be a slight increase

(i) Soft X-ray lightcurve



(ii) Hard X-ray lightcurve

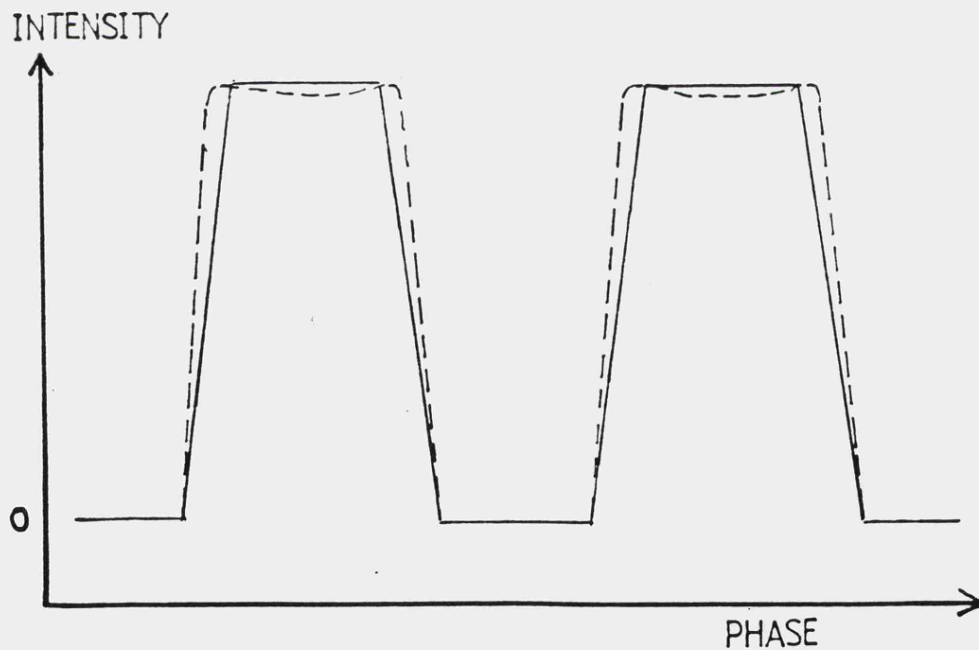


Figure 6.3 Effect of model atmosphere effects on light-curve shape. Solid curve is non-atmosphere calculation (black body and thermal bremsstrahlung) while dashed curve shows expected light-curve for a model atmosphere (limb-darkening of soft X-rays with albedo component included in hard X-rays).

in the observed flux and the limb brightening seen in the albedo component may cause a dip in the lightcurve when the polecap is nearly face on but this will only be evident for large albedos and certain geometries. Figure 6.3(ii) shows the differences that may occur in the hard X-ray lightcurve when a strong albedo component is introduced.

I will show later the real differences that are seen but for now, once the geometry of the system has been determined, it is possible to use atmosphere models to find estimates for the effective temperature of the polecap, the relative strength of the shock and the distance to the source. We have seen in Chapter 5 that a black body can give erroneous values for the effective temperature of an observed source but that the inferred luminosity is roughly correct. In this case we do not have the freedom to vary the emitting area, f , to compensate for the error in the inferred temperature (giving approximately correct values for the luminosity) since f is fixed by the lightcurve fitting (assuming that the polecap is filled and doesn't change), thus a black body used here would give incorrect estimates of both the luminosity and effective temperature of the source.

Concluding, it is possible, through the use of model atmospheres in simulated lightcurves, to find estimates for :-

- (i) the fractional area of the polecap
- (ii) the angle between the magnetic and rotational axes
- (iii) the angle between the rotational axis and the line of sight

- (iv) the effective temperature of the polecap
- (v) the relative strength of the shock (related to the percentage of X-ray illumination)
- (vi) the distance to the source

with improved accuracy as compared with black bodies.

6.4 Calculating a simulated lightcurve

As the polecap is situated on a sphere each region of the polecap presents a different angle to the line of sight. By breaking the polecap up into flat sections the curvature of the polecap can be approximated (assuming enough sections are used); this has the advantage that each section of the polecap can be treated as a polecap in its own right but with one angle to the line of sight, by summing each sections contribution the total flux from the polecap can be found (the sections are made to be of equal area and are assumed to radiate with the same effective temperature, T_{eff}). Since our polecap is assumed to be circular, the easiest way to break it into equal sections is to divide it into rings and then break each ring into equal areas, as shown in Figure 6.4.

The area of each ring is given by

$$A = \pi(\theta + \Delta\theta)^2 - \pi\theta^2 = 2\pi\theta\Delta\theta + \pi\Delta\theta^2 \quad (6.1)$$

If we consider the mth ring then

$$\theta = (m-1)\Delta\theta \quad (6.2)$$

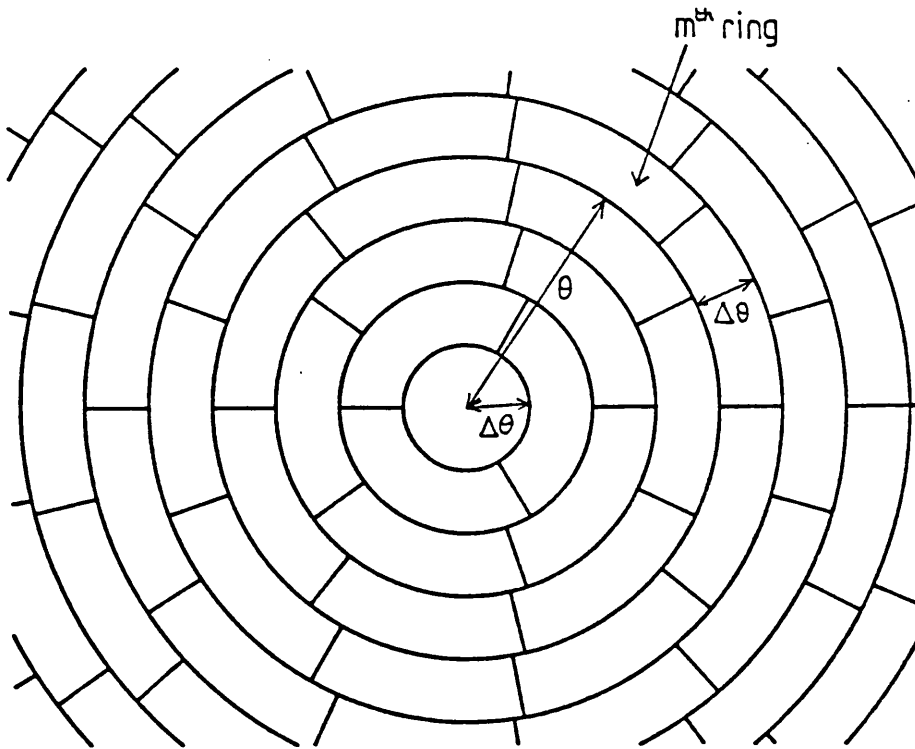


Figure 6.4 Dividing up the polecap into equal sections.

So therefore

$$A = 2\pi(m-1)\Delta\theta^2 + \pi\Delta\theta^2 \quad (6.3)$$

We require the area of each section to be the same, i.e., equal to the area of the first ring, $\pi\Delta\theta^2$. So the number of sectors in ring m is

$$n = (2\pi(m-1)\Delta\theta^2 + \pi\Delta\theta^2) / \pi\Delta\theta^2 = 2m-1 \quad (6.4)$$

And the total number of sectors contained within a radius $(\theta+\Delta\theta)$ is given by

$$N = \pi(\theta+\Delta\theta)^2 / \pi\Delta\theta^2 = \pi((m-1)\Delta\theta+\Delta\theta)^2 / \pi\Delta\theta^2 = m^2 \quad (6.5)$$

So, if there are M rings in the polecap of width $\Delta\theta$ then

there are $2m+1$ sectors in each ring m ($m=1,2,\dots,M$) and M^2 sectors in all.

For calculating the angle to the line of sight we can assume the radius of the white dwarf to be unity. If β is the half-angle subtended by the polecap at the centre of the white dwarf then the fractional area of the polecap is given by

$$f = \pi\beta^2/4\pi R^2 = \beta^2/4 \quad (6.6)$$

If β is small then

$$\cos\beta = 1 - 1/2\beta^2 \quad (6.7)$$

Substituting from equation (6.6) and rearranging,

$$\beta = \cos^{-1}(1 - 2f) \quad (6.8)$$

Given a value for f the polecap can be broken up into the nearest integer number of rings necessary to fill it and then further divided into equal area sectors. An area of 10^{-4} was chosen for the sector, thus giving 100 sectors for $f=10^{-2}$.

The next step is to calculate the angle to the line of sight of each sector at each phase. Before I describe this it is important to mention the effects not included in the simulation. It was decided not to try to model occultations by the accretion stream and/or the secondary star. Obscuration by the accretion column itself was also ignored. Since these effects only occur for special

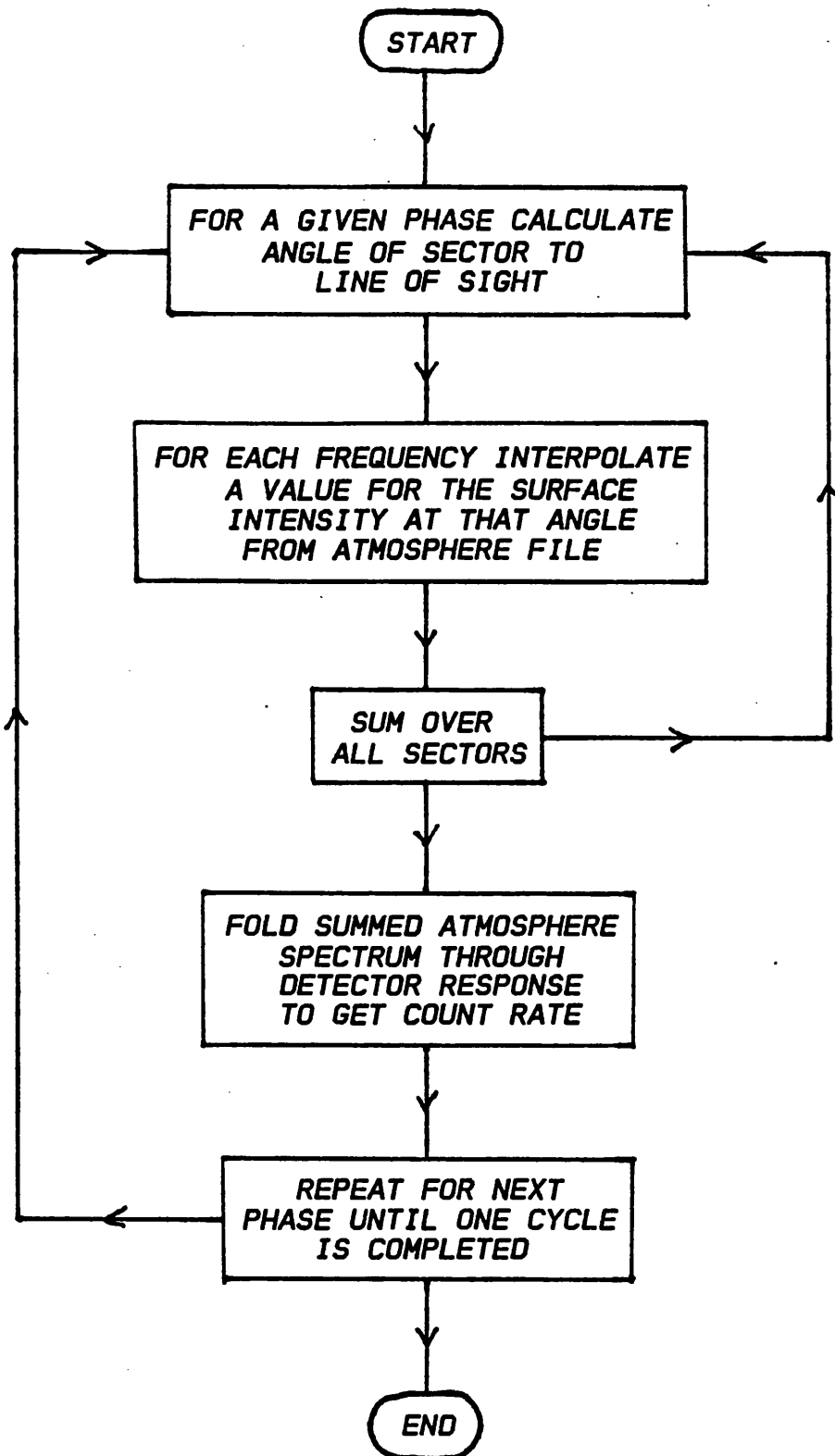


Figure 6.5 Flow diagram for calculating a simple light-curve.

geometries their absence will not impair the fitting of the majority of the observable lightcurves. Figure 6.5 shows the flow diagram for the calculation of a simple lightcurve; each step in the calculation is described below.

6.4.1 Calculating the angle to the line of sight

With reference to Figure 6.6, let r be the distance of each sector from the magnetic pole and θ be its position angle. Let m be the angle between the magnetic and rotational axes and i be the angle between the rotational axis and the line of sight, also let ϕ be the phase angle (phase 0.0 = away from the observer). By transforming the coordinates four times it is possible to find the angle of each sector to the line of sight.

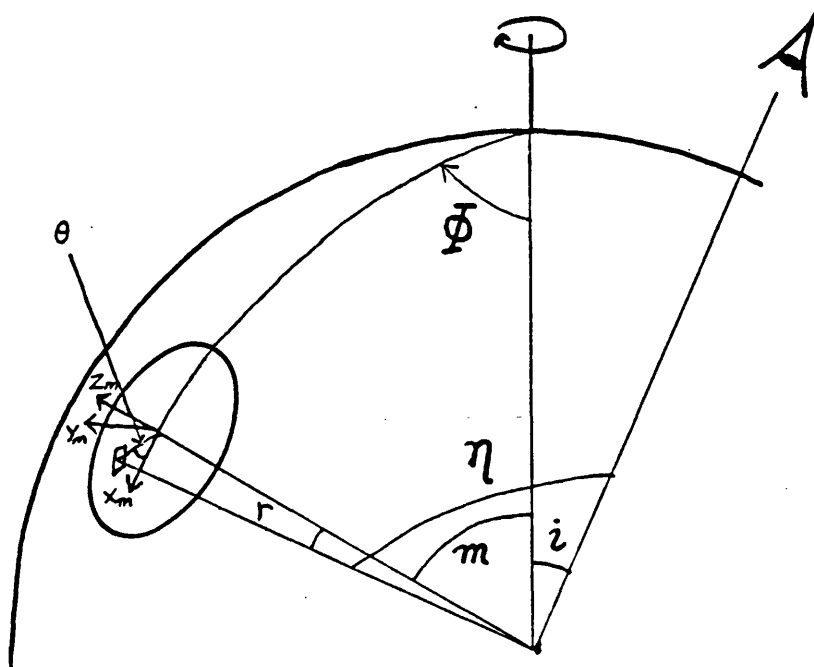


Figure 6.6 Orientation of the polecap.

1) Transform sector coordinates to cartesian coordinates with respect to the magnetic axis :

$$\begin{aligned} z_m &= \cos r \\ x_m &= \sin r \cos \theta \\ y_m &= \sin r \sin \theta \end{aligned} \quad (6.9)$$

2) Transform magnetic axis coordinates to rotational axis coordinates :

$$\begin{aligned} z_R &= z_m \cos m - x_m \sin m \\ x_R &= x_m \cos m + z_m \sin m \\ y_R &= y_m \end{aligned} \quad (6.10)$$

3) Rotate coordinates to line of sight in phase :

$$\begin{aligned} z_\phi &= z_R \\ x_\phi &= x_R \cos \phi + y_R \sin \phi \\ y_\phi &= y_R \cos \phi - x_R \sin \phi \end{aligned} \quad (6.11)$$

4) Rotate coordinates to line of sight :

$$\begin{aligned} z_s &= z_\phi \cos i + x_\phi \sin i \\ x_s &= x_\phi \cos i - z_\phi \sin i \\ y_s &= y_\phi \end{aligned} \quad (6.12)$$

Now $z_s = \cos \eta$ where η is the angle of the sector to the line of sight so if z_s is negative then the sector is behind the white dwarf and does not contribute to the flux. If the sector is visible then the intensity seen at each frequency

must be found.

6.4.2 Calculating the observed flux from the polecap

In Chapter 3 I mentioned that the six outward surface intensities at each frequency are stored for any model completed. These intensities are used to find the correct intensity for each sector at any phase. If the angle of the sector to the line of sight is known then a value for the intensity at that angle can be interpolated from the intensities at the angles nearest to it. Let $I_{n\nu}$ be the intensity at a frequency ν for sector n . The total flux F_ν is given by the summation, over all the visible sectors, of the product of the interpolated intensity and the angle to line of sight $z_{s,n}$ (optically thick radiation only). That is,

$$F_\nu = \sum 4\pi\Delta f z_{s,n} I_{n\nu} \quad (6.13)$$

where Δf is the fractional area of each sector. Adding in the isotropic contribution from the shock equation (6.13) becomes

$$F_\nu = \sum 4\pi\Delta f (z_{s,n} I_{n\nu} + I_\nu^x) \quad (6.14)$$

F_ν is the flux at the 'source', the detected spectrum/count rate depends on the response of the detector used. The most recent observations of magnetic polars have been done using the detectors on the European X-ray Astronomy Satellite (EXOSAT).

6.4.3 The EXOSAT detectors

EXOSAT was launched in May 1983 and successfully carried out observations of all known X-ray sources, including AM Herculis systems, and previously unknown ones. The programme lasted until April 1986 when problems were encountered with the attitude and orbital control system (AOCS) causing a loss of telemetry. Three types of detector were carried; two low energy imaging telescopes with either a position sensitive proportional counter

Table 6.1 The EXOSAT detectors

Medium Energy Experiment (ME)

Total effective area : 1500 cm²
Effective energy range : 1-20 keV (Argon counters)
5-50 keV (Zenon counters)
Energy resolution : 51/E (keV)^{0.5} % FWHM (Argon)
($\Delta E/E$) 18% for 10keV < E < 30keV (Zenon)

Gas Scintillation Proportional Counter (GSPC)

Total effective geometrical area : 150 cm²
Effective energy range : 2-18 keV or 2-40 keV (depending on gain setting)
Energy resolution : 27/E (keV)^{0.5} % FWHM
($\Delta E/E$)

Low Energy Experiment (LE)

	<u>CMA</u>	<u>PSD</u>
Energy range	: 0.04-2.0 keV	0.3-2.0 keV
Energy resolution	: Five filters available for broad-band spectroscopy plus grating (500/1000 lines mm ⁻¹)	: ($\Delta E/E$)=41/E (keV) ^{0.5} FWHM
Effective area	: Depends on filter used and energy	: Depends on energy
Broad-band filters	: No. Type	
	2 Polypropylene	
	3 Lexan (thick)	
	6 Parylene-N + Al	
	7 Lexan (thin)	
	8 Boron + polyprop.	

detector (PSD) or channel multiplier array (CMA) placed at the X-ray prime focus; a medium energy large area proportional counter array; and a gas scintillation proportional counter (GSPC). Table 6.1 shows a summary of the detector characteristics. Referring to the table, the low energy CMA's have only limited spectral resolution capability, broad band filters being used to extract some spectral information. However it is these detectors, along with the medium energy (ME) detector, that are primarily used to observe AM Her systems.

Figure 6.7 shows the effective collecting area of each of the five broad-band filters as a function of energy. Note the similar responses of filter numbers 2,3 and 7. Spectral information can only be extracted by comparing the count rates in filters 2,3 and 7 with those in filters 6 and 8 but this information is severely affected by interstellar absorption of the soft X-rays.

Interstellar absorption of soft X-rays

Soft X-rays (< 1 keV) are absorbed by the K-shells of helium, carbon, nitrogen and oxygen. The amount of these elements that are present along the line of sight to the source is parameterised by the hydrogen column density, N_H . For sources like magnetic polars N_H is assumed to lie in the range $10^{19} - 10^{21}$ cm^{-2} . If $f(E)$ is the source spectrum then $f_{obs}(E)$, the observed spectrum, is given by

$$f_{obs}(E) = f(E) \exp[-N_H A(E)] \quad (6.15)$$

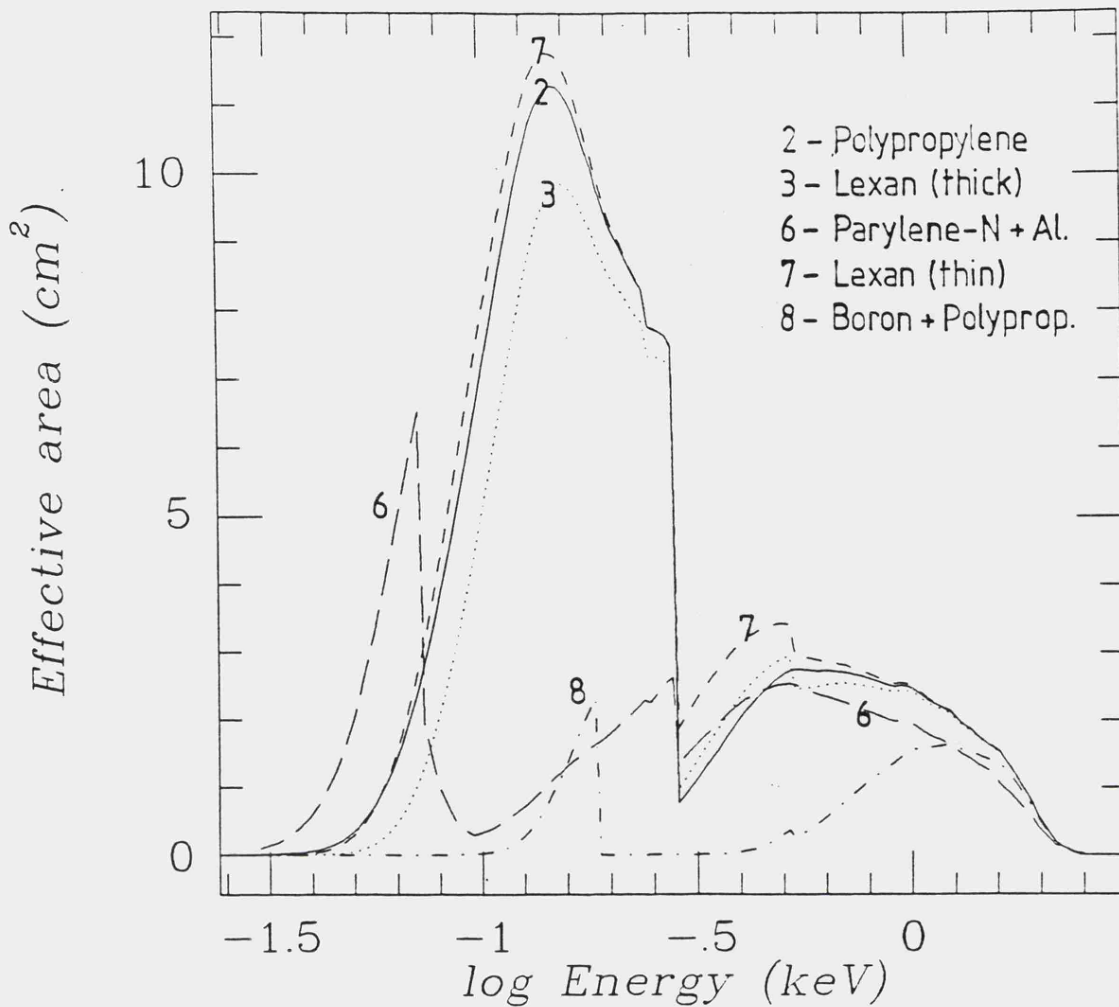


Figure 6.7 Effective areas of the EXOSAT broad-band filters as a function of energy.

where $A(E)$ is the effective absorption cross-section per hydrogen atom (cm^2). Figure 6.8 shows $A(E)$ plotted as a function of energy. Figure 6.9 shows the effective response for three values of N_H ; 1.0×10^{19} , 3.0×10^{19} and $1.0 \times 10^{20} \text{ cm}^{-2}$.

Equation 6.15 can be combined with the filter responses to give a 'virtual' response for each filter, this is shown in Figure 6.10, for the same column densities used in Figure 6.9. It clearly shows that filter 6 is badly affected by interstellar absorption, losing its soft X-ray

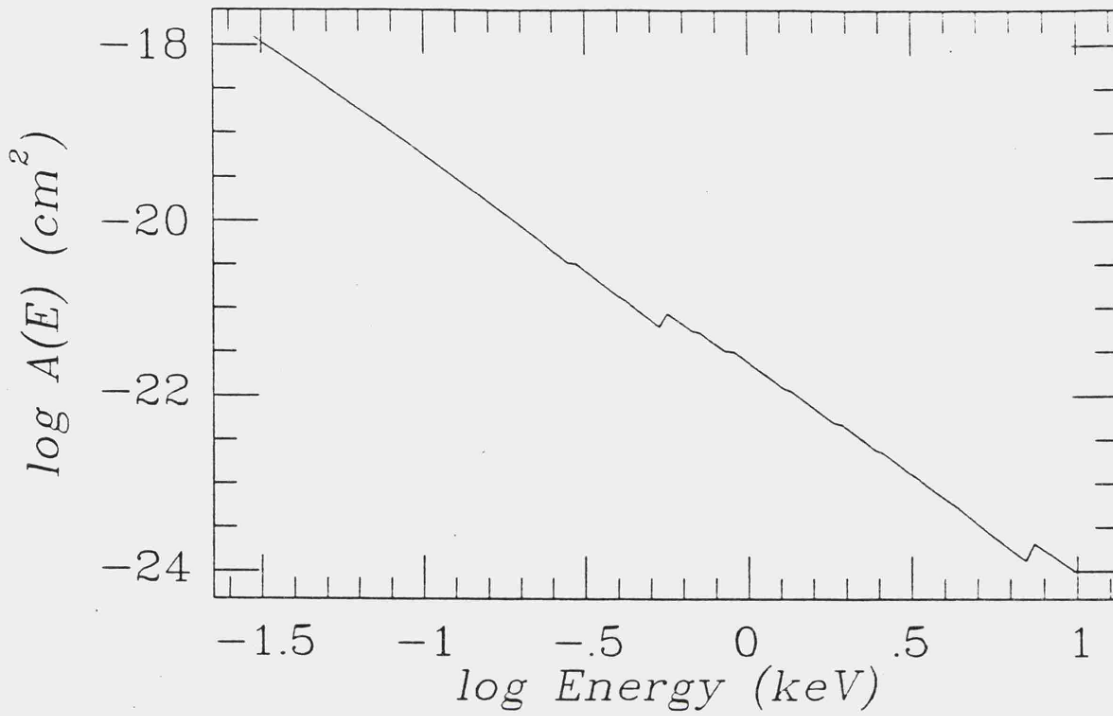


Figure 6.8 Effective cross-section per hydrogen atom, $A(E)$, plotted as a function of energy.

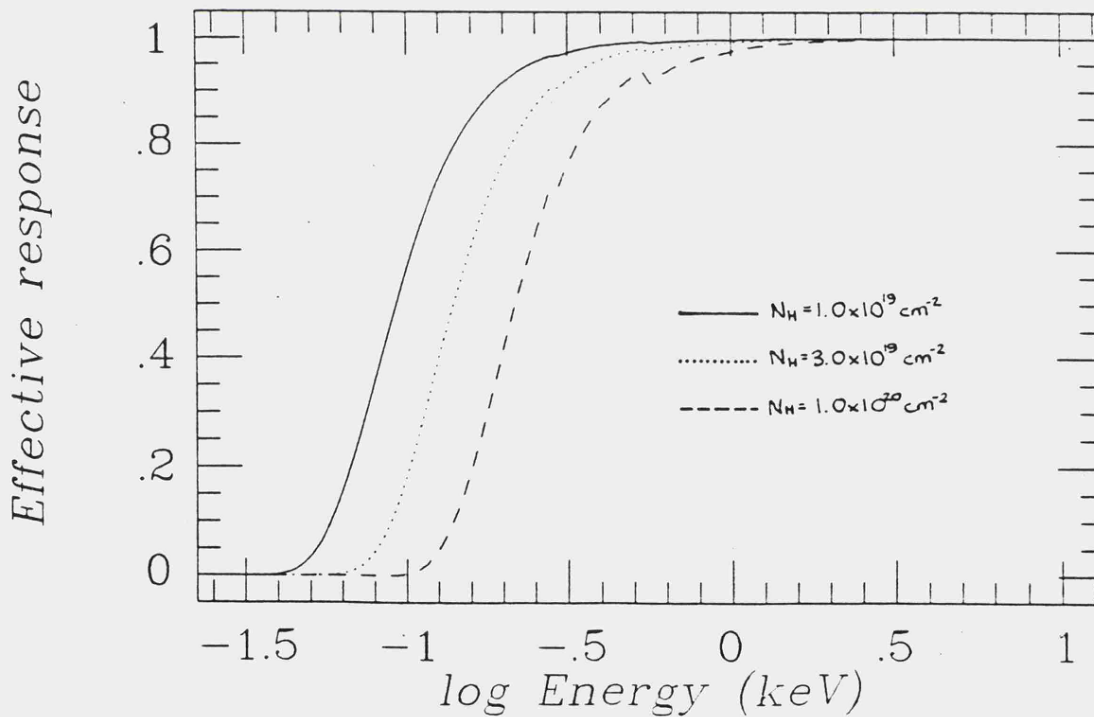


Figure 6.9 Effective response for three values of the hydrogen column density, N_H : $1.0 \times 10^{19} \text{ cm}^{-2}$, $3.0 \times 10^{19} \text{ cm}^{-2}$ and $1.0 \times 10^{20} \text{ cm}^{-2}$.

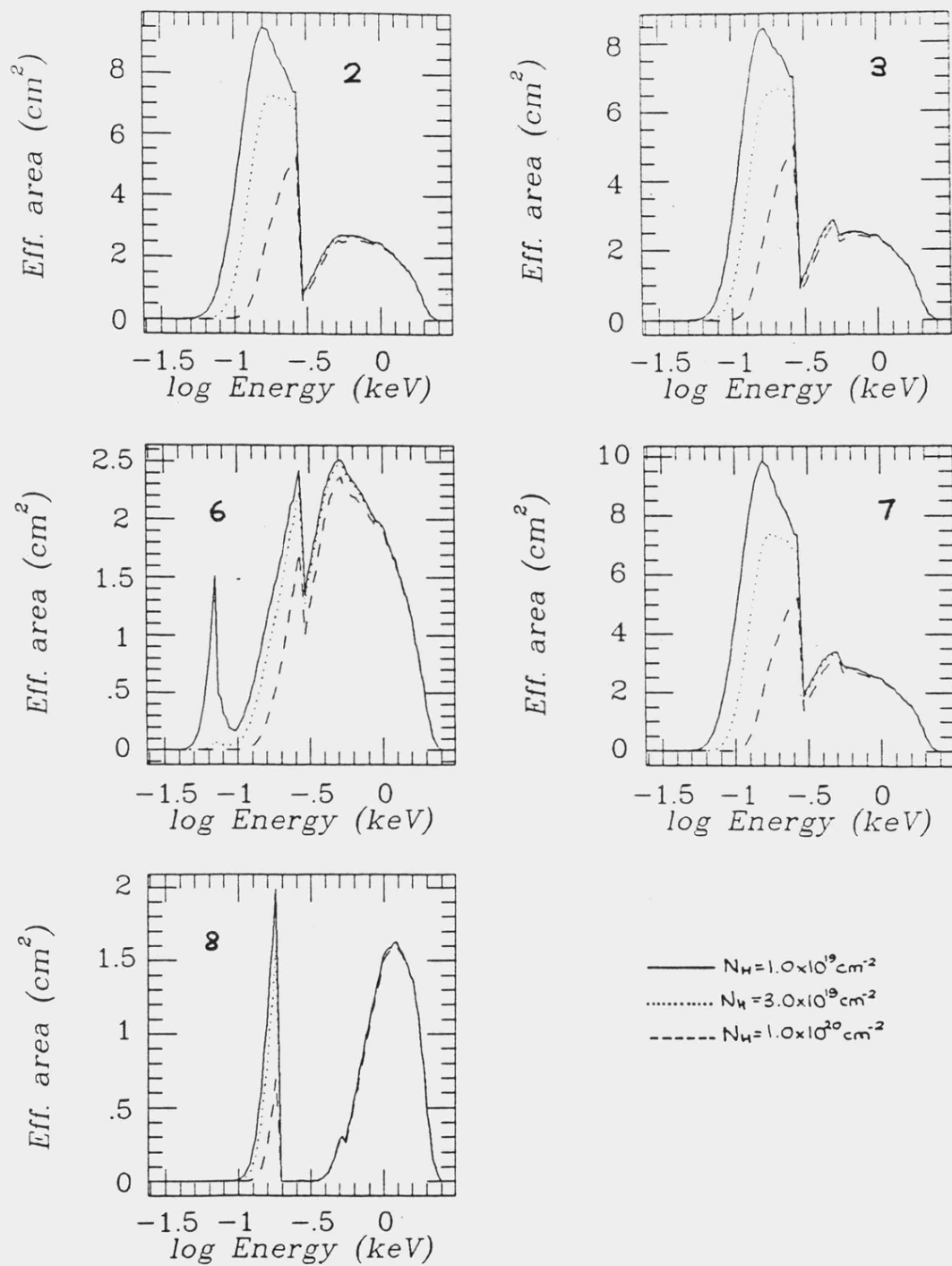


Figure 6.10 Effective area of the EXOSAT broad-band filters with interstellar absorption included. The values for the hydrogen column density are the same as in Figure 6.9.

peak for column densities greater than $1.0 \times 10^{19} \text{ cm}^{-2}$ and since filter 8 has such a small effective area that only the brightest sources will be visible in it the retrieval of spectral information from these filters is almost impossible, the use of the grating in front of the detector improves the situation but it has a low throughput and therefore can only be used for very strong sources (in fact it malfunctioned early into the programme and could not be used from then on). Since the thin Lexan filter (number 7) is the most responsive it is used primarily in observations.

6.4.4 The 'observed' lightcurve

At each phase we have calculated the outward flux from the visible areas of the polecap, $f(\nu)$. This has the units of $\text{erg cm}^{-2} \text{ s}^{-1} \text{ Hz}^{-1}$. Converting this to photons $\text{s}^{-1} \text{ keV}^{-1}$ ($f(E)$) using

$$f(E) = 2.418 \times 10^{14} f(\nu) / h\nu \quad (6.16)$$

the count rate observed using filter X in conjunction with the CMA is then given by

$$C_X = \int_{0.03}^{2.5} f(E) \exp[-N_H A(E)] F_X(E) dE \quad (6.17)$$

where $F_X(E)$ is the filter response. The procedure for calculating the counts in the ME detector is the same except that the interstellar absorption term is negligible and the filter response is constant.

Repeating the whole process at each phase thus gives the complete lightcurve through the chosen filter. In this calculation I have assumed that the whole of the polecap is emitting and since this may not necessarily be so some method was needed to simulate a polecap with some sectors effectively 'turned off'.

6.4.5 The random polecap.

A look at any observed X-ray lightcurve would be enough to persuade the casual observer that there is nothing 'simple' about their shape. They all show varying amounts of what appears, at first sight, to be random noise over and above the errors associated with the observation. This persistent flickering in the source can only be due to variations in the strength and homogeneity of the accretion stream on timescales less than the orbital period.

To model this effect it was decided to blank out some sectors in the model polecap at each phase. Rather than try to fix a shape for the polecap (i.e. crescent, ellipsoid, etc.) it was decided to turn the sectors randomly on or off. Inputting the required sectors for a given shape would be a tedious process and since the idea was to illustrate, rather than fit, choosing the sectors randomly has advantages in terms of speed and variability.

Random numbers generated by a computer have the range 0 to 1. If we fix a limit of >0.5 for the sector to be 'on' then roughly half the polecap will be emitting. By varying the limit we can model polecaps where only a little of the

pole is actually emitting to those where nearly all is. The random orientation of the sectors can be fixed with phase or can vary with phase in order to model flickering on timescales of $100 < t < 300$ seconds (e.g. timescales that are seen in EF Eri for instance, Watson et al., (1985)).

As I mentioned above, the random effects are only illustrative; no actual fitting can be attempted, only an idea of the strength of the variations (i.e., fraction of the polecap emitting) can be found by comparison with observed lightcurves; fitting the geometry of the source requires the use of non-random lightcurves (as we will see later)¹. In the next section some sample lightcurves are illustrated.

6.5 Sample lightcurves

Figures 6.11, 6.12 and 6.13 show the variations in lightcurve shape for different magnetic axis angles, line of sight inclinations and fractional polecap areas. In each case the diagrams (a)-(c) are for the ME detector and (d)-(f) are for the LE detector with the thin Lexan filter (number 7). The parameters for each figure are shown in Table 6.2, all the figures are for a 100,000 K, 1 solar mass model atmosphere with 10% hard X-ray illumination, at a distance of 100 parsec. For the LE lightcurves the hydrogen column density was $1.0 \times 10^{20} \text{ cm}^{-2}$.

Referring to the figures, in the ME lightcurves the dotted curve shows, for comparison purposes, a lightcurve calculated using a thermal bremsstrahlung source with no albedo component, normalised with respect to the maximum

Table 6.2 Parameters for Figures 6.11 - 6.13

Figure number	Fractional polecap area, f	Magnetic axis angle, m (°)
6.11(a),(d)	0.005	15.0
6.11(b),(e)	"	45.0
6.11(c),(f)	"	75.0
6.12(a),(d)	0.01	15.0
6.12(b),(e)	"	45.0
6.12(c),(f)	"	75.0
6.13(a),(d)	0.05	15.0
6.13(b),(e)	"	45.0
6.13(c),(f)	"	75.0

atmosphere count rate. In the case of the LE lightcurves the dashed line shows a lightcurve calculated using a black body source spectrum but since the black body gives fewer counts than an atmosphere at the same effective temperature the black body lightcurve is normalised with respect to its own maximum, in order that the difference between the atmosphere and black body lightcurves can be seen.

Surprisingly the shock-only and shock+albedo ME lightcurves are almost exactly the same: the limb effects in the albedo component do not affect the lightcurve shape at all. However the differences between a black body and model atmosphere lightcurve are quite striking and are exactly what we expected; the model atmospheres limb darkening giving peakier lightcurves. As the inclination to the line of sight increases the atmosphere lightcurves flatten out much quicker than black body lightcurves due to the limb effects.

Looking again at the ME lightcurves and considering the work of King and Shaviv (1984) we see precisely the sort of lightcurve shapes they discussed. For small polecap areas flat-topped and flat-bottomed lightcurves dominate while

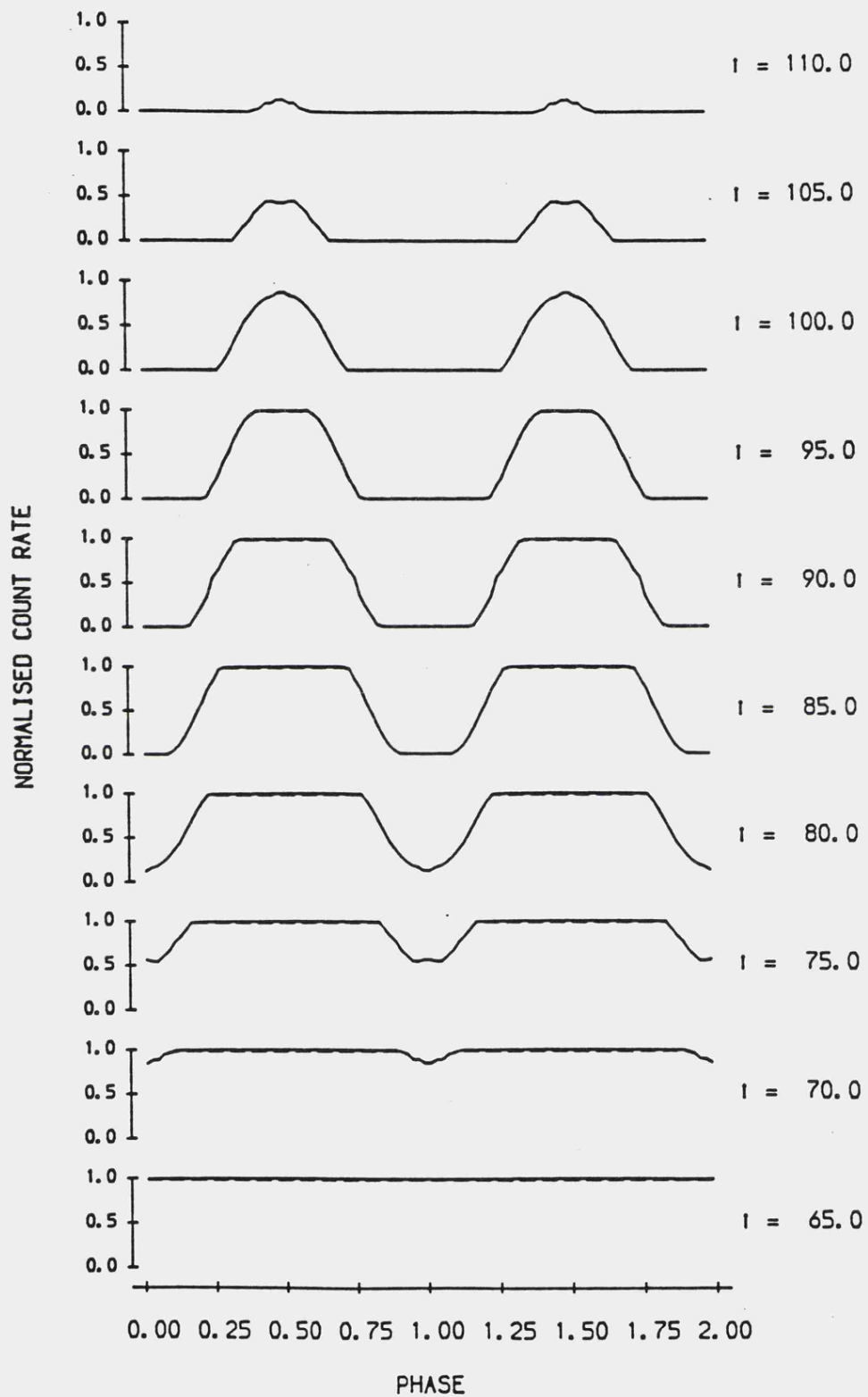


Figure 6.11(a) Sample ME lightcurve shapes.

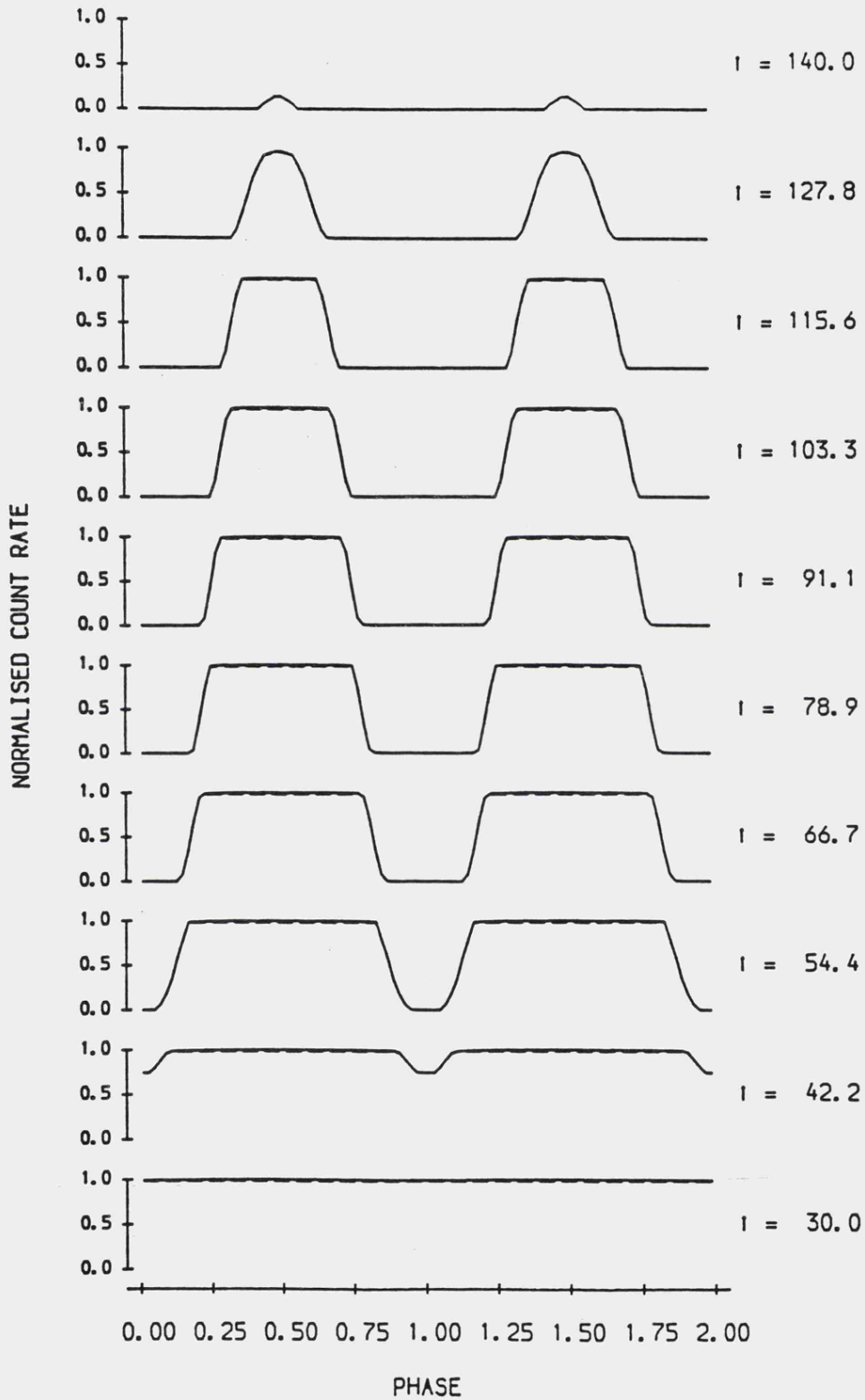


Figure 6.11(b) Sample ME lightcurve shapes.

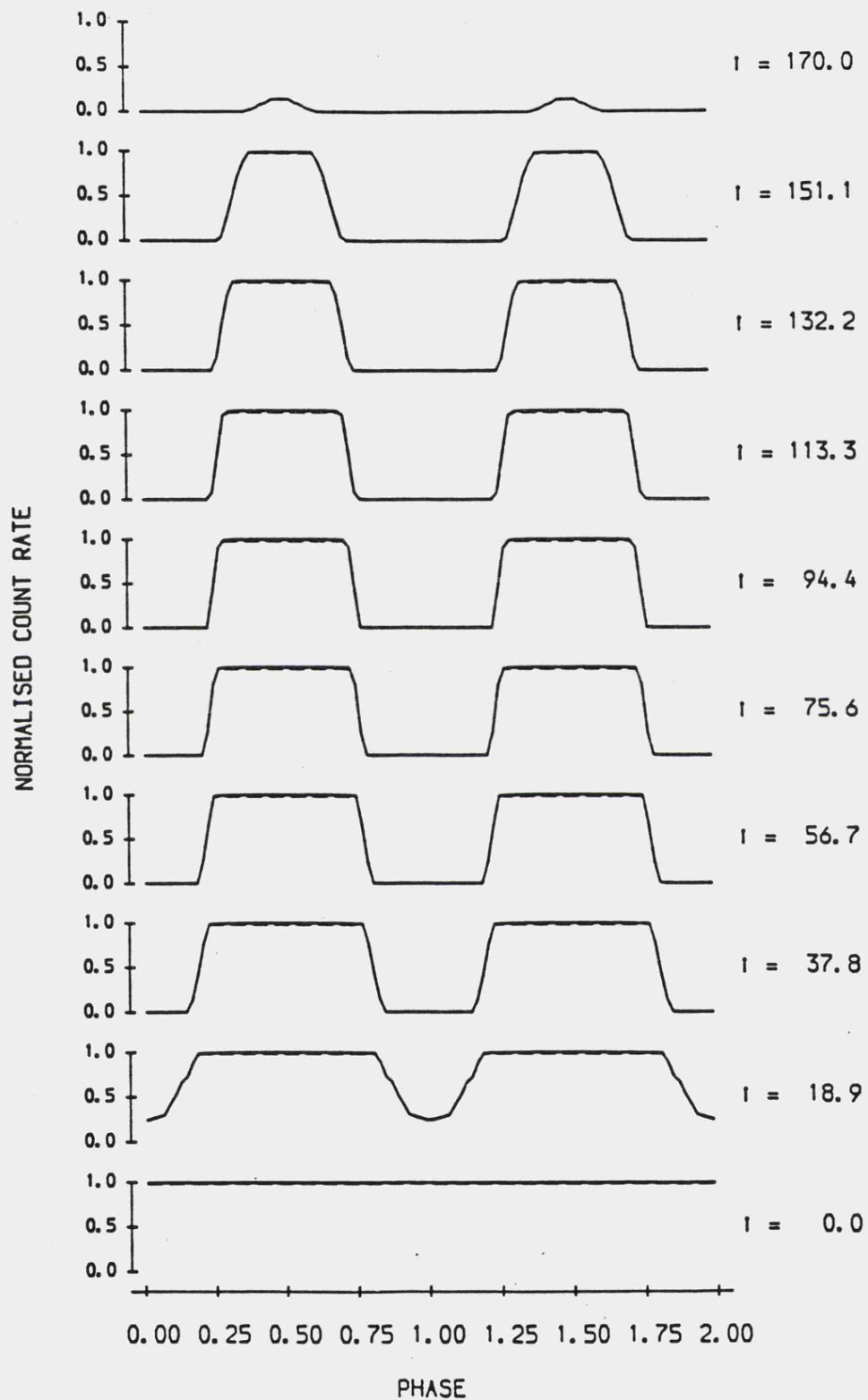


Figure 6.11(c) Sample ME lightcurve shapes.

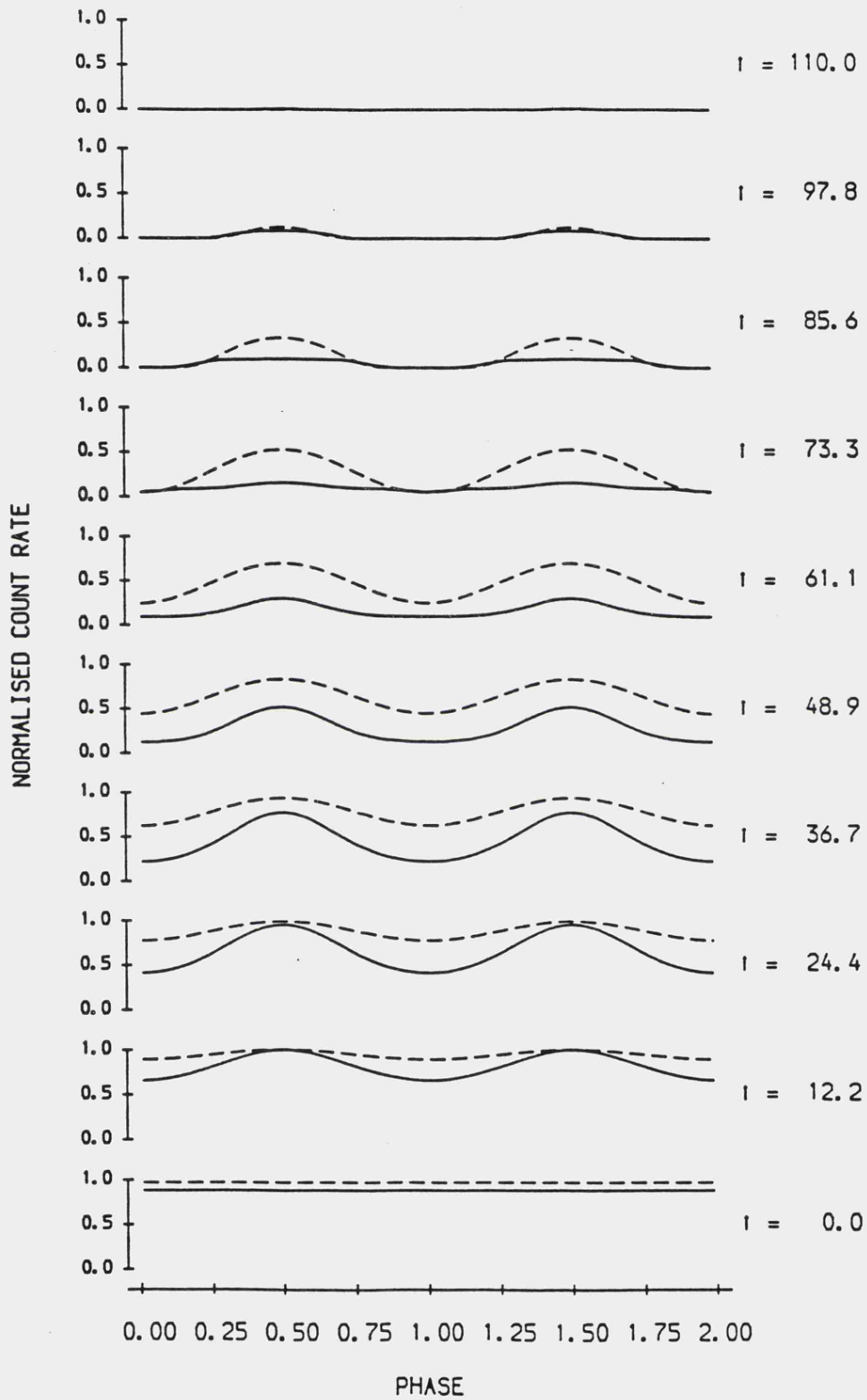


Figure 6.11(d) Sample LE lightcurve shapes.

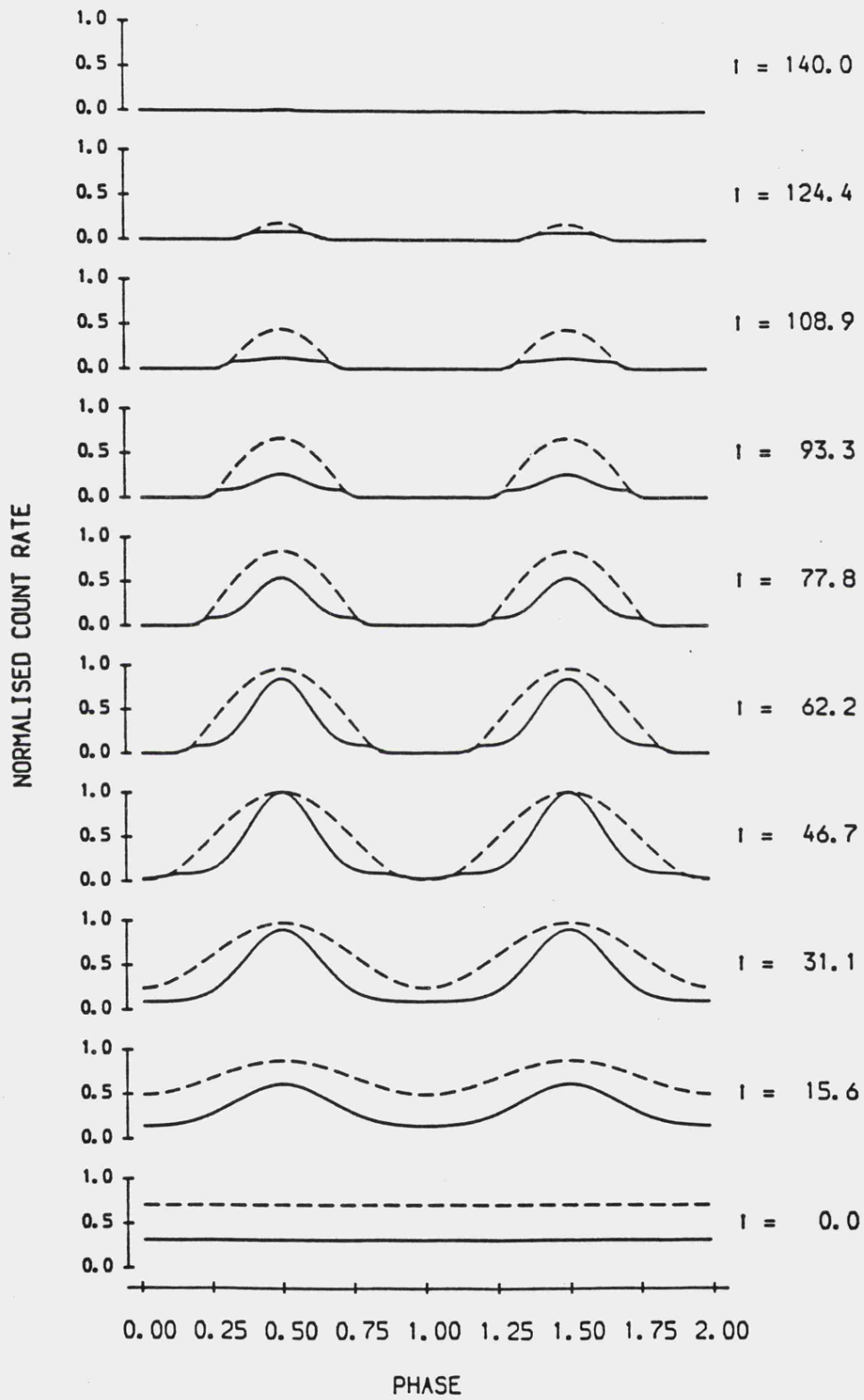


Figure 6.11(e) Sample LE lightcurve shapes.

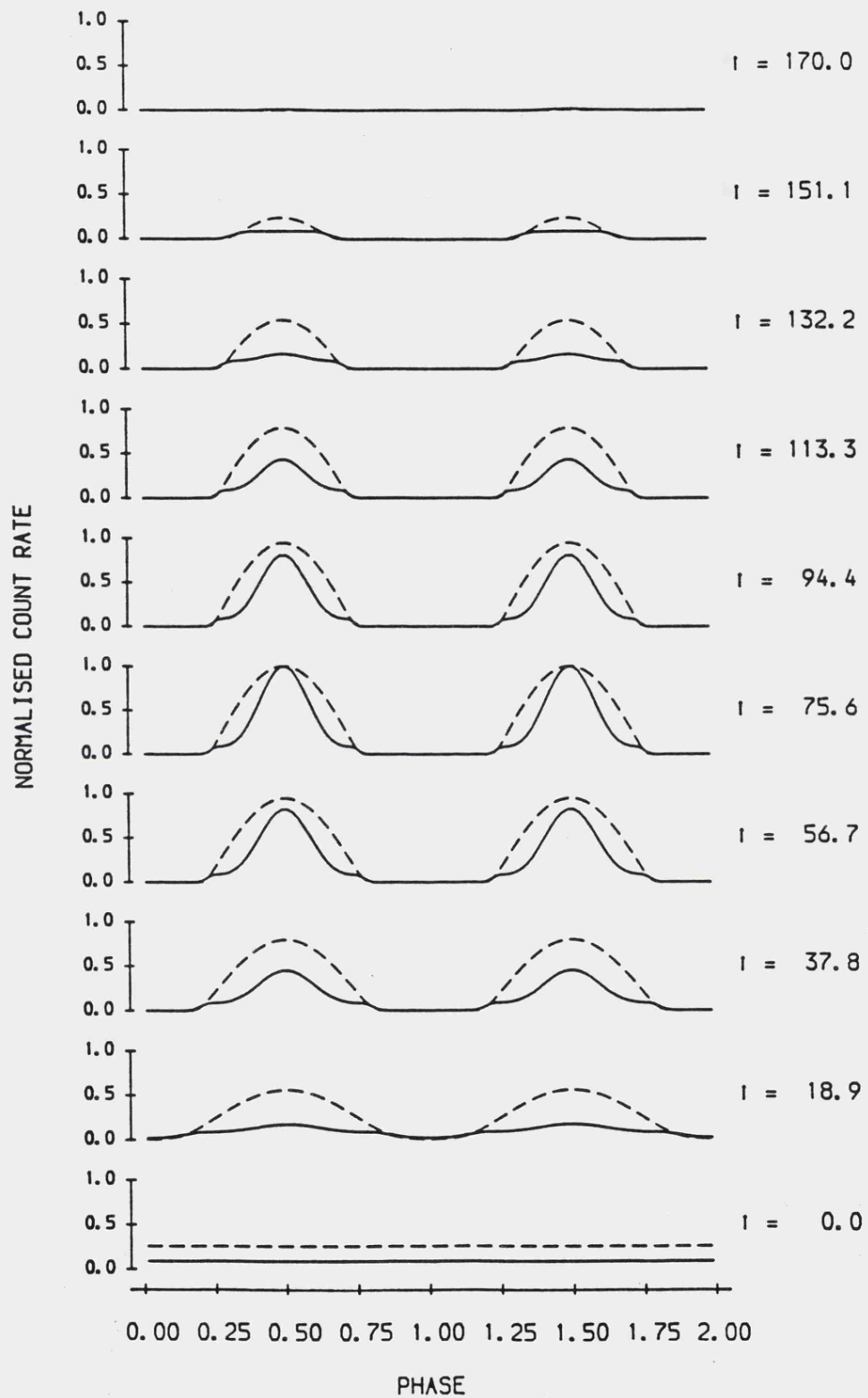


Figure 6.11(f) Sample LE lightcurve shapes.

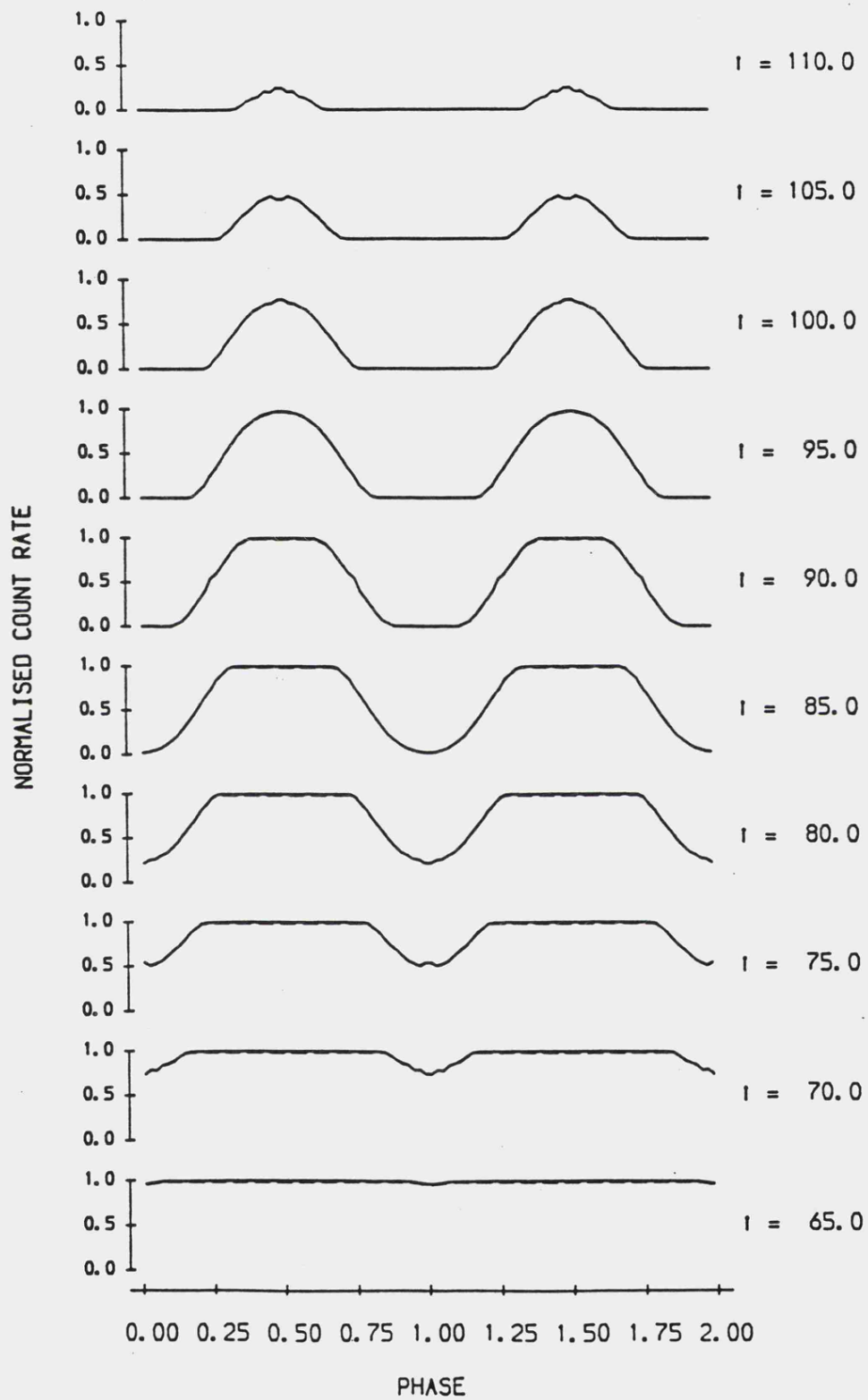


Figure 6.12(a) Sample ME lightcurve shapes.

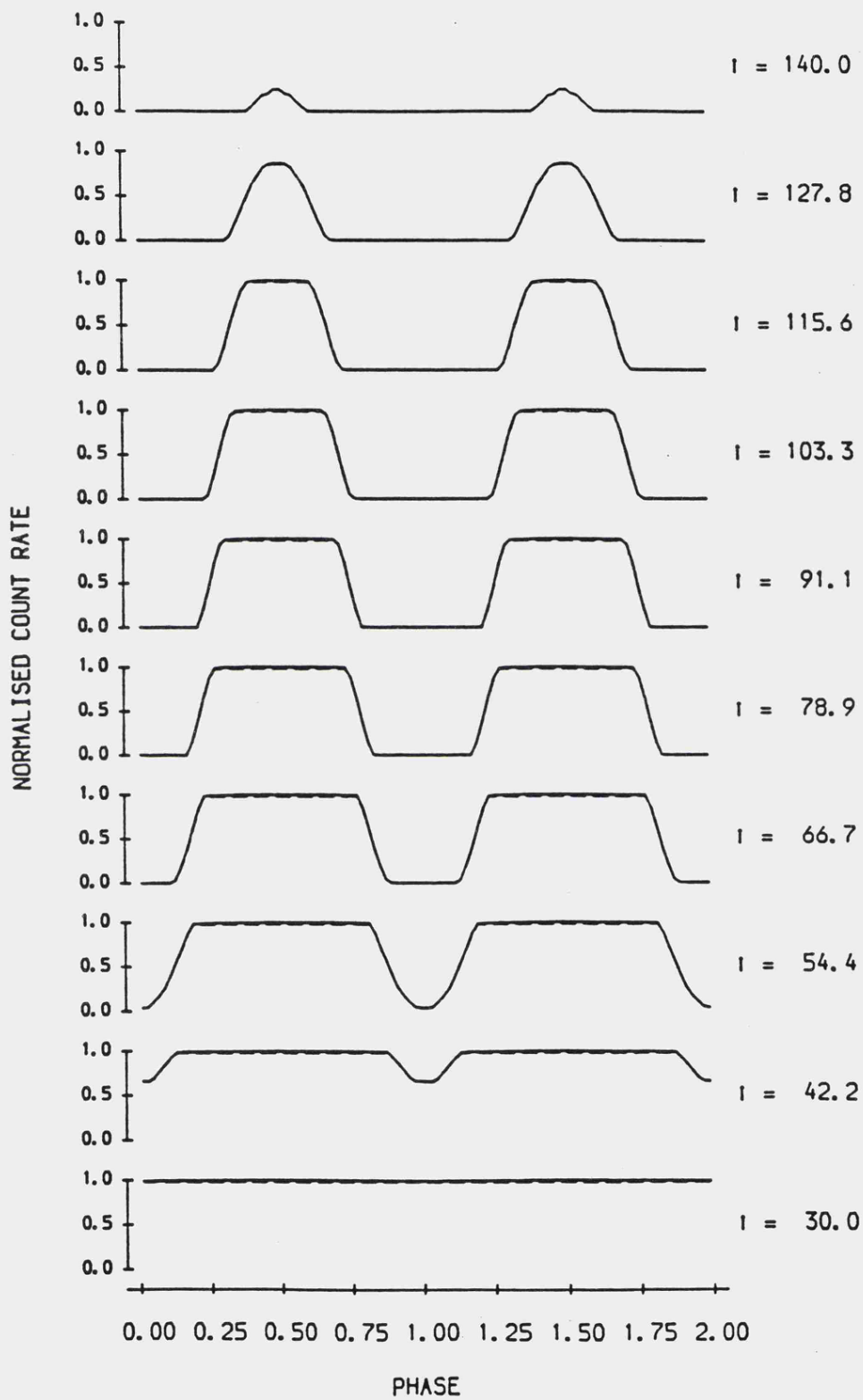


Figure 6.12(b) Sample ME lightcurve shapes.

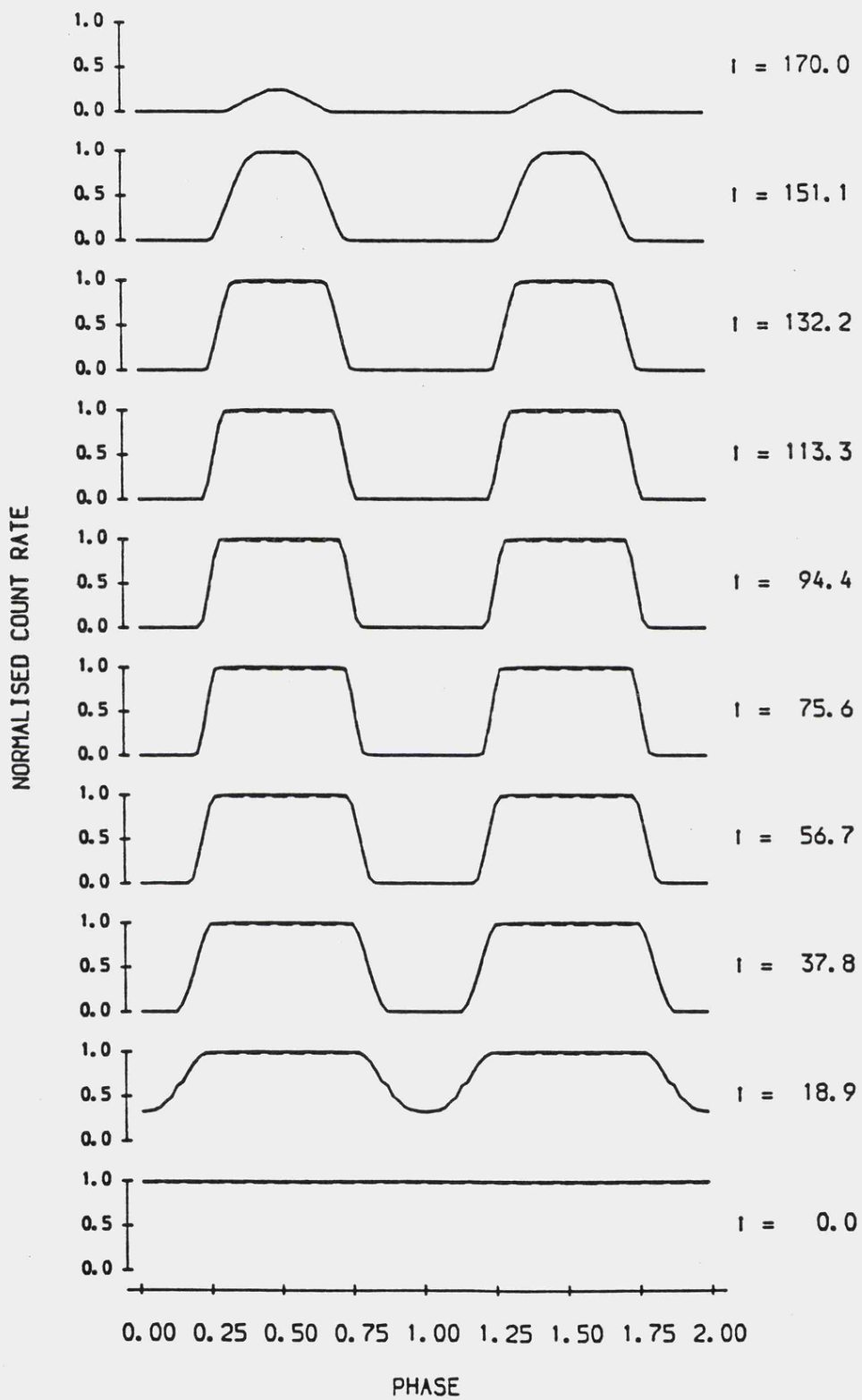


Figure 6.12(c) Sample ME lightcurve shapes.

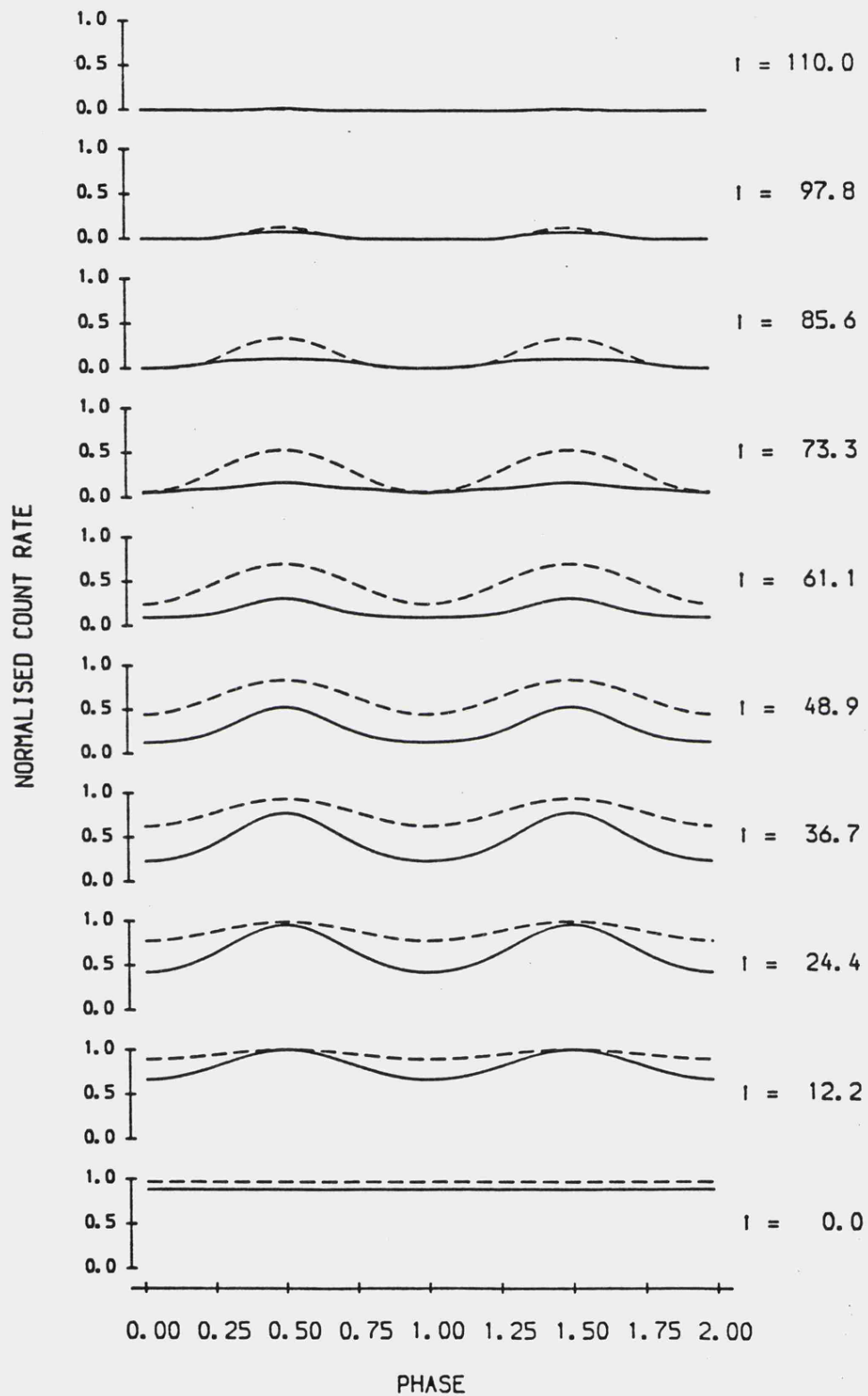


Figure 6.12(d) Sample LE lightcurve shapes.

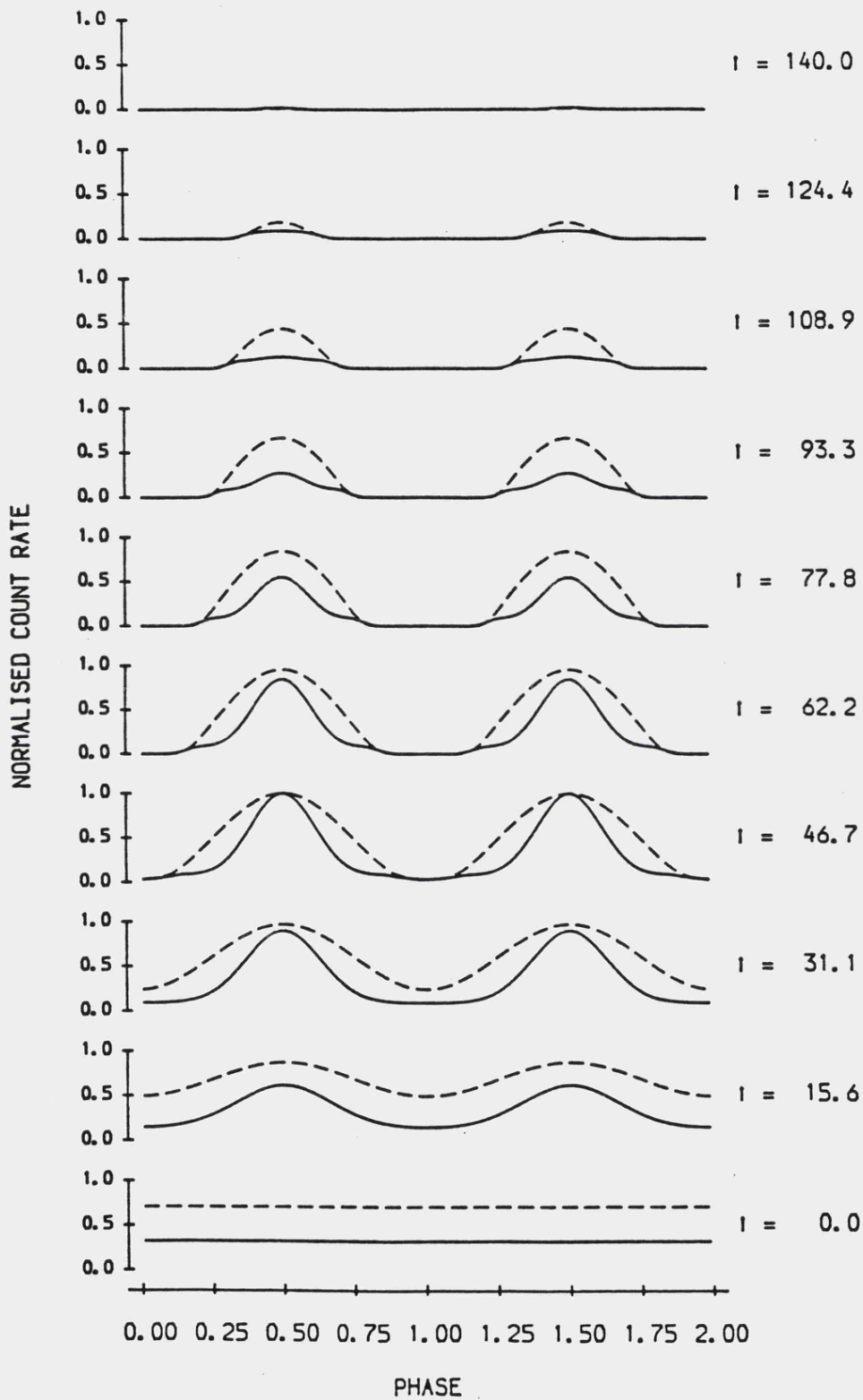


Figure 6.12(e) Sample LE lightcurve shapes.

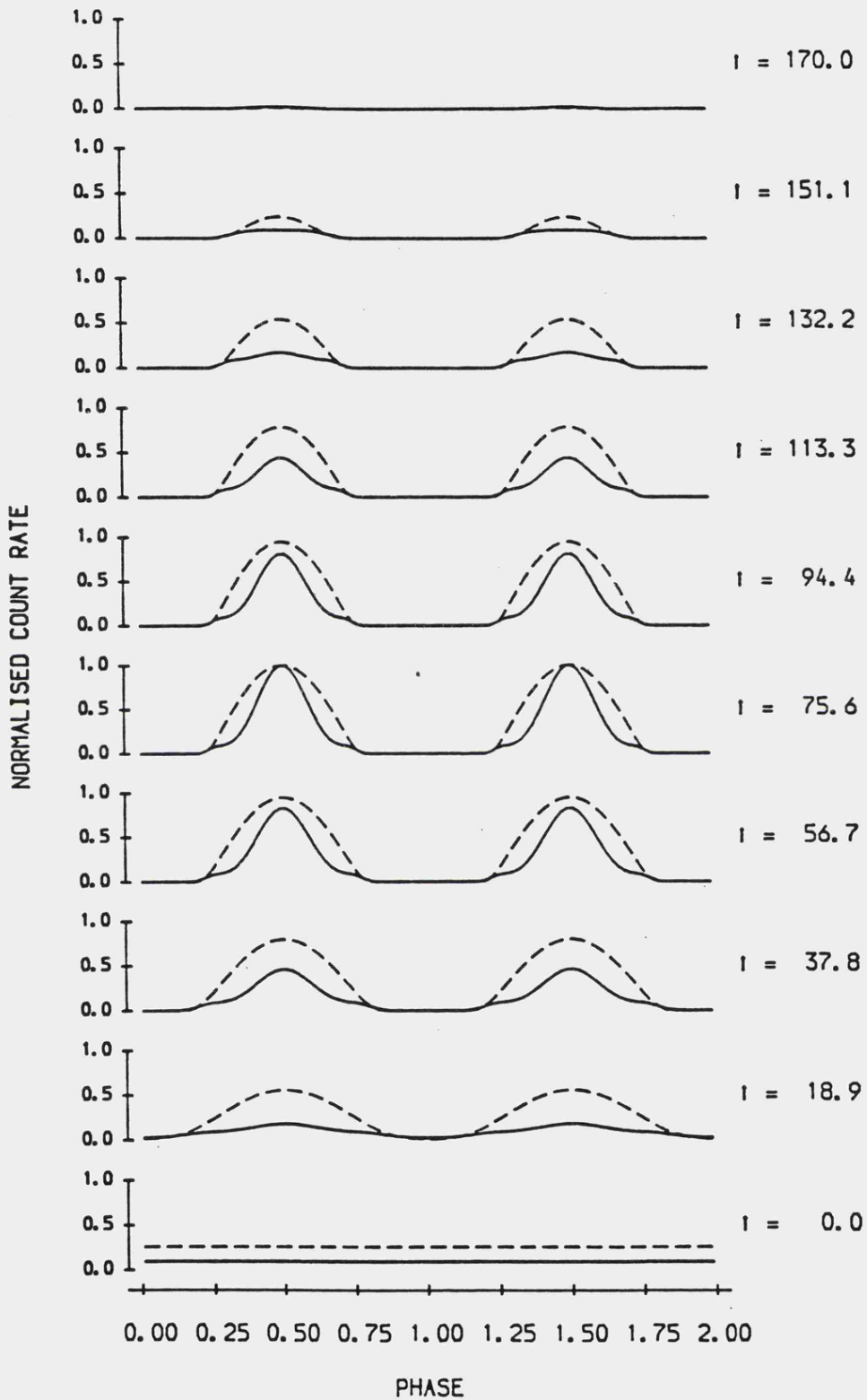


Figure 6.12(f) Sample LE lightcurve shapes.

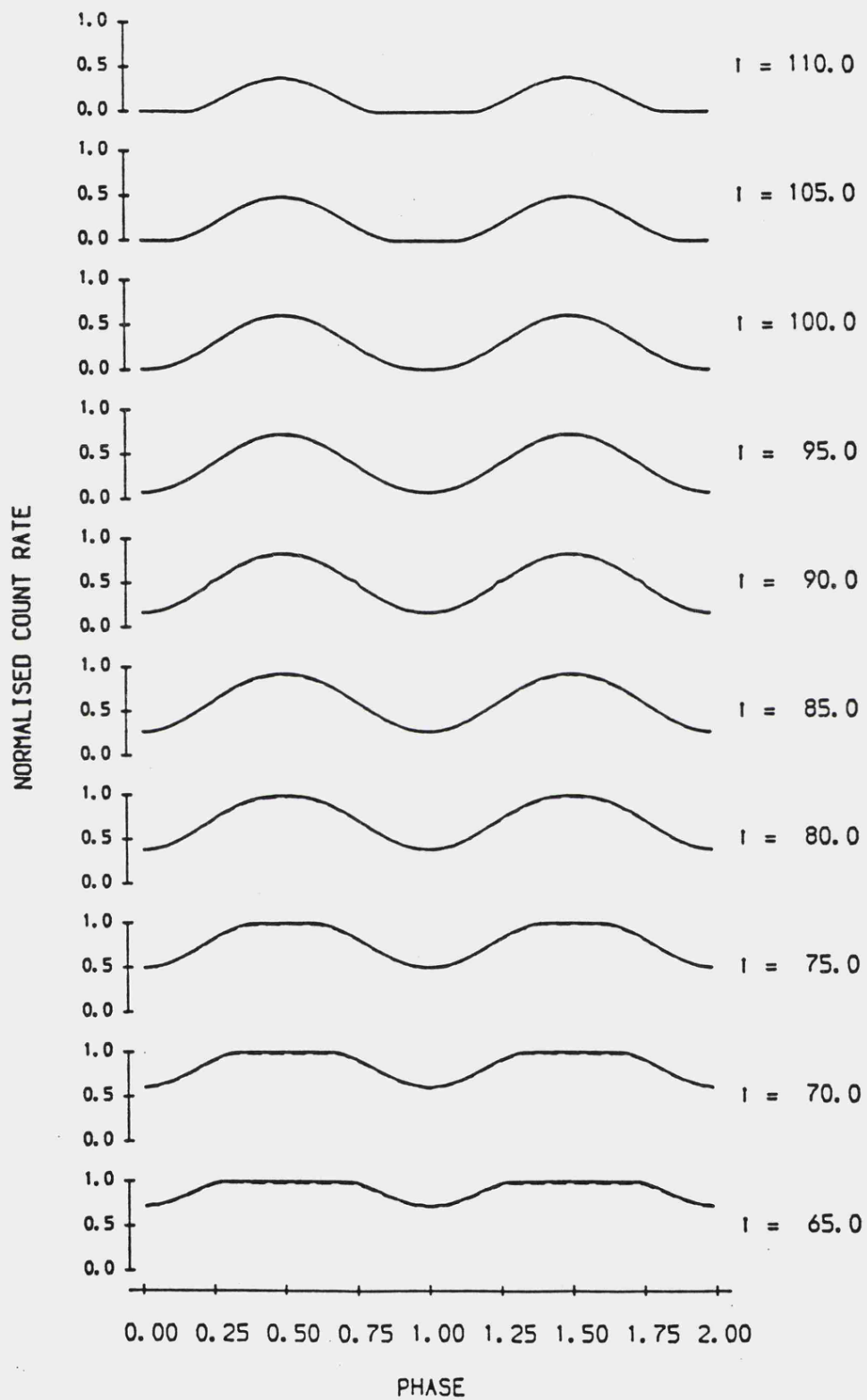


Figure 6.13(a) Sample ME lightcurve shapes.

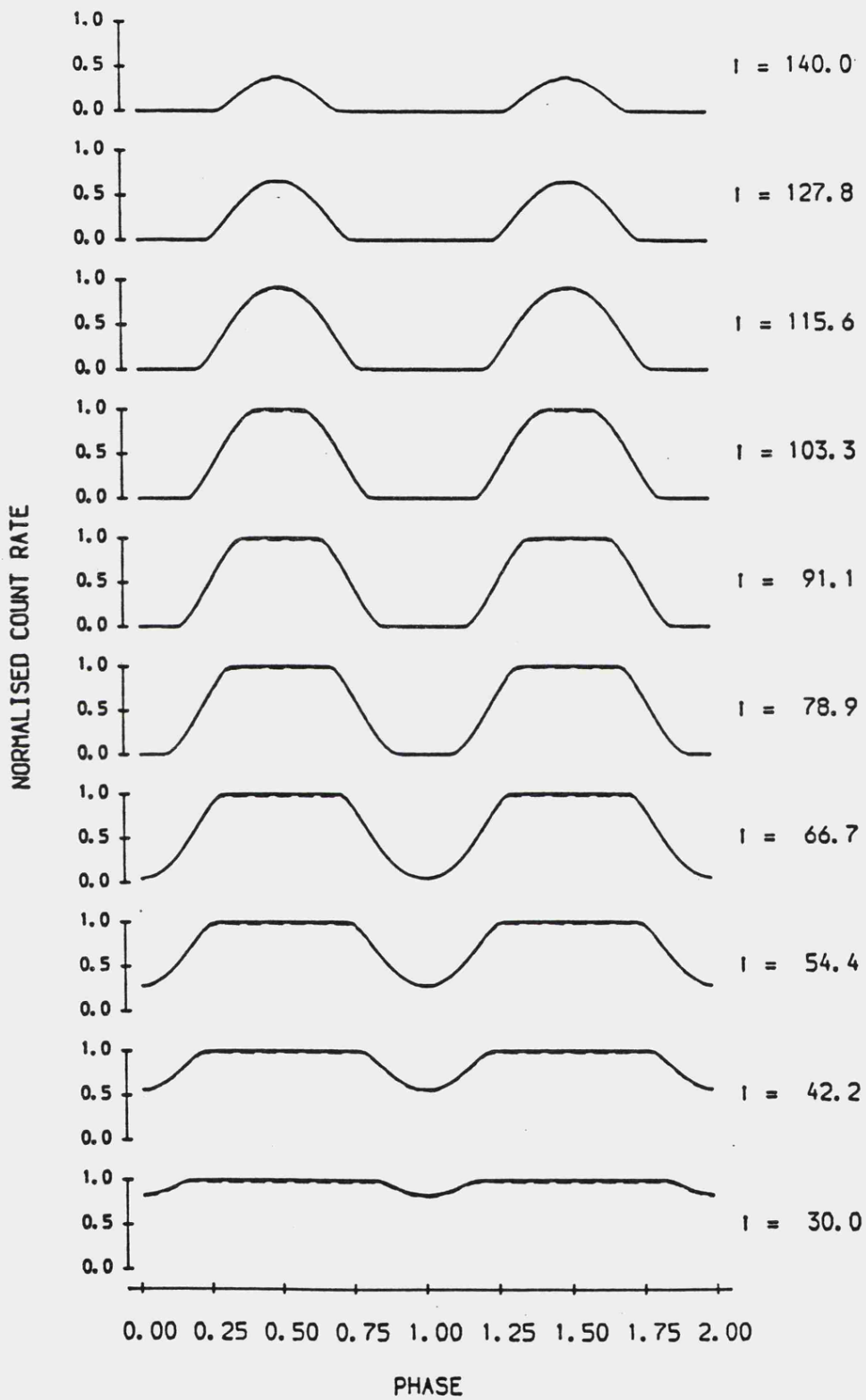


Figure 6.13(b) Sample ME lightcurve shapes.

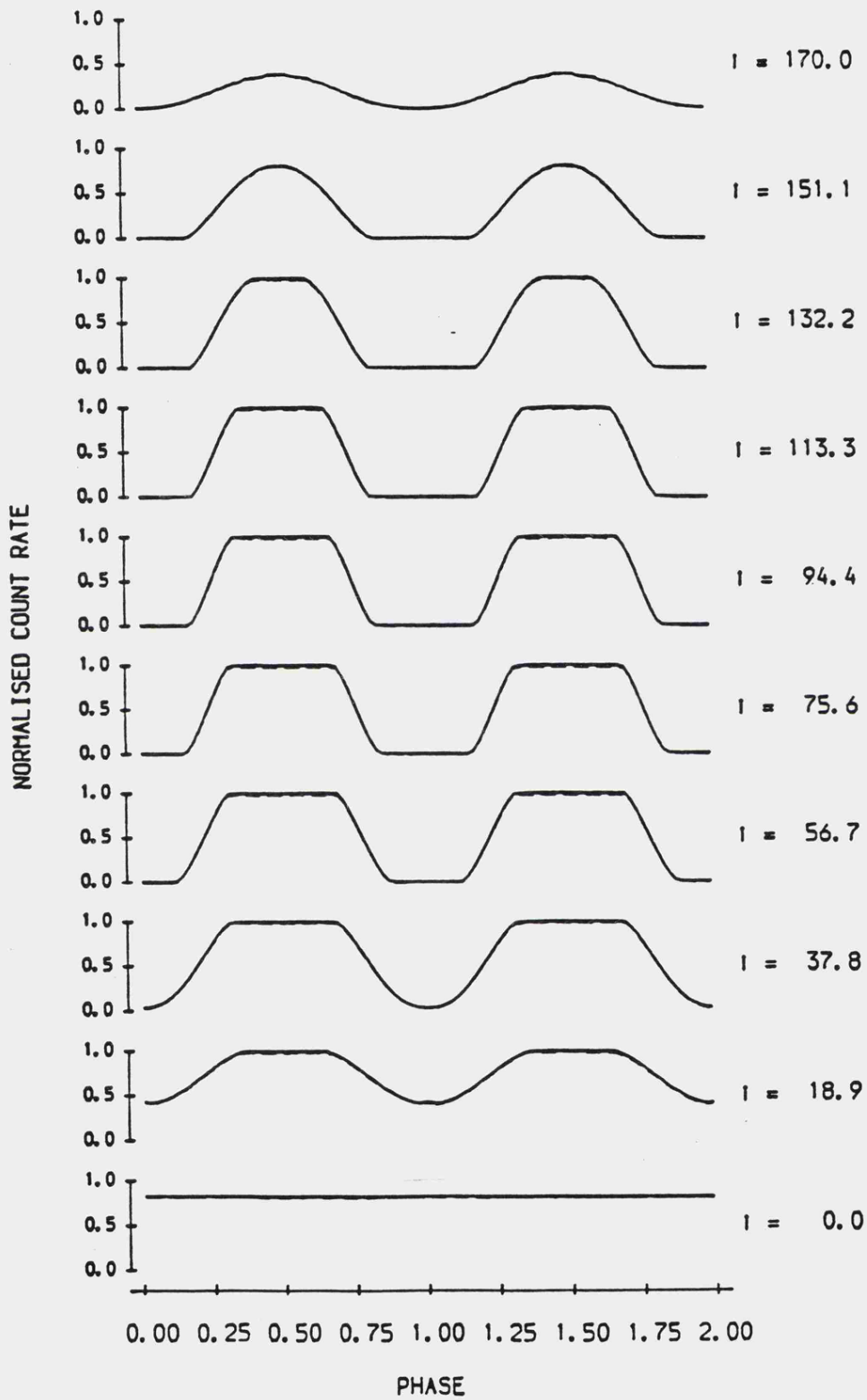


Figure 6.13(c) Sample ME lightcurve shapes.

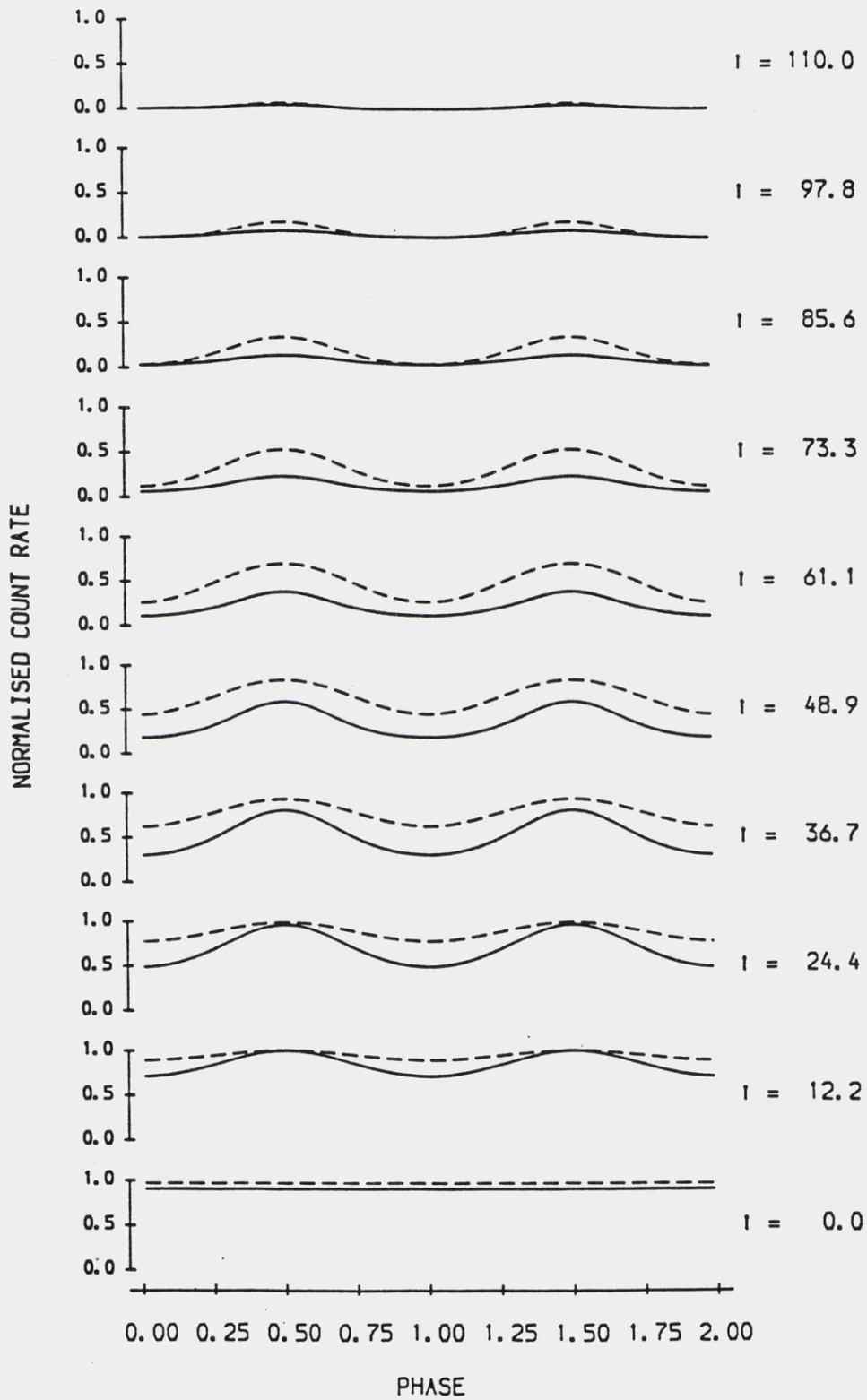


Figure 6.13(d) Sample LE lightcurve shapes.

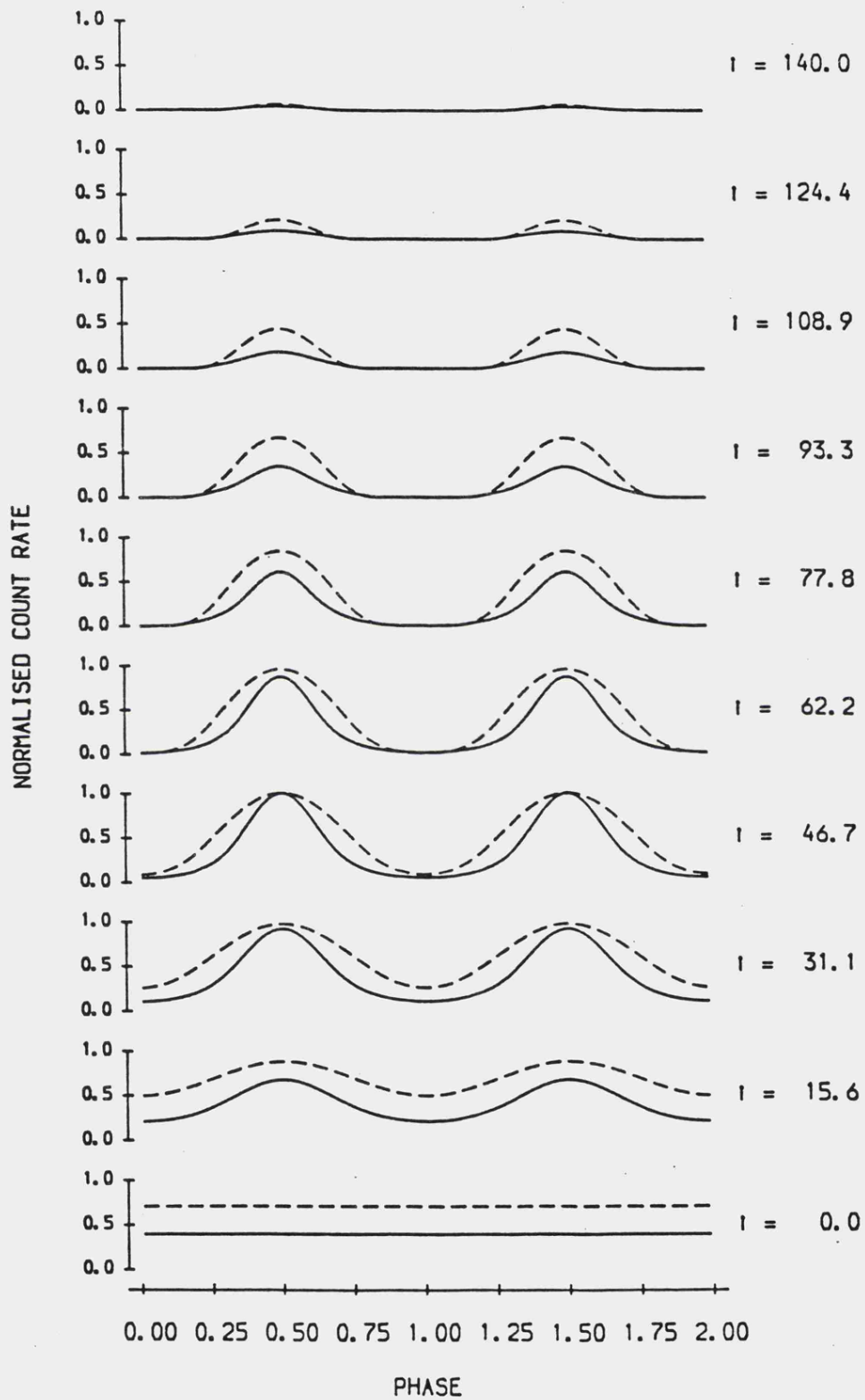


Figure 6.13(e) Sample LE lightcurve shapes.

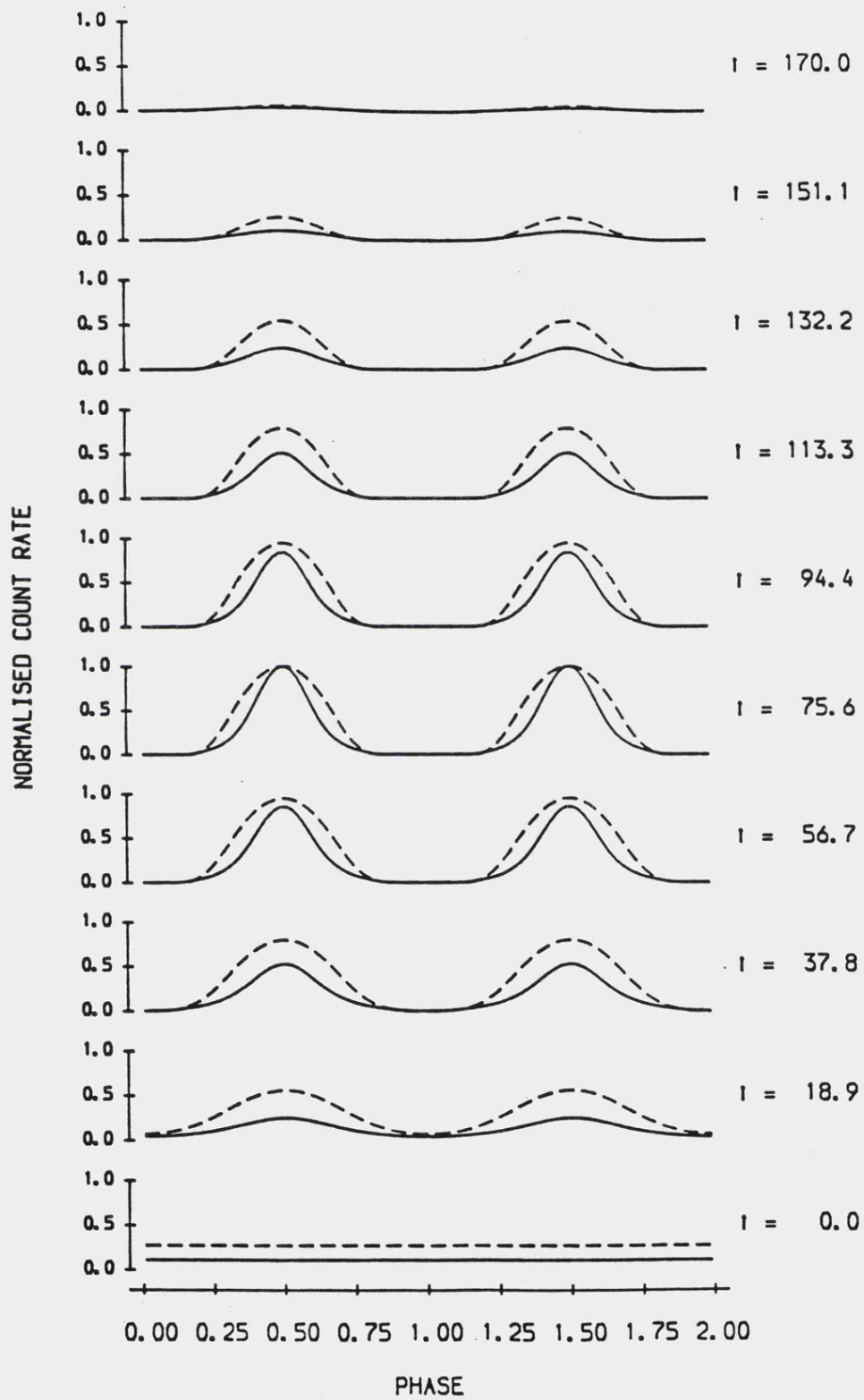


Figure 6.13(f) Sample I.E lightcurve shapes.

sinusoidal shapes are more common for large polecaps ($f > 0.05$). The LE lightcurves show a similar dependence on polecap size in terms of the probability of seeing a flat-bottomed lightcurve.

An effect not previously discussed can be seen in Figures 6.11 to 6.13, diagram (c). Here we see a flattening out of the lightcurve before it finally rises to its peak. The reason for this is simple, the hard X-ray shock extends down into the soft X-ray region (to about 1 keV) and at low temperatures with reasonable illumination and with the polecap on the limb the shock can dominate the limb darkened atmosphere contribution and give rise to an ME-like lightcurve. As the pole rotates round to the line of sight the atmosphere contribution increases and we see a smooth variation up to the maximum. As the fractional area of the polecap increases the effect is smoothed out in a similar way as for the ME lightcurves themselves.

So the shape of the LE lightcurve, unlike the ME lightcurve, depends not only on the geometry of the system but on the relative strengths of the hard and soft X-ray fluxes. These relative strengths of these components could change if the effective temperature is varied, for constant X-ray illumination, or if the hydrogen column density is varied. Increasing the effective temperature increases the relative strength of the soft X-ray flux; decreasing the hydrogen column density has the same effect. Figure 6.14 shows the variation in the shape of the LE lightcurve with hydrogen column density for a 50,000 K, 1 solar mass model atmosphere with 10% X-ray illumination, $f=0.01$, $i=45^\circ$ and $m=45^\circ$. Each curve is normalised to unity. With

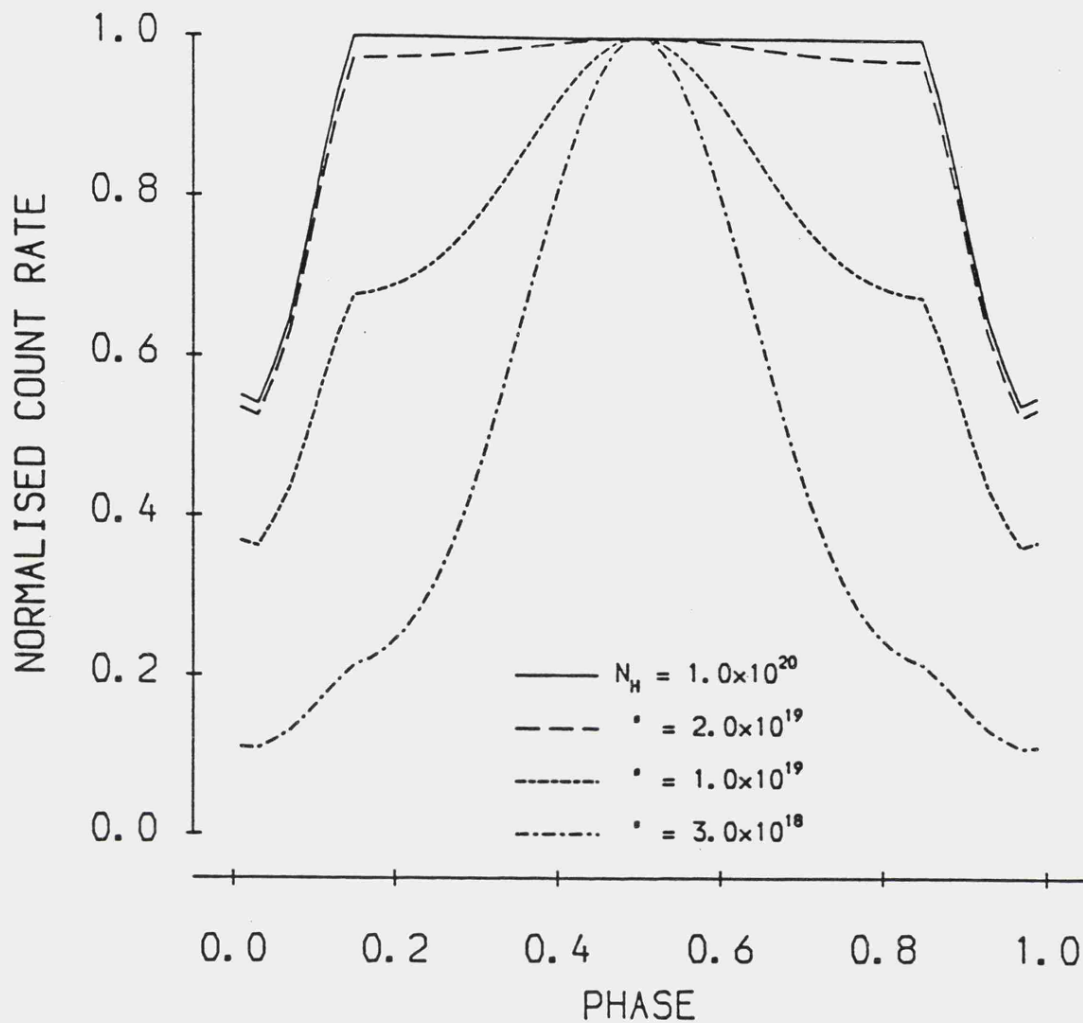


Figure 6.14 Shape of the LE lightcurve as a function of the hydrogen column density N_H ; for $f=0.01$, $m=45^\circ$, $i=45^\circ$, $T_{eff}=5.0 \times 10^4$ K and $P_{111}=10.0\%$. Each curve is normalised to unity.

$N_H = 1.0 \times 10^{20} \text{ cm}^{-2}$ the lightcurve is ME-like, reducing N_H to $3.0 \times 10^{18} \text{ cm}^{-2}$ causes the soft X-rays to dominate giving a smooth sinusoidal lightcurve. Figure 6.15 on the other hand shows the variation in the LE lightcurve shape with effective temperature. The parameters are the same as in Figure 6.14 except N_H is kept constant at $1.0 \times 10^{20} \text{ cm}^{-2}$. As before, the isotropic shock dominates for $T_{eff} < 100,000$ K but for $T_{eff} > 150,000$ K the soft X-rays dominate, the differing strengths of limb darkening being responsible for

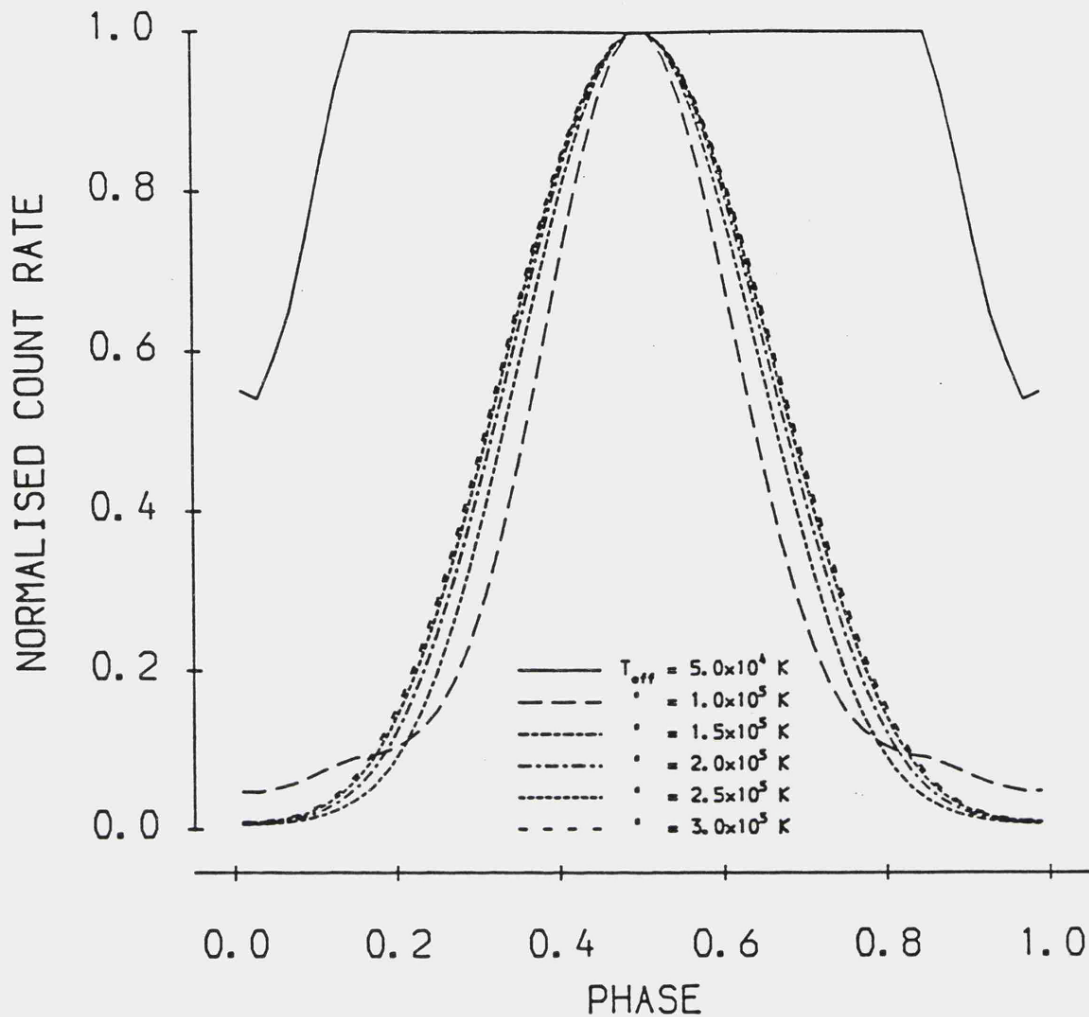


Figure 6.15 Shape of the LE lightcurve as a function of the effective temperature T_{eff} (parameters are the same as for Figure 6.14 except N_H is constant at $1.0 \times 10^{20} \text{ cm}^{-2}$). The curves are again normalised to unity.

the slight variations in the shape.

With random variations included the shapes of the lightcurves are no longer smooth. The two cases considered are; the random orientation of the polecap is constant with phase; the random orientation varies with phase. Figures 6.16(a) and (b) show the effect of the former on the ME and LE lightcurves respectively ($T_{eff} = 100,000 \text{ K}$, 10% hard X-ray illumination, $i=55^\circ$, $m=45^\circ$ and $f=0.01$), for four

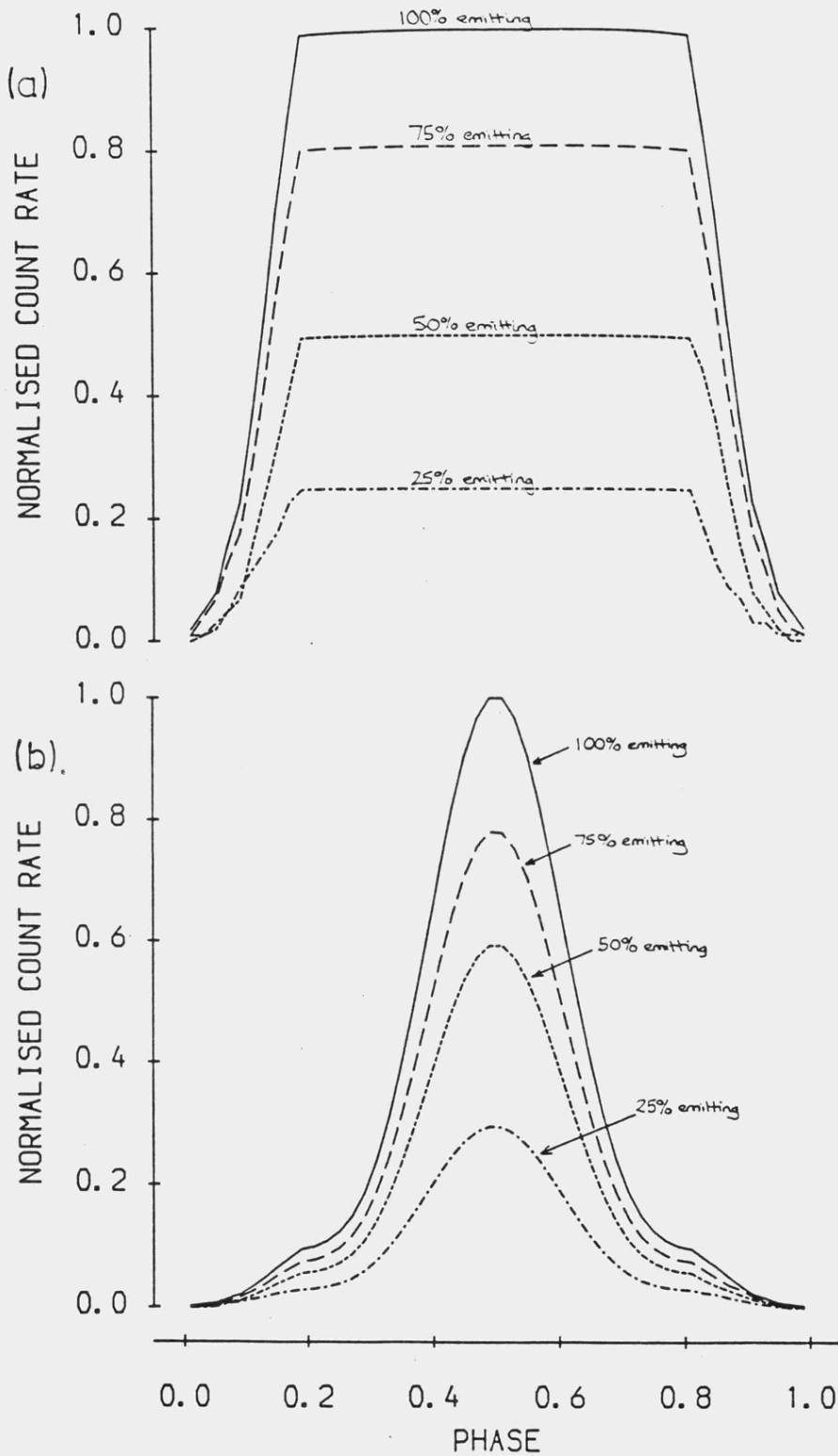


Figure 6.16 Lightcurve shapes for a random orientation of the polecap that is constant with phase; (a) ME and (b) LE. The curves are normalised to the 100% emitting lightcurve ($T_{\text{eff}} = 1.0 \times 10^5$ K, $m = 45^\circ$, $i = 55^\circ$, $f = 0.01$ and $P_{111} = 10^{0.6\%}$).

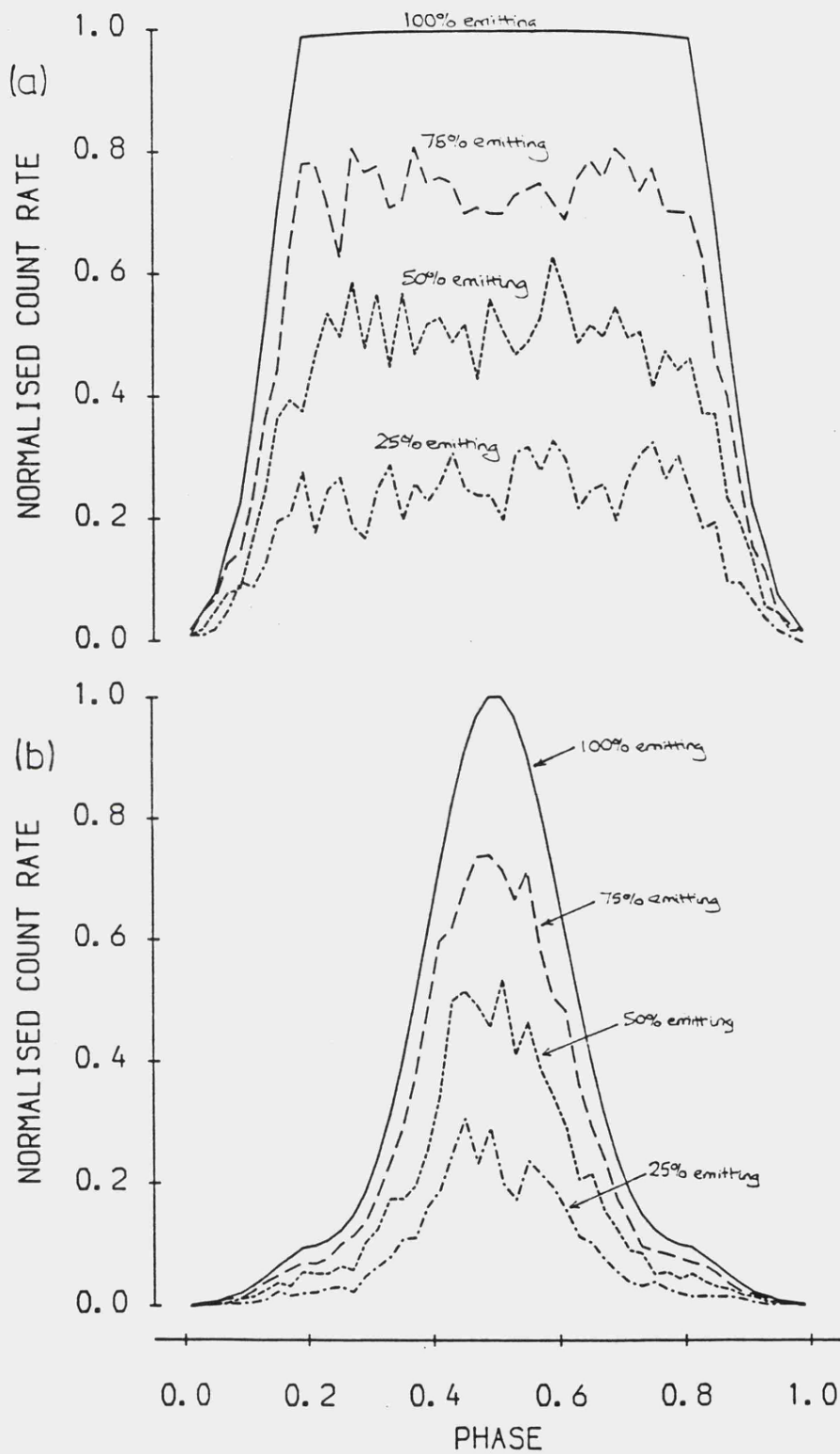


Figure 6.17 Lightcurve shapes for a random orientation of the polecap that is varying with phase; (a) ME and (b) LE. Each curve is normalised to the 100% emitting lightcurve (parameters as for Figure 6.16).

different fractional emitting areas. Each curve is normalised with respect to the '100% emitting' lightcurve. We see that fixing the random variation in phase has little effect on the overall shape of the lightcurves for both detectors. In contrast the lightcurves shown in Figures 6.17(a) and (b), which are for random orientations that are varying with phase, show quite strong flickering in both detectors, mimicking the observed variations quite well (geometry as in previous figure). With more phase bins the effect would be even more startling.

Summary

In this section I have shown the range of lightcurve shapes that are possible with this simple approach to simulating actual observations. We have seen that a model atmosphere gives realistic lightcurve shapes that include limb darkening in the soft X-rays but that the albedo component in the hard X-rays has no real affect on the shape. The hard X-ray lightcurves are exactly those predicted by King and Shaviv, sinusoidal variations being rare for small polecaps. An unpredicted effect was the two-component nature of the soft X-ray lightcurve, for some illuminations, temperatures and column densities the LE lightcurve can look distinctly hard X-ray like due to the isotropic hard X-ray component dominating the optically thick soft X-ray component (in the overlapping region of the ME and LE detectors). Lastly, by randomly varying the orientation of the emitting sectors within the polecap it was possible to mimic the flickering seen in observed

lightcurves.

The ultimate test of any model system is to use it to fit an observed system. In order to test this lightcurve model, AM Herculis was chosen as the source to be modelled as it is the brightest known source and high quality data is available from recent EXOSAT observations. The next section describes the procedure adopted to carry out the task.

6.6 A full parameter fit to AM Herculis

AM Herculis has been observed many times with X-ray satellites (for example; Hearn and Richardson, 1977; Bunner, 1978; Tuohy et al., 1978; Hayakawa et al., 1979; Rothschild et al., 1981; Fabbiano et al., 1981 and Heise et al., 1985). The X-ray emission has been seen to be variable but is generally characterised by broad, nearly total, eclipses in both the hard and soft X-ray regions with a period of 3.09 hours. With pre-EXOSAT observations the eclipses in the hard and soft X-rays were synchronised but when it was observed by Heise et al., (1985) the eclipses had shifted so that they were now 180° out of phase. This is known as the 'anomalous' state of AM Her. Heise's two observations were performed during the performance/verification phase of EXOSAT. Table 6.3 shows the observing log.

Table 6.3 EXOSAT observations of AM Her (Heise et al.)

	Date	Instrument	Exposure time (secs)
*	June 29 1983	CMA1,thin Lexan	48472
	June 30 1983	CMA2,thin Lexan + grating	48472
*	June 29 1983	ME	46540
*	Aug 10 1983	CMA1,thin Lexan + grating	68024
	Aug 10 1983	CMA2,thin Lexan + grating	61152
*	Aug 10 1983	ME	57620

6.6.1 The X-ray lightcurves of AM Herculis

The data from the observations marked with asterisks were folded on the current epheremis (MJD 2443014.265 = phase zero, period = 11139.292 seconds) into 50 phase bins. The resultant lightcurves are shown in Figures 6.18 and 6.19. The lightcurves are background subtracted and corrected for any telescope/detector errors. The count rates in the second CMA observation are reduced due to the presence of the grating in front of the detector.

The anti-phase relationship of the lightcurves can clearly be seen. The count rates in the second ME observation had increased by a factor of 1.8 compared with those in the first but the ratio between the maximum and minimum counts had decreased from ~ 2.4 to ~ 1.4 . Allowing for the reduction in flux due to the grating ($\sim 90\%$ is lost) there is little change in the LE lightcurve between the two observations.

Heise et al. assumed that since the ME lightcurve eclipse had originally been full and was now non-total that the extra flux at the minimum was coming from a second

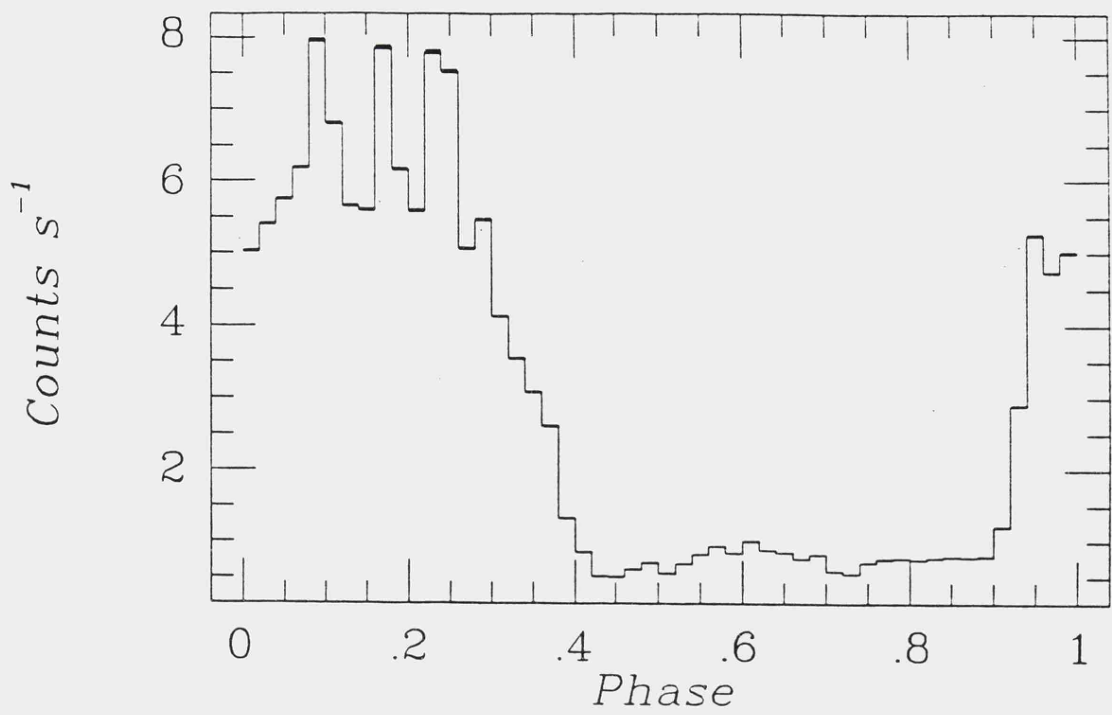


Figure 6.18(a) LE lightcurve from first observation (thin Lexan filter).

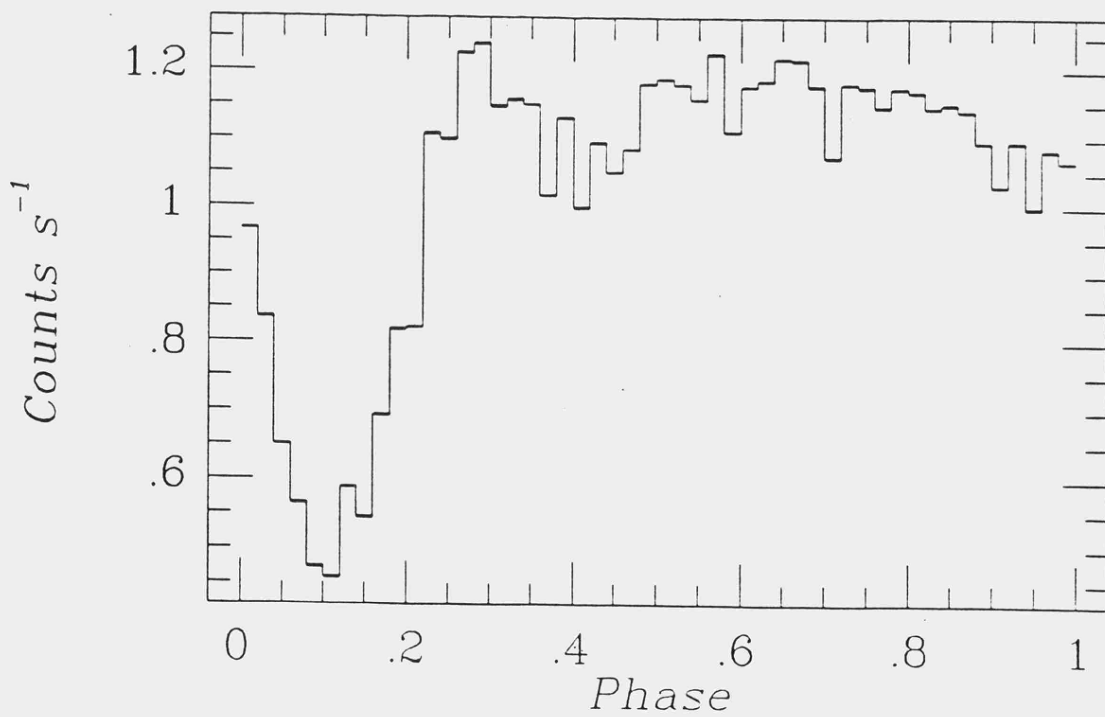


Figure 6.18(b) ME lightcurve from first observation.

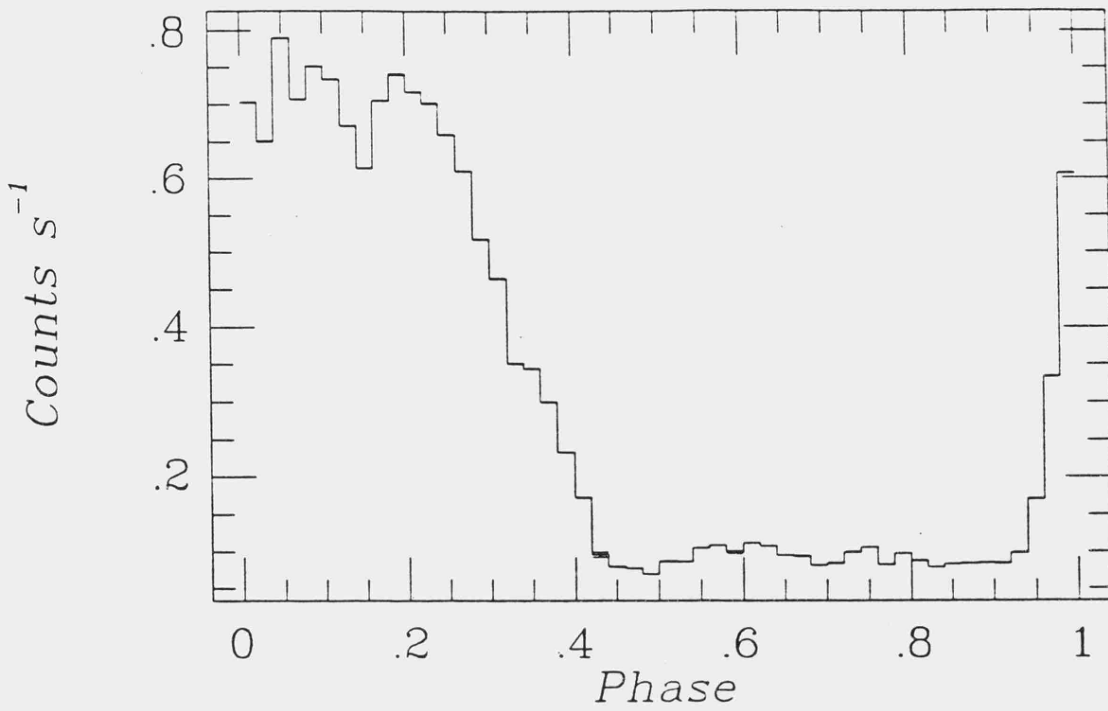


Figure 6.19(a) LE lightcurve from second observation (thin Lexan filter).

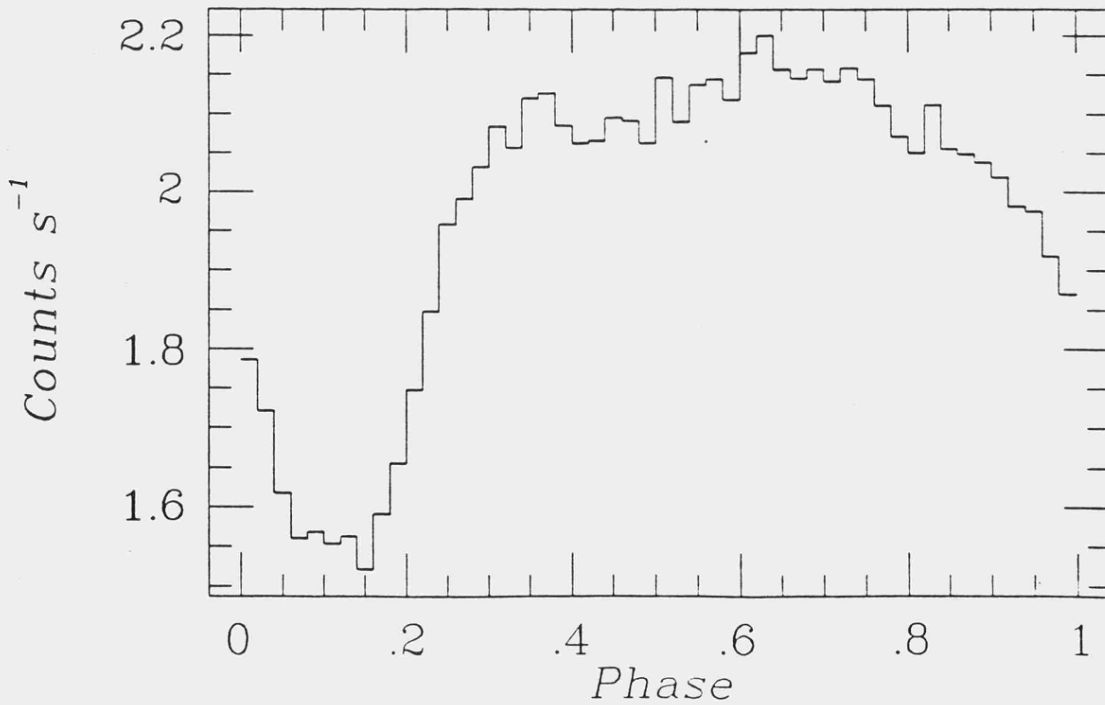


Figure 6.19(b) ME lightcurve from second observation.

pole, 180° away from the primary pole. The anti-phase soft X-ray lightcurve being entirely due to this secondary pole. At first glance this might seem reasonable but bearing in mind what we have seen before for the shapes of ME lightcurve possible there is a problem with this assumption. A two pole system is the only way to reproduce the out-of-phase lightcurves seen in AM Herculis. If we assume that the poles are exactly 180° apart, exactly the same size, and exactly the same temperature, then as one pole goes into eclipse the other is coming out of eclipse, the result is that we see no variation at all in the hard X-ray lightcurve. So in order to reproduce the ME lightcurve in AM Her from a two pole system, in the way that Heise et al. suggested, we must assume some asymmetry. The minimum comes from the secondary pole therefore that pole must be weaker than the primary in X-ray illumination (same effective temperature) or colder (less X-ray intensity needed to heat the atmosphere). In order to get only a single minimum from a double poled hard X-ray emitter the poles must be exactly the same size so that each poles' contributions match and a smooth drop is seen. Figure 6.20 shows the resultant hard X-ray lightcurve for various polecap asymmetries (assuming the secondary pole is weaker than the primary). Only for equal area poles do we see a single minimum, but this is a flat minimum which the observed lightcurve does not have. To get a smooth quasi-sinusoidal minimum requires that one or other of the poles is only partially eclipsed, meaning that the poles are dissimilar in size as well (otherwise they would both be partially visible at some time resulting in a quasi-

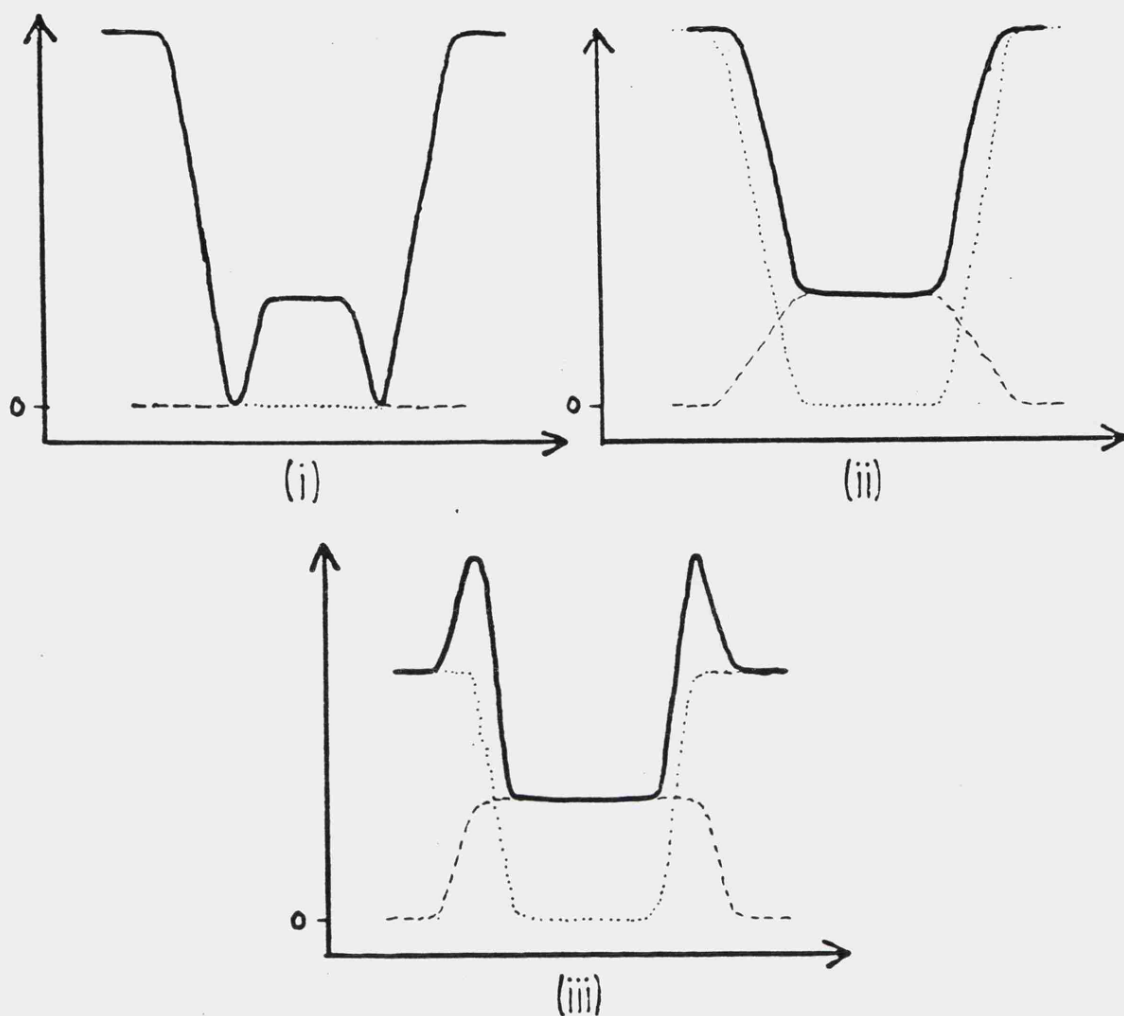


Figure 6.20 Hard X-ray eclipses for a two-pole system with one pole weaker than the other; (i) Primary pole larger than the secondary; (ii) Poles equal size; and (iii) Primary pole smaller than secondary. The dotted and dashed lines show each poles contribution.

sinusoidal variation) or that the poles are the same size but not 180° apart (the secondary is fully visible/eclipsed while the primary is only partially eclipsed). Considering the former, to get the right sized polecaps with the right relative intensities to give the observed lightcurve would be very rare indeed as two minima or maxima would be most likely to result with this system. The latter however is

more likely to give the required lightcurve but it still has the constraint that the poles are the same size and that the primary pole dominates the X-ray emission.

There is one assumption that Heise et al. did not make, that the ME lightcurve is due to one pole only. Since the hard X-ray lightcurve was originally a one pole lightcurve there is no reason why the accretion geometry could not change so as to make the pole only partially eclipsed. If the accretion rate increased then the primary pole would increase in size and some material might spill around into the secondary pole causing its luminosity to increase and give rise to the anti-phase lightcurves. When AM Her returns to its low state the secondary pole will turn off and the lightcurves return to their original phase relationship. This simple explanation leaves a lot less to chance than the above and still allows for a two pole system, the soft X-ray flux from this pole giving rise to the small 'hump' seen in the minimum of the LE lightcurve at around phase 0.6. So this geometry was adopted for AM Herculis and the actual fitting of the lightcurves could then be undertaken. The assumption that the ME lightcurve came only from the primary pole was the only major assumption made in the fitting of the EXOSAT lightcurves, described in the next few sections.

Note : All fitting was done using one solar mass model atmospheres (i.e., gravity , $g = 4.45 \times 10^8 \text{ cm s}^{-2}$)

6.6.2 Fitting the ME lightcurve from the first observation

We have seen in Section 6.5 that the shape of the hard

X-ray lightcurve depends on three parameters only; the fractional area of the polecap, f ; the magnetic axis angle, m and the inclination of the rotational axis to the line of sight, i . By choosing different fractional areas the best fitting values for i and m can be found by searching the i and m parameter space for the lowest value of the chi-squared errors in the fit.

To fit the shape only, the distance, effective temperature and percentage of X-ray illumination are kept constant at some arbitrary values. The errors in the observed counts were used to derive non-reduced chi-square errors for the fit (the chi-squares were not reduced since the same number of points were used throughout the fitting). These were expected to be high, due to the small errors in the count rates coupled with the large variations in the lightcurve. For shape fitting the lightcurve is normalised to give the best fit by multiplying it by α where α is given by

$$\alpha = \frac{\sum_i y(i)f(i)}{\sum_i f(i)^2} \quad (6.18)$$

$y(i)$ are the observed count rates and $f(i)$ are the calculated count rates. Since the phase used in our calculation may not be the same phase used in the observed lightcurve, shifting of the observed lightcurve in phase was allowed, in order to find the best agreement with the calculated lightcurve.

Table 6.4 shows the results of the shape fitting of the ME lightcurve. The best values of i and m for each f are shown along with the associated chi-squared errors. It

Table 6.4 Results of fitting the shape of the ME lightcurve from the first observation.

Fractional area of polecap, f	Best fitting m (°) (all $\pm 0.5^\circ$) ⁺	Best fitting i (°) (all $\pm 0.5^\circ$) ⁺	χ^2 ($\times 10^5$)	Phase shift
0.05	42.8	44.4	3.829	0.12
0.01	42.4	48.4	1.639	0.12
* 0.008	49.0	42.0	1.612	0.12
* 0.007	"	"	"	"
0.006	52.5	38.5	1.579	0.12
0.005	52.5	38.5	1.580	0.12

* same number of sectors used in polecap

⁺ the $\pm 0.5^\circ$ errors indicate that the fit could only be determined to $\pm 0.5^\circ$ (due to computational time limits), not that $\pm 0.5^\circ$ gives an acceptable fit (as is shown in Figure 6.21)

shows that the best fit to the shape comes from $f=0.006$, $m=52.5^\circ \pm 0.5^\circ$ and $i=38.5^\circ \pm 0.5^\circ$. Figure 6.21 shows the fit graphically and we see that the sinusoidal minimum is fitted almost exactly, with good agreement with the flat-topped maximum. Note that the $\pm 0.5^\circ$ error 'fits' (shown by the dotted lines) are not acceptable, indicating the strong dependence of the lightcurve fit on i and m . Figure 6.21A shows the lightcurve fits for all the fits shown in the table. Note that the lightcurves for $f=0.10$, 0.008, 0.006 and 0.005 are very similar in shape, the only difference being the eclipse depths; the figure shows that these lightcurves are, in fact, more acceptable as fits than the $\pm 0.5^\circ$ lightcurves !

The next step is to find values for the effective temperature, T_{eff} , percentage X-ray illumination, P_{ill} and the distance to the source, d_{pc} . There is a limit on these since the resultant LE count rates must not exceed the 'hump' in the LE lightcurve. The strength of the random

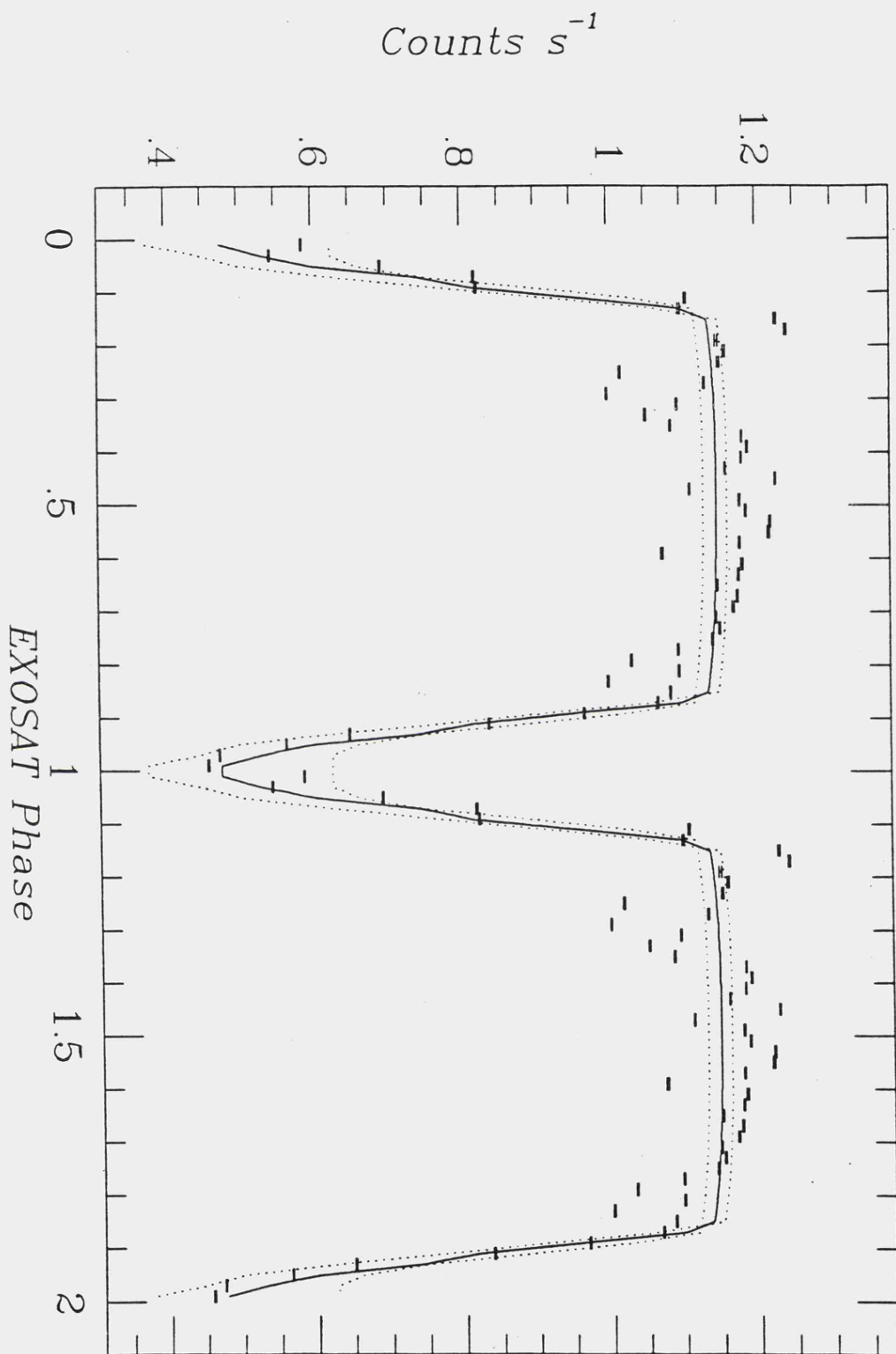


Figure 6.21 Best fit to the shape of the ME lightcurve from the first observation (repeated twice for clarity). Best fit is $f=0.006$, $m=52.5^\circ$ and $i=38.5^\circ$. The $\pm 0.5^\circ$ lightcurves are shown by dotted lines.

variations in the lightcurve can also be fitted to some extent so as to give a value for f_{emit} , the fraction of the polecap actually emitting. The random variations were allowed to vary with phase as this gave more observational-like lightcurves. The random fitting was done by trial and error until the strength of the calculated and observed flickering was about the same. It is easier, initially, to fit the count rates with non-random counts, the normalisation factor α can then be related directly to the actual distance, d_{pc} , by

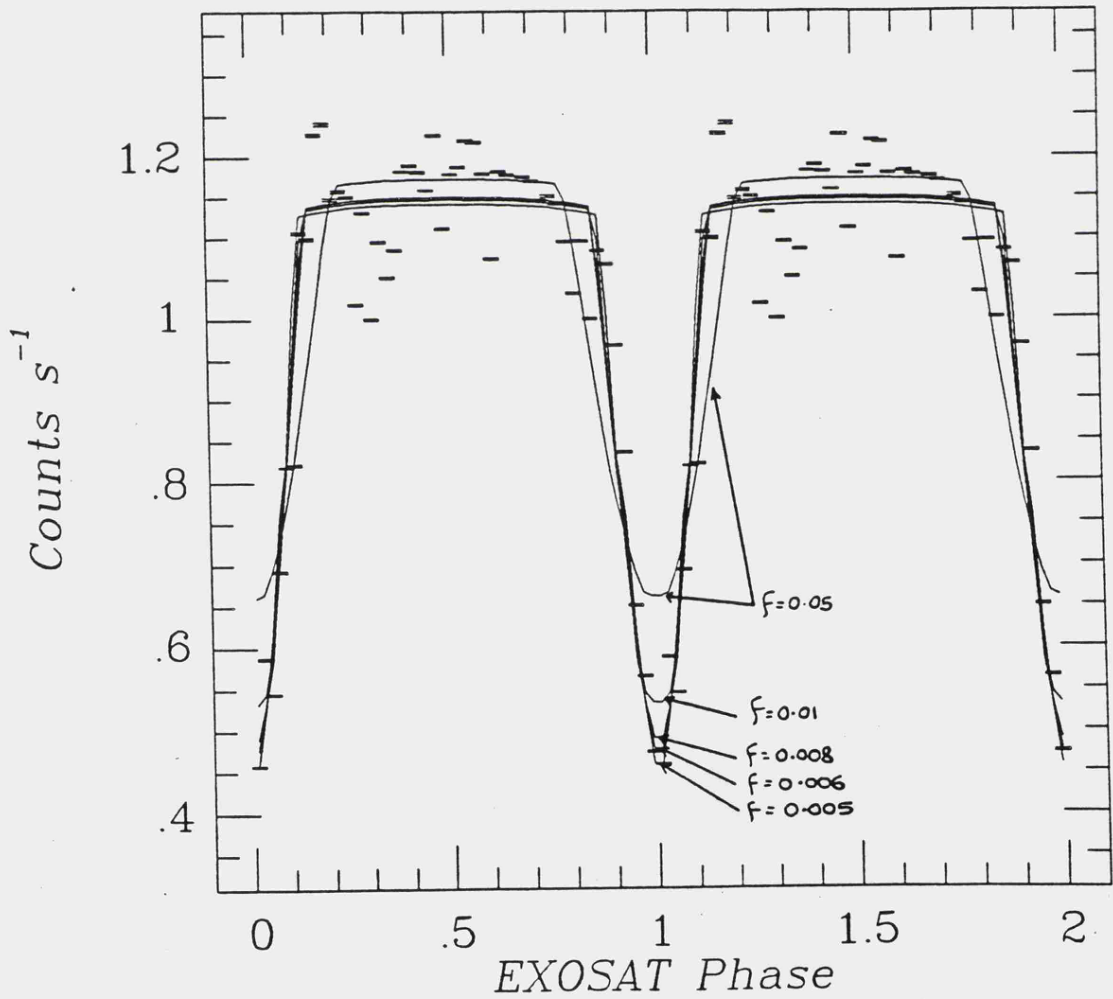


Figure 6.21A Best fits to observed ME lightcurve from Table 6.4. Note that the curves for $f=0.01$, 0.008 , 0.006 and 0.005 are very similar, the only distinguishing feature being the eclipse depth.

$$d_{pc} = \alpha^{-1/2} d_x \quad (6.19)$$

where d_x is the fitting distance chosen arbitrarily before. Once an idea of the best fit values is found the random variations can be put in and the distance, temperature or illumination corrected to give the correct count rates. The energy range for the calculated spectrum was chosen to be the same as the energy range in the observation (i.e., 1.9 - 8.5 keV). Table 6.5 shows the results of this fitting, included in the table are the maximum LE count rates through the thin Lexan filter, LE_7 for two hydrogen column densities, N_H .

Any model that gives a distance less than 50 parsec can be excluded since no parallax has been observed for AM Her. Analysis of the LE lightcurve shows that the second maximum

Table 6.5 Results of fitting the LE lightcurve from the first observation.

P_{111} (%)	T_{eff} ($\times 10^5$)	d_x	α	d_{pc}	N_H ($\times 10^{20}$)	LE_7 (s^{-1})	Comments
10.0	1.0	100.0	34.1	17.1	-	-	too near
10.0	2.0	100.0	1.87	73.1	1.0	~ 54	too many LE cnts
50.0	1.0	100.0	6.82	38.3	1.0 0.1	~ 0.5 ~ 1.5	too near
50.0	1.5	100.0	1.27	88.7	1.0	~ 5.0	too many LE cnts
50.0	2.0	100.0	0.417	154.9	1.0	~ 10	too many LE cnts
99.9	1.0	100.0	3.63	52.5	1.0 0.1	~ 0.3 ~ 0.9	OK
99.9	1.15	100.0	1.93	72.0	1.0 0.1	~ 0.7 ~ 3.0	OK too many LE cnts
99.9	1.5	100.0	0.667	122.4	1.0	~ 2.0	too many LE cnts
99.9	2.0	100.0	0.202	222.5	1.0	~ 3.5	too many LE cnts

peaks at about one count per second so any model giving more counts than this can also be excluded. So from the table, bearing the above in mind, we see that only three models give the required ME and LE count rates. They are all 99.9% illuminated and have the following parameters :-

- (1) $T_{\text{eff}} = 100,000 \text{ K}$, $N_{\text{H}} = 1.0 \times 10^{19} \text{ cm}^{-2}$, $d_{\text{pc}} = 52.5 \text{ parsec}$
- (2) $T_{\text{eff}} = 100,000 \text{ K}$, $N_{\text{H}} = 1.0 \times 10^{20} \text{ cm}^{-2}$, $d_{\text{pc}} = 52.5 \text{ parsec}$
- (3) $T_{\text{eff}} = 115,000 \text{ K}$, $N_{\text{H}} = 1.0 \times 10^{20} \text{ cm}^{-2}$, $d_{\text{pc}} = 72.0 \text{ parsec}$

The accepted value for the distance to AM Herculis, from observations of the secondary star, is 71 ± 18 parsec (Young and Schneider, 1981) so model number (3) gives the best fit.

By trial and error it was found that if 0.85 of the polecap was emitting then the random variations introduced were of approximately the same order as those seen in the observed lightcurves. Reducing the emitting area by 0.15 reduces the flux by the same amount so to correct this the distance could be decreased to 66.4 parsec or the effective temperature could be increased. Since we require the distance to be approximately 71 parsec the effective temperature was increased in 5000 K steps until the fitted distance agreed, as near as possible, with the accepted distance. It was found that a 120,000 K, 99.9% illuminated model gave a distance to AM Her of 72.6 parsec with a maximum LE count rate of 0.9 counts per second. Figure 6.22 shows graphically this best fitting model compared with the observed ME lightcurve. Note how the random variations mimic rather well those actually seen. Figure

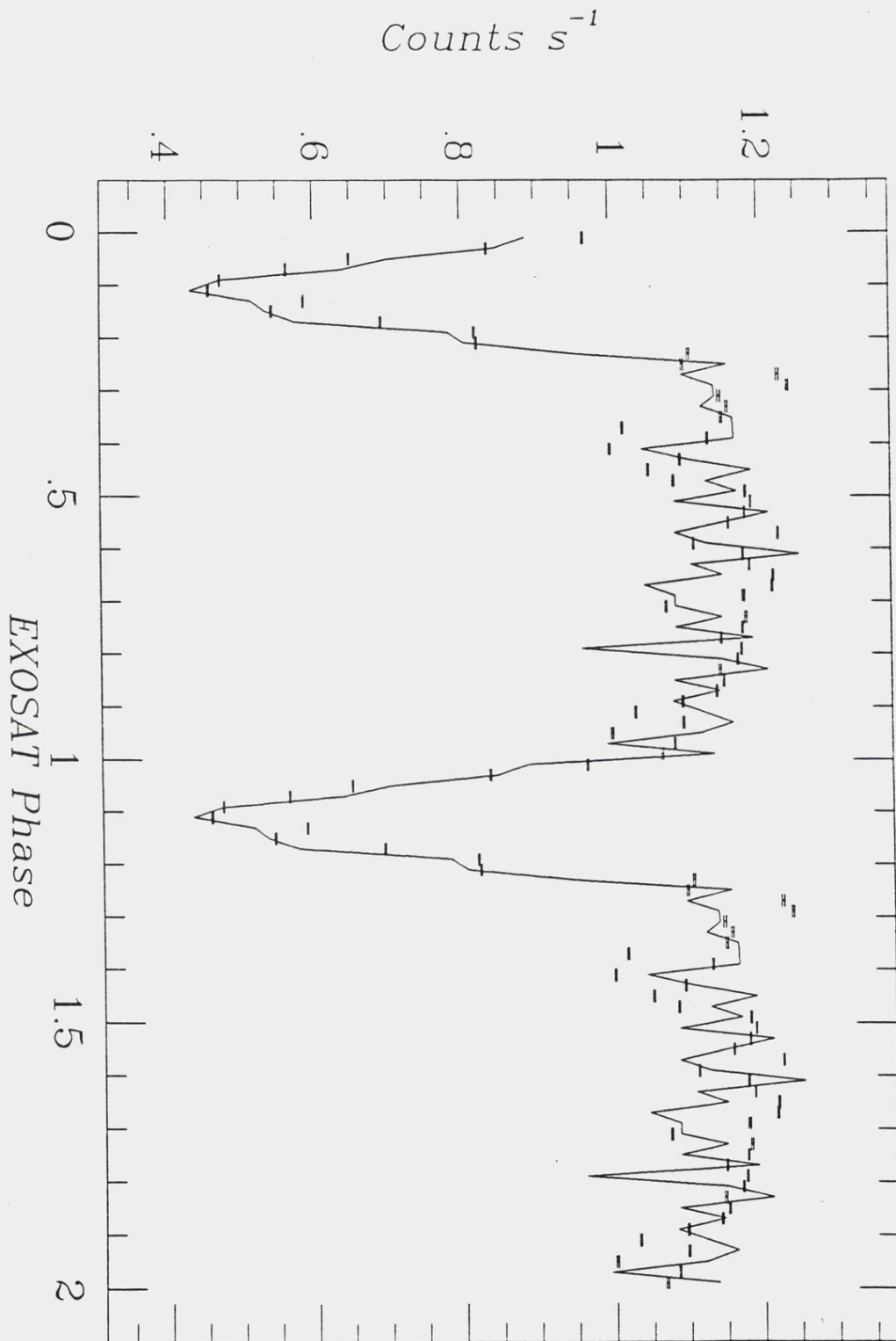


Figure 6.22 Best fit to the shape and count rates of the ME lightcurve from the first observation. Parameters are; $m=52.5^\circ$, $i=38.5^\circ$, $f=0.006$, $f_{\text{em}}=0.85$, $T_{\text{eff}}=1.2 \times 10^5 \text{ K}$, $p=99.9\%$, $d_{pc}^{emit}=72.6 \text{ parsec}$ and $N_{\text{H}}=1.0 \times 10^{20} \text{ cm}^{-2}$.

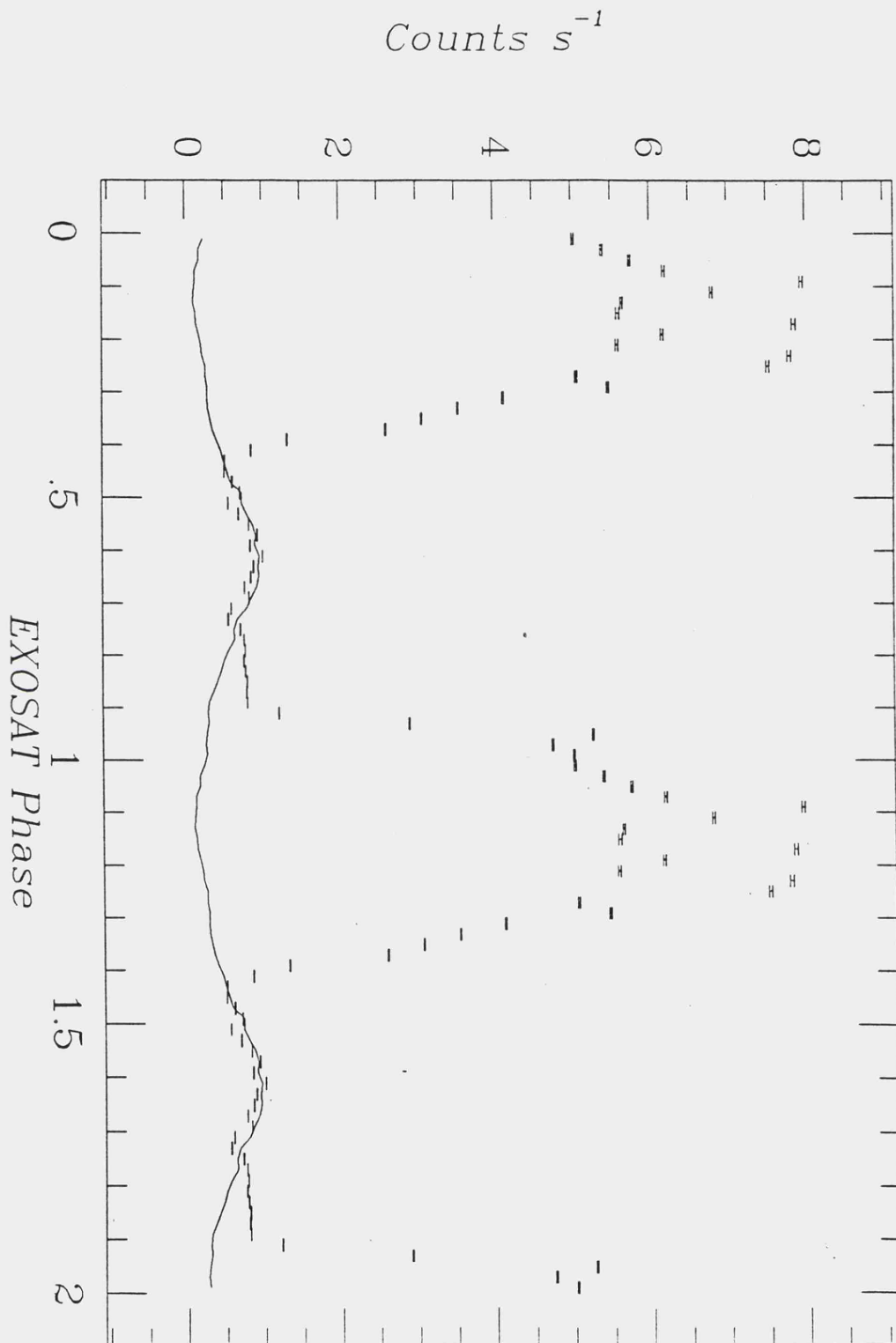


Figure 6.23 Primary pole's contribution to the LE lightcurve from the first observation.

6.23 shows the contribution to the LE lightcurve from this fit. Note that the 'hump' at phase 0.6 is fitted almost exactly.

To recap then, the inferred values for the geometry etc., of the primary pole in AM Herculis are :-

Inclination to the line of sight	= 38.5°
Angle between rotational and magnetic axes	= 52.5°
Fractional area of the polecap	= 0.006
Fractional area of the polecap emitting	= 0.85
Fractional emitting area (0.006x0.85)	= 5.1×10^{-3}
Effective temperature	= 1.2×10^5 K
Percentage of X-ray illumination	= 99.9%

The distance to AM Herculis was assumed to be 72.6 parsec with a hydrogen column density of $1.0 \times 10^{20} \text{ cm}^{-2}$. From the fitting it was found that phase zero used in the calculations was in fact equivalent to phase 0.12 in the EXOSAT ME lightcurve. A comparison between the values of i and m shown above and those from polarisation arguments is discussed later in this chapter.

6.6.3 Fitting the soft X-ray lightcurve

The first step is to subtract the contribution of the primary pole to this lightcurve. Figure 6.24 shows the resultant lightcurve. We have seen that the shape of a soft X-ray lightcurve is not just a function of the geometry, it is also a function of the effective temperature. This makes the fitting of the LE lightcurve

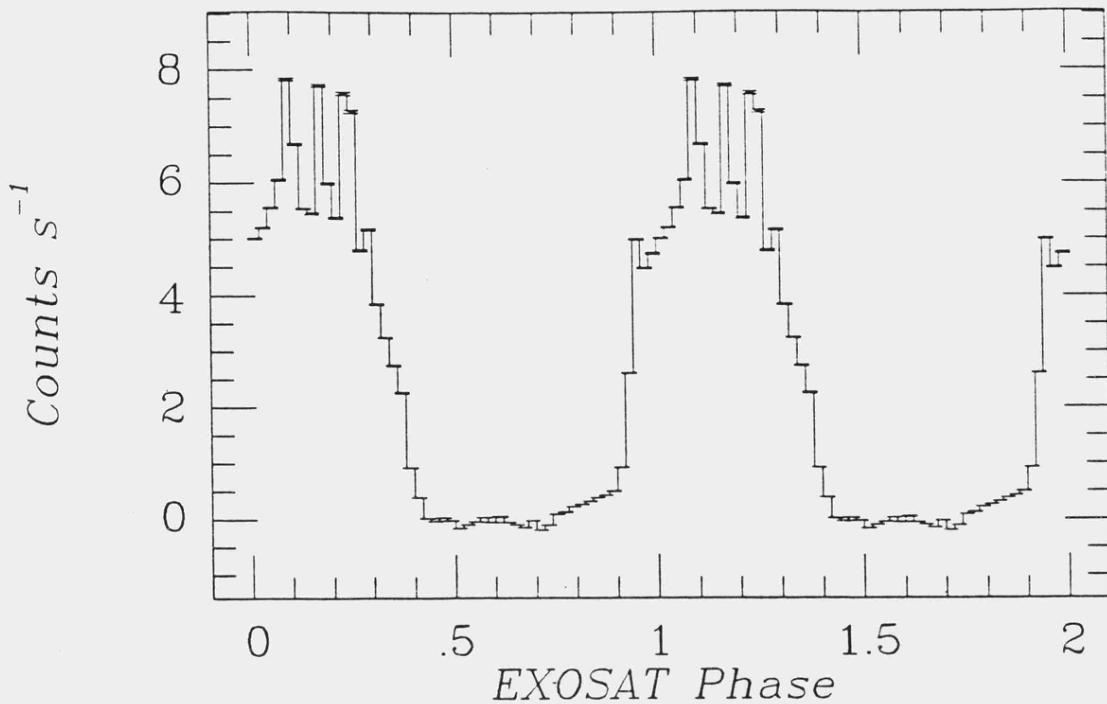


Figure 6.24 First observation LE lightcurve with primary pole's contribution subtracted.

difficult in that it is not possible to fit the shape and the count rates separately. However since we already know one angle in the geometry, the inclination to the line of sight, this problem is not as bad as it may seem.

By fitting the shape of the LE lightcurve a normalisation factor α is found, in the ME lightcurve fitting this was related to the fitted distance but in the LE lightcurve fitting it can be related to the fractional area of the polecap emitting, f_{emit} . So if $\alpha > 1$ the model, and all other models below this effective temperature, can be ignored. Also, if the fitting of a particular model gives $\alpha < 10^{-2}$ then that model and all models with effective temperatures greater than that can be ignored, for the reason that the smaller the fractional area emitting, the greater the random variations introduced; for $\alpha < 10^{-2}$ the random variations could give rise to lightcurves with huge

'steps' in the counts. There is another limit on the necessary parameter space that needs to be searched. This comes from considering the hard X-ray emission from this pole. We have assumed that there is essentially no hard X-ray emission from this pole. However a hard X-ray flux of about 5% of that seen from the primary pole would be undetectable in the lightcurve (i.e., $\sim 6.0 \times 10^{-2}$ count s^{-1}). Thus any model which gives a hard X-ray flux greater than this can be ignored. Since the strength of the illumination has the most effect on the hard X-ray flux it was expected that only approximately unilluminated atmospheres would fit this criterion.

Bearing all the above in mind, for a chosen effective temperature, percentage of illumination and fractional polecap area the best fitting magnetic axis angle was found by the same method used before in the fitting of the shape of the ME lightcurve. The best fitting fractional area, for each temperature and illumination, was taken to be that with the lowest value of chi-squared. The values for the effective temperature and percentage of X-ray illumination were chosen bearing the above limits in mind.

Table 6.6 shows the results of this fitting, assuming that the inclination to the line of sight was 38.5° , the distance was 72.6 parsec and the hydrogen column density was 1.0×10^{20} cm^{-2} . The maximum ME count rate is only shown for the best fitting polecap area at each temperature and illumination. The high values for the chi-squared errors are due to the small error bars combined with the large random flickering in the observed lightcurve. Considering Table 6.6, effective temperatures less than 150,000 K were

Table 6.6 Results from fitting the first observation
LE lightcurve (primary pole subtracted).
($i=38.5^\circ$, $d_{pc}=72.6$ parsec, $N_H=1.0 \times 10^{20}$ cm^{-2})

P_{ill} (%)	T_{eff} ($\times 10^5$ K)	f	m ($\pm 0.5^\circ$)	χ^2 ($\times 10^5$)	α (= f_{emit})	P_{sh}	ME (s^{-1})	
0.01	1.5	0.02	293.0	5.624	0.311	0.14		
"	"	0.01	295.5	5.570	0.565	0.14		} $\sim 10^{-4}$ A
"	"	0.008	296.0	5.565	0.687	0.14		
"	"	0.006	"	5.564	0.868	0.14		
"	"	0.005	296.5	5.562	1.117	0.14		
"	"	0.004	297.0	5.563	1.500	0.14		
"	2.0	0.02	288.0	5.567	0.042	0.14		
"	"	0.01	290.0	5.437	0.105	0.14	$\sim 10^{-4}$	B
"	"	0.008	290.5	5.440	0.128	0.14		
"	2.5	0.02	285.5	5.395	0.018	0.14		
"	"	0.01	287.5	5.372	0.033	0.14	$\sim 10^{-4}$	C
"	"	0.008	288.0	5.379	0.040	0.14		
1.0	1.5	0.01	294.5	5.560	0.627	0.14		} $\sim 10^{-2}$ D
"	"	0.008	"	5.554	0.712	0.14		
"	"	0.006	295.0	5.552	0.962	0.14		
"	"	0.005	295.5	5.551	1.239	0.14		
"	"	0.004	"	5.553	1.683	0.14		
"	2.0	0.02	287.5	5.449	0.060	0.14		
"	"	0.01	289.5	5.416	0.112	0.14	$\sim 10^{-2}$	E
"	"	0.008	290.0	5.420	0.136	0.14		
"	2.5	0.02	285.0	5.272	0.023	0.14		
"	"	0.01	287.0	5.248	0.041	0.14	$\sim 10^{-2}$	F
"	"	0.008	287.5	5.253	0.063	0.14		

m = best fitting magnetic axis angle
 P = phase shift for best fit
 ME^h = maximum count rate in ME filter

found to give fractional emitting areas greater than one, conversely, effective temperatures greater than 250,000 K were found to give fractional emitting areas less than 1.0×10^{-2} . X-ray illuminations greater than 1.0% gave ME count rates above the maximum allowed. We have six best fits from the table, A-F.

Fit A: Due to the small variations in the chi-squared values this fit gives a fractional polecap area from 0.004 - 0.01, with corresponding values of f_{emit} from 1.5 -

0.565. The preferred value for f_{emit} (by observation) was approximately 0.8-0.9 so $f=0.006$ was chosen as this gives a reasonable value of $f_{\text{emit}}=0.868$. The ME count rate is well within the allowed limit.

Fit B: f_{emit} for this fit is smaller than the light-curve would indicate. The ME count rate is satisfactorily reproduced.

Fit C: f_{emit} is very small. The actual emitting area would be 3.3×10^{-4} which is much smaller than normally associated with these systems: this fit was discounted.

Fit D: This is similar to fit A. The best fit is again variable but $f=0.006$ ($f_{\text{emit}}=0.962$) gives the best results.

Fit E: As for fit B.

Fit F: As for fit C.

Figures 6.25 to 6.28 show graphically the fits A,B,D and E to the primary-subtracted LE lightcurve. The random variations have been included and are phase variable. It is obvious that fits A and D give the best approximations to the flickering in the observed lightcurve.

The fitting of the lightcurves from the first observation is now complete, a full list of the fitted parameters is shown in Table 6.7. Due to the time consuming nature of the soft X-ray fitting the effective temperature inferred for the secondary pole is not as accurate as that for the primary pole. The soft X-ray fitting strongly depends on the assumed value for the hydrogen column density, a few percent each way can give large changes in the fitted temperature. However, assumptions have to be made in all kinds of spectral fitting and as such the

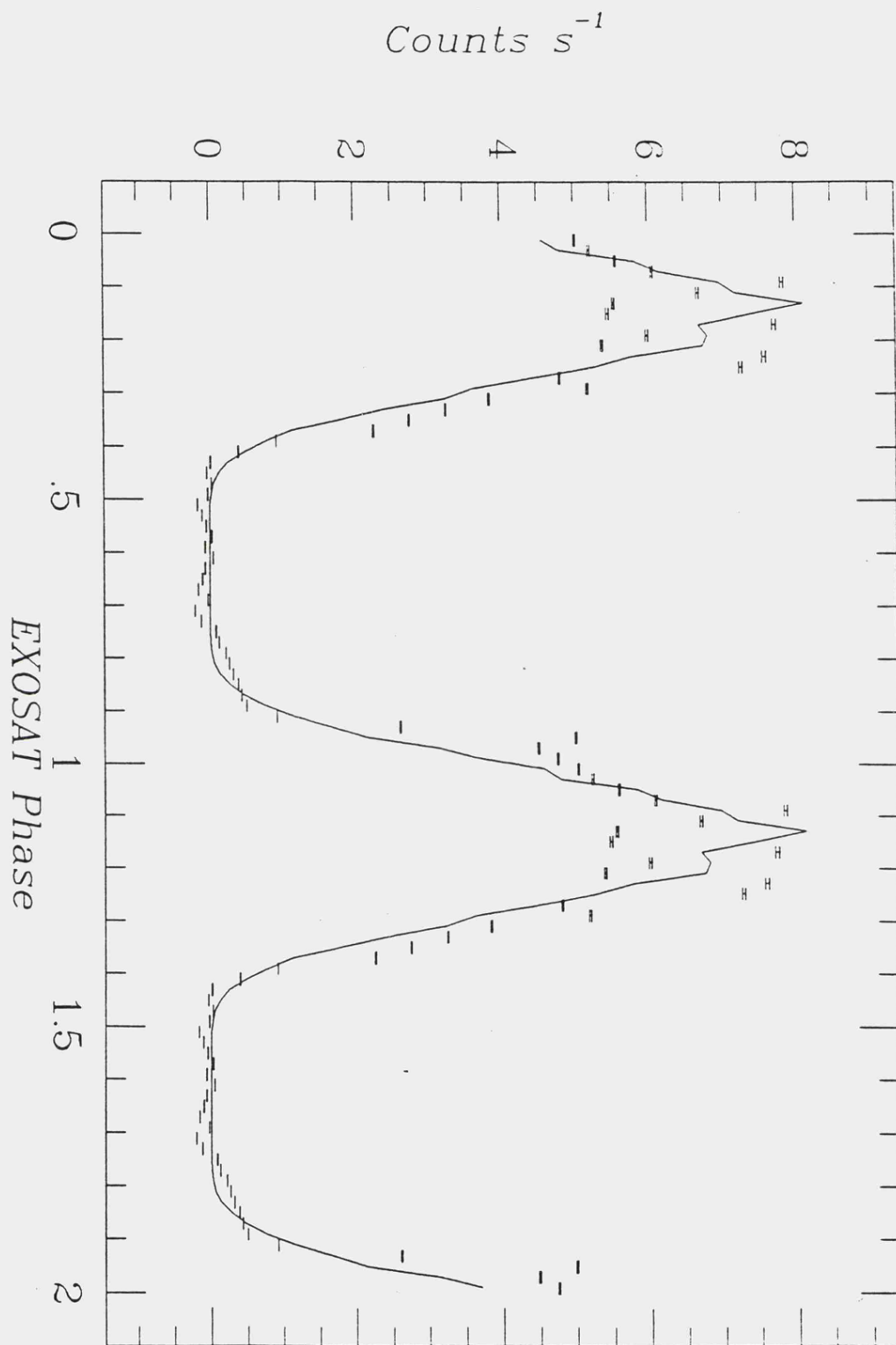


Figure 6.25 Best fit A to the LE lightcurve from the first observation (see Table 6.6 for best fit parameters).

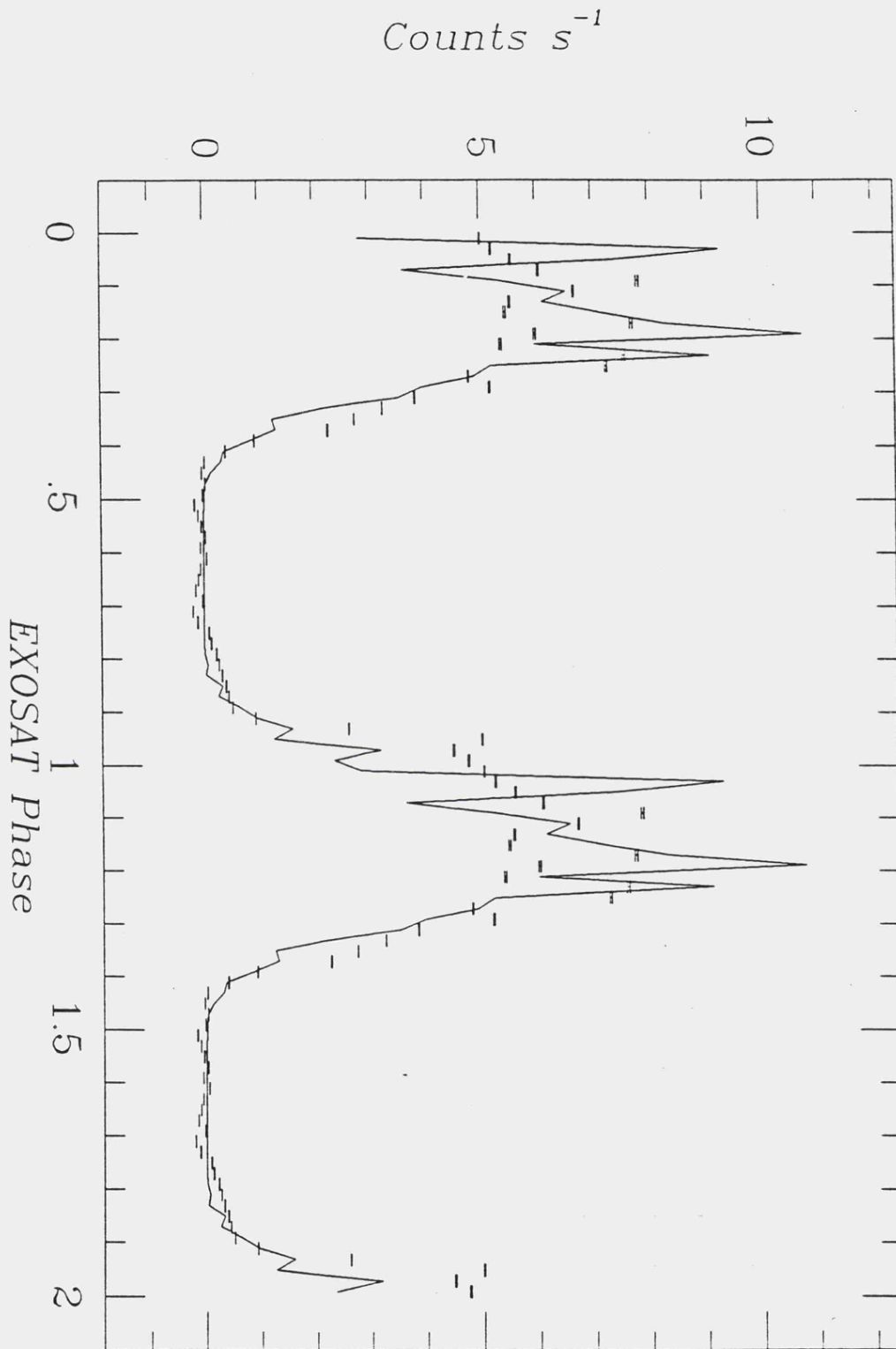


Figure 6.26 Best fit B to the LE lightcurve from the first observation (see Table 6.6 for best fit parameters).

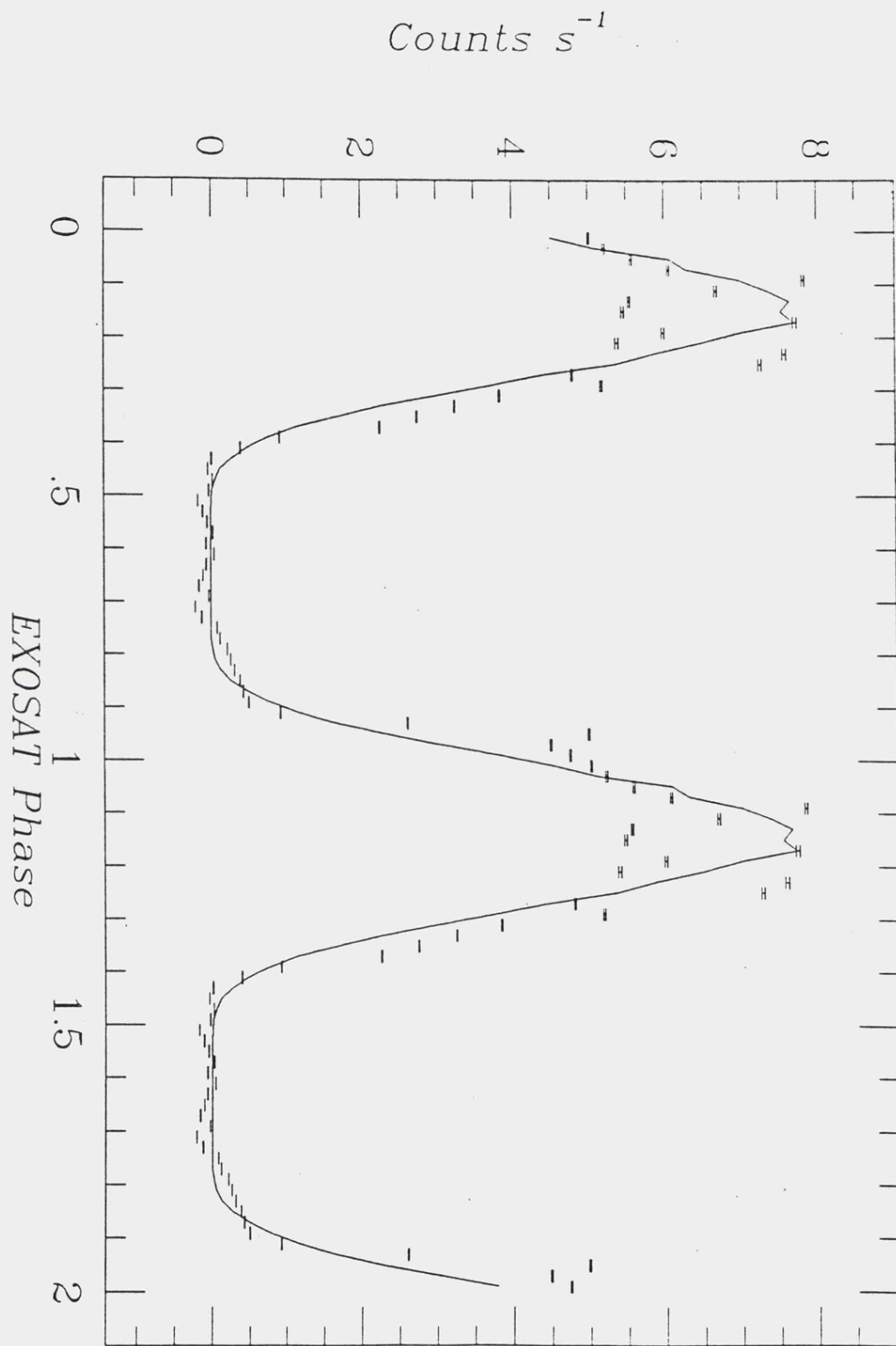


Figure 6.27 Best fit D to the LE lightcurve from the first observation (see Table 6.6 for best fit parameters).

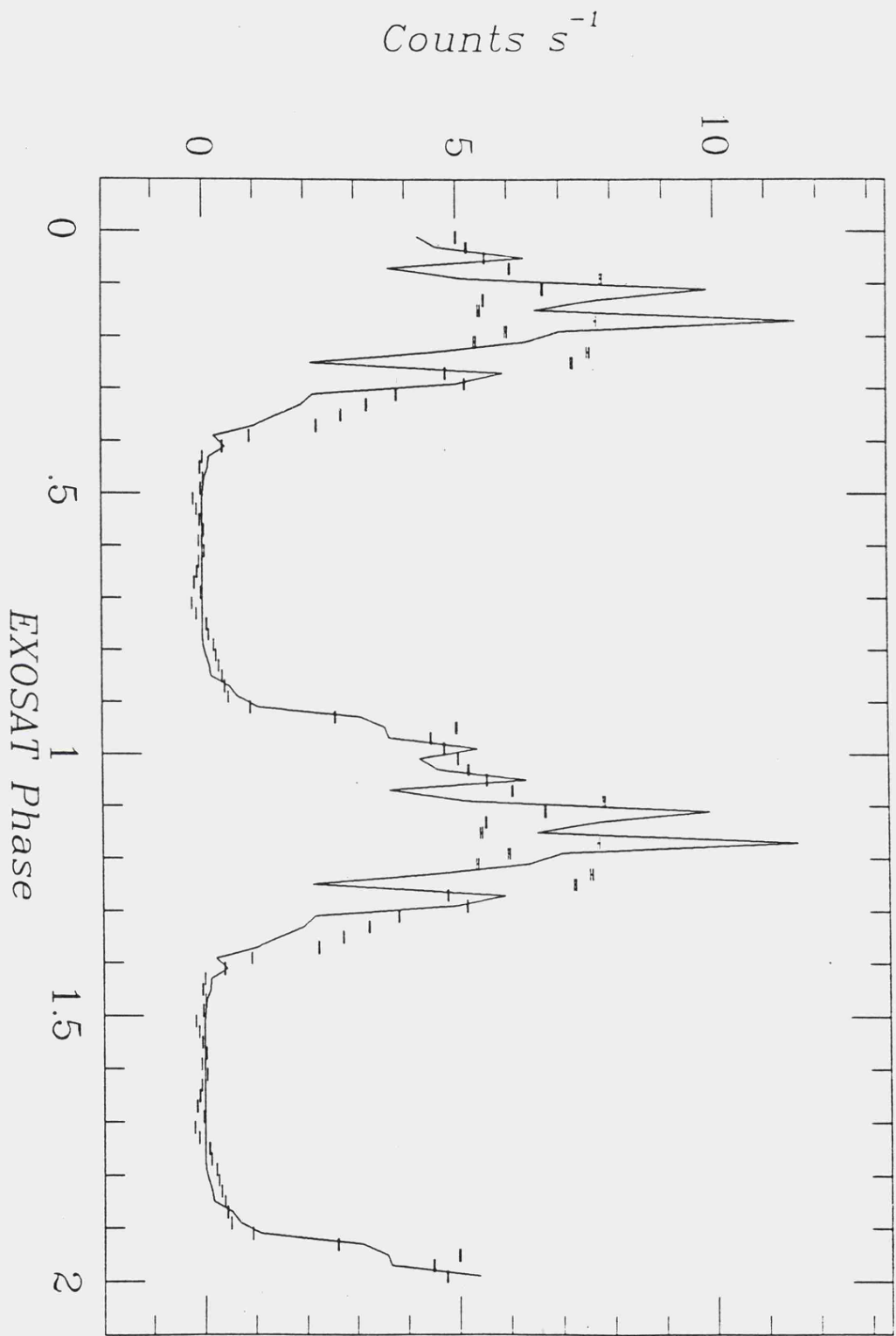


Figure 6.28 Best fit E to the LE lightcurve from the first observation (see Table 6.6 for best fit parameters).

Table 6.7 Parameters for AM Herculis derived from fitting the first observation lightcurves.

Distance to source	:	72.6 parsec		
Hydrogen column density	:	$1.0 \times 10^{20} \text{ cm}^{-2}$		
White dwarf mass (assumed)	:	1 solar mass		
Inclination to the line of sight	:	$38.5^\circ \pm 0.5^\circ$		
Magnetic axis angles -				
primary pole	:	$52.5^\circ \pm 0.5^\circ$		
secondary pole	:	$295.5^\circ \pm 0.5^\circ$		
Angle between poles -				
latitude	:	$117^\circ \pm 1.0^\circ$		
longitude	:	172.8°		
Fractional polecap areas -				
primary pole	:	0.006		
secondary pole	:	0.006		
Fractional area of pole emitting -				
primary pole	:	0.85		
secondary pole	:	0.85 - 0.95		
Fractional emitting areas				
(f_{emit}) - primary pole	:	5.1×10^{-3}		
secondary pole	:	$(5.1 - 5.7) \times 10^{-3}$		
Effective temperature -				
primary pole	:	$1.2 \times 10^5 \text{ K}$		
secondary pole	:	$\sim 1.5 \times 10^5 \text{ K}$		
X-ray illumination -				
primary pole	:	99.9 %		
secondary pole	:	0.01 - 1.0 %		
Luminosities (erg s^{-1}) :		L_x	L_{soft}	(L_x/L_{soft})
primary pole -		3.155×10^{32}	1.885×10^{32}	1.670
secondary pole -		8.604×10^{28}	5.236×10^{32}	1.64×10^{-4}
total -		3.156×10^{32}	7.121×10^{32}	0.443

results presented here can be thought of as being reasonable approximations to the truth. By analysing the results in more detail it is possible to draw some important conclusions from this fitting.

6.6.4 Conclusions from the fitting of the first observation lightcurves

I have derived values for the inclination to the line of sight and the angle between the rotational and magnetic axes of 38.5° and 52.5° respectively. These compare very

well with the values stated in Brainerd and Lamb (1985), which were derived from the polarisation properties of the source, i.e., $i=38.5^\circ \pm 5^\circ$ and $m=58^\circ \pm 5^\circ$. Both poles are of approximately the same size and emitting area and have similar effective temperatures. The secondary pole has effectively no shock at all as there is no appreciable hard X-ray emission. The magnetic polecap latitudes are only separated by 117° indicating either that the magnetic axis is off-centred or that higher (e.g. quadrupole) magnetic field multipoles are important near the white dwarf. Figure 6.29 shows the geometry inferred for AM Her from this observation. Assuming that the primary pole faces

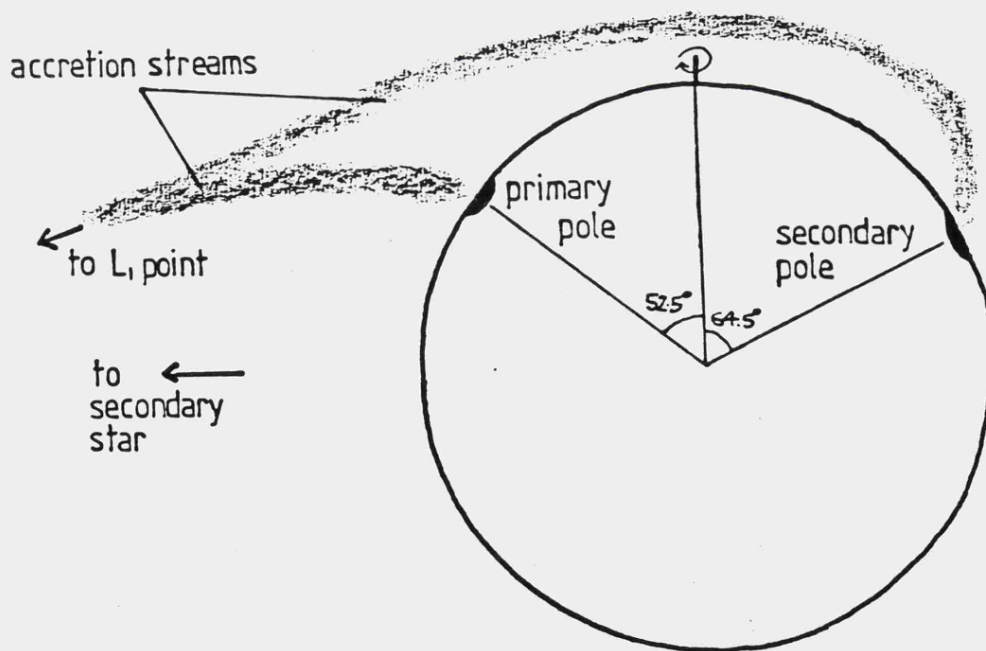


Figure 6.29 Inferred geometry for AM Herculis from fitting the first observation lightcurves.

directly towards the secondary star we see that some material passes the magnetic 'junction' above the primary pole and follows the magnetic field around to the secondary pole on the opposite side giving rise to the strong soft X-ray emission seen. The scenario predicted by our fitting does not seem unreasonable as a shifting of the orientation of the magnetic axis with respect to the secondary star could result in the secondary pole switching on and off. I will discuss this in more detail later in this chapter.

The predicted luminosities for AM Her give a hard/soft luminosity ratio of 1.67 for the primary pole, 1.64×10^{-4} for the secondary pole and 0.443 as a whole. These are the observed hard/soft ratio's, the actual values would be much smaller than this. Thus this fitting shows that the secondary pole of AM Herculis has a strong soft X-ray excess whereas the primary pole has approximately the correct hard/soft ratio for a radiative accretion column. The accretion rates for the poles are $1.888 \times 10^{15} \text{ g s}^{-1}$ for the primary pole and $1.962 \times 10^{15} \text{ g s}^{-1}$ for the secondary pole, indicating a slight preference for the material to accrete onto the secondary pole. The total accretion rate is $3.85 \times 10^{15} \text{ g s}^{-1}$ which is typical for these systems.

Looking at Figures 6.25 to 6.28 in more detail we see that none of the calculated lightcurves were able to fit convincingly the fast rise in the lightcurve at phase 0.8 (EXOSAT phase 0.94). The lightcurve rises to over half its maximum in only 14.4° of rotation. By experiment it was found that no surface feature could give such a fast rise as this as all optically-thick radiation is modified by the

projection effect to give a slower rise to maximum. This fast rise is therefore most probably due to an area of optically thick emission orientated approximately perpendicular to the photosphere which appears and disappears with the rotation of the white dwarf (first discussed by Heise et al., 1985). Since the transition between the high and low states takes place over approximately 4% of the rotation period the vertical extent of this feature must be of the order 4% of the white dwarf radius (i.e., $\sim 2 \times 10^7$ cm). Since this feature is not mirrored in the trailing edge of the lightcurve the feature must be asymmetrical about the polecap, perhaps having a wedge-shaped cross-section with respect to the white dwarf surface. I will not discuss any possible reasons for this feature but save to say that it is permanent in that it appears in the LE lightcurve for the second observation as well. The fitting of the second observation lightcurves is discussed in the next section.

6.6.5 Fitting the second observation lightcurves

Essentially this is a simpler task than before as we have already found three important parameters; the inclination to the line of sight, i (38.5°); the distance to AM Her, d_{pc} (72.6 parsec) and the hydrogen column density in the direction of AM Her, N_H ($1.0 \times 10^{20} \text{ cm}^{-2}$). Fitting the ME lightcurve is a similar procedure to that used before except this time i is kept constant, m being

Table 6.8 Results of fitting the second observation ME lightcurve ($i=38.5^\circ$).

f	m ($\pm 0.5^\circ$)	χ^2 ($\times 10^5$)	Phase shift
0.08	37.5	5.873	0.12
0.06	40.0	4.947	0.12
0.05	41.0	4.750	0.12
0.04	42.5	5.227	0.12
0.02	45.5	8.988	0.12

allowed to vary, as we do not expect the magnetic axis to stay fixed. Table 6.8 shows the results of fitting the shape of the ME lightcurve. Analysing the results in the same way as before gives us a best fit of $m=41.0^\circ \pm 0.5^\circ$ and a fractional polecap area of 0.05. Figure 6.30 shows this fit graphically. Again we see that the calculated lightcurve is almost a perfect fit to the observed one, apart from the flickering at the maximum. The count rates were fitted in the same way as before and the results are shown in Table 6.9. The preferred value for the fractional area of the polecap emitting, by observation, was 0.90-0.95. The maximum soft X-ray counts are shown for the thin Lexan filter but this time the grating had been in front of the detector, reducing the count rates by a factor of ~ 0.9 . Figure 6.31 shows the effective area of the thin Lexan filter when used with the grating, calculated using the energy dependent response of the grating. Models which gave LE count rates above the maximum seen in the 'hump' of the LE lightcurve (~ 0.11 counts s^{-1}) were discounted.

From Table 6.9 we see that the best fit to the ME count rate is a model with an effective temperature of 100,000 K and an X-ray illumination of 44%, with a fractional

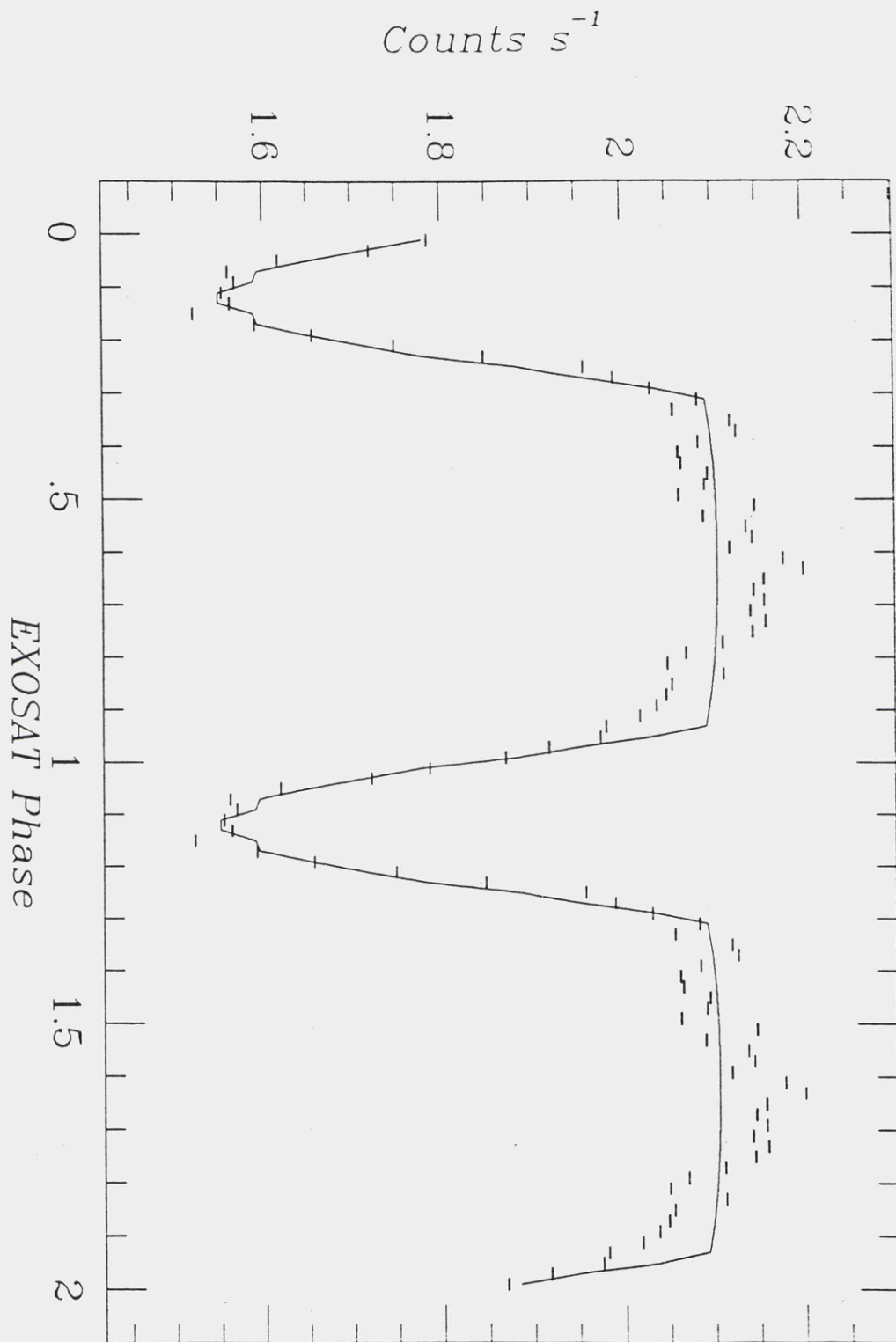


Figure 6.30 Best fit to the shape of the ME lightcurve from the second observation ($i=38.5^\circ$, $m=41.0^\circ$ and $f=0.05$).

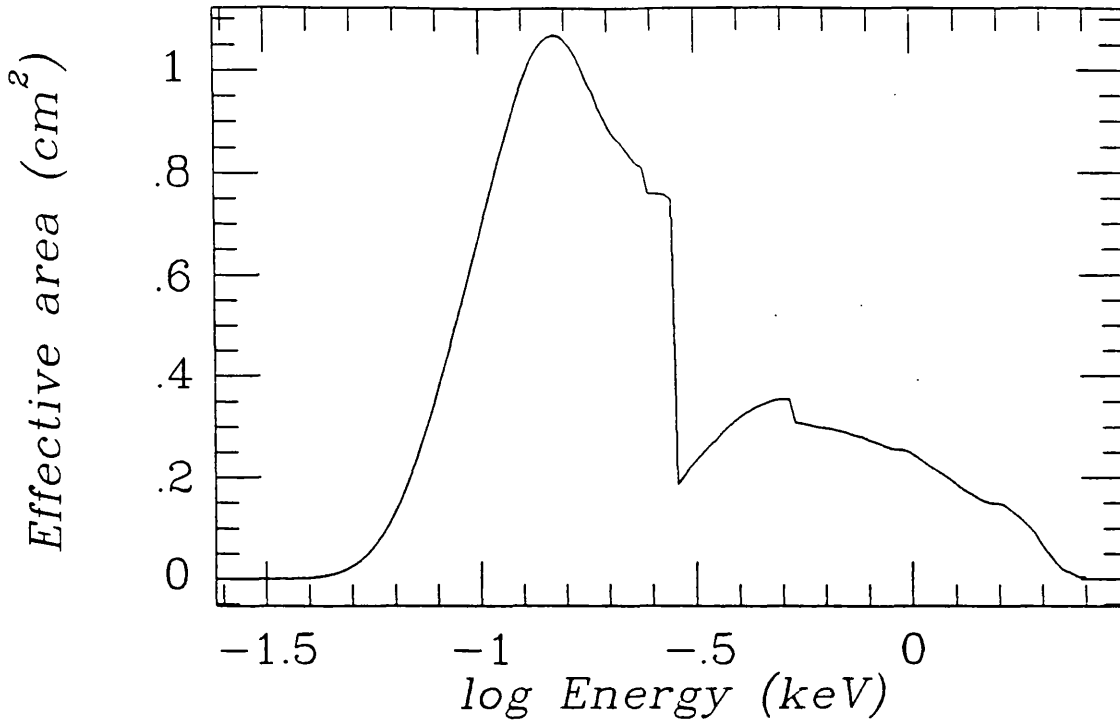


Figure 6.31 Response of the CMA through the thin Lexan filter when the grating is in place.

Table 6.9 Results of fitting the ME count rate ($d_{pc} = 72.6$ parsec).

P_{ill} (%)	T_{eff} ($\times 10^5$ K)	α	LE_7 (s^{-1})	Comments
99.9	1.0	0.425	-	α too small
"	1.5	0.078	-	" " "
50.0	1.0	0.798	~ 0.09	α almost OK
"	1.5	0.149	~ 0.30	α too small
44.0	1.0	0.894	~ 0.11	best fit

LE_7 = maximum count rate in thin Lexan filter + grating

emitting area of 0.894. Figure 6.32 shows this best fit graphically. The strength of the flickering is modelled quite well with approximately 0.9 of the polecap emitting. Figure 6.33 shows the contribution to the LE lightcurve from the primary pole, the 'hump' being fitted quite well.

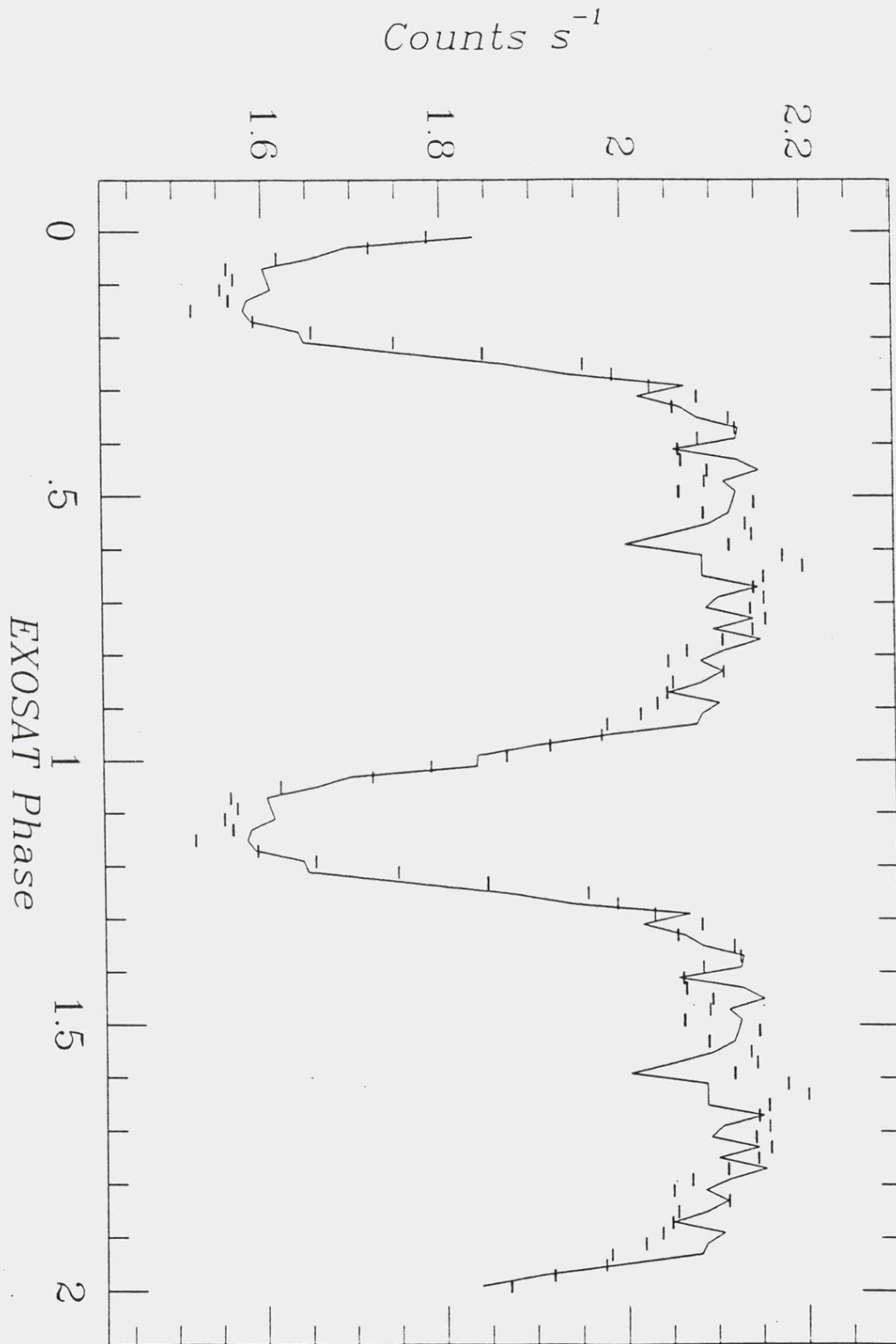


Figure 6.32 Best fit to the shape and count rates of the ME lightcurve from the second observation; $f=0.05$, $\mu=41.0^\circ$, $i=38.5^\circ$, $f_{\text{int}}=0.894$, $T_{\text{eff}}=1.0 \times 10^5$ K and $P_{\text{int}}=44.0\%$ (all other parameters the same as for the first observation).

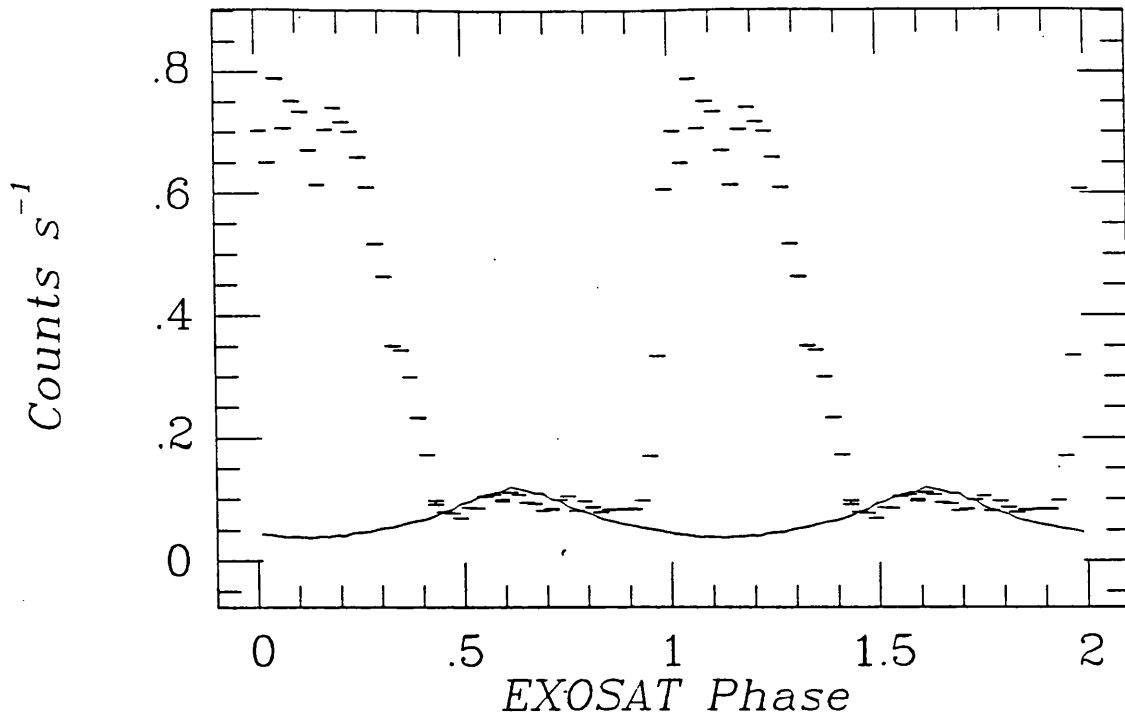


Figure 6.33 Contribution of the LE lightcurve from the primary pole to the observed LE lightcurve from the second observation.

Having subtracted the contribution from the primary pole to the LE lightcurve the LE lightcurve was fitted in the same way as for the first observation, the results of which are presented in Table 6.10. Referring to the table, it was found that unlike the first observation there were no really clear fits to the lightcurve. For all the temperatures and illuminations tried the values of chi-squared had very shallow minima (with respect to the polecap area) and so deciding which was the best fit was largely arbitrary (i.e., choosing those that give the best values for the fractional emitting area, f_{emit}). There were five 'best' fits, A-E, of which only two, B and D, gave values for f_{emit} close to the required value of 0.90-0.95, without reducing the polecap area to less than

Table 6.10 Result of fitting the primary subtracted LE lightcurve from the second observation.

P_{ill} (%)	T_{eff} ($\times 10^5$)	f	m ($\pm 0.5^\circ$)	χ^2 ($\times 10^6$)	α	P_{sh}	ME (s^{-1})
0.01	1.5	0.01	291.5	2.924	0.676	0.16	
"	"	0.008	292.0	2.913	0.822	0.16	
"	"	0.006	292.5	2.903	1.023	0.16	
"	"	0.005	"	2.895	1.334	0.16	(no fit)
"	2.0	0.01	286.0	2.814	0.127	0.16	
"	"	0.008	286.5	2.806	0.154	0.16	
"	"	0.006	"	2.800	0.194	0.16	
"	"	0.005	287.0	2.794	0.250	0.16	
"	"	0.004	287.5	2.790	0.335	0.16	
"	"	0.003	"	2.786	0.482	0.16	
"	"	0.002	"	2.784	0.752	0.16	$\sim 10^{-4}$ A
"	"	0.001	288.0	2.782	1.317	0.16	
"	2.15	0.002	286.5	2.768	0.513	0.16	
"	"	0.001	287.0	2.766	0.898	0.16	$\sim 10^{-4}$ B
"	"	0.0004	"	2.767	2.020	0.16	
"	2.5	0.003	284.5	2.744	0.154	0.16	
"	"	0.002	285.0	2.741	0.237	0.16	$\sim 10^{-4}$ C
"	"	0.001	"	2.742	0.421	0.16	
1.0	2.15	0.002	286.5	2.768	0.515	0.16	
"	"	0.001	"	2.767	0.915	0.16	$\sim 10^{-2}$ D
"	"	0.0004	"	2.768	2.057	0.16	
"	2.5	0.002	284.5	2.733	0.248	0.16	
"	"	0.001	285.0	2.732	0.433	0.16	$\sim 10^{-2}$ E
"	"	0.0004	"	2.733	0.975	0.16	

P_{sh} = phase shift for best fit

10^{-3} . So the inferred values for the secondary pole's parameters are; effective temperature of 215,000 K; hard X-ray illumination of 0.01-1.0%; fractional polecap area of 0.001 with 0.9-0.92 actually emitting and a magnetic axis angle, m , of $286.5^\circ \pm 0.5^\circ$. Phase zero for the calculated lightcurve was equivalent to phase 0.16 in the EXOSAT lightcurve. Figures 6.34 and 6.35 show the two fits graphically, note that the calculated lightcurves are again unable to fit the fast rise in the observed lightcurve. Table 6.11 shows a full list of the fitted parameters for the second EXOSAT observation of AM Herculis.

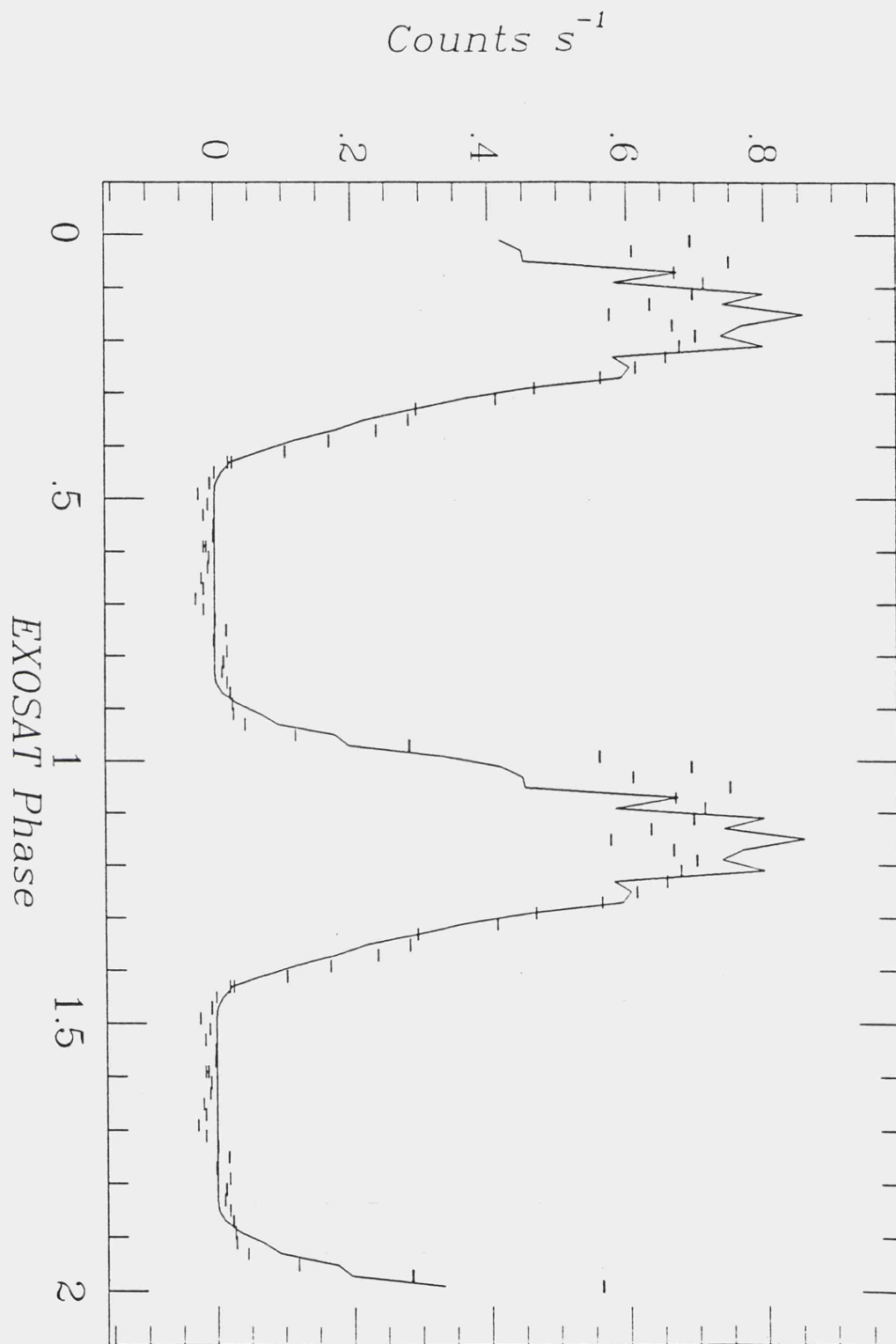


Figure 6.34 Best fit B to the LE lightcurve from the second observation (see Table 6.10 for parameters).

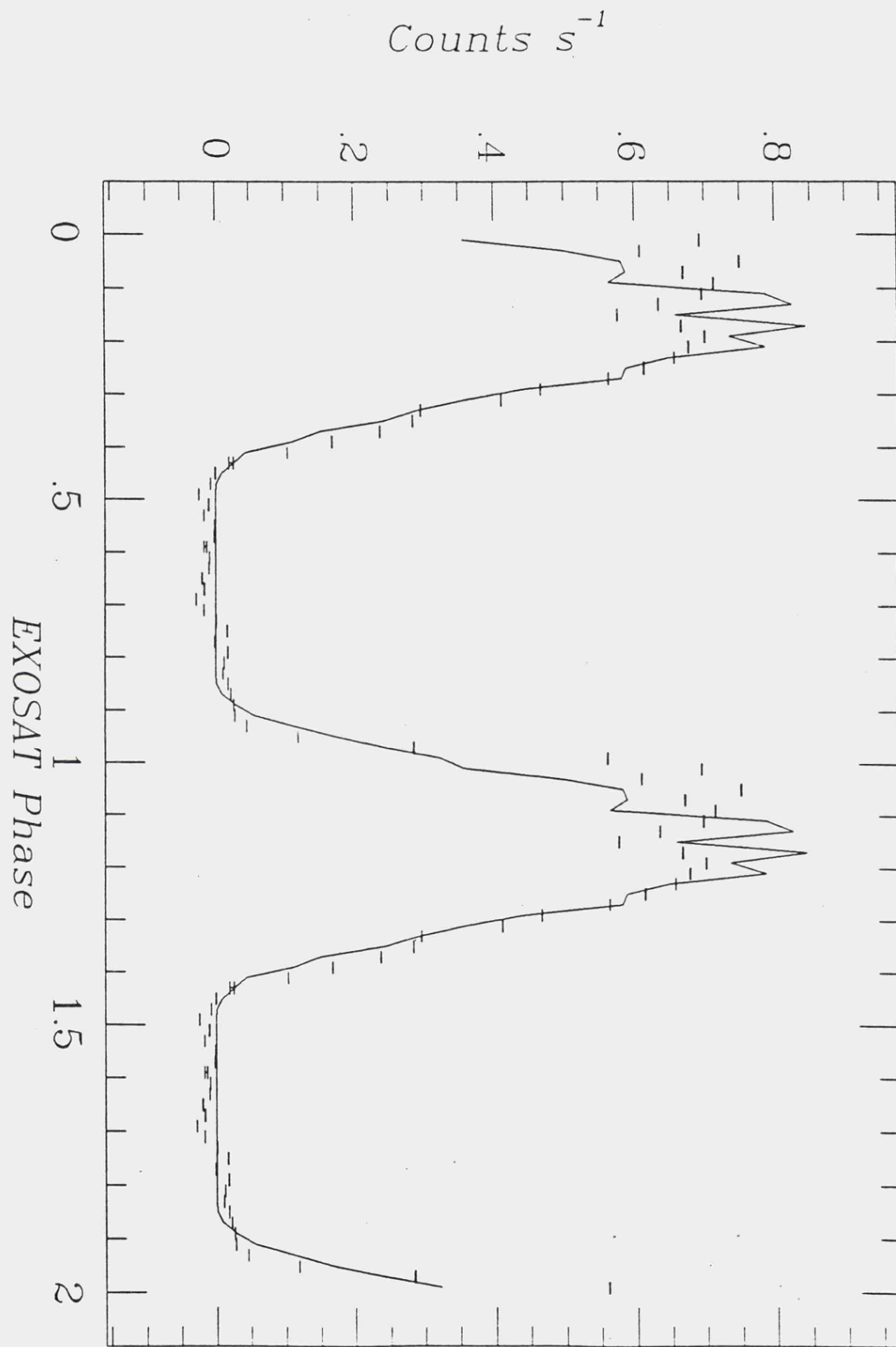


Figure 6.35 Best fit D to the LE lightcurve from the second observation (see Table 6.10 for parameters).

Table 6.11 Parameters for AM Herculis derived from fitting the second observation lightcurves.

Magnetic axis angles -			
	primary pole :	41.0° ± 0.5°	
	secondary pole :	286.5° ± 0.5°	
Angle between poles -			
	latitude :	114.5° ± 1.0°	
	longitude :	165.6°	
Fractional polecap areas -			
	primary pole :	0.05	
	secondary pole :	0.001	
Fractional area of pole emitting -			
	primary pole :	0.894	
	secondary pole :	0.90 - 0.92	
Fractional emitting areas			
($f_{x \text{ emit}}$) -	primary pole :	0.045	
	secondary pole :	(9.0 - 9.2) × 10 ⁻⁴	
Effective temperature -			
	primary pole :	1.0 × 10 ⁵ K	
	secondary pole :	2.15 × 10 ⁵ K	
X-ray illumination -			
	primary pole :	44.0 %	
	secondary pole :	0.01 - 1.0 %	
Luminosities (erg s ⁻¹) :			
	L_x	L_{soft}	(L_x / L_{soft})
primary pole -	5.660 × 10 ³²	7.832 × 10 ³²	0.723
secondary pole -	5.733 × 10 ²⁸	3.490 × 10 ³²	1.64 × 10 ⁻⁴
total -	5.661 × 10 ³²	1.132 × 10 ³³	0.500

Having successfully modelled the lightcurves from both EXOSAT observations the fitting of AM Herculis is now complete. The next section discusses the changes, that our fits have implied to have taken place, between the two observations and suggests possible reasons for these.

6.6.6 Comparison of the two fits to AM Herculis

A full list of all the fitted parameters for both observations is shown in Table 6.12, so as to allow easy comparison between the results from the two observations.

Considering the positions and sizes of the poles first we see that apparent positions of the poles have altered

Table 6.12 Fitted parameter list for both observations of AM Herculis.

Parameter	First observation	Second observation	Comparison
Magnetic axis angle:			
primary pole	52.5° ± 0.5°	41.0° ± 0.5°	Decrease: -11.5°
secondary pole	295.5° ± 0.5°	286.5° ± 0.5°	Decrease: -9.0°
Pole displacement:			
latitude	117.0° ± 1.0°	114.5° ± 1.0°	Decrease: -3.0°
longitude	172.8°	165.6°	Decrease: -7.2°
Polecap areas:			
primary	0.006	0.05	Increase: x8.3
secondary	0.006	0.001	Decrease: x0.16
Emitting areas:			
primary	5.1x10 ⁻³	0.045	Increase: x8.8
secondary	5.1-5.7x10 ⁻³	9.0-9.2x10 ⁻⁴	Decrease: x0.16
Effective temperatures:			
primary	1.2x10 ⁵ K	1.0x10 ⁵ K	Decrease: x0.83
secondary	1.5x10 ⁵ K	2.15x10 ⁵ K	Increase: x1.4
ILLumination strength:			
primary	99.9%	44.0%	Decrease: x0.43
secondary	0.01-1.0%	0.01-1.0%	Same
Hard X-ray Luminosity:			
primary	3.155x10 ³² erg s ⁻¹	5.660x10 ³² erg s ⁻¹	Increase: x1.8
secondary	8.604x10 ²⁸ erg s ⁻¹	5.733x10 ²⁸ erg s ⁻¹	Decrease: x0.66
TOTAL	3.156x10 ³² erg s	5.661x10 ³² erg s	Increase: x1.8
Soft X-ray Luminosity:			
primary	1.885x10 ³² erg s ⁻¹	7.832x10 ³² erg s ⁻¹	Increase: x4.2
secondary	5.236x10 ³² erg s ⁻¹	3.490x10 ³² erg s ⁻¹	Decrease: x0.66
TOTAL	7.121x10 ³² erg s	1.132x10 ³³ erg s	Increase: x1.6
(L _{hard} /L _{soft}):			
primary	1.67	0.723	Decrease: x0.43
secondary	1.64x10 ⁻⁴	1.64x10 ⁻⁴	Same
TOTAL	0.443	0.500	Increase: x1.1

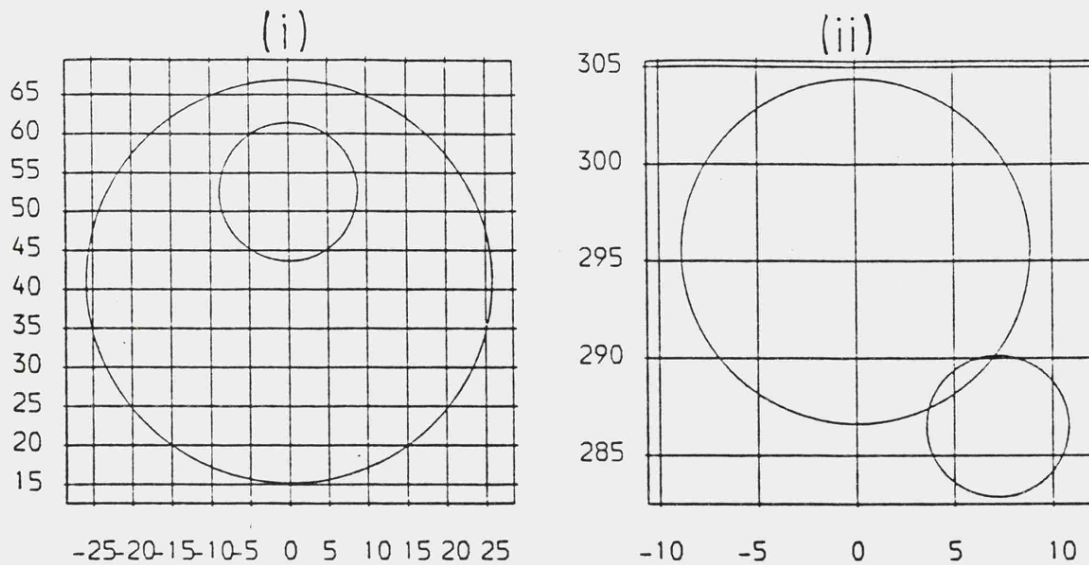


Figure 6.36 Relative positions of the magnetic poles in the two observations; (i) Primary, (ii) Secondary.

between the two observations. Figure 6.36 shows the relative positions of the poles in the first and second observations. It shows that the primary pole in the first observation is wholly contained within the primary pole in the second observation. The change in the inferred position of the primary's magnetic axis does not necessarily indicate a change in the orientation of the magnetic axis since the model's magnetic axis is only a reference point to which the individual sectors in the pole refer, the true magnetic axis may not even lie inside the model polecap ! The shift in the position of the model pole only indicates that the region of accretion on the white dwarf's surface has moved. In the case of the secondary pole, the position on the surface of the accretion area had also moved between the two observations, in a way so as to keep the angle between the primary and

secondary poles approximately constant, but in this case the two poles are not located within the same area of the white dwarf. It may well be that the magnetic axis has shifted slightly between the two observations but the change in the apparent positions of the poles could also be due to different sections of a much larger 'polecap' turning on and off, possibly due to a change in the accretion rate. Generally, the derived sizes of the poles are larger than the values usually associated with these systems. This fact, plus the necessity for large polecaps in order to explain the quasi-sinusoidal lightcurves in EF Eri and V834 Cen (E1405-451), adds further weight to the argument for systematically larger polecaps for polar systems. The assumed values for polars usually arise from luminosity fits using black bodies which, as we saw in Chapter 5, give smaller f 's than expected, therefore geometrically large polecaps (geometrically large to give the correct lightcurve shape but the actual emitting area could still be small) of the order 10^{-2} to 10^{-3} of the white dwarf area may well be the norm in polar systems.

Considering the poles themselves; the effective temperature of the primary pole decreased from 120,000 K to 100,000 K which is most probably due to the decrease in the hard X-ray illumination from 99.9% to 44%. In the case of the secondary pole the effective temperature increased from 150,000 K to 215,000 K while the accreting area decreased by a factor of six. The accretion rates are 5.055×10^{15} g s⁻¹ for the primary pole and 1.308×10^{15} g s⁻¹ for the secondary pole so we see that the accretion rate onto the secondary has decreased, hence the reduction in size of the

secondary pole, while the accretion rate onto the primary pole has more than doubled, hence the enormous increase in size of this pole. In order to explain the changes in the accretion rates we could assume that the orientation of the magnetic axis with respect to the secondary changed slightly between the observations, causing more material to accrete onto the primary pole and less onto the secondary pole. This possibility, which is related to how strong the phase-locking of the white dwarf's rotation is, will be discussed in more detail later. It is interesting to note that although great changes have occurred at the secondary pole there was no great increase in the observed count rates which indicates how the effects of changes in the effective emitting area, effective temperature and strength of X-ray illumination weigh off against each other.

Finally, the inferred total luminosities for AM Herculis show an increase of 1.6 between the first and second observations most of which is due to the increase in the soft X-ray luminosity of the primary pole. The hard/soft ratio stayed approximately the same at ~ 0.5 , indicating a strong soft X-ray excess.

6.6.7 Conclusions from this lightcurve fitting

By fitting simulated model atmosphere lightcurves to the EXOSAT observations of AM Herculis made in the summer of 1983 I have derived the geometry and accretion parameters for the system. These results were shown in Table 6.12 and discussed in the previous section.

We have seen that changes in the system occur on all

timescales, from the ~ 4 minute flickering seen in the observed lightcurves to the longer term changes that have occurred between observations separated by years. The reasons for the short period flickering are much clearer than the reasons for the change from a one pole to a two pole system. The flickering is most probably due to inhomogeneous accretion onto the polecap, possibly due to small fluctuations in the magnetic field near the polecap or cooling instabilities in the accretion stream. The non-correlation of the soft and hard X-ray flickering is probably due to absorption by tenuous and inhomogeneous material near the base of the column, possibly a wind driven off the surface of the white dwarf (c.f. EF Eri, Watson et al., 1987). The longer period changes in the system bring into consideration the strength of the phase-locking of the white dwarf's rotation to its orbital period.

In Chapter 1 I discussed the general structure of a magnetic polar system. One of the more important features that sets these systems apart from other cataclysmic variables is that the white dwarf spin period is phase-locked to its orbital motion. However, Campbell (1983) pointed out that complete synchronisation of the white dwarf spin to the orbital revolution may well not occur; the spin-up torque due to accretion has to be balanced by a synchronising torque. Most of these torques, for example magnetic coupling between the white dwarf and the secondary, require a slow relative motion between the white dwarf and the orbit, resulting in a 'synodic' precession. Observational evidence from the eclipsing

system E1114+182 (Biermann et al., 1985) suggests that the orbital precession is very slow, >100 years. However, King and Williams (1985) have argued that the opposing torques, and hence the rate of precession, will be less when the accretion stream deviates least from the path it would normally take if no magnetic field were present. The system would thus spend most of its time in this position with rapid precession through the rest. This preferred position is with one pole leading the secondary by approximately 30° . As shown by Liebert and Stockman (1985) the observed angles indeed cluster around 30° the most notable exception being AM Herculis itself with an angle of $\sim 60^\circ$. This then indicates that AM Her is in an orientation which is likely to change quite rapidly, with consequent rapid changes in its X-ray lightcurves (although the existence of two more rapidly changing systems, QQ Vul and V834 Cen, may indicate that these epochs of rapid change may not be all that short lived). It is tempting to see this as an explanation for the 'anomalous' state that we see AM Her in now, with the system almost side-on and accreting down both magnetic poles.

Returning, for the moment, to the magnetic poles themselves, I have previously mentioned that the inferred position for the magnetic axis from my fitting does not necessarily give the true position of the magnetic axis, it may be that regions around the true magnetic pole are turned on and off over long timescales, mimicking a movement of the pole over the surface. From the first observation I derived values of $m=52.5^\circ$ for the primary pole and $m=295.5^\circ$ for the secondary. In the second

observation the fitted values were $m=41.0^\circ$ (primary) and $m=286.5^\circ$ (secondary). Since the inferred size of the primary polecap is so large in the second observation and it contains within it the inferred position of the primary pole from the first observation it is tempting to assume that the true magnetic axis angle for the primary pole is in fact 41° . In the case of the secondary pole, the position of the magnetic axis could be taken to be the centroid of the two inferred positions i.e., latitude= 291° , longitude= 169.2° . The apparent movement of the magnetic poles over the surface of the white dwarf could easily explain why the hard X-ray lightcurve changed from being fully eclipsed to only partially eclipsed (as AM Her moved into its anomalous phase). Comparing the positions of the magnetic poles we get a pole displacement of 110° in latitude and 169.2° in longitude, indicating that the magnetic axis is strongly off-centred. Observational evidence for the off-centred nature of AM Her's magnetic axis comes from spectroscopic observations of the system in 1979 by Latham et al. (1981), made while AM Her was in a low state (cyclotron emission down by ~ 2 magnitudes). Wickramasinghe and Martin (1985) used these observations, which were dominated by Zeemanised hydrogen lines, to deduce that structure of the magnetic field of the white dwarf. They found that an offset dipole magnetic field, with the dipole axis displaced by approximately 0.17 radii opposite to the direction of the axis, gave the best agreement with observation. Clearly the offset nature of the magnetic axis adds further complications to the interaction of the spin-up and spin-down torques in the

system and could cause quite varied changes in the precession rate.

Finally, Figures 6.37 and 6.38 show the orientation of AM Her at some chosen EXOSAT phases for both observations. The random positions of the emitting regions are shown for illustration only. In a similar way, Figure 6.39 shows the positions of the poles from the two observations combined, but, for clarity, the random sections of the polecaps are not shown.

In conclusion, the fitting of the EXOSAT lightcurves of AM Herculis was very successful in that the results obtained compared favourably with the previous knowledge of the system. The complex interaction of the opposing torques should lead to many more changes in the geometry of the system. With repeated monitoring of AM Herculis by new X-ray satellites (e.g., Ginga (ASTRO C) and ROSAT) we will hopefully come to understand more clearly what is happening to the system and perhaps predict possible future changes in other magnetic polars. The technique of lightcurve fitting will be invaluable in this work.

6.7 Conclusions and further work possible

I have described the calculation of simple magnetic polar lightcurves with random variations included in order to try to model the flickering seen observationally (e.g. EF Eri). These lightcurves were then used to find the geometric and accretion properties of AM Herculis, the brightest known magnetic polar. The calculated lightcurves

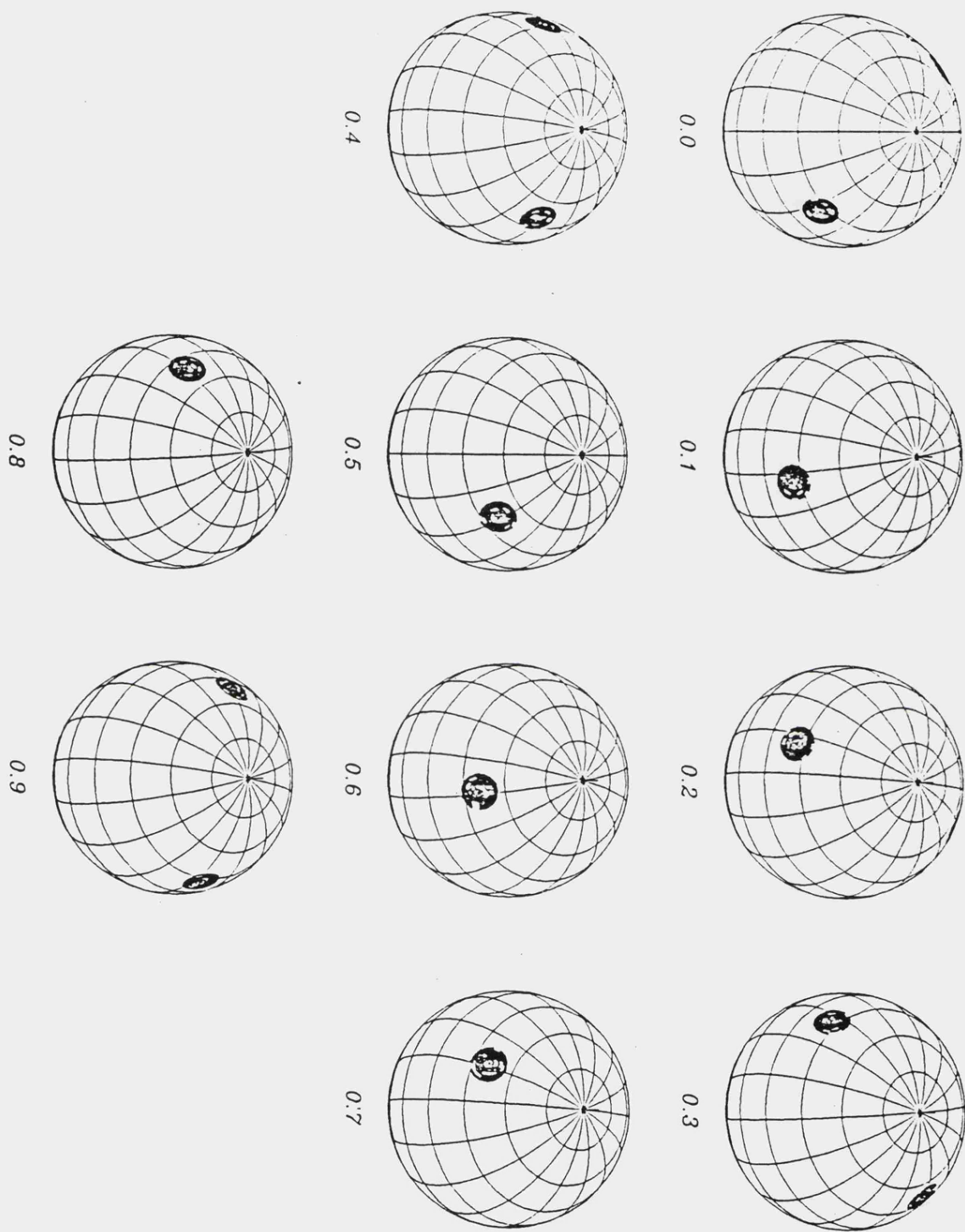


Figure 6.37 Orientation of AM Herculis at some chosen EXOSAT phases; as inferred from the first observation lightcurves. The pole seen nearly face on at EXOSAT phase 0.1 is the SECONDARY pole. The random flickering of sections of each polecap is shown.

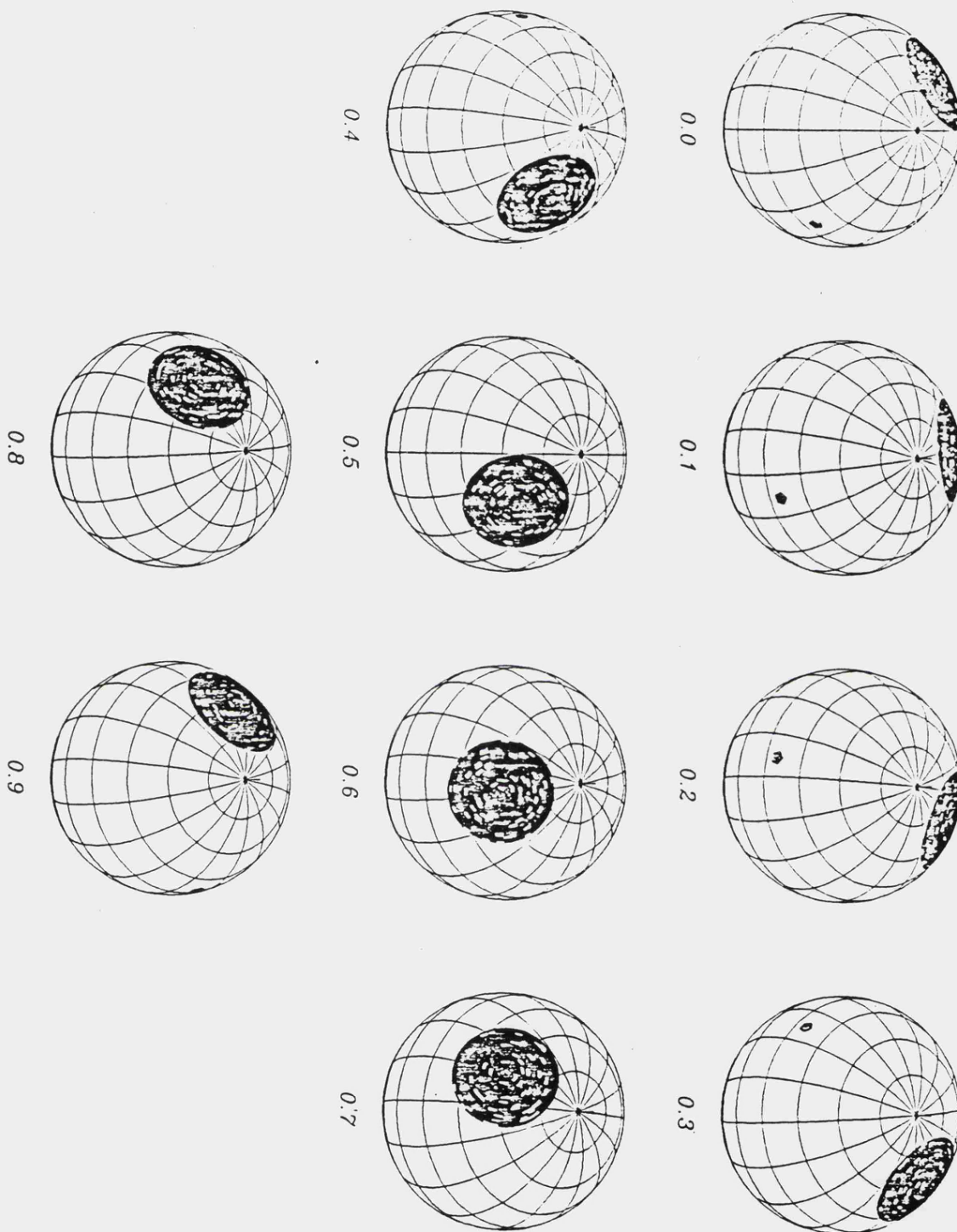


Figure 6.38 As for Figure 6.37 except this shows the inferred positions of the poles from the second observation. Note the vast difference in size between the poles (the secondary pole appears pentagonal due to plotting difficulties).

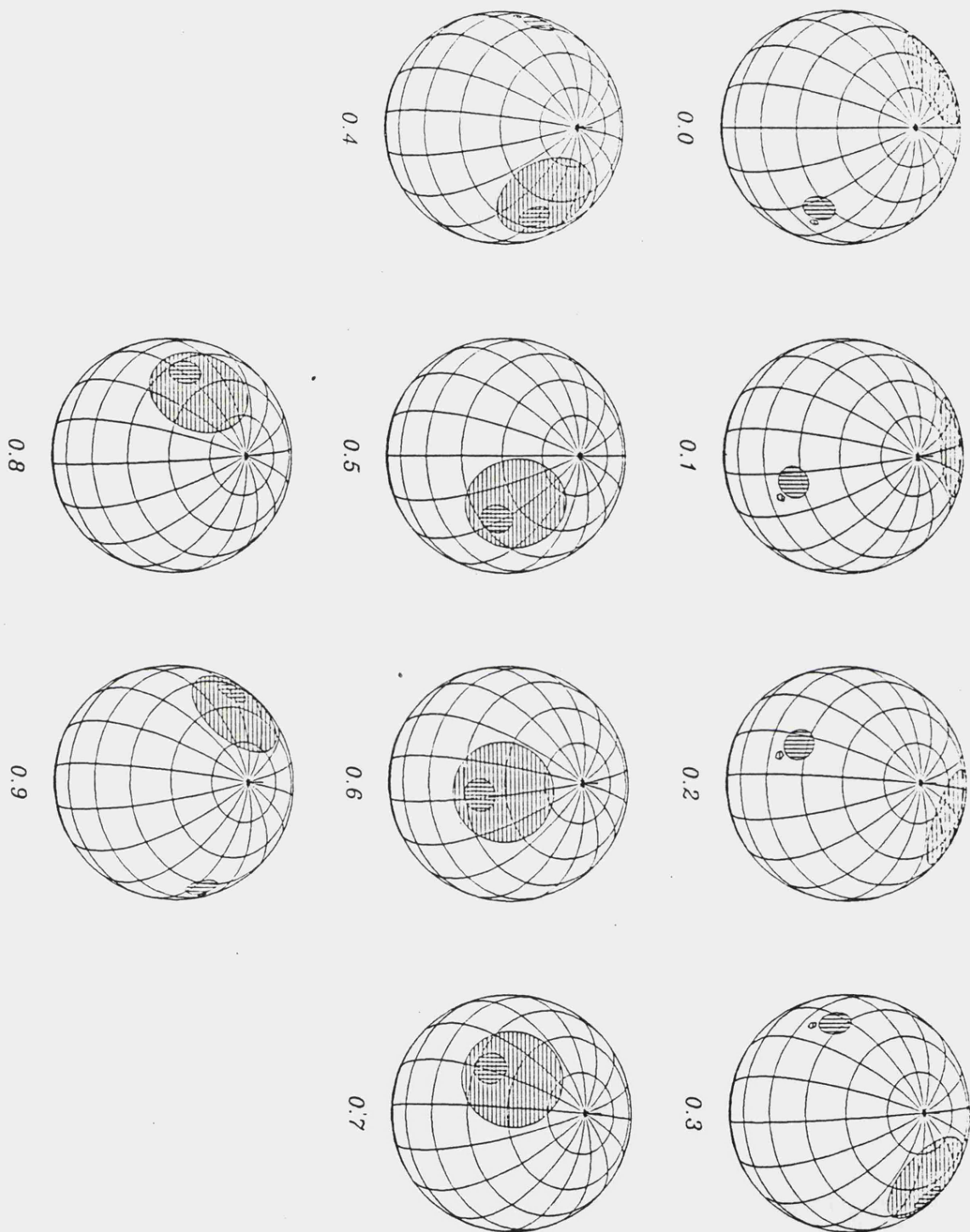


Figure 6.39 The orientation of AM Herculis as inferred from both observations. The positions of the poles from each observation are shown; vertical hatching for the first observation, horizontal hatching for the second observation. The random sections of each polecap are not shown for clarity.

gave very good fits to the observed EXOSAT lightcurves and the accretion properties were then derived with reasonable accuracy. The results indicate that AM Her undergoes changes in its accretion geometry over a wide range of timescales, from rapid flickering to a slow yearly precession of its magnetic axis. In all kinds of fitting assumptions have to be made; the major assumption made in the lightcurve fitting, i.e., that the ME lightcurve came from only one pole, did not restrict the fitting to any extent and gave no erroneous results; the assumed values for the distance to AM Her (taken from Young and Schneider, 1981) and the hydrogen column density in the direction of the source ($1.0 \times 10^{20} \text{ cm}^{-2}$) were the only other major assumptions made. The implications of this fitting were discussed above.

In order to improve the simulation of these lightcurves other effects must be included. In the case of AM Her we have seen that some of the soft X-ray emission comes from a region which is perpendicular to the white dwarf's surface. This region could be modelled by placing vertically orientated, equally-sized sectors at the edge of the polecap. The rest of the polecap is then placed at the same vertical height as these sectors. The extra sectors can be assumed to radiate at the same effective temperature as the rest of the polecap. This would unfortunately introduce another free parameter, the vertical extent of the polecap, thus making actual fitting more difficult.

We have seen that for systems where $i > 0$ there would be eclipses of the polecap by the accretion stream. The depths and widths of these eclipses could be modelled

separately from the main lightcurve fitting by calculating the trajectory of the accretion stream (for a given orbital separation, field strength and accretion rate) and, for a given hydrogen column density, the resultant absorption feature. The trajectory of the accretion stream gives the time of intersection of the stream with the line of sight to the polecap. Actual fitting would be difficult as this introduces many more parameters but as an illustration of possible eclipse forms it would prove useful.

Obscuration by the accretion column and occultations of the white dwarf by the secondary star are the two other types of eclipse not included in this simulation. Absorption of the soft X-rays by the accretion column could be modelled by increasing the line of sight column density while occultations by the secondary star would again require modelling of the orbital geometry. Again, due to the inclusion of extra parameters, actual fitting of the absorption features produced by these situations would prove difficult.

Whether the above are included or not, the final test for any 'model' is to test it against observation. To date only AM Herculis has been fitted to any great extent. Since there are many more polar systems, most of which have soft and hard X-ray lightcurves, the next step would be to repeat the fitting procedure for as many of these systems as possible in order to see if there is any bias in the fitting. Only then would it be possible to say whether the results derived here give a true indication of what AM Herculis is really like.

¹ This method of producing the flickering seen in these systems is not the only way to model these variations. If the flickering is assumed to be due to variations in M then a random variation of the effective temperature of each sector could equally well produce these effects (a small change in the effective temperature can produce a large change in the flux seen in the soft X-ray region). Alternatively, variations in the homogeneity of the accretion stream could be modelled by varying N_H for each sector (again this would produce a large change in the soft X-ray flux but this has the disadvantage that no change in the hard X-ray flux occurs). However, random blanking of the sectors was chosen as this gives the required effect simply and easily and it also has some observational significance (it may be that all the polecap is not emitting, fluctuations in the magnetic field close to the surface may disrupt the uniform nature of the accretion giving rise to regions where there is little accretion taking place).

Obviously it is impossible to fit a 'flickering' observed lightcurve with a 'flickering' model lightcurve, the geometry of the source must be determined using non-random lightcurves, but the strength of the flickering can be fitted with these random lightcurves by eye, so as to determine a value for the fraction of the polecap actually emitting. This is the only time where they can be used for fitting purposes, elsewhere they are purely for illustration.

CHAPTER 7

MODELLING OF ACCRETION DISCS IN ACTIVE GALACTIC NUCLEI

7.1 Introduction

In addition to our own galaxy there are millions of other galaxies in the observable universe. With the increase in our ability to observe these in different spectral regions it became clear that some of them were not 'normal'. These 'active' galaxies showed strong emission in spectral regions where a normal galaxy is weak, e.g., radio, infrared, etc. This emission was seen to be variable, in a large number of cases, over a variety of timescales. For a few of these active galaxies optical observations showed massive disruption of the galaxy (for example, M87 in Ursae Majoris), clearly showing that something had occurred, or was still occurring, deep in the heart of the galaxy. Since the bulk of the active emission in these galaxies seemed to emanate from the nucleus these regions became known as an active galactic nuclei (AGN's).

AGN's are characterised by being apparently stellar sources but with non-thermal spectra and, in the case of quasi-stellar objects, significant red-shifts that indicate great distance. AGN's can be broken in sub-classifications according to their appearance, for example the main classes are: radio galaxies (seemingly normal but with visible disruption, e.g., M87); Seyferts (variable galaxies with bright, star-like nuclei, e.g., NGC4151) and quasars (star-like sources with extreme variability down to very short timescales, e.g., 3C273). The size of an AGN can be determined from observation but usually to only give an upper limit. In the optical region the size is of order 1-10 parsec; in the radio region, ~ 1 parsec and from

variability arguments, sizes down to 10^{15} cm, although variability arguments are not good estimates of the true size of the source. A reasonable estimate of the size of the central 'engine' can be taken to be 10^{15} - 10^{16} cm. The mass, from luminosity arguments, is in the range 10^6 - 10^8 solar masses, so clearly there is a lot of material contained within a very small volume of space.

Many suggestions have been made about the nature of the central object, or objects. Compact star clusters, supermassive stars and supermassive black holes are the strongest candidates at the moment. Each has its own advantages but the first two always end up evolving into the latter over timescales much shorter than the suggested timescale for activity in these systems. Therefore a supermassive black hole is the likely candidate for the power source behind active nuclei. The differences seen between the sub-classifications can be explained in terms of the age of the system. Since quasars are at great distances they are young compared to the relatively nearby Seyferts, therefore there will be a great deal of material within the central region available for accretion, hence the nucleus will be very luminous. As we move nearer to home and look at older systems we see a decrease in the luminosity of the central region due to the reduction in the available material for accretion. This argument can also explain why some galaxies are 'normal', since if the central region around the black hole is devoid of material, due to the age of the system, there will be no emission from the nucleus and the galaxy will appear to be normal ! Unfortunately there is no definite proof that supermassive

black holes exist at all but they seem to have the answer to most of the questions concerning AGN's, so for the rest of this chapter I will assume that they do exist and that they are responsible for the emission from active nuclei.

7.1.1 Accretion into a supermassive black hole

If we assume a supermassive black hole of mass M resides at the centre of an active nucleus then material from the surrounding region will be accreted into it. Since we expect the material to be rotating around the centre, with angular momentum per unit mass, l , then it will approach the centre to within a radius, R_{min} , given by,

$$R_{min} \sim l^2/GM \quad (7.1)$$

If $R_{min} > R_{sch}$, the Schwarzschild radius of the black hole, then in order for accretion to occur at all angular momentum must be lost. This is achieved in a similar way as in cataclysmic variables; by the formation of an accretion disc (see Chapter 1 for a discussion of the formation of an accretion disc in a binary system). In fact, for AGN's, $R_{min} \sim 10^{20}$ cm and $R_{sch} \sim 10^{13}$ cm (for a 10^8 solar mass black hole) so clearly a disc might form in order for accretion to occur. Further evidence for accretion discs in these systems comes from the presence of a 'blue-bump' in their spectra. This extra emission has a characteristic temperature of $\sim 10^5$ K, which is typical of an accretion disc. Therefore, from these two arguments,

there is some evidence that accretion into a supermassive black hole in an AGN may take place via an accretion disc. Other possibilities are not forbidden however, for example, if the material is not rotating spherical accretion, directly into the black hole, will occur. For my purposes however it will be assumed that an accretion disc forms around the black hole. A further assumption is that the disc is thin, like in cataclysmic variables, since this allows us to use simplistic formulae for the disc structure.

7.1.2 Structure of a thin accretion disc

In Chapter 1 I described the process by which accreting material forms an accretion disc around a compact object. The material spirals in via successive circular orbits, the loss of angular momentum being due to internal torques in the disc (e.g., viscosity). The derivation of the disc structure equation, by relating the momentum losses to the energy production, will not be described here and the reader should consult Frank, King and Raine (1985, Chapters 4 and 5) for a complete derivation. From the above, assuming that the disc is geometrically thin and optically thick in the z-direction (perpendicular to the disc), each element of the disc will radiate at a temperature, $T_{eff}(R)$, given by equating the dissipated flux per unit area $D(R)$ to the emitted flux, i.e.,

$$\sigma T_{eff}^4(R) = D(R) = 3GM\dot{M}/8\pi R^3 [1 - (R_*/R)^{1/2}] \quad (7.2)$$

where \dot{M} is the accretion rate (gs^{-1}), M is the black hole mass, R is the radius of the emitting element and R_* is the inner edge of the disc (the inner edge is the position of the last stable circular orbit, $\sim 6R_{sch}$). If we parameterize the radius scale by putting R in terms of the inner edge radius R_* using $X=R/R_*$ then equation (7.2) becomes

$$T_{eff}(X) = [3GM\dot{M}/8\pi R_*^3 \sigma]^{1/4} X^{-3/4} [1 - X^{-1/2}]^{1/4} \quad (7.3)$$

If we define a characteristic temperature for the disc, T_* , given by

$$T_* = (3GM\dot{M}/8\pi R_*^3 \sigma)^{1/4} \quad (7.4)$$

we have

$$T_{eff}(X) = T_* X^{-3/4} [1 - X^{-1/2}]^{1/4} \quad (7.5)$$

and, from $R_* = 6GM/c^2$, we get

$$\begin{aligned} T_* &= (3GM\dot{M}c^6/1728\pi G^3 M^3 \sigma)^{1/4} \\ &= 2.51 \times 10^5 M_8^{-1/2} \dot{M}_{26}^{1/4} \end{aligned} \quad (7.6)$$

where M_8 is the mass of the black hole in units of 10^8 solar masses and \dot{M}_{26} is the accretion rate in units of 10^{26} gs^{-1} . The effective gravity at each point in the disc is given by

$$g_{eff}(X) = (GM/R_*^2) X^{-2} (H/R) \quad (7.7)$$

where H is the height of the disc at a point X . If we let $\theta=H/R$ be the opening angle of the disc then we have

$$g_{eff}(X) = 1.65 \times 10^6 M_8^{-1} X^{-2} \theta \quad (7.8)$$

Strictly speaking θ is given by

$$\theta = H/R = c_s/v_\phi = [kT_{eff}/(GM/R)]^{1/2} \quad (7.9)$$

where c_s is the sound speed and v_ϕ is the rotational velocity; so in fact θ is a function of X but since it only varies as $\sim X^{1/8}$ a constant opening angle will be assumed. The values chosen for θ will be discussed later in this chapter.

To summarize, we now have the disc structure given by $T_{eff}(X)$ and $g_{eff}(X)$, where $X=R/R_*$. By choosing appropriate values for θ the temperature and gravity structure throughout the disc can be quickly calculated. Two major assumptions have been made during this derivation; the accretion disc is assumed to be thin and to have constant opening angle (the disc will be thin provided its cooling is efficient, see Frank, King and Raine, Chapter 5, 1985). There are no compelling reasons to expect that these are good approximations to the truth but since we have no real idea what the disc looks like in these systems there is no reason not to make these assumptions.

7.1.3 The emitted spectrum

If we assume that each region of the disc radiates

locally with an emitted intensity I_ν then we can integrate the contributions from each part of the disc to get the total emitted spectrum. If we assume that the disc extends to a distance X_{\max} and is at an inclination i to the observer then we have

$$F_\nu = (2\pi \cos i R_*^2 / D^2) \int_1^{X_{\max}} I_\nu X dX \quad (7.10)$$

since a ring between radii X and dX subtends a solid angle $2\pi R_* X dX \cos i / D^2$ at a distance D from the source. I_ν is a function of $T_{\text{eff}}(X)$, $g_{\text{eff}}(X)$ and i for a model atmosphere but only a function of $T_{\text{eff}}(X)$ for a black body.

Calculations of F_ν where each part of the disc is assumed to radiate as a black body have been discussed in, for example, Bechtold et al. (1984) and Elvis, Czerny and Wilkes (1986). Modified black bodies, to include opacity effects, have also been used (Czerny and Elvis, 1987) but neither give good agreement with observation. By using model atmospheres instead it was hoped that this problem may be reduced.

7.2 Stellar atmosphere disc models

The motivation for constructing accretion disc models using stellar atmospheres, rather than black bodies, was the same as that for calculating model atmospheres in the first place, namely that black bodies do not give a realistic idea of the emission from a source whereas a self consistent atmosphere model should. The atmosphere code described in Chapters 2 and 3 was written for the polecap

of a magnetic white dwarf. Clearly this is not a good approximation for any region of an accretion disc but the code has enough flexibility that some of these differences can be accommodated.

7.2.1 Accretion disc .v. magnetic polecap

A magnetic polecap has the following important properties:

- (i) isotropic, hard X-ray irradiation of the white dwarf surface
- (ii) surface pressure due to the accreting material
- (iii) strong magnetic field preventing convective flux transport

Considering each of these in turn, with an AGN accretion disc in mind, we find for (i) that an accretion disc around a supermassive black hole would also be irradiated by hard X-rays but these would probably not be isotropic, indeed the precise orientation of them to each part of the accretion disc would probably be different. In order to simplify this problem it was decided to assume that the disc was unilluminated, since removing the X-ray illumination doesn't have an enormous effect on the observed spectrum. For (ii), there is no surface pressure on an accretion disc; unfortunately, the removal of surface pressure from the atmosphere code is not a simple task and so it proved necessary to leave it in. However, examination of the values for the accretion pressure, P_{acc}

and the photospheric pressure, P_{ph} , over a wide range of temperatures and gravities suggests that P_{acc} never exceeds P_{ph} to any great extent and so the inclusion of P_{acc} in the code will not greatly affect the final result. Lastly, for (iii), there is not expected to be any appreciable magnetic field in an AGN accretion disc and so convection is not strictly forbidden. For low effective temperatures and gravities convective flux transport would probably become important but, again, the inclusion of convection into the atmosphere model is a complex task, which must be tackled in future treatments.

It is clear that there are strong differences between the two situations that will be modelled. The complete removal of which was not possible in the time remaining. As a result these models can only at best be illustrative of what the true spectrum may look like. For this reason no actual observational fitting was carried out using the calculated spectra.

7.2.2 A model atmosphere grid

If the accretion disc spectrum were to be calculated in the same way as one with black bodies then it would be necessary to run a different atmosphere model at each point on the disc. This is clearly very time consuming and it would have to be repeated for each new disc model. The simplest way to overcome this problem is to have a grid of model atmospheres from which the corresponding intensities for a particular effective temperature and gravity can be

for a particular effective temperature and gravity can be found. This would allow different disc models to be run quickly and easily from the one grid of atmosphere models.

While this at first sight seems a simple task this was in fact not so. Firstly, due to lack of storage space, it was only possible to store one atmosphere grid, i.e., only one outward ray for each model was stored. Therefore it had to be assumed that the disc was at an inclination of 0° (face on) so that the ray normal to the atmosphere was used from each model; this had the added effect that doppler effects did not have to be included in the calculation.

In order to cover all possible disc models the temperature range for the grid was from 2.0×10^4 K (the coldest atmosphere that the code could run) to 4.0×10^5 K. The range in gravity was from the minimum gravity possible for $T_{\text{eff}} = 2.0 \times 10^4$ K, 160.0 cm s^{-2} (see Chapter 4 for the discussion of minimum gravities), to an arbitrary maximum of $1.0 \times 10^9 \text{ cm s}^{-2}$. With such a large range in the values of both parameters it was necessary to use a 20×20 grid with models spaced logarithmically in temperature and gravity. Since it would be extremely time consuming to run 400 atmosphere models it was decided to run a smaller grid of models and interpolate a 20×20 grid from that. Obviously the small grid had to have the same range in temperature and gravity; the values of temperature chosen were evenly spaced values from the chosen values in the large grid (to give the maximum accuracy possible for the interpolation). The gravities used for the small grid were the minima for each temperature, in this way it was possible to say which models in the large grid would be

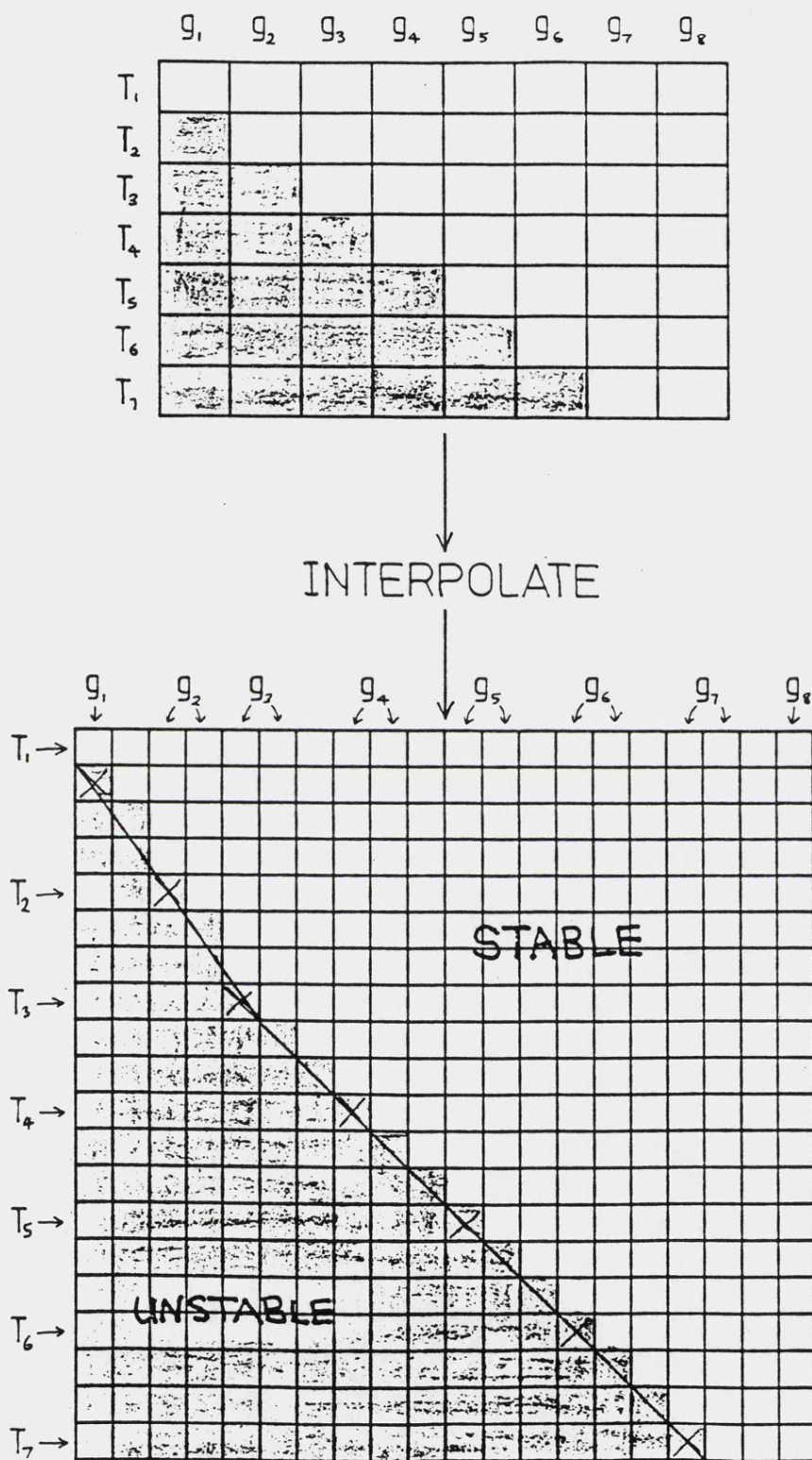


Figure 7.1 Producing a large 20x20 grid from a calculated 7x8 grid of atmosphere models (see text for a description of the symbols).

radiatively unstable. Figure 7.1 shows how this worked. The shaded areas in the small grid are the models which are radiatively unstable. In order that the large grid can be interpolated artificial intensities had to be put in for these models, these were calculated by extrapolating from the higher gravity models at each temperature. After the interpolation of the 20x20 grid has taken place these unstable models appear at the points in the large grid marked by X's; by 'joining' these together the grid is broken into stable and unstable regions. Note that the X's mark the nearest gravity below the limiting gravity for each particular temperature since, unlike the temperature points, the gravity points for the calculated models could not be chosen from the grid directly (the limiting gravity is not a simple function of temperature). When the accretion disc model is calculated any pair of T_{eff} and g_{eff} that occur inside the shaded region of the large grid can then be flagged as radiatively unstable, indicating that the disc would be disrupted at this point. The extrapolated intensities used for the unstable models in the small grid had no effect on the interpolated intensities of the stable models in the large grid.

The actual interpolation of the large grid is made more complicated because of the fact that each atmosphere model has a different range of frequency points. The only solution was to choose the frequency points for the hottest model and use those throughout the interpolation, interpolating the intensities at those frequencies from the intensities of the nearest neighbours. The interpolation routine used was a two-dimensional array interpolation

routine from the NAG subroutine library (namely, E01ACF) and the interpolated values should be accurate to a fraction of a percent.

Even with this 20x20 grid of models simply reading the intensities from the nearest model to the required one would not prove accurate, due to the gross changes that occur in the spectrum with changes in the effective temperature. It was therefore necessary to do a further interpolation, this time from the model grid itself, for the intensity at any frequency, temperature and gravity, from the nearest values in the grid. Again the errors involved in this were expected to be less than 1.0%. This then gave the values of I_{ν} to be used at any point in the accretion disc.

Summarizing, the atmosphere model file contained 400 models, each model having 100 optical/UV frequency points. The ray normal to the atmosphere was used throughout. Each model was unilluminated but had surface pressure included. Unstable models in the grid were flagged so as to warn of an unstable disc model. With the model file created all that remains is to calculate the emergent spectrum.

7.2.3 Calculating the emergent spectrum

Using equations (7.5), (7.6) and (7.8) the temperature and gravity at each point X in the disc can be calculated. The correct intensity at each frequency for each region of the disc has to then be interpolated from the grid of atmosphere models. In some cases this interpolation requires the use of unstable models, Figure 7.2 shows the

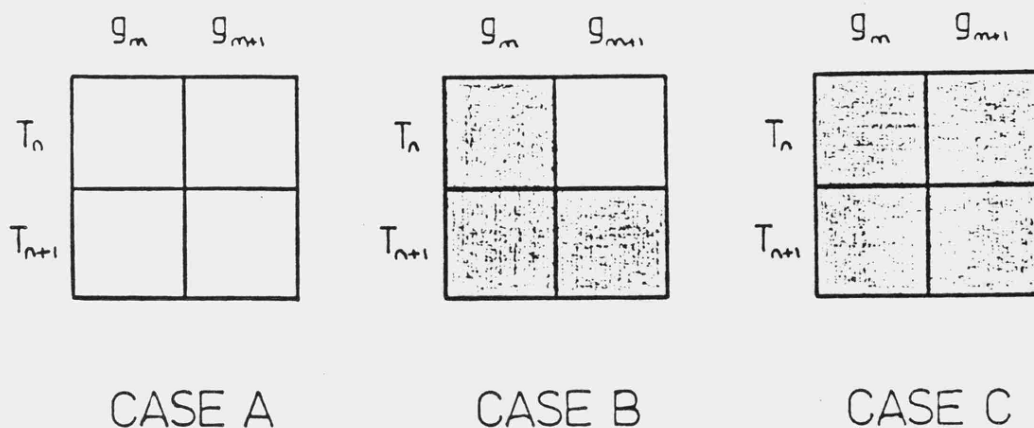


Figure 7.2 Interpolating from the model file - the three possible cases.

possible cases where this may occur; again the shaded regions indicate unstable models. In each case the required effective temperature and gravity is given by $T_n < T_{eff} < T_{n+1}$ and $g_m < g_{eff} < g_{m+1}$ respectively. In case A none of the models is radiatively unstable and so the interpolated intensities should be relatively accurate. Case B however represents the worst possible case of not all the models being unstable but since g_{eff} may or may not be less than the minimum stable gravity there is no way of knowing whether the interpolated model would in fact be radiatively unstable or not. It is this case where the accuracy of the interpolated model is questionable since the shaded areas were not calculated directly, however, inspection of the data contained in the model file suggested that any intensities used for cases like this would not be unreasonably erroneous. Lastly, for case C, the use of an interpolated model in this case would be clearly inaccurate since it would definitely have been

radiatively unstable had it have been calculated in the normal way.

Before the calculation of the total spectrum it was necessary to choose a value for θ . This was largely a free parameter but it is constrained to a maximum of about 1.5 (so as to keep the disc essentially 'thin'). The minimum value for θ was governed by the stability of the resultant disc, taking θ too small made the disc radiatively unstable in places. θ was therefore chosen to be the minimum possible for a wholly stable disc; for some discs however this gave values of θ that clearly indicated that the thin disc approximation was not valid.

Assuming that the required values of T_{eff} and g_{eff} gave a stable disc the contribution from each part of the disc could then be summed to give an emergent spectrum for the whole disc. The values of X were chosen so as to give as many points as possible over regions where the temperature was changing rapidly. The value of X_{max} was taken to be the radius where the effective temperature fell below 2.0×10^4 K. There would still be appreciable emission in the optical region from this section of the disc to the outer edge so it was necessary to use black body spectra (suitably normalised so as to look like atmosphere spectra in that region) from X_{max} outwards. The summation was completed when the contribution at each frequency was less than 0.01% of the total flux. The addition of black bodies to the spectrum tended to cause an underestimation of the strength of the HI and HeI absorption features however, as these are strong for $T_{eff} < 5.0 \times 10^4$ K. In order to understand the calculation more clearly Figure 7.3 shows a

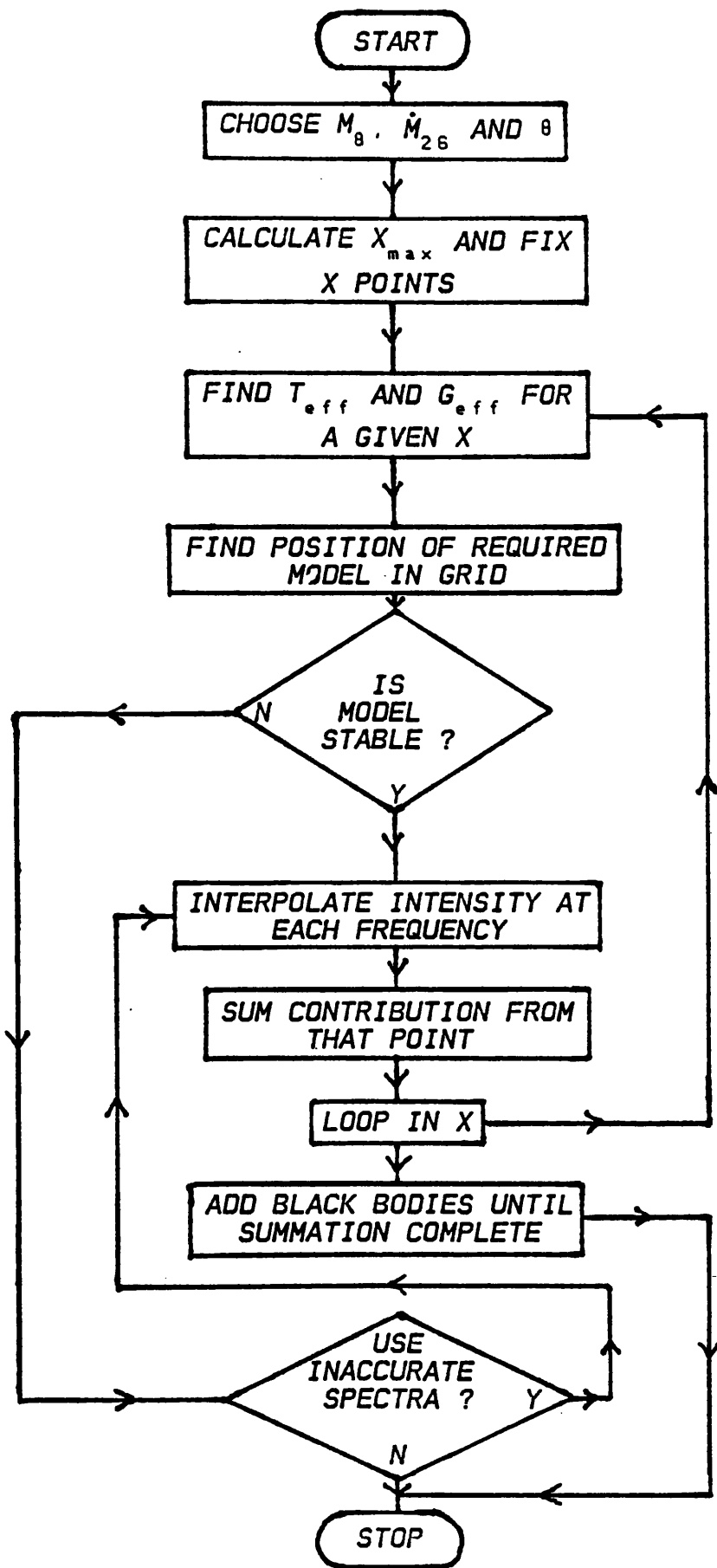


Figure 7.3 Flow diagram for the calculation of an AGN accretion disc spectrum using model atmospheres.

full flow diagram for the calculation of an AGN accretion disc spectrum using intensities from a grid of model atmospheres. The results of such a calculation can be seen in the next section.

7.3 The results of an AGN disc calculation

In this section I will show the general results of an accretion disc calculation using model atmospheres as the outward spectrum from each part of the disc. As these are only illustrative no observational fitting will be shown.

7.3.1 The AGN disc structure

Figure 7.4 shows the effective temperature in the disc, T_{eff} , as a function of the parameterized radius X , for three values of the accretion rate. For these; $M_g = 1.0$, $\theta = 0.5$ and \dot{M}_{26} has the values 0.1, 1.0 and 10.0. The critical temperature structure, T_{crit} , for a stable disc, with the same parameters, is also shown; it is the same for all three models since the gravity structure is only a function of M_g and θ . The figure shows that the effective temperature in the disc has a fast rise between $\log X = 0.0$ and $\log X = 0.15$ and then a slow decline; a large number of disc points were needed to cover the inner region accurately. The figure also shows that for $\dot{M}_{26} = 10.0$ the disc will be radiatively unstable over most of its area; by increasing θ this model could be made stable but if θ is made too large then the thin disc approximation will not hold. The discontinuities in the variation of T_{crit} are

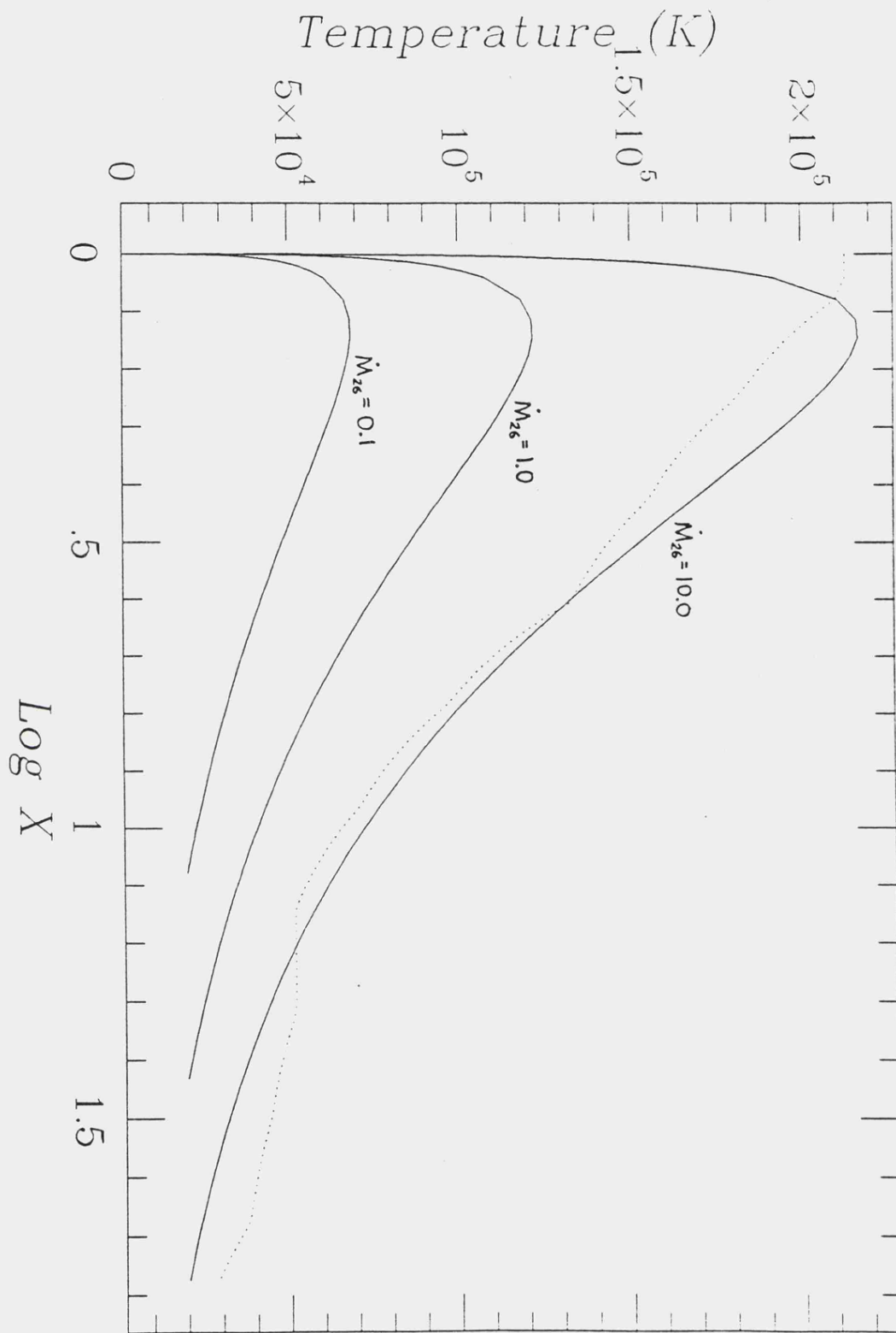


Figure 7.4 The effective temperature of the disc, T_{eff} , as a function of the radius parameter X for $M_b = 1.0$, $h = 0.5$ and $\dot{M}_{26} = 0.1, 1.0$ and 10.0 . The variation of $T_{\text{crit}, 26}$, the critical temperature, over the disc is also shown (dotted line).

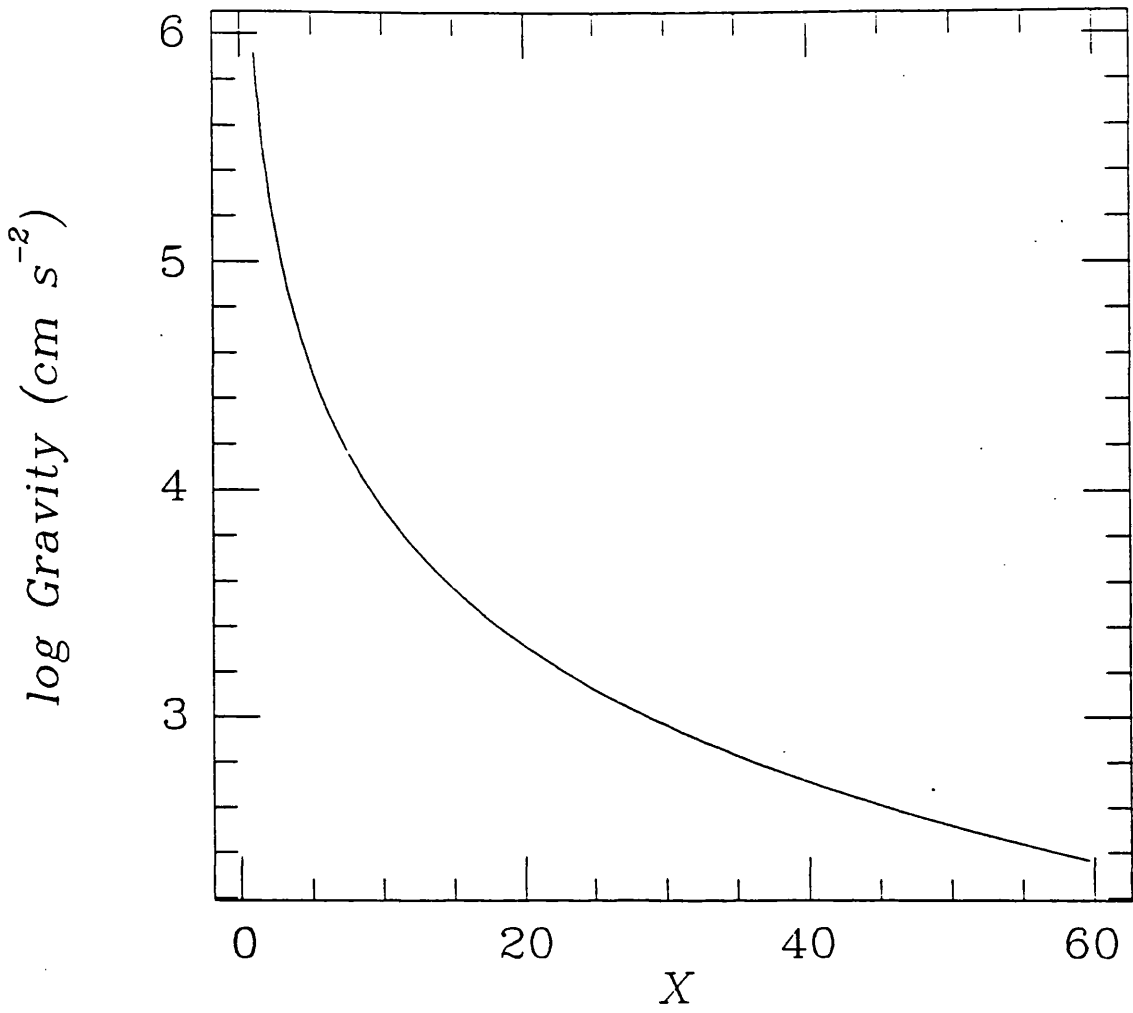


Figure 7.5 Effective gravity, g_{eff} , within the disc as a function of the radius parameter X for $M_g=1.0$, $\theta=0.5$ and $\dot{M}_{2g}=1.0$.

due to the limited number of critical temperatures in the atmosphere model file; a single disc model only covers a small region of the file.

Figure 7.5 shows the effective gravity in the disc, g_{eff} , as a function of X , for $M_g=1.0$, $\dot{M}_{2g}=1.0$ and $\theta=0.5$. As g_{eff} is a simple function of X no other curves are shown. Finally, Figure 7.6 shows the observed spectrum ($XI_V(X)$) at each point in the disc for M_g and \dot{M}_{2g} equal to unity. The variation in the strength of the absorption features over the disc can clearly be seen (note: the

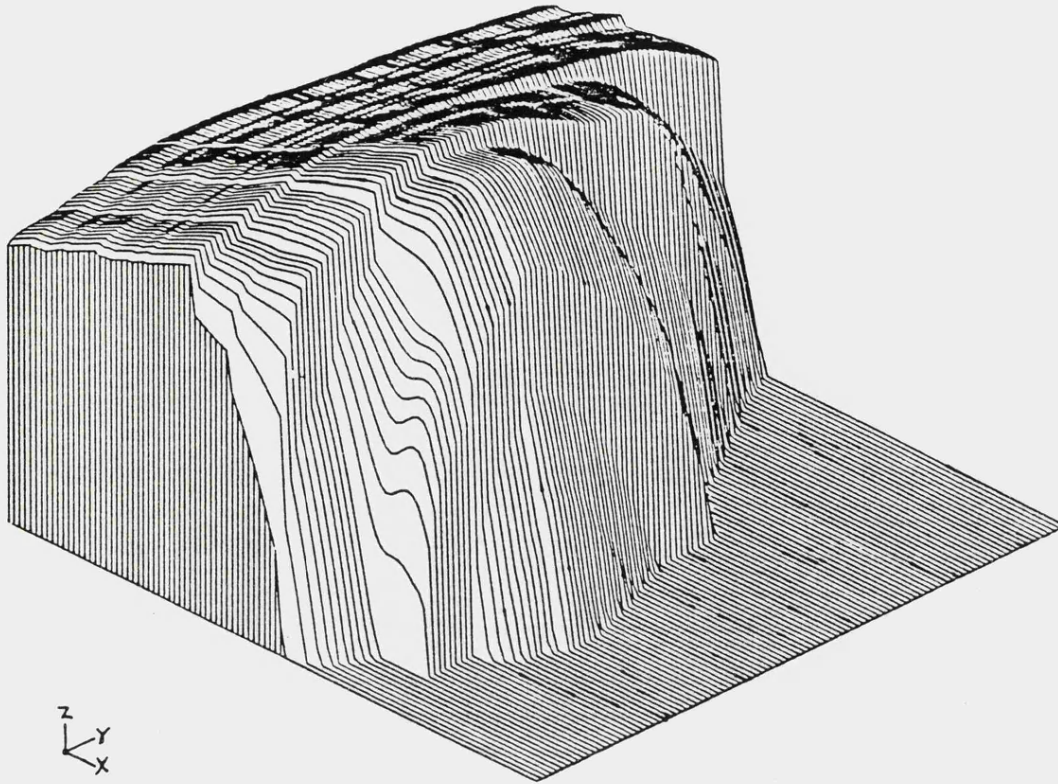


Figure 7.6 The observed spectrum, $XI_v(X)$, at each point in the disc for M_8 and $\dot{M}_{2.6}$ equal to unity ($\theta=0.5$). The axes are; x =frequency, y =radius (not to scale) and z =flux.

y -axis is not to scale).

7.3.2 Calculated AGN spectra

Figure 7.7 shows the observed spectrum at the source for $M_8=1.0$, $\dot{M}_{2.6}=1.0$ and $\theta=0.5$. The calculated spectrum using atmospheres only is shown on the figure by a dashed line. The 'filling out' of the spectrum in the optical region by the black bodies can clearly be seen, while the absorption strengths are unaffected. Comparison with an

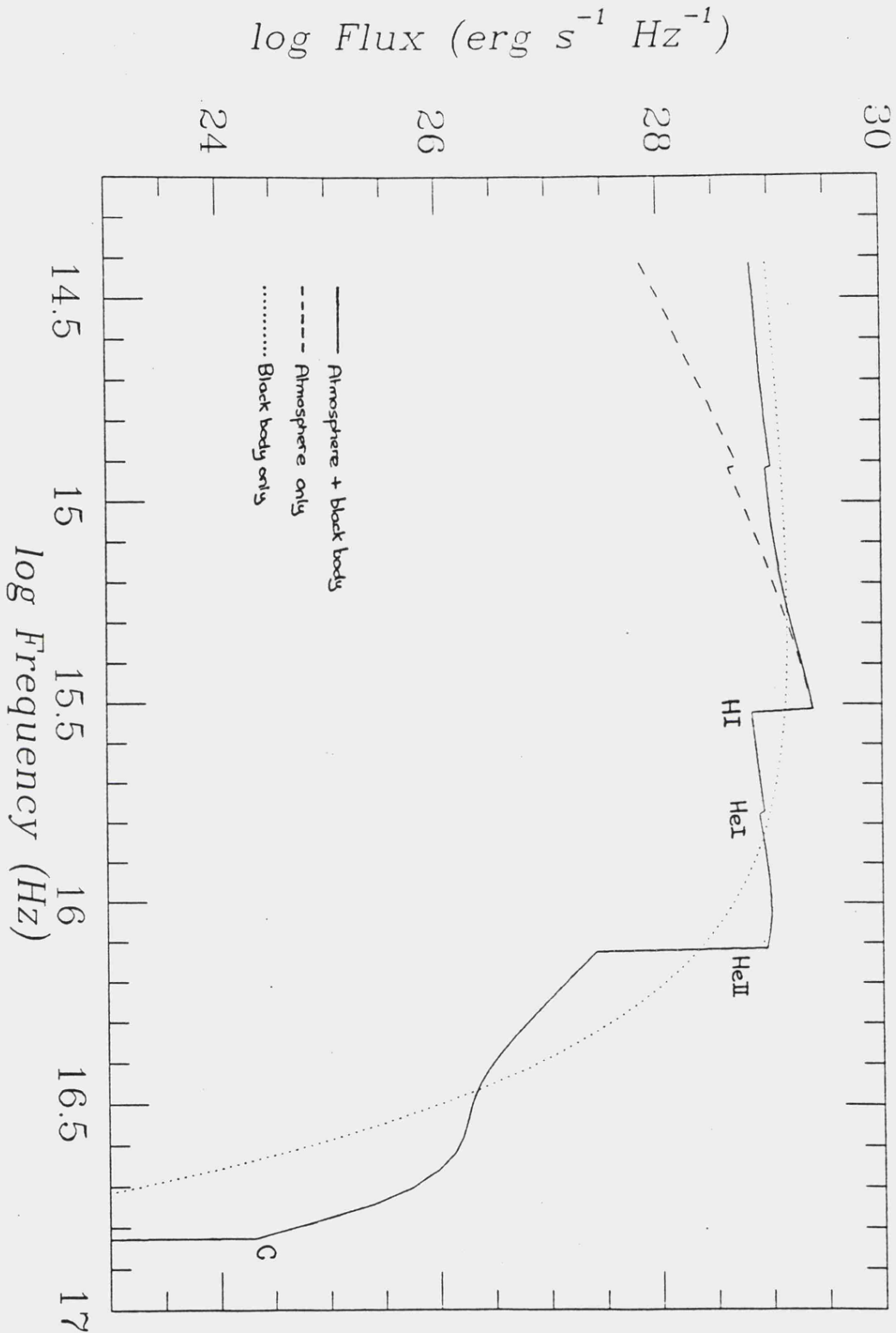


Figure 7.7 Calculated disc spectrum (at the source) for $M_g=1.0$, $M_{26}=1.0$ and $\theta=0.5$. The resultant spectrum using just model atmospheres is shown by the dashed line, a black body disc spectrum is also shown (dotted line). The absorption features are labelled with the elemental ionisation state responsible.

AGN spectrum calculated using black bodies only (shown by the dotted line) shows that two models have a similar 'hardness' in the soft X-ray continuum. The presence of low temperature models in the outer regions of the disc cause the absorption features to be large compared to the rest of the spectrum and features are seen that would not normally be seen in a single temperature atmosphere with $T_{\text{eff}} = T_{\text{max}}$, the maximum temperature in the disc (in this case $T_{\text{max}} \sim 1.2 \times 10^5$ K but the HeI feature at $\log v = 15.77$ is clearly seen).

Figure 7.8 shows a comparison between two AGN models. One is a high temperature model; $T_{\text{max}} = 3.8 \times 10^5$ K, with $M_g = 0.01$, $\dot{M}_{26} = 0.01$ and $\theta = 1.0$, while the other is a low temperature model; $T_{\text{max}} = 3.8 \times 10^4$ K with $M_g = 10.0$, $\dot{M}_{26} = 1.0$ and $\theta = 0.05$. Surprisingly the low temperature disc has the strongest optical continuum but, as expected, the high temperature disc has the stronger X-ray continuum. Both models have a similar soft X-ray 'hardness' to their black body counterparts (again shown by dotted lines in the figure). As in the first figure, even for the high temperature disc the absorption edges are fairly strong. The possible significance of the results from these calculations will be discussed next.

7.4 Discussion of results and possible improvements

In section 7.2.1 I discussed the differences between the magnetic polecap of a white dwarf and a small region of an accretion disc around a supermassive black hole. Taking these strong differences into account accretion disc models

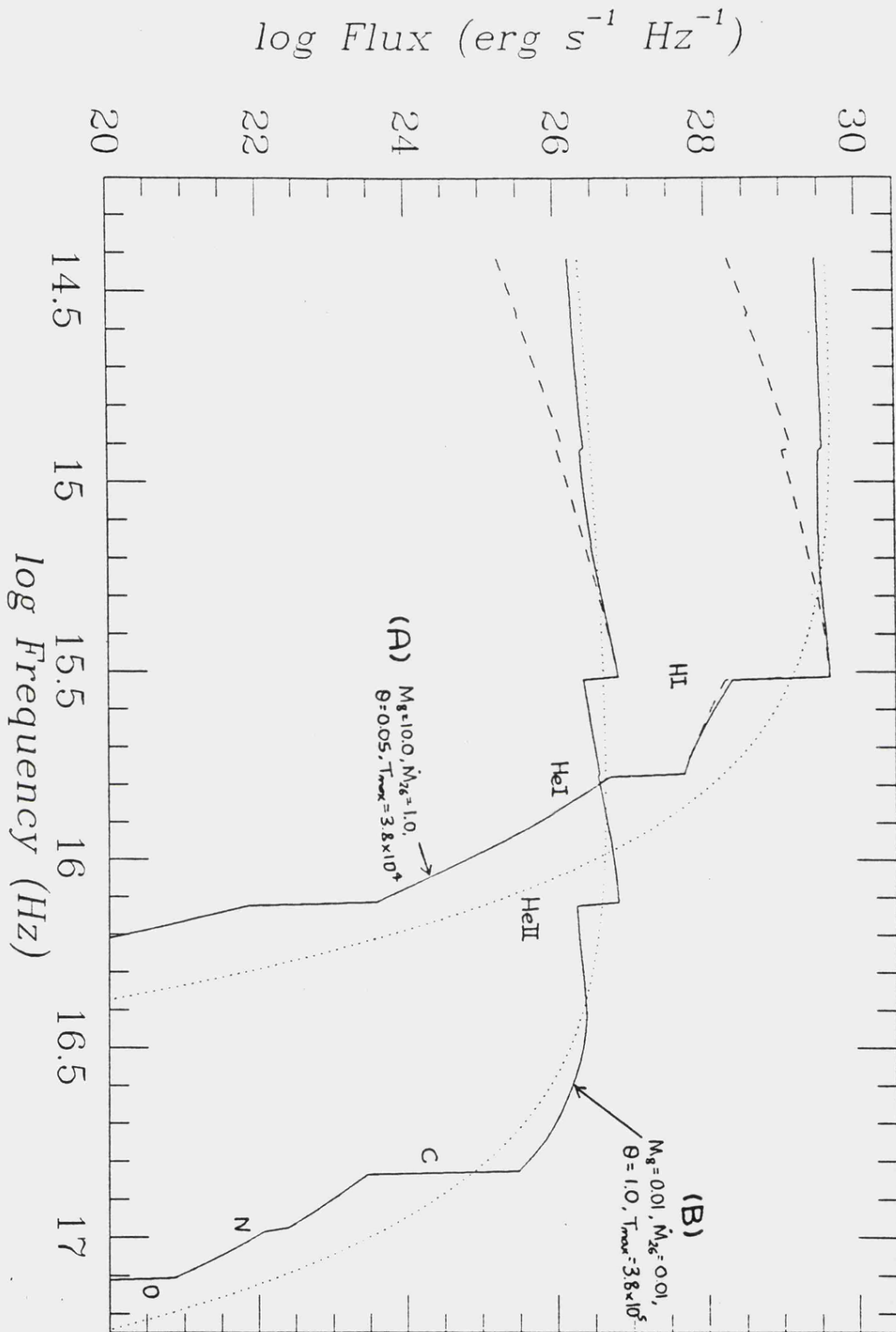


Figure 7.8 Comparison between two AGN models; a low temperature model (A), with $M_B=10.0$, $\dot{M}_{26}=1.0$ and $\theta=0.05$ ($T_{\text{max}}=3.8 \times 10^4$ K); and a high temperature model (B), with $M_B=0.01$, $\dot{M}_{26}=0.01$ and $\theta=1.0$ ($T_{\text{max}}=3.8 \times 10^5$ K). Atmosphere only and black body disc spectra are also shown (as in Figure 7.7).

were calculated using atmospheres originally used for the modelling of the magnetic polecap. The results of this were seen above. In drawing conclusions from these it is important to keep in mind the changes that would occur if the differences described before could be resolved.

The main reason for using model atmospheres in these disc calculations was to see if they gave a better representation for the emergent spectrum of an accretion disc than one calculated using black bodies. We have seen the differences between the two spectra quite clearly and in a general way a model atmosphere AGN spectrum is better than a black body one but before model atmospheres can be used in observational fitting the problems outlined in section 7.2.1 must be resolved.

Unilluminated model atmospheres were used in the calculation of the AGN spectra. In reality there would be hard X-ray illumination of the surface of the disc and we would expect it to be anisotropic. We have seen in Chapter 4 that irradiating a model atmosphere reduces the temperature gradient, making the spectrum 'softer'; whether making the irradiation ray-dependent would lead to a harder spectrum is unknown but this is unlikely, so including X-ray irradiation will lead to even softer AGN spectra.

The first of two major problems with the use of these model atmospheres was that there was no easy way to remove the surface pressure from the top of the atmosphere. An atmosphere without surface pressure may be more susceptible to radiation instabilities; the limiting gravities in the model file may in fact be underestimates of the true gravity limit and some previously stable disc models may

become unstable if this change was made. Clearly the range of stable θ , M_8 and M_{26} would then be greatly reduced.

The second major problem with these model atmospheres is the omission of convection. An AGN accretion disc will not have a strong magnetic field (what field there is will be a dynamo-type field that will only be strong near the inner edge of the disc, where there is little contribution to the overall flux), so convection will not be suppressed. The changes that could be expected if convection was included in the atmosphere code are unknown but the resultant models may become more stable, enabling lower gravities to be used for a given effective temperature. It is also expected that it would be possible to run models with $T_{eff} < 2.0 \times 10^4$ K. This would enable a more accurate representation of the outer, cooler, regions of the disc.

All of the above improvements could have been accomplished, given more time. Despite their omission the results presented here clearly show what can be achieved in this area by the use of model atmospheres. Although only intended to be illustrative only these models have appeared in the literature, fitted to observational sources. For example, Pounds et al. (1987) show one of these models fitted to the observed spectrum of a Seyfert I galaxy, Markarian 335. However no conclusions were drawn from this fit. In conclusion, the use of model atmospheres in the calculation of AGN disc spectra shows great promise, with the major differences resolved they could prove useful for the fitting of observed spectra. The major disappointment throughout this work is the number of assumptions that have to be made in order to begin the calculation, i.e. thin

disc, constant opening angle, etc., indeed the existence of discs at all in these systems has still yet to be proven conclusively. There is clearly still a lot of work to be done in this relatively new area of astronomy.

CHAPTER 8

CONCLUSION

8. Conclusion

The use of self-consistent model atmospheres instead of black bodies has definite advantages in all forms of spectral fitting and simulation. The model atmospheres described in this work were calculated in order to give a more realistic representation of the spectrum for the accretion column of a magnetic white dwarf. It was hoped that they would go some way to quantifying and understanding the soft X-ray excess associated with polar systems. The results of black body fitting to the atmosphere spectra (see Chapter 5) showed that this excess was not removed by using model atmospheres. Although the fitted temperature could be wrong by up to a factor of two or more, and the polecap fractional area by factors up to 10^2 , the two errors tended to cancel each other out to give a fitted luminosity that, for most effective temperatures, was correct to within a factor of two.

In Chapter 6 I described the calculation of lightcurves and their subsequent use in fitting the EXOSAT lightcurves of AM Herculis. The results indicate that this lightcurve fitting was a great success; the inferred values for the magnetic axis angle of the primary pole and the inclination to the line of sight agreed very well with the values inferred from observation (Brainerd and Lamb, 1985) and the off-centred nature of the magnetic axis seemed to confirm in principle the conclusions of Wickramasinghe and Martin (1985). The simulation of these lightcurves could be further improved by adding in other effects that had previously been ignored, e.g., occultations of the polecap

by the accretion stream or the accretion column itself. However, as the lightcurve modelling stands at present there is considerable precedence for keeping the model as simple as possible and using it to fit other lightcurves first, in order to check for any fitting 'bias' (in fact only a few of the observed lightcurves show any of the effects ignored by this simplistic approach).

The final use for these model atmospheres was described in Chapter 7: the calculation of accretion disc spectra for active galactic nuclei. It was here that the inadequacies of the present atmosphere model, when used for disc accretion, became apparent; namely the lack of convective flux transport and the presence of accretion pressure at the surface when there should be none. Further problems with this calculation were the number of assumptions that had to be made in order to be able to calculate a disc model in the first place. These assumptions can be justified if we note that they have not prevented the calculation and use of black body accretion disc spectra in the fitting of observed sources (e.g., Bechtold et al., 1984 and Elvis et al., 1986). However, no actual fitting was undertaken in this case as it was felt that this should wait for a more realistic atmosphere model, taking account of the special requirements necessary for an accretion disc. Given more time it would have been possible to remove the inadequacies mentioned above, the inclusion of convective flux transport being a very important improvement in general.

Summarizing, the results of this work indicate that

model atmospheres have a definite part to play in the fitting of spectra from accreting systems. The limited fitting undertaken in this work has shown what can be expected from their further use. With the improvements mentioned above included in the model it could become a very powerful tool indeed. In the future it could be used for regions that as yet have not been modelled in any way. There is still a lot of ground to be covered in this field.

REFERENCES

REFERENCES

- Athay, R. (1972). Radiative Transport in Spectral Lines. Reidel Publ. Co.
- Auer, L.H. and Mihalas, D. (1970). Mon. Not. R. Astron. Soc. 149, 60.
- Bailey, J., Hough, J.H., Gilmozzi, R. and Axon, D.J. (1984). Mon. Not. R. Astron. Soc. 207, 777.
- Barnett, S. (1979). Matrix Methods for Engineers and Scientists, p34. McGraw-Hill (UK) Ltd., Maidenhead, Berks.
- Bechtold, J., Green, R.F., Weymann, R.J., Schmidt, M., Estabrook, F.B., Sherman, R.D., Wahlquist, H.D. and Heckman, T.M. (1984). Astrophys. Journ. 281, 76.
- Biermann, P., Schmidt, G.D., Liebert, J., Stockman, H.S., Tapia, S., Kuhr, H., Strittmatter, P.A., West, S. and Lamb, D.Q. (1985). Astrophys. Journ. 293, 303.
- Bonnet-Bidaud, J.M., Beuermann, K., Charles, P., Maraschi, L., Motch, C., Mouchet, M., Osborne, J., Tanzi, E. and Treves, A. (1985). Recent Results on Cataclysmic Variables, p155. (Proceedings of an ESA workshop held at Remeis Observatory, Bamberg, F.R. Germany, 17-19 April 1985). ESA Spec. Publ. ESA SP-236.
- Brainerd, J.J. and Lamb, D.Q. (1985). Cataclysmic Variables and Low Mass X-ray Binaries, p247. Reidel Publ. Co., eds. Lamb, D.Q. and Patterson, J.
- Bunner, A.N. (1978). Astrophys. Journ. 220, 261.
- Campbell, C.G. (1983). Mon. Not. R. Astron. Soc. 205, 1031.
- Czerny, B. and Elvis, M. (1987). Astrophys. Journ. In press.

- Elvis, M., Czerny, B. and Wilkes, B.J. (1986). The Physics of Accretion onto Compact Objects, p389. Springer.
- Hayakawa, S., Iwanami, H., Kunleida, H., Nagase, F. and Yamashita, K. (1979). X-ray Astronomy, p159. Eds. Baity, W.A. and Peterson, L.E. (Cospar).
- Fabbiano, G., Hartmann, L., Raymond, J., Steiner, J., Branduardi, G. and Matilsky, T. (1981). Astron. Astrophys. 134, 328.
- Feautrier, P. (1964). C.R. Acad. Sci. Paris 258, 3189.
- Frank, J. and King, A.R. (1984). Astron. Astrophys. 134, 328.
- Frank, J., King, A.R. and Lasota, J.P. (1983). Mon. Not. R. Astron. Soc. 202, 183.
- Frank, J., King, A.R. and Raine, D.J. (1985). Accretion Power in Astrophysics. Cambridge University Press.
- Hearn, D.R. and Richardson, J.A. (1977). Astrophys. Journ., Lett. 213, L115.
- Heise, J. (1982). Some observational aspects of Compact Galactic X-ray sources. PhD thesis, University of Utrecht.
- Heise, J., Brinkmann, A.C., Gronenschild, E., Watson, M.G., King, A.R., Stella, L. and Kieboom, K. (1985). Astron. Astrophys. 148, L14.
- King, A.R. to appear in Classical Novae, Chapter 2. (eds. Bode, M.F., Evans, A. and Wiley, J.).
- King, A.R. and Shaviv, G. (1984). Mon. Not. R. Astron. Soc. 211, 883.
- King, A.R. and Williams, G.A. (1985). Mon. Not. R. Astron. Soc. 215, 1P.
- Kurucz, R.L. (1979). Astrophys. J., Suppl. Ser. 40, 1

- Latham, D.W., Liebert, J. and Steiner, J.E. (1981).
Astrophys. Journ. 246, 919.
- Liebert, J. and Stockmann, H.S. (1985). Cataclysmic
Variables and Low Mass X-ray Binaries, p151. Reidel
Publ. Co., eds. Lamb, D.Q. and Patterson, J.
- Mark, C. (1947). Phys. Rev. 72, 558.
- Mason, K.O. (1985). Space Sci. Rev. 40, 99.
- Mihalas, D. (1978). Stellar Atmospheres (2nd Ed.). W.H.
Freeman and Company, San Francisco.
- Milgrom, M. and Salpeter, E.E. (1975). Astrophys. Journ.
196, 583.
- Nauenberg, M. (1972). Astrophys. Journ. 175, 417.
- Pounds, K.A., Stanger, V.J., Turner, T.J., King, A.R. and
Czerny, B. (1986). Mon. Not. R. Astron. Soc. 224,
443.
- Osborne, J.P., Bonnett-Bidaud, J.M., Bowyer, S., Charles,
P., Chiappetti, L., Clarice, J.T., Henry, P., Hill,
G., Kahn, S., Maraschi, L., Mukai, K., Treves, A.
and Vrtilik, S. (1986a). Mon. Not. R. Astron. Soc.
221, 823.
- Osborne, J.P., Mukai, K., Beuermann, K., et al. (1986b).
Poster paper presented at the Tenerife Workshop,
April 1986 (Accretion onto Compact Objects).
- Osborne, J.P., Mukai, K., Bonnett-Bidaud, J.M., Charles,
P., Corbet, R., Henry, P., Hill, G., Kahn, S., van
der Klis, M., Maraschi, L., Treves, A. and Vrtilik,
S. (1985). Recent Results on Cataclysmic Variables,
p161 (Proceedings of an ESA workshop held at Remeis
Observatory, Bamberg, F.R. Germany, 17-19 April
1985). ESA Spec. Publ. ESA SP-236.

- Rothschild, R.E., Gruber, D.E., Knight, F.K., Matteson, J.L., Nolan, P.L., Swank, J.H., Holt, S.S., Serlemitsas, P.J., Mason, K.O. and Tuohy, I.H. (1981). *Astrophys. Journ.* 250, 723.
- Rybicki, G.B. (1971). *Journ. Quant. Spectrosc. Radiat. Transfer* 11, 589.
- Schwope, A. and Beuermann, K. (1985). *Recent Results on Cataclysmic Variables*, p173 (Proceedings of an ESA workshop held at Remeis Observatory, Bamberg, F.R. Germany, 17-19 April 1985). *ESA Spec. Publ. ESA SP-236*.
- Tuohy, I.R., Lamb, F.K., Garmire, G.P. and Mason, K.O. (1978). *Astrophys. Journ., Lett.* 226, L17.
- Watson, M.G. (1986). *The Physics of Accretion onto Compact Objects*, p97. Springer.
- Watson, M.G., King, A.R. and Williams, G.A. (1987). *Mon. Not. R. Astron. Soc.* 226, 867.
- Watson, M.G., King, A.R., Williams, G.A, Heise, J. and Beuermann, K. *Recent Results on Cataclysmic Variables*, p169 (Proceedings of an ESA workshop held at Remeis Observatory, Bamberg, F.R. Germany, 17-19 April 1985). *ESA Spec. Publ. ESA SP-236*.
- Wickramasinghe, D.T. and Martin, B. (1985). *Mon. Not. R. Astron. Soc.* 212, 353.
- Young, P.J. and Schneider, D.P. (1981). *Astrophys. Journ.* 247, 960.

APPENDIX

ASTROPHYSICAL TERMS

The Radiation Field

The specific intensity $I(\underline{r}, \underline{n}, \nu, t)$ of radiation at position \underline{r} , travelling in direction \underline{n} , with frequency ν , at time t is defined such that the amount of energy transported in a time interval dt by radiation of frequencies $\nu \rightarrow \nu + d\nu$ across an element of area dS into a solid angle $d\omega$ is

$$dE = I(\underline{r}, \underline{n}, \nu, t) dS \cos\theta d\omega d\nu dt \quad (\text{A.1})$$

where θ is the angle between the direction of the beam and the normal to the surface, see Figure A.1. In atmosphere theory we are only concerned with planar geometry. We employ cartesian co-ordinates (x, y, z) with planes of constant z being the layers of the atmosphere, the x and y dependence of all the variables can then be ignored. If \underline{n} is specified by two angles, polar θ and azimuthal ϕ then in one dimensional planar geometry I will be independent of ϕ . Hence we can write $I = I(z, \theta, \nu, t)$; z being measured positively upward, opposite to the direction of gravity. The variable θ is replaced with $\mu \equiv \cos\theta$, so $I = I(z, \mu, \nu, t)$. It should be noted that I has been defined in such a way as to be independent of the distance between the source and the observer, thus I at the source can be determined by measuring the amount of energy falling in a given time, within a specific frequency band, onto a receiver of known

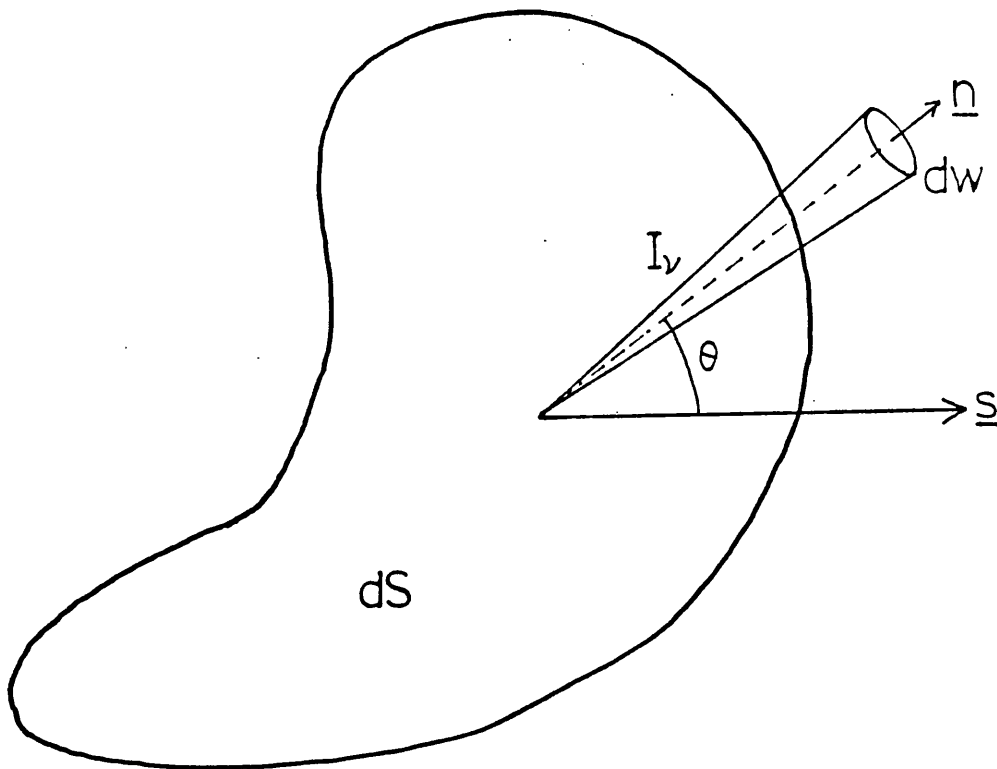


Figure A.1 Definition of specific intensity. Vector \underline{n} is the direction of propagation of the radiation while \underline{s} is the unit vector normal to the surface dS .

collecting area from a source subtending a definite solid angle. The requirement that dw is specified limits the determination of I to sources that are spatially resolved, e.g., nebulae, galaxies, the Sun, etc.

Mean Intensity and the Flux

In the description of the radiation field it is useful to employ various angular averages, or moments. The mean intensity is defined to be the straight average (zero-order moment) of the specific intensity over all solid angles, i.e., for one dimensional atmospheres

$$\begin{aligned}
J(z, \nu, t) &= (1/4\pi) \int_0^{2\pi} d\phi \int_{-1}^{+1} I(z, \mu, \nu, t) d\mu \\
&= 1/2 \int_{-1}^{+1} I(z, \mu, \nu, t) d\mu
\end{aligned}
\tag{A.2}$$

The flux is defined to be the net rate of radiant energy flow across an arbitrarily orientated surface dS per unit time and frequency interval, i.e.,

$$\underline{F}(\underline{r}, \nu, t) = \int I(\underline{r}, \underline{n}, \nu, t) \underline{n} d\omega
\tag{A.3}$$

Note that \underline{F} is the first moment of the radiation field with respect to angle. If the radiation field is symmetric with respect to an axis it follows that there will be a ray-by-ray cancellation of energy transport across a surface perpendicular to this axis and that the net flux is zero across this surface. For a planar atmosphere only F_z can be non-zero. We refer to this as "the" flux and write,

$$F(z, \nu, t) = 2\pi \int_{-1}^{+1} I(z, \mu, \nu, t) \mu d\mu
\tag{A.4}$$

Another 'flux', the 'astrophysical' flux is defined as

$$F(z, \nu, t) = (1/\pi) F(z, \nu, t)
\tag{A.5}$$

and further, regarding the flux as one of a series of moments with respect to μ , one may define the Eddington flux

$$\begin{aligned}
 H(z, \nu, t) &= (1/4\pi)F(z, \nu, t) = 1/4 F(z, \nu, t) \\
 &= 1/2 \int_{-1}^{+1} I(z, \mu, \nu, t) \mu d\mu \qquad (A.6)
 \end{aligned}$$

The energy received from a star by an observer can be directly related to the flux F_ν emitted at the surface. If the distance D to the star is very much larger than the stellar radius r_* , all the rays from the star can be considered parallel. The energy received per unit area normal to the line of sight is $df_\nu = I_\nu dw$ where dw is the solid angle subtended by the area. Considering Figure A.2 we see that $r = r_* \sin\theta$ so that the differential annulus has an area $dS = 2\pi r dr = 2\pi r_*^2 \mu d\mu$. The solid angle subtended, dw , is given by $dw = dS/D^2$ i.e., $dw = 2\pi (r_*/D)^2 \mu d\mu$. Integrating over the disc we find

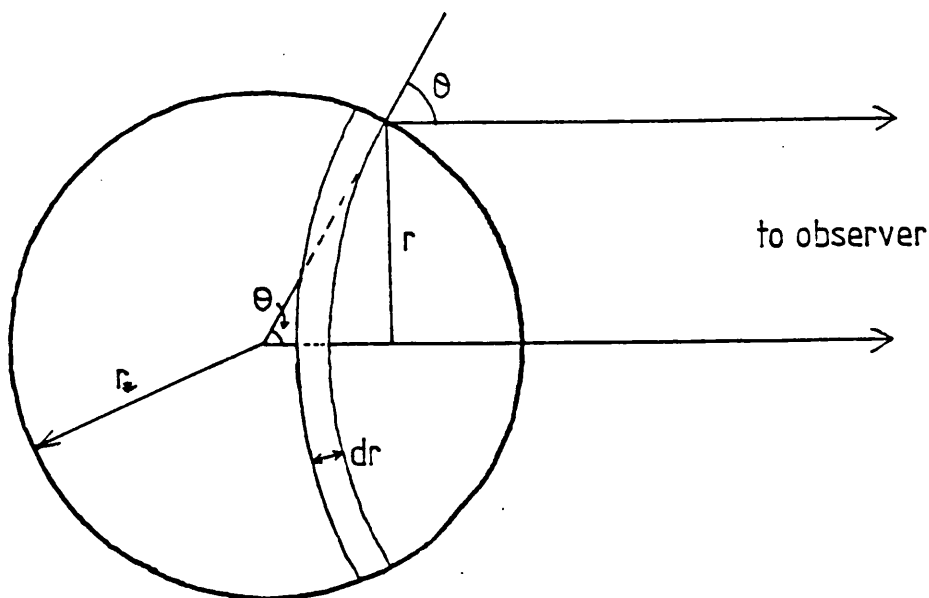


Figure A.2 Observational significance of the flux.

$$\begin{aligned}
 f_{\nu} &= 2\pi(r_*/D)^2 \int_0^1 I(r_*, \mu, \nu) \mu d\mu \\
 &= (r_*/D)^2 F(r_*, \nu)
 \end{aligned}
 \tag{A.7}$$

Thus the flux falls off as the inverse square of the distance. If the angular diameter is known then the absolute flux at the star can be found from the absolute flux at the Earth.

The Radiation Pressure Tensor

The second moment of the specific intensity yields a tensor quantity called the radiation pressure tensor, where

$$P(\underline{r}, \nu, t) = c^{-1} \oint I(\underline{r}, \underline{n}, \nu, t) \underline{n} \underline{n} dw
 \tag{A.8}$$

In a one-dimensional planar atmosphere we can define a single scalar P_R as "the" radiation pressure, where

$$P_R(z, \nu, t) = (4\pi/c)K(z, \nu, t)
 \tag{A.9}$$

$$\text{and } K(z, \nu, t) = 1/2 \int_{-1}^{+1} I(z, \mu, \nu, t) \mu^2 d\mu
 \tag{A.10}$$

$K(z, \nu, t)$ is the second moment of the radiation field in Eddington's notation.

The Interaction of Radiation with Matter

(i) The Extinction Coefficient

The removal of energy from the radiation field by matter is described by introducing a coefficient $\chi(\underline{r}, \underline{n}, \nu, t)$ called the extinction coefficient or opacity. It is defined such that the amount of energy δE removed from a beam with specific intensity $I(\underline{r}, \underline{n}, \nu, t)$ propagating in a direction normal to an element of material of cross-section dS and length ds into a solid angle $d\omega$ with frequency band $d\nu$ in a time dt is given by

$$\delta E = \chi(\underline{r}, \underline{n}, \nu, t) I(\underline{r}, \underline{n}, \nu, t) dS ds d\omega d\nu dt \quad (\text{A.11})$$

$\chi(\underline{r}, \underline{n}, \nu, t)$ is the product of an atomic absorption cross-section and the number density of absorbers summed over all states that can interact with photons of frequency ν . It has the dimension cm^{-1} and is isotropic for static media. In atmosphere theory we assume that the level populations can be calculated by local application of the thermodynamic equilibrium relations, this is the local thermodynamic equilibrium, or LTE, approximation.

It is useful to distinguish between the true absorption and scattering, hence we introduce $\kappa(\underline{r}, \nu, t)$ and $\sigma(\underline{r}, \nu, t)$ the absorption and scattering coefficients respectively. The total extinction is given by

$$\chi(\underline{r}, \nu, t) = \kappa(\underline{r}, \nu, t) + \sigma(\underline{r}, \nu, t) \quad (\text{A.12})$$

Corrections for stimulated emission, where radiation induces a downward transition from an upper state, must be included into the opacity because the process is proportional to $I(\underline{r}, \underline{n}, \nu, t)$ and it effectively cancels out

some of the opacity.

(ii) The Emission Coefficient

The emission of radiation from stellar material is described by introducing an emission coefficient $\eta(\underline{r}, \underline{n}, \nu, t)$ defined such that the amount of energy released from an element of material of cross-section dS and length ds , into a solid angle $d\omega$, within a frequency band $d\nu$, in a direction \underline{n} , in a time dt is,

$$\delta E = \eta(\underline{r}, \underline{n}, \nu, t) dS ds d\omega d\nu dt \quad (\text{A.13})$$

The emissivity is calculated by summing products of upper state populations and transition probabilities over all relevant processes that can release a photon at frequency ν . Its dimensions are $\text{ergs cm}^{-3} \text{ sr}^{-1} \text{ Hz}^{-1} \text{ sec}^{-1}$ and is isotropic for static media.

In the case of strict thermodynamic equilibrium (T.E.) we can find an important relation between the absorption and emission coefficients. If we consider an adiabatic enclosure in steady-state equilibrium containing a homogeneous medium we know that the material must have the same temperature T throughout (otherwise the second law of thermodynamics would be violated). Also, the radiation field must be isotropic and homogeneous otherwise a directional transport of energy would result, from beams of dissimilar energy travelling in opposite directions, again in direct violation of the second law of thermodynamics. If steady-state equilibrium is to be achieved then the

thermal emission is given by

$$\eta^t(\nu) = \kappa(\nu)I(\underline{n}, \nu) \quad (\text{A.14})$$

since the amount of energy absorbed by the material must equal the amount emitted (in a time interval dt , over a frequency range $d\nu$ and in an angle range $d\omega$). This is known as Kirchoff's Law. For strict T.E. $I_\nu = B_\nu(T)$ so,

$$\eta^t(\nu) = \kappa(\nu)B_\nu(T) \quad (\text{A.15})$$

Since we will be assuming LTE throughout our atmosphere then

$$\eta^t(\underline{r}, \nu, t) = \kappa(\underline{r}, \nu, t)B_\nu[T(\underline{r}, t)] \quad (\text{A.16})$$

The Transfer Equation

We will now examine the flow of energy through a fixed volume element in a definite time interval. We will assume that the radiation field is, in general, time dependent and that the material is at rest, χ and η will then be isotropic. If we consider the energy in a frequency interval $d\nu$, passing in time dt , through a volume element of length ds and cross-section dS orientated normal to a ray travelling in direction \underline{n} , into solid angle $d\omega$ (see Figure A.3). The difference between the incident and emergent energy must equal the amount created by emission from the material in the volume minus the amount absorbed. That is,

$$[I(\underline{r}+\Delta\underline{r}, \underline{n}, \nu, t+\Delta t) - I(\underline{r}, \underline{n}, \nu, t)] dS d\omega d\nu dt$$

$$= [\eta(\underline{r}, \underline{n}, \nu, t) - \chi(\underline{r}, \underline{n}, \nu, t) I(\underline{r}, \underline{n}, \nu, t)] ds dS d\omega d\nu dt$$

(A.17)

If we denote the path length along the ray as s then

$\Delta t = \Delta s / c$ and

$$I(\underline{r}+\Delta\underline{r}, \underline{n}, \nu, t+\Delta t) = I(\underline{r}, \underline{n}, \nu, t) + [c^{-1} (\partial I / \partial t) + (\partial I / \partial s)] ds$$

(A.18)

Substituting equation (A.18) into equation (A.17) we get

the transfer equation,

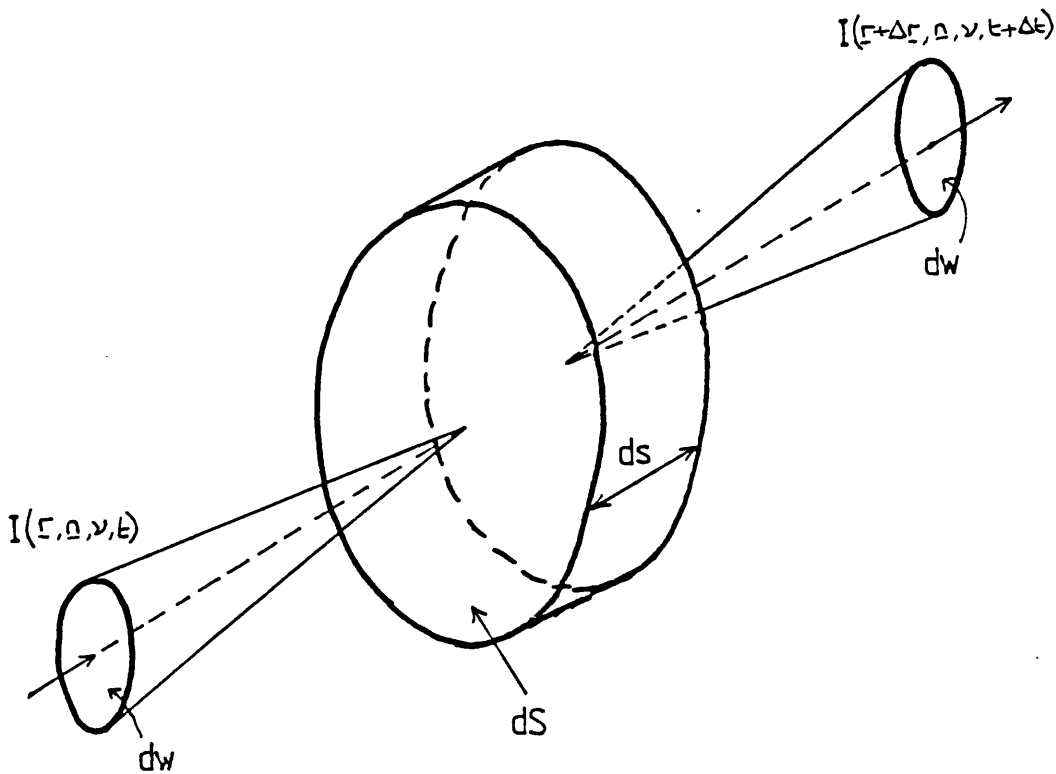


Figure A.3 Element of absorbing material considered in transfer equation.

$$[c^{-1}(\partial/\partial t) + (\partial/\partial s)]I(\underline{r}, \underline{n}, \nu, t)$$

$$= \eta(\underline{r}, \underline{n}, \nu, t) - \chi(\underline{r}, \underline{n}, \nu, t)I(\underline{r}, \underline{n}, \nu, t) \quad (\text{A.19})$$

The derivative along the ray may be re-expressed in terms of an orthogonal coordinate system

$$\frac{\partial I}{\partial s} = \left(\frac{\partial x}{\partial s}\right)\left(\frac{\partial I}{\partial x}\right) + \left(\frac{\partial y}{\partial s}\right)\left(\frac{\partial I}{\partial y}\right) + \left(\frac{\partial z}{\partial s}\right)\left(\frac{\partial I}{\partial z}\right)$$

$$= n_x \frac{\partial I}{\partial x} + n_y \frac{\partial I}{\partial y} + n_z \frac{\partial I}{\partial z} \quad (\text{A.20})$$

where n_x , n_y and n_z are the components of the unit vector \underline{n} . We can then re-write equation (A.19) as

$$[c^{-1}(\partial/\partial t) + (\underline{n} \cdot \nabla)]I(\underline{r}, \underline{n}, \nu, t)$$

$$= \eta(\underline{r}, \underline{n}, \nu, t) - \chi(\underline{r}, \underline{n}, \nu, t)I(\underline{r}, \underline{n}, \nu, t) \quad (\text{A.21})$$

For a one-dimensional planar atmosphere; $n_z = (dz/ds) = \cos\theta = \mu$; derivatives $(\partial/\partial x)$ and $(\partial/\partial y)$ are zero, so we obtain

$$[c^{-1}(\partial/\partial t) + \mu(\partial/\partial z)]I(z, \underline{n}, \nu, t)$$

$$= \eta(z, \underline{n}, \nu, t) - \chi(z, \underline{n}, \nu, t)I(z, \underline{n}, \nu, t) \quad (\text{A.22})$$

or, for the time-independent case,

$$\mu[(\partial I(z, \underline{n}, \nu)/\partial z)] = \eta(z, \underline{n}, \nu) - \chi(z, \underline{n}, \nu)I(z, \underline{n}, \nu) \quad (\text{A.23})$$

Equation (A.23) is the 'standard' transfer equation for plane-parallel model atmosphere calculations. For static media η and χ reduce to $\eta(z, \nu)$ and $\chi(z, \nu)$. If η contains scattering terms the transfer equation becomes an integro-differential equation containing angle and frequency integrals of I .

If we define an optical depth scale $\tau(z, \nu)$ such that $d\tau(z, \nu) = -\chi(z, \nu)dz$ we get the integrated absorptivity of the material along the line of sight as

$$\tau(z, \nu) = \int_z^{z^{\max}} \chi(z', \nu) dz' \quad (\text{A.24})$$

The negative sign is introduced so that the optical depth increases inwards thus providing a measure of how deep into the material an observer can see. We also define the source function to be

$$S(z, \nu) = \eta(z, \nu)/\chi(z, \nu) \quad (\text{A.25})$$

the ratio between the total emissivity and the total opacity. If we simplify the notation by suppressing the explicit reference to z and μ and denote the frequency dependence with a subscript ν then the transfer equation may be written in its standard form

$$\mu(\partial I_\nu / \partial \tau_\nu) = I_\nu - S_\nu \quad (\text{A.26})$$

If we enforce LTE then from equation (A.15) the source

function can be written as

$$S_{\nu} = B_{\nu} \quad (\text{A.27})$$

If we assume that the opacity is made up of a contribution from thermal absorption and emission plus a contribution from scattering then we can write

$$\chi_{\nu} = \kappa_{\nu} + \sigma_{\nu} \quad (\text{A.28})$$

and $S_{\nu} = (\kappa_{\nu} B_{\nu} + \sigma_{\nu} J_{\nu}) / (\kappa_{\nu} + \sigma_{\nu})$ (A.29)

Defining

$$e_{\nu} = \sigma_{\nu} / (\kappa_{\nu} + \sigma_{\nu}) \quad (\text{A.30})$$

then the source function becomes

$$S_{\nu} = e_{\nu} J_{\nu} + (1 - e_{\nu}) B_{\nu} \quad (\text{A.31})$$

If $e_{\nu} = 0$, i.e., no scattering, then the source function is simply the Planck function. In the solution to the transfer equation this would prove useful, as we shall see, but in the real case $e_{\nu} \neq 0$ and the solution of the transfer equation for J_{ν} has to be done by iteration.

Moments of the Transfer Equation

For the zero-order moment of the time-independent transfer equation for a one-dimensional planar atmosphere

we integrate equation (A.26) over all angles, i.e.,

$$\int_{-1}^{+1} \mu (\partial I_{\nu} / \partial \tau_{\nu}) d\mu = \int_{-1}^{+1} I_{\nu} d\mu - \int_{-1}^{+1} S_{\nu} d\mu \quad (\text{A.32})$$

Since in a static atmosphere S_{ν} is isotropic (from equation (A.25)) and substituting from equations (A.2) and (A.6), equation (A.32) reduces to

$$(\partial H_{\nu} / \partial \tau_{\nu}) = J_{\nu} - S_{\nu} \quad (\text{A.33})$$

The first-order moment of the time-independent transfer equation for a one-dimensional planar atmosphere is given by

$$\int_{-1}^{+1} \mu \mu (\partial I_{\nu} / \partial \tau_{\nu}) d\mu = \int_{-1}^{+1} \mu I_{\nu} d\mu - \int_{-1}^{+1} \mu S_{\nu} d\mu \quad (\text{A.34})$$

Again, for a static atmosphere, S_{ν} is isotropic so the integral of S_{ν} vanishes. Substituting from equations (A.9), (A.10) and (A.6) we get

$$[\partial p_{\mu}(\tau, \nu) / \partial \tau_{\nu}] = -(4\pi/c) H_{\nu} \quad (\text{A.35})$$

or $(\partial K_{\nu} / \partial \tau_{\nu}) = H_{\nu} \quad (\text{A.36})$

Radiative Equilibrium

In normal stars there is no creation of energy within the atmosphere itself, and the atmosphere purely transports outward the energy it receives. There are two basic methods of transporting energy through an atmosphere;

radiation and convection. For our purposes radiation is taken to be the dominant process involved and thus we have the condition of radiative equilibrium. If we consider a static medium with a time-independent radiation field passing through it then, from our previous discussions, the total energy removed from the beam is

$$\int_0^{\infty} \int d\omega \chi(\underline{r}, \nu) I(\underline{r}, \underline{n}, \nu) = 4\pi \int_0^{\infty} \chi(\underline{r}, \nu) J(\underline{r}, \nu) d\nu \quad (\text{A.37})$$

The total energy given to the radiation field by the material is

$$\int_0^{\infty} d\nu \int d\omega \eta(\underline{r}, \nu) = 4\pi \int_0^{\infty} \chi(\underline{r}, \nu) S(\underline{r}, \nu) d\nu \quad (\text{A.38})$$

η has been replaced from equation (A.25). The condition of radiative equilibrium requires that the total energy absorbed by a given volume of the material must equal the total amount emitted, thus at each point in the atmosphere

$$4\pi \int_0^{\infty} -\chi(\underline{r}, \nu) [J(\underline{r}, \nu) - S(\underline{r}, \nu)] d\nu = 0 \quad (\text{A.39})$$

From equation (A.33), for a one-dimensional planar atmosphere, we get

$$4\pi \int_0^{\infty} -\chi(z, \nu) (\partial H(z, \nu) / \partial \tau_{\nu}) d\nu = 0 \quad (\text{A.40})$$

i.e.
$$4\pi \int_0^{\infty} (\partial H(z, \nu) / \partial z) d\nu = 0 \quad (\text{A.41})$$

This implies that the total flux is constant in radiative equilibrium. If we assign a stellar temperature T_* to this

flux then radiative equilibrium is defined as

$$4\pi \int_0^\infty H_\nu d\nu = \int_0^\infty F_\nu d\nu = \sigma_s T_*^4 \quad (\text{A.42})$$

This condition is modified for regions where there is incoming radiation being absorbed (see Chapter 3.1).

The Transfer Equation - a formal solution

For our formal solution we will impose two boundary conditions; at the top

$$I(\tau_\nu=0, \mu, \nu) = 0 \quad (\text{A.43})$$

and at the bottom

$$\lim_{\tau \rightarrow \infty} I(\tau_\nu, \mu, \nu) e^{-\tau_\nu/\mu} = 0 \quad (\text{A.44})$$

The reason for the choice of the latter will become clear later on. Regarding S_ν as given then equation (A.26) is a linear first-order differential equation with constant coefficients and must therefore have an integrating factor. This is simply $\exp(-\tau_\nu/\mu)$ so that

$$\partial [I_\nu \exp(-\tau_\nu/\mu)] / \partial \tau_\nu = -(1/\mu) S_\nu \exp(-\tau_\nu/\mu) \quad (\text{A.45})$$

Integrating equation (A.45) gives

$$I(\tau_1, \mu, \nu) = I(\tau_2, \mu, \nu) e^{-(\tau_2 - \tau_1)/\mu} + (1/\mu) \int_{\tau_1}^{\tau_2} S_\nu(t) e^{-(t - \tau_1)/\mu} dt \quad (\text{A.46})$$

If we apply equation (A.46) at an arbitrary point in a semi-infinite atmosphere for just $\mu > 0$ (outgoing radiation only) and set $\tau_1 = \tau_\nu$ and $\tau_2 = \infty$ and impose equation (A.44) we get

$$I(\tau_\nu, \mu, \nu) = \int_{\tau_\nu}^{\infty} S_\nu(t) e^{-(t - \tau_\nu)/\mu} (1/\mu) dt \quad (\text{A.47})$$

$$(0 < \mu < 1)$$

For incoming radiation set $\tau_2 = 0$ and apply equation (A.43); we obtain

$$I(\tau_\nu, \mu, \nu) = \int_0^{\tau_\nu} S_\nu(t) e^{-(\tau_\nu - t)/-\mu} (1/-\mu) dt \quad (\text{A.48})$$

$$(-1 < \mu < 0)$$

Equations (A.47) and (A.48) will be used in the solution of the transfer equation at great depth, the Diffusion Approximation.

The Diffusion Approximation

At great depth in the atmosphere the radiation is effectively trapped, becoming isotropic and eventually approaching thermal equilibrium ($S_\nu \rightarrow B_\nu$). If we choose a

reference point $\tau_v \gg 1$ and expand S_v as a power series

$$S_v(t_v) = \sum_{n=0}^{\infty} [d^n B_v / d\tau_v^n] (t_v - u_v)^n / n! \quad (\text{A.49})$$

For $0 < \mu < 1$, using equation (A.47), we have

$$\begin{aligned} I_v(\tau_v, \mu) &= \sum_{n=0}^{\infty} \mu^n (d^n B_v / d\tau_v^n) \\ &= B_v(\tau_v) + \mu (dB_v / d\tau_v) + \mu^2 (d^2 B_v / d\tau_v^2) + \dots \end{aligned} \quad (\text{A.50})$$

For $-1 < \mu < 0$ we have a similar result from equation (A.48) which differs only by terms of order $\exp(-t/\mu)$. At great depth these terms vanish so equation (A.50) applies to the full range $-1 < \mu < 1$. By substituting equation (A.50) into the appropriate definitions for the moments we have

$$\begin{aligned} J_v(\tau_v) &= \sum_{n=0}^{\infty} (2n+1)^{-1} (d^{2n} B_v / d\tau_v^{2n}) \\ &= B_v(\tau_v) + 1/3 (d^2 B_v / d\tau_v^2) + \dots \end{aligned} \quad (\text{A.51a})$$

$$\begin{aligned} H_v(\tau_v) &= \sum_{n=0}^{\infty} (2n+3)^{-1} (d^{2n+1} B_v / d\tau_v^{2n+1}) \\ &= 1/3 (dB_v / d\tau_v) + \dots \end{aligned} \quad (\text{A.51b})$$

and

$$\begin{aligned} K_v(\tau_v) &= \sum_{n=0}^{\infty} (2n+3)^{-1} (d^{2n} B_m / d\tau_v^{2n}) \\ &= 1/3 B_v(\tau_v) + 1/5 (d^2 B_v / d\tau_v^2) + \dots \end{aligned} \quad (\text{A.51c})$$

The ratio of successive terms in each series is of the order $(1/\tau_v^2)$ which at great depth ($\tau_v \gg 1$) means the series converge rapidly so the first term in each series is all that is needed. So at the limit of large depth we may write

$$I_v(\tau_v, \mu) \approx B_v(\tau_v) + \mu(dB_v/d\tau_v) \quad (\text{A.52a})$$

$$J_v(\tau_v) \approx B_v(\tau_v) \quad (\text{A.52b})$$

$$H_v(\tau_v) \approx 1/3(dB_v/d\tau_v) \quad (\text{A.52c})$$

$$K_v(\tau_v) \approx 1/3(B_v(\tau_v)) \quad (\text{A.52d})$$

Considering equation (A.33) we have, in effect, the condition that at great depth the transfer equation reduces to

$$H_v = \frac{1}{3} \left(\frac{dB_v}{d\tau_v} \right) = - \frac{1}{3} \left(\frac{1}{\chi_v} \frac{\partial B_v}{\partial T} \right) \left(\frac{dT}{dz} \right) \quad (\text{A.53})$$

Equations (A.52) and (A.53) are used to set the lower boundary conditions in a semi-infinite atmosphere.

Hydrostatic Equilibrium

In a static atmosphere the weight of the overlying layers is supported by the total pressure. This balance determines the density structure of the medium. Thus

$$\nabla P = \rho g \quad (\text{A.54})$$

where; P is the total pressure, given by

$$P = P_g + P_R \quad (A.55)$$

P_g is the gas pressure, given by $P_g = NkT$ and P_R is the radiation pressure, given by equation (A.9) integrated over frequency, i.e.,

$$P_R = (4\pi/c) \int K_\nu d\nu \quad (A.56)$$

In equation (A.54) g is the gravity and ρ is the mass density. If we define a column mass m measured from the outer surface inward then

$$dm = -\rho dz \quad (A.57)$$

and equation (A.54) becomes $dP/dm = g$ which yields an exact integral $P(m) = gm + c$. This is clearly advantageous as the choice of m instead of z has no significant effect on the transfer equation. So we have $d(P_g + P_R)/dm = g$, expanding gives,

$$\begin{aligned} (dP_g/dm) &= g - (dP_R/dm) = g - (1/\rho)(dP_R/dz) \\ &= g - (\chi_\nu/\rho)(dP_R/d\tau_\nu) \end{aligned} \quad (A.58)$$

Substituting from equation (A.35) integrated over all frequencies we have

$$(dP_g/dm) = g - (4\pi/c) \int_0^\infty (\chi_\nu/\rho) H_\nu d\nu \quad (A.59)$$

This shows that the radiation forces tend to reduce the gravitational forces and produce a smaller pressure gradient in the atmosphere.

secondary poles approximately constant, but in this case the two poles are not located within the same area of the white dwarf. It may well be that the magnetic axis has shifted slightly between the two observations but the change in the apparent positions of the poles could also be due to different sections of a much larger 'polecap' turning on and off, possibly due to a change in the accretion rate. Generally, the derived sizes of the poles are larger than the values usually associated with these systems. This fact, plus the necessity for large polecaps in order to explain the quasi-sinusoidal lightcurves in EF Eri and V834 Cen (E1405-451), adds further weight to the argument for systematically larger polecaps for polar systems. The assumed values for polars usually arise from luminosity fits using black bodies which, as we saw in Chapter 5, give smaller f 's than expected, therefore geometrically large polecaps (geometrically large to give the correct lightcurve shape but the actual emitting area could still be small) of the order 10^{-2} to 10^{-3} of the white dwarf area may well be the norm in polar systems.

Considering the poles themselves; the effective temperature of the primary pole decreased from 120,000 K to 100,000 K which is most probably due to the decrease in the hard X-ray illumination from 99.9% to 44%. In the case of the secondary pole the effective temperature increased from 150,000 K to 215,000 K while the accreting area decreased by a factor of six. The accretion rates are 5.055×10^{15} g s⁻¹ for the primary pole and 1.308×10^{15} g s⁻¹ for the secondary pole so we see that the accretion rate onto the secondary has decreased, hence the reduction in size of the

MODEL ATMOSPHERES FOR ACCRETING SYSTEMS

by J.R.E. Brooker

ABSTRACT

This thesis presents the results of calculating model atmospheres for the accretion column of a magnetic white dwarf. A basic stellar atmosphere calculation is refined to model the specific conditions at the base of an accretion column. Calculated spectra for a variety of different input conditions are shown.

The calculated spectra are fitted with black body spectra in order to ascertain the errors associated with black body fitting of observed spectra.

Simulated lightcurves are calculated using these model atmosphere spectra. The resultant lightcurves are folded through the EXOSAT (European X-ray Observatory Satellite) detectors and used to fit lightcurves from the magnetic polar system AM Herculis.

Following the assumption that a thin accretion disc around a supermassive black hole is the central power source for active galactic nuclei (AGN's) a large grid of model atmospheres is calculated. This grid is then used to calculate the spectrum from such a disc.